PHYSICAL AND NUMERICAL MODELLING OF PIPE/SOIL INTERACTION EVENTS FOR LARGE DEFORMATION GEOHAZARDS

by

© Kenton Pike

A Thesis submitted to the

School of Graduate Studies

in partial fulfillment of the requirements for the degree of

Doctor of Philosophy

Faculty of Engineering and Applied Science

Memorial University of Newfoundland

October 2016

St. John's Newfoundland

ABSTRACT

Large deformation, differential ground movement events on buried pipelines involve large strain, nonlinear contact interaction, and soil strain localization and failure mechanisms. This study is focused on advancing finite element modelling procedures through laboratory tests to enhance soil constitutive models, physical models to verify simulation tools and algorithms to improve simulation tools that capture realistic behaviour for cohesive and cohesionless soils. The outcomes provide a robust framework for improved confidence in predicted outcomes to support engineering design.

The large deformation, ice gouge events, in cohesive soil, and pipe/soil interaction events, in cohesive and cohesionless soil, were simulated using the Coupled Eulerian Lagrangian (CEL) formulation within ABAQUS/Explicit modelling framework.

For ice gouge events, the numerical simulation was conducted using total stress analysis and the von Mises yield criterion. The numerical modelling procedures are improved by incorporating the distribution of soil properties, including elastic modulus and shear strength, throughout the domain without the need to develop complex user material subroutines. The numerical predictions were in agreement with available data in the literature and exhibited improved accuracy with respect to the keel reaction forces and subgouge soil deformations. The major contribution was to improve the benchmark and state-of-art for the numerical simulation of ice gouge events in cohesive soil.

Having developed confidence in the numerical simulation of large deformation events in cohesive soil, the research focused on advancing the modelling procedures for cohesionless soil. Large-scale, physical tests on lateral pipe/soil interaction events in sand

investigated the effects of pipe diameter (254 mm, 609.6 mm), burial depth to pipe diameter ratio (1, 3, 7) and soil density (14.7 kN/m^3, 15.6 kN/m^3). The main objective was to provide a verification basis for the numerical modelling procedures with respect to the force–displacement response and localized soil failure mechanisms. The physical tests contributed to the limited database, for the range of pipe diameters examined, and the first large-scale lateral pipe/soil interaction tests to provide detailed soil deformation and strain fields using particle image velocimetry (PIV) technique.

In parallel with the physical testing program, an enhanced constitutive model for cohesionless soil was advanced through the development of a user-subroutine that accounts for the effects of soil friction angle and dilation angle as a function of plastic shear strain. Laboratory triaxial and direct shear tests were used to characterize the strength parameters. This contribution has practical applications for pipe/soil interaction events in granular soils, particularly at shallow burial depth with low confining pressure, large soil deformations and strains, and dense sand states with strain softening behaviour.

Integrating the enhanced constitutive soil models, the numerical modelling procedures, were verified through comparison with the large-scale pipe/soil interaction tests conducted in this study and third-party physical modelling data. An extended study was conducted to assess the verified simulation tool across a range of practical engineering design scenarios. The outcomes from this study illustrated the improved accuracy and confidence in the numerical predictions, based on the tools developed in this study, that provide a significant contribution to the field of buried pipeline design against large deformation ground movement events.

ACKNOWLEDGEMENTS

During my program of studies at the Memorial University of Newfoundland, I have been afforded tremendous opportunities to develop personally and professionally. This positive and rewarding experience would not have been possible without the financial support provided by the Research and Development Corporation of Newfoundland and Labrador (RDC) under the Ocean Industries Student Research Awards program, the NSERC CREATE Offshore Technology program, the Wood Group Chair in Arctic and Harsh Environments Engineering, and the Faculty of Engineering and Applied Science. The funding contributions allowed me to maintain a comfortable lifestyle, which enhanced my ability to stay focused on the work. I was also able to travel to several key industry conferences to present my work which enriched the overall learning experience, expanded my professional network, gave me invaluable experience in summarizing and presenting my work, and allowed me to see different parts of the world. For this I am tremendously grateful.

I wish to thank my friends, colleagues and mentors that have supported me through this challenge. First and foremost, Dr. Shawn Kenny has been my mentor and guide for ten years at this point, in various capacities. His guidance has fostered the growth of my technical skillset and critical thinking capability that has served me well in industry and academia. His time and attention devoted to the countless hours of teaching, discussion, thorough review and constructive criticism has contributed immeasurably to my professional growth. I extend my sincere appreciation.

My co-supervisor Dr. Bipul Hawlader provided geotechnical engineering expertise and was fundamental in helping to guide the outcomes of this work. I thank him for his insight, time and attention. Dr. Mike Paulin was also on my supervisory committee and I thank him for his time and effort to review the work and provide insight. While not directly involved in my research, I would also like to thank Dr. Amgad Hussein for his support in helping me realize my goals extending from undergraduate studies.

I was privileged to be a visiting researcher at the world-class GeoEngineering Centre at Queen's University in Kingston, Ontario. It was a pleasure working with Master of Engineering student Alex Burnett, and lab technician Graeme Boyd, where I helped with the design, set up and execution of large-scale lateral pipe/soil interaction tests during a couple of extended visits to the facility. During that time, I was very fortunate to have helpful discussions with distinguished teachers Dr. Ian Moore, and Dr. Andy Take. The overall experience was memorable, and contributed greatly to the academic experience and technical outcomes of this work.

I would like to dedicate this thesis to my immediate family, my parents Paul and Laura, my sister Krysta, and my brother Klark. Their love, patience, understanding and encouragement was constant, and above all gave me the strength and motivation to stay the course. Of course my girlfriend Christa Marie had to exhibit the greatest amount of patience, and I am fortunate to have had her unconditional love and support through it all. I look forward to the next chapter, of life.

Table of Contents

ABSTRACT ii
ACKNOWLEDGEMENTS iv
Table of Contents vi
List of Tables x
List of Figures xii
Nomenclature xxii
List of Appendices xxvi
1 Introduction 1
1.1 Background and Motivation 1
1.2 Study Framework 8
1.3 Thesis Organization 11
2 Literature Review 16
2.1 Context 16
2.2 Ice Gouging in Cohesive Soil 17
2.2.1 Physical Model Testing of Ice Gouging 18
2.2.2 Numerical Simulation of Ice Gouging 25
2.3 Pipe/Soil Interaction in Cohesive Soil 31
2.3.1 Overview 31
2.3.2 Lateral Bearing Interaction 34
2.3.3 Oblique Lateral/Axial Interaction 40
2.4 Cohesionless Soil Behaviour 43
2.4.1 Peak Friction Angle 47
2.4.2 Critical State Friction Angle 62
2.4.3 Dilation Angle 68
2.4.4 Mobilization of Frictional Strength and Dilation 70
2.5 Pipe/Soil Interaction in Cohesionless Soil 76
2.5.1 Review of Previous Physical Tests 77
2.5.2 Failure Mechanisms 81
2.5.3 Summary of Guideline Recommendations 83
2.5.4 Previous Numerical Studies 89
3 Constitutive Models 97
3.1 Constitutive Model for Undrained Cohesive Soil 97

3.1.1 Constitutive Model Enhancements 101
3.2 Constitutive Model for Cohesionless Soil 107
3.2.1 The Mohr-Coulomb Model 107
3.2.2 Constitutive Model Enhancements 113
3.2.3 Characterization and Behaviour of Synthetic Olivine 126
3.3 Summary 133
4 Development of Finite Element Models 135
4.1 Coupled Eulerian Lagrangian Finite Element Modelling 136
4.1.1 Introduction 136
4.1.2 Initializing Eulerian Material 137
4.1.3 Eulerian-Lagrangian Contact 137
4.1.4 Solution Advection 138
4.2 Free-field Ice Gouging 139
4.2.1 Element Selection 139
4.2.2 Initial Conditions 140
4.2.3 Boundary Conditions 141
4.2.4 Keel/Soil Contact 142
4.2.5 Analysis Steps 143
4.3 Orthogonal Pipe/Soil Interaction 144
4.3.1 Element Selection 144
4.3.2 Initial Conditions 145
4.3.3 Boundary Conditions 146
4.3.4 Pipe/Soil Contact 148
4.3.5 Analysis Steps 148
4.4 Oblique Pipe/Soil Interaction 148
4.4.1 Element Selection 149
4.4.2 Initial Conditions 149
4.4.3 Boundary Conditions 149
4.4.4 Pipe/Soil Contact 150
4.5 Decoupled Ice/Soil/Pipeline Interaction 151
4.5.1 Element Selection 152
4.5.2 Boundary Conditions 152
4.5.3 Analysis Steps 152

4.6 Coupled Ice/Soil/Pipeline Interaction 153
4.6.1 Element Selection 155
4.6.2 Structural Model Extension 155
4.6.3 Analysis Steps 155
5 Physical Model Testing of Lateral Pipe/Soil Interaction in Cohesionless Soil 157
5.1 Large-Scale Lateral Pipe-Soil Interaction Physical Testing Program 157
5.1.1 Candidate Contribution to Testing Program 158
5.1.2 Testing Program and Results Summary 159
5.2 Analysis of Physical Test Data 166
5.2.1 Pipe Diameter and Model Scale Effects 169
5.2.2 Recommendation for Ultimate Lateral Soil Resistance 174
5.2.3 Recommendation for Ultimate Lateral Displacement 179
5.3 Summary 181
6 Finite Element Model Applications 184
6.1 Ice Gouging in Cohesive Soil 185
6.1.1 Mesh Sensitivity 185
6.1.2 Effect of Undrained Cohesive Constitutive Model 192
6.1.3 Verification of Free Field Ice Gouge Analysis 196
6.1.4 Effect of Ice Keel Shape on Subgouge Soil Deformation 207
6.1.5 Effect of Geotechnical Properties on Subgouge Soil Deformation 212
6.1.6 Summary 215
6.2 Pipe/Soil Interaction in Cohesive Soil 216
6.2.1 Lateral Pipe/Soil Interaction 216
6.2.2 Oblique Lateral-Axial Pipe/Soil Interaction 225
6.2.3 Summary 241
6.3 Coupled Ice/Soil/Pipeline Interaction in Cohesive Soil 242
6.3.1 Motivation 242
6.3.2 Numerical Modelling Framework 245
6.3.3 Relative Performance of Structural and Continuum Modelling Techniques – Parameter Case Study 267
6.3.4 Summary 279
6.4 Numerical Modelling of Lateral Pipe/Soil Interaction in Granular Material 281
6.4.1 Finite Element Analysis of Queen's Lateral Pipe/Soil Interaction Tests 282
6.4.2 Description of Constitutive Model Sensitivity Parameters 283

6.4.3 Mesh Sensitivity Study 288
6.4.4 Comparison of Physical and Numerical Results 297
6.4.5 Residual Friction Angle and Effective Cohesion Effect on Pipe/Soil Interaction 319
6.4.6 Summary 323
7 Conclusions and Recommendations 325
7.1 Overview 325
7.2 Cohesive Soil 326
7.2.1 Free-Field Ice Gouging 326
7.2.2 Pipe/Soil Interaction 327
7.2.3 Ice/Soil/Pipeline Interaction 328
7.3 Cohesionless Soil 329
7.3.1 Physical Modelling 329
7.3.2 Constitutive Modelling 330
7.3.3 Numerical Modelling Procedures 332
7.4 Recommendations 332
7.4.1 Pipeline Design Against Ice Gouging 332
7.4.2 Pipe/Soil Interaction 334
8 References 336
9 Appendices 355
Appendix A – Physical Pipe/Soil Interaction Test Dataset 355
Appendix B – Synthetic Olivine Direct Shear Test Results 359
Appendix C – Sand Characterization for Physical Test Dataset 361
Appendix D – Sand Characterization for Plane Strain Test Data 362
Appendix E – Sand Characterization for Triaxial Test Data 363
Appendix F – Relevant Publications: Ice/Soil/Pipeline Interaction in Cohesive Soil 364
Appendix G – Relevant Publications: Pipe/Soil Interaction in Cohesionless Soil 373

List of Tables

Table 2.1. Parameters to determine lateral bearing capacity factor (PRCI, 2009) 85

Table 3.1. Sample input deck material templates for undrained behaviour.....101

Table 3.2. Abaqus input parameters for varying E and s_u profiles 106

Table 3.3. Basic Mohr-Coulomb parameters for triaxial element test.....111

Table 3.4. Triaxial element test cases to demonstrate VUSDFLD subroutine 123

Table 3.5. Modified Mohr-Coulomb Input Deck Template (Case 1) 124

Table 4.1. Summary of finite element model solver and formulation applications.....135

Table 5.1. Summary of Queen's large scale lateral pipe/soil interaction test series.....161

Table 6.1. Mesh convergence study for free-field ice gouge simulations 186

Table 6.2. Analysis cases for undrained free-field ice gouging (24 CPUs).....192

Table 6.3. Free-field ice gouging constitutive model sensitivity study 198

Table 6.4. Mesh sensitivity analyses for lateral pipe/soil interaction in clay 217

Table 6.5. Analyses to test effect of constitutive model on lateral pipe/soil interaction .220

Table 6.6. Summary of FE runs for examination of friction properties.....234

Table 6.7. Structural model analysis definition 269

Table 6.8. Constitutive model sensitivity study (plasticity).....284

Table 6.9. Mesh sensitivity element sizes.....289

Table 9.1. Experimental lateral pipe/soil interaction data 355

Table 9.2. Summary of direct shear tests conducted on synthetic olivine sand.....359

Table 9.3. Sand characterization for physical lateral pipe/soil test dataset.....361

Table 9.4. Sand characterization for plane strain test data.....362

Table 9.5. Sand characterization for triaxial test data.....363

List of Figures

Figure 1.1. Spring analog for analyzing pipeline/soil interaction: a) actual continuum pipe/soil interaction b) mechanical idealization using beam and spring structural elements c) sample spring resistance curves (after ALA, 2001; PRCI, 2009).....3

Figure 2.1. Seafloor gouging by ice keel and subgouge deformation (Lele et al., 2013)..18

Figure 2.2. Three-dimensional schematic of subgouge soil displacement field.....20

Figure 2.3. Definition of gouge parameters.....22

Figure 2.4. Steady-state keel reaction forces in clay centrifuge tests (after Lach, 1996)..23

Figure 2.5. Centrifuge subgouge soil deformation data (Lach, 1996) and PRISE engineering equation.....24

Figure 2.6. Soil particle trajectories during ice gouging in clay (Been et al., 2008).....25

Figure 2.7. Winkler spring model for soil/pipeline structural analysis (Been et al., 2011) 26

Figure 2.8. Buried pipe nomenclature definitions.....33

Figure 2.9. Typical variation of plane strain stress ratio and volume change for a dense sand specimen (Jiang & Zhang, 2015).....46

Figure 2.10. Peak plane strain friction angle vs. confining pressure for sands.....49

Figure 2.11. Plane strain friction angle vs. confining pressure for sands 50

Figure 2.12. ϕ'_p-ϕ'_{cv} vs. ψ_p for triaxial test dataset.....51

Figure 2.13. Peak dilation angle vs. relative dilatancy index 52

Figure 2.14. Peak dilation angle vs. state parameter.....52

Figure 2.15. ϕ'^{tx}_p - ϕ'_{cv} vs. p' ($0.75 < Dr \leq 1.0$).....54

Figure 2.16. ϕ'^{tx}_{p} - ϕ'_{cv} vs. p' ($0.5 < Dr \leq 0.75$) 54

Figure 2.17. ϕ'^{tx}_{p} - ϕ'_{cv} vs. p' ($0.25 < Dr \leq 0.5$) 55

Figure 2.18. ϕ'^{tx}_{p} - ϕ'_{cv} vs. p' ($0.0 < Dr \leq 0.25$) 55

Figure 2.19. Difference between plane strain and triaxial compression friction angle vs. confining pressure 59

Figure 2.20. Critical state friction angle vs. confining stress for plane strain tests on various sands (after Tong, 1970) 63

Figure 2.21. Classification of grain shapes (Foseco, 2000) 64

Figure 2.22. Effect of particle shape on critical state friction angle (after Cho et al., 2006) 65

Figure 2.23. Measured shear strength of Ottawa sand and crushed limestone vs. void ratio at σ'_3 = 100 kPa (Guo & Su, 2007) 67

Figure 2.24. An alternative conceptual model for shear resistance of granular materials (Guo & Su, 2007) 67

Figure 2.25. Variation of friction angle and dilation angle (Anastasopoulos et al., 2007) 71

Figure 2.26. Idealized simple shear conditions: left) finite element computed shear strain, right) post-peak shear strain along the shear band (Anastasoploulos et al., 2007) 72

Figure 2.27. Strain softening reflection point (Hsu and Liao, 1998) 75

Figure 2.28. Depiction of shallow (left) and deep (right) failure modes for pipes (Rajah, 2014) 82

Figure 2.29. Shallow burial soil failure mechanisms (Burnett, 2015) 83

Figure 2.30. Force diagram for passive wedge failure in sands (Rajah, 2014) 86

Figure 2.31. Peak normalized lateral force vs. H/D ratio at ϕ = 45° based on guidelines and analytical equations 88

Figure 3.1. Undrained shear strength obtained from unconsolidated-undrained triaxial tests on fully saturated cohesive soil (after Das, 2002) 98

Figure 3.2. Schematic representation of Tresca and von Mises failure surfaces (Left: Wikipedia, 2016; Right: Tho et al., 2013) 100

Figure 3.3. Undrained shear strength and overconsolidation profile (after Lach, 1996) 102

Figure 3.4. Rigidity index vs. overconsolidation ratio (after Keaveny and Mitchell, 1986) 103

Figure 3.5. Temperature profile output for pseudo-depth dependency 105

Figure 3.6. Mohr-Coulomb yield surface in the meridional plane (Abaqus, 2016) 109

Figure 3.7. Mohr-Coulomb parameter effects 112

Figure 3.8. K_{70} approach of bilinear model for dimensionless force-displacement curve (Jung, 2011) 115

Figure 3.9. Friction angle dependency on mean effective pressure (after Lau and Bolton, 2011) 118

Figure 3.10. VUSDFLD subroutine flowchart for updating field variables 121

Figure 3.11. Three-dimensional representation of stress and strain dependent friction and dilation angles 122

Figure 3.12. Effective friction angle vs. mean effective stress response 125

Figure 3.13. Deviatoric stress vs. deviatoric strain response 125

Figure 3.14. Synthetic olivine gradation (Burnett, 2015) 127

Figure 3.15. Triaxial and plane strain friction angle and dilation angle variance with mean effective stress 130
Figure 3.16. Mobilized Friction and Dilation Angles 131
Figure 3.17. Deviatoric stress response for varying σ'_3; test data vs. FEA prediction (data from Lapos and Moore, 2002) 132
Figure 4.1. Operator split for Eulerian formulation (Benson and Okazawa, 2004b) 139
Figure 4.2. Free-field ice gouge model boundary conditions 142
Figure 4.3. Illustration of the volume fraction tool used in the CEL method 146
Figure 4.4. Orthogonal pipe/soil interaction model dimensions and boundary conditions 147
Figure 4.5. ALE pipe/soil interaction model 150
Figure 4.6. Lateral-axial oblique pipeline movement 150
Figure 4.7. Longitudinal pipe logarithmic strain due to subgouge soil displacement 151
Figure 4.8. Coupled ice/soil/pipeline model mesh design 153
Figure 4.9. Coupled ice/soil/pipeline interaction model 154
Figure 5.1. Test set up with the a) plan view (all dimensions in m) b) elevation view (definition of boundary conditions) c) 3-D oblique view (Burnett, 2015) 160
Figure 5.2. Uncorrected normalized force-displacement data a) dense b) loose 164
Figure 5.3. Dimensionless forces compared against guideline curves a) dense b) loose 165
Figure 5.4. Distribution of pipe diameters for lateral pipe/soil interaction tests 167
Figure 5.5. Distribution of H/D ratio for lateral pipe/soil interaction tests 167
Figure 5.6. Pipeline diameter vs. H/D ratio for lateral pipe/soil interaction tests 168
Figure 5.7. N_{qh} vs. H/D with varying D (loose conditions) 172

Figure 5.8. N_{qh} vs. H/D for varying D (dense conditions) 172

Figure 5.9. Distribution of D/d_{50} ratio for lateral pipe/soil interaction tests 173

Figure 5.10. N_{qh} vs. H/D (loose conditions) 175

Figure 5.11. N_{qh} vs. H/D ratio (dense conditions) 175

Figure 5.12. Lateral pipe/soil interaction test data in dense conditions for D > 75 mm .. 177

Figure 5.13. Lateral pipe/soil interaction test data in loose conditions for D > 75 mm .. 177

Figure 5.14. Normalized pipe displacement vs. guideline recommendation 179

Figure 5.15. Normalized pipe displacement vs. H/D ratio 180

Figure 6.1. Ice gouge simulation geometry schematic 187

Figure 6.2. Mesh design schematic for ice gouge simulation 188

Figure 6.3. Mesh size effect on horizontal subgouge soil displacement 189

Figure 6.4. Mesh size effect on horizontal keel reaction force 191

Figure 6.5. Mesh size effect on vertical keel reaction force 191

Figure 6.6. Undrained cohesive constitutive model effect on horizontal subgouge soil displacement 193

Figure 6.7. Undrained constitutive model effect on horizontal keel reaction forces 195

Figure 6.8. Undrained constitutive model effect on vertical keel reaction forces 195

Figure 6.9. Varying undrained shear strength and assumed yield stress profiles 199

Figure 6.10. Comparison of horizontal subgouge soil deformations 200

Figure 6.11. Comparison of vertical subgouge soil deformations 202

Figure 6.12. Comparison of global horizontal keel reaction forces 204

Figure 6.13. Comparison of global vertical keel reaction forces 204

Figure 6.14. Berm height/gouge depth vs. gouge depth/gouge width in clay 205

Figure 6.15. Experimental and numerical soil berm development 206
Figure 6.16. Analyzed keel shapes, from left to right: (a) shallow angle, (b) rectangular prism, (c) gouge curvature, and (d) transverse curvature 211
Figure 6.17. Shallow and steep keel induced subgouge soil displacements 212
Figure 6.18. Undrained shear strength profiles of some Beaufort Sea clays 213
Figure 6.19. Effect of varying soil strength profiles on horizontal subgouge soil deformations 214
Figure 6.20. Case 1 mesh size schematic 218
Figure 6.21. Initial resolution of pipe/soil contact interface 219
Figure 6.22. Mesh size effect on lateral pipe/soil interaction force-displacement response 219
Figure 6.23. Undrained constitutive model effect on lateral pipe/soil interaction force-displacement response 221
Figure 6.24. Lateral soil resistance vs. normalized pipe displacement 222
Figure 6.25. Failure mechanisms for lateral pipeline/soil interaction analysis with increasing H/D ratio 223
Figure 6.26. Estimate of horizontal bearing capacity factor as a function of H/D ratio ..225
Figure 6.27. Effect of mesh design on adaptive mesh configuration after pipe displacement 228
Figure 6.28. Effect of mesh density and design on the lateral force-displacement response 228
Figure 6.29. Pipe-soil interface contact during oblique lateral-axial pipe movement 229
Figure 6.30. Normalized axial soil reaction force vs. oblique angle 231

Figure 6.31. Normalized lateral soil reaction force vs. oblique angle 232

Figure 6.32. Axial-lateral interaction force diagram..... 233

Figure 6.33. Effect of friction coefficient on normalized axial soil resistance..... 235

Figure 6.34. Effect of clay sensitivity on normalized axial soil resistance..... 236

Figure 6.35. Effect of not enforcing the interface shear stress limit..... 237

Figure 6.36. Free-field ice gouge model tracer particle deformations..... 248

Figure 6.37. Centerline subgouge soil displacement in horizontal direction against subgouge depth 249

Figure 6.38. Centerline subgouge soil displacement in vertical direction against subgouge depth..... 250

Figure 6.39. Free-field subgouge soil displacements from CEL model and PRISE equation..... 251

Figure 6.40. Plane strain model for CEL FEA soil resistance curves..... 254

Figure 6.41. Plastic strain (max. in-plane principal) contours for CEL pipe/soil interaction analyses 255

Figure 6.42. Force-displacement curves 257

Figure 6.43. Seabed reaction forces in free-field and coupled simulations 263

Figure 6.44. Pipe trajectory at gouge centerline 264

Figure 6.45. Comparison of free-field and coupled CEL subgouge soil displacements at the pipe springline..... 265

Figure 6.46. Structural model pipe displacements..... 271

Figure 6.47. Distribution of logarithmic axial strain for the decoupled structural models for the a) trailing and b) leading edges of the pipe 274

Figure 6.48. Effect of adhesion factor on structural pipe compressive strain (α_{LB} = 0.22, α_{UB} = 0.54) 276
Figure 6.49. Structural and continuum pipe displacements along the pipe axis 277
Figure 6.50. Comparative distribution of logarithmic axial strain for the decoupled structural models (Coupled CEL, CEL & Free Field CEL, CEL) and fully coupled continuum model along the a) trailing and b) leading edges of the pipeline 278
Figure 6.51. Case 4 variation of parameters 287
Figure 6.52. Case 5 variation of parameters 288
Figure 6.53. Force-displacement response mesh sensitivity (MC; H/D = 3).....290
Figure 6.54. Pipe uplift response mesh sensitivity (H/D = 3).....290
Figure 6.55. Case 1A plastic deviatoric strain contour 292
Figure 6.56. Case 1B plastic deviatoric strain contour 292
Figure 6.57. Case 1C plastic deviatoric strain contour 292
Figure 6.58. Case 1D plastic deviatoric strain contour 293
Figure 6.59. Force-displacement response mesh sensitivity (MMC; H/D = 3) 294
Figure 6.60. Pipe uplift response mesh sensitivity (MMC; H/D = 3).....294
Figure 6.61. Case 3A plastic strain deviatoric contour 296
Figure 6.62. Case 3B plastic deviatoric strain contour 296
Figure 6.63. Case 3C plastic deviatoric strain contour 296
Figure 6.64. Case 3D plastic deviatoric strain contour 297
Figure 6.65. Case 1 and 2 force-displacement response 299
Figure 6.66. Case 1 and 2 vertical pipe displacement.....299
Figure 6.67. Case 3 to 5 force-displacement response.....301

Figure 6.68. Case 3 to 5 vertical pipe displacement 301
Figure 6.69. Incremental displacement field plot; Test 07 H/D = 1 (Burnett, 2015).....303
Figure 6.70. Incremental shear strain plot; Test 07 H/D = 1 (Burnett, 2015).....303
Figure 6.71. Case 1 plastic deviatoric strain contour plot (H/D = 1).....304
Figure 6.72. Case 2 plastic deviatoric strain contour plot (H/D = 1).....304
Figure 6.73. Case 3 plastic deviatoric strain contour plot (H/D = 1).....305
Figure 6.74. Case 4 plastic deviatoric strain contour plot (H/D = 1).....305
Figure 6.75. Case 5 plastic deviatoric strain contour plot (H/D = 1).....305
Figure 6.76. Case 3 mean effective stress contour plot (H/D = 1).....306
Figure 6.77. Case 5 mean effective stress contour plot (H/D = 1).....306
Figure 6.78. Force-displacement response Case 1 and 2 (H/D = 3) 308
Figure 6.79. Pipe uplift response Case 1 and 2 (H/D = 3) 308
Figure 6.80. Force-displacement response Case 3 to 5 (H/D = 3).....310
Figure 6.81. Pipe uplift response Case 3 to 5 (H/D = 3).....310
Figure 6.82. Incremental displacement field plot; Test 11 H/D = 3 (Burnett, 2015).....312
Figure 6.83. Incremental shear strain plot; Test 11 H/D = 3 (Burnett, 2015).....312
Figure 6.84. Case 1 plastic deviatoric strain contour (H/D = 3) 313
Figure 6.85. Case 2 plastic deviatoric strain contour (H/D = 3) 313
Figure 6.86. Case 3 plastic deviatoric strain contour (H/D = 3) 314
Figure 6.87. Case 4 plastic deviatoric strain contour (H/D = 3) 314
Figure 6.88. Case 5 plastic deviatoric strain contour (H/D = 3) 314
Figure 6.89. Case 3 mean effective stress contour plot (H/D = 3).....316
Figure 6.90. Case 5 mean effective stress contour (H/D = 3).....316

Figure 6.91. Force-displacement response for Case 5 (H/D = 7) 317

Figure 6.92. Pipe uplift response for Case 5 (H/D = 7) 317

Figure 6.93. Plastic deviatoric strain contour plot (H/D = 7) 319

Figure 6.94. Strain softening to residual vs. critical state friction angle.....320

Figure 6.95. Effect of residual friction angle and cohesion on force-displacement response (H/D = 1).....322

Figure 9.1. Shear stress vs. horizontal shear box displacement.....360

Figure 9.2. Vertical displacement vs. horizontal shear box displacement.....360

Nomenclature

ACRONYMS

A	Angular particle shape
ALE	Arbitrary Lagrangian Eulerian
ASCE	American Society of Civil Engineers
CEL	Coupled Eulerian Lagrangian
FE	Finite element
FEA	Finite element analysis
MC	Mohr-Coulomb
MMC	Modified Mohr-Coulomb
OCR	Overconsolidation ratio
PRISE	Pressure ridge ice scour experiment
R	Rounded particle shape
SA	Subangular particle shape
SR	Subrounded particle shape

LATIN UPPERCASE

A_c	Pipe/Soil contact area
A', B'	Hyperbolic curve constants for P-y relationship
B	Gouge breadth (width)
D	Gouge depth, External pipeline diameter, Rowe's dilatancy factor
D_r	Relative density
C_u	Coefficient of uniformity
C_c	Coefficient of consolidation
E	Young's Modulus
F_m, F_{max}	Maximum soil resistance against pipeline movement
F_{res}	Residual soil resistance against pipeline movement
G	Soil shear modulus
G_s	Specific Gravity
H	Soil depth to pipeline springline, i.e. centerline (burial depth)
H_c	Soil depth to top of pipeline (cover depth)
H_e	Soil depth to bottom of pipeline (embedment depth)

I_r	Rigidity index
I_R	Relative dilatancy index
K	Bulk soil modulus, Janbu coefficient
K_0	At-rest lateral earth pressure coefficient
K_h	Horizontal soil stiffness
L	Pipeline length
N_{qh}	Horizontal bearing capacity factor for sand (0 for ϕ=0°)
N_{ch}	Horizontal bearing capacity factor for clay (0 for c=0)
N_{ch}*	Horizontal bearing capacity factor associated with soil strength
PI	Plasticity index
P, P_u	Lateral soil resistance against pipeline movement, ultimate
Q, Q_u	Vertical soil resistance against pipeline movement, ultimate
R	Stress ratio
R_1	Resultant of the lateral earth pressure on left side of soil wedge
R_2	Resultant of shear and normal forces acting on passive soil wedge
T, T_u	Axial soil resistance against pipeline movement, ultimate
S_t	Soil sensitivity (ratio of undisturbed to remolded undrained shear strength)
W	Weight of soil included in soil wedge
W_P	Submerged pipe unit weight

LATIN LOWERCASE

c'	Effective soil cohesion
c_k	Factor for estimating horizontal soil stiffness
d_{50}	Mean grain size
e_{min}	Minimum void ratio
e_{max}	Maximum void ratio
f	Friction resistance factor
p'	Effective mean stress
$p_{u-oblique}$	Ultimate oblique soil resistance against pipeline movement per unit length
$\bar{p}$	Lateral soil resistance normalized by P_u
q	Deviatoric stress
s_u	Soil undrained shear strength

t	Pipe wall thickness
x	Axial pipe movement
x_u	Axial pipe movement to achieve maximum soil resistance
y	Lateral pipe movement
y_u	Lateral pipe movement to achieve maximum soil resistance
$\bar{y}$	Lateral pipeline displacement normalized by y_u
z	Vertical pipe movement
z_u	Vertical pipe movement to achieve maximum soil resistance

GREEK

α	Interface adhesion factor
β	Factor to account for soil weight
δ	Interface friction angle
δx_f	Horizontal direct shear displacement at start of residual shear stress
δx_p	Horizontal direct shear displacement at peak shear stress
δx_y	Horizontal direct shear displacement at soil yield
γ	Total soil unit weight
γ'	Submerged unit weight of soil
γ_d	Dry soil unit weight of soil
γ_w	Unit weight of water
γ_{dev}^p	Plastic deviatoric (octahedral) shear strain
γ_f^p	Plastic deviatoric shear strain at onset of critical state
δ	Interface friction angle
μ	Interface tangential friction coefficient
ϕ'	Effective internal friction angle
ϕ'_{mob}	Mobilized effective internal friction angle
ϕ'_{cv}	Constant volume friction angle (critical state)
ϕ_f	Rowe's friction angle
ϕ_μ	Interparticle friction angle
ϕ_p^{DS}	Peak friction angle from direct shear test
τ_{max}	Maximum interface shear strength

ψ	Soil dilation angle
ψ_{mob}	Mobilized soil dilation angle
ψ_{p}	Peak soil dilation angle
ν	Poisson's Ratio
σ'_{N}	Effective normal stress
σ'_{V}	Effective vertical soil stress
σ_3	Confining pressure
Ψ	State parameter
ϵ_N	Octahedral normal strain
ϵ_a^p	Axial plastic strain
ϵ_r^p	Radial plastic strain
ϵ_v^p	Volumetric plastic strain

List of Appendices

Appendix A – Physical Pipe/Soil Interaction Test Dataset.....355

Appendix B – Synthetic Olivine Direct Shear Test Results 359

Appendix C – Sand Characterization for Physical Test Dataset.....361

Appendix D – Sand Characterization for Plane Strain Test Data 362

Appendix E – Sand Characterization for Triaxial Test Data 363

Appendix F – Relevant Publications: Ice/Soil/Pipeline Interaction in Cohesive Soil 364

Appendix G – Relevant Publications: Pipe/Soil Interaction in Cohesionless Soil 373

1 Introduction

1.1 Background and Motivation

Pipelines used for hydrocarbon transport are often buried to meet operational requirements (e.g. flow assurance, hydrodynamic stability), and mitigate the effects of external loads and interference (e.g. geohazards, trawl gear, ship anchors, dropped objects, excavators). Common pipeline geohazards include slope failures, fault movements, earthquakes, and seabed erosion due to wave or current action. The surrounding soil imposes reaction forces on the pipeline due to operational load effects (i.e. pressure, temperature) and geohazards impose differential ground movement on buried pipelines. Large deformation geohazards could impose pipeline deformations and curvatures that may exceed serviceability (e.g. ovalization) and ultimate (e.g. tensile rupture, local buckling) limit states.

In arctic and northern latitudes, the presence of ice features, such as ice ridges and icebergs, with sufficient draft to contact the seabed may initiate large deformation, large strain ground movement events known as ice gouging (ice scouring), which represent significant potential threats to pipeline integrity (Palmer and Been, 2011). These pipeline geohazards exist in areas comprised of soil deposits with varying spatial distribution and stratigraphy characteristics in terms of soil type (i.e. cohesive, granular), strength (e.g. friction angle) and deformation behaviour (e.g. compaction, dilation).

Since there is active commercial interest in oil and gas exploration, development and production in these areas (and others) with varying seabed conditions, it is practical

to develop engineering tools that support pipeline engineering design in a range of soil conditions. Modelling soil/structure interaction in cohesive and cohesionless soils requires separate treatment of soil constitutive relationships to simulate undrained and effective stress behaviour depending upon rate of loading. The undrained shear strength typically governs the response in clay (cohesive) soils where loading events (e.g. ice gouging) are shorter in duration than the time required for pore water pressure dissipation. Typically, cohesive soils in northern latitudes are overconsolidated. In granular materials, the response is relatively complex in that density and pressure effects, and strain hardening and softening must be accounted for in the numerical modelling procedures.

The pipeline design philosophy against ice gouging has been to optimize burial depths to avoid contact with gouging ice keels and maintain strain demand due to subgouge soil deformation below acceptable levels (e.g. Lanan et al., 2001; King et al., 2009). Conventional practice for buried pipeline design is to idealize (Figure 1.1) pipe/soil interaction using a series of specialized beam and spring elements to represent the pipe and soil mechanical response, respectively (e.g. ASCE, 1984; ALA, 2001; PRCI, 2009). The available guidelines provide soil resistance–displacement recommendations for both clay under total stress conditions, and sand under effective stress conditions.

Structural type finite element (FE) modelling procedures are commonly used to simulate the pipe/soil interaction event using beam (with pipe cross section accounting for internal pressure) and discrete independent orthogonal (axial, lateral, and vertical uplift and bearing) spring elements (e.g. Kenny et al., 2004). To assess the effects of subgouge soil deformation due to ice gouging on the pipe mechanical response, the horizontal sub-

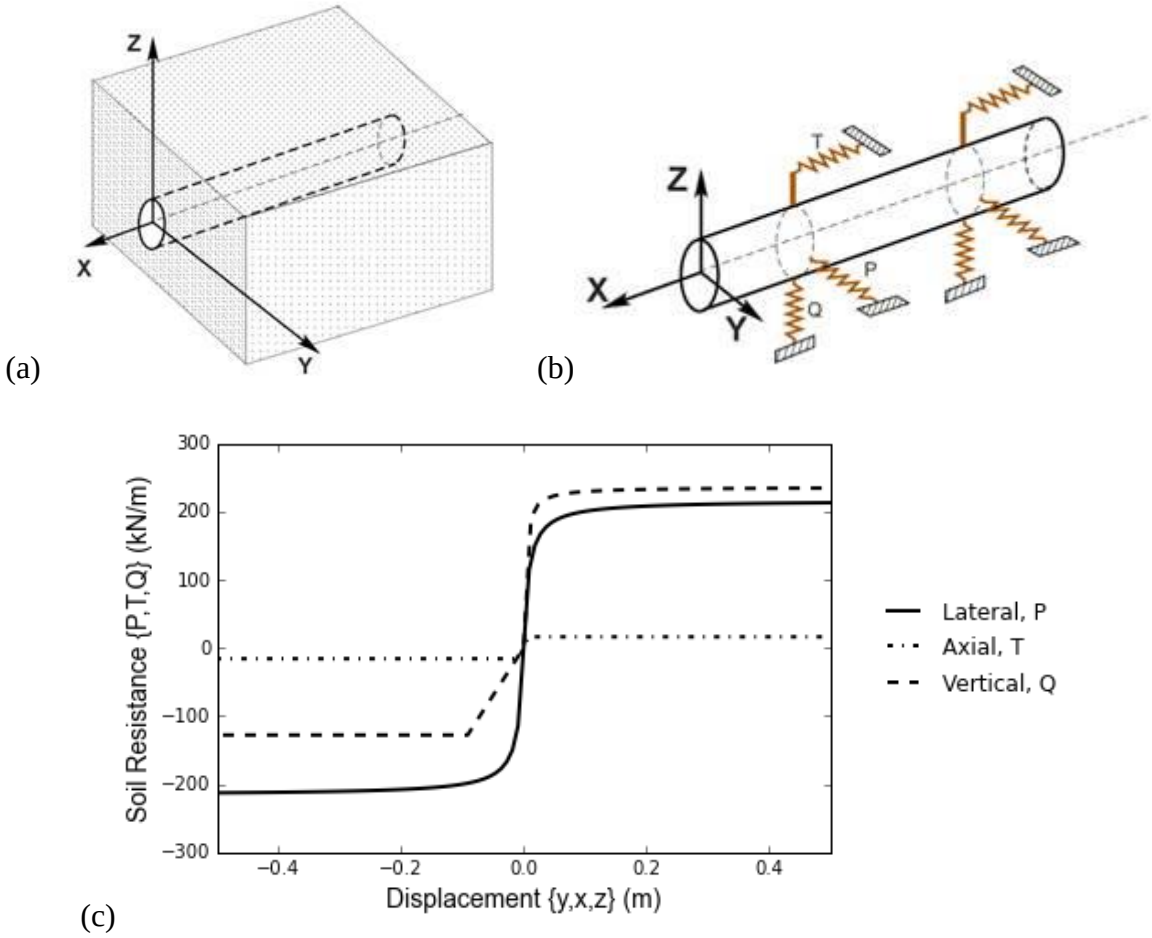

Figure 1.1. Spring analog for analyzing pipeline/soil interaction: a) actual continuum pipe/soil interaction b) mechanical idealization using beam and spring structural elements c) sample spring resistance curves (after ALA, 2001; PRCI, 2009)

gouge soil deformations, based on keel width and gouge depth, at the pipe burial depth are applied to the lateral soil springs (e.g. Lanan et al., 2001). The subgouge soil deformation field variation (mainly for clay) was an outcome of the Pressure Ridge Ice Scour Experiments (PRISE) during the 1990's, as outlined by Woodworth-Lynas et al. (1996). The empirical relationships were based on a limited number of centrifuge tests

with shallow keel attack angles and provide a conservative bound to the experimental dataset.

Recent studies have demonstrated that the structural beam/spring approach is better suited to problems with simple loading conditions (e.g. operational loads, small local displacements of soil or supports), but has been shown to be conservative in some cases of ice keel/soil/pipe interaction (e.g. Konuk et al., 2006; Abdalla et al., 2009; Peek and Nobahar, 2012). Peek and Nobahar (2012) discuss in detail the underlying assumptions in applying the structural model to the ice/soil/pipeline interaction scenario, and suggest the structural model superposition error is of critical importance. In addition, recent physical and computational modelling studies have highlighted other deficiencies in the structural model related to the independent soil spring response (i.e. lack of coupled interaction behaviour), which is considered to be important for large deformation ground movement events with oblique loading (Phillips et al., 2004a; Pike and Kenny, 2012a,b,c; Lele et al., 2013).

Advancements in software and hardware technology have led to recent developments in three-dimensional (3D) continuum FE tools to simulate complex, nonlinear, large deformation problems, with contact, for problems in geomechanics with buried infrastructure. These robust 3D continuum simulation tools can be used to address model uncertainty of the structural beam/spring models and reliability of the predicted engineering outcomes. Continuum FE tools have been developed and partially validated for ice/soil and pipe/soil interaction in clay (e.g. Abdalla et al., 2009; Phillips and Barrett, 2010; Pike and Kenny, 2012a) and sand (e.g. Phillips and Barrett, 2011; Eskandari et al.,

2012; Lele et al., 2013). Integrating complementary tools, such as laboratory testing to develop constitutive models, and physical modelling to verify the numerical modelling procedures are needed to enhance confidence in the predicted outcomes.

Ice gouge events involve complex, nonlinear behaviour with large deformations and strains, elastic-plastic behaviour and contact interaction between the ice keel, seabed and buried pipe. Full-scale datasets on coupled ice keel/seabed/pipe interaction events are very limited and proprietary (e.g. Sancio et al., 2011). Consequently the strategy has typically been to utilize a decoupled problem that involves separate ice keel/seabed and pipe/soil interaction events.

There is greater volume of available studies (e.g. Barrette, 2011) on free-field (i.e. ice keel/seabed) ice gouge events from reduced-scale centrifuge (e.g. Hynes, 1996; Lach, 1996; Panico et al., 2012; Yang, 2009) and 1-g physical models (e.g. Been et al., 2008), and structural and continuum numerical modelling procedures (e.g. Phillips et al., 2010; Phillips and Barrett, 2011). Recent studies have been conducted for ice gouge events in sand and demonstrated correspondence with physical modelling data using effective friction angle (Panico et al., 2012) or dilation (Phillips and Barrett, 2011) softening material models, and complex material subroutines; such as NorSand (Eskandari et al., 2011).

Large-scale datasets for pipe/soil interaction events, in cohesive and granular soil test beds, are more common (e.g. Paulin, 1998; Trautmann, 1983) that can be used to verify pipe/soil interaction failure mechanisms and the soil force-displacement response. These studies simulate plane strain, rigid (negligible pipe deformation) pipeline

movement and have conducted tests mainly in sands across a range of parameters that include pipe diameter, pipe burial depth, soil unit weight, strength properties and loading directions. The physical data has been fundamental in the development of empirical relationships defining the force-displacement relationships during pipe/soil interaction events (e.g. ASCE, 1984; ALA, 2001; PRCI, 2009).

The numerical simulation of undrained pipe/soil interaction in clay (e.g. Popescu et al., 2002; Phillips et al., 2004a,b) and sand (e.g. Yimsiri et al., 2004; Jung and Zhang, 2011; Roy et al., 2016) is relatively well established. However, the majority of these studies used 2D plane strain element models that cannot be readily extended more complex 3D interactions involving severe soil deformation (e.g. ice/soil/pipeline interaction). The development and verification of large deformation explicit (e.g. Coupled Eulerian Lagrangian) numerical modelling procedures for pipe/soil interaction in cohesive and cohesionless materials was identified as a technical gap and is addressed in the present study.

Furthermore, in the analysis of free-field ice gouging in cohesive soils, studies generally assume uniform soil properties that are known not to exist in the field or in centrifuge test soil beds. The study addressed this shortcoming by proposing a method to account for varying shear strength and stiffness profiles using a straightforward method whereby the undrained shear strength and elastic modulus are specified using a dummy temperature field that is related directly to the soil depth. The model enhancement provided an improved response in terms of keel reaction forces and horizontal subgouge soil deformations. This is a significant technical outcome, as the approach is relatively

easy to implement, does not require a user subroutine, and helps improve the simulated response towards reducing uncertainty and conservatism.

Assembling the free-field and pipe/soil interaction aspects into a fully integrated complex 3D continuum finite element model has been achieved in previous work (Peek and Nobahar, 2012; Lele et al., 2013), though decoupling of the free-field subgouge soil displacement and pipe/soil interaction response does not provide a consistent basis for assessing the relative performance of the idealized structural models used in conventional engineering design. The present study addresses the influence of the buried pipe obstruction on the subgouge soil deformation field and performs the comparison on a consistent basis.

There was a requirement for granular constitutive models to account for strain hardening/softening that are relatively easy to implement, compared to complex user material subroutines (e.g. NorSand), in FEA for practical pipeline design applications. This study addresses this by developing a modified Mohr-Coulomb model that is formulated for 3D applications and is relatively straightforward to implement. The constitutive model is used with the CEL FE method applied to lateral pipe/soil interaction. The verification of the CEL method for this application was identified as a technical gap and was addressed in this study. A large-scale lateral pipe/soil interaction physical test program was conducted at Queen's University as part of the present study research scope to provide the necessary dataset as the basis for verification of the constitutive and numerical modelling procedures.

The present work presents a detailed summary and analysis of previously existing lateral pipe/soil interaction test data and summarizes the collaboration between Memorial University of Newfoundland, Queen's University and NSERC that involved large-scale lateral pipe/soil interaction tests in dry sand, laboratory mechanical soil testing, and development of continuum numerical tools. The experiments add to the large-scale test dataset for plane-strain pipe/soil interaction using synthetic olivine sand that has not been utilized previously, and provide state-of-the-art data analysis in terms of soil deformation and strain fields using a plane-strain test set-up that allowed for real-time image capture and post-processing using particle image velocimetry (PIV).

1.2 Study Framework

From the discussion presented in Section 1.1, pipeline design for ice gouging involves a multidisciplinary approach that requires collaboration across technical fields that include geotechnical engineering, pipeline engineering, ice mechanics, physical modelling, and numerical simulation. The present study focuses on aspects of geotechnical engineering and finite element modelling related to ice gouging, buried pipe/soil interaction, and fully coupled ice/soil/pipeline interaction events in clay, and lateral buried pipe/soil interaction events in sand. The integrated framework encompassed methodologies and philosophies from other researchers (e.g. Burland, 1987; Randolph and House, 2001) that incorporated laboratory testing, soil constitutive model development, physical modelling and advancement of FE modelling procedures. The majority of the finite element analysis was conducted using a relatively novel approach, the CEL method, which has emerged as the state-of-the-art for simulating large

deformation geomechanics problems. The expected outcomes can be used to support the development of practical, safe, reliable and cost-effective design solutions for challenging environments with large deformation pipeline geohazards.

The research conducted in this thesis study was conducted in two phases including: I) large deformation events in cohesive soil including free field and coupled ice gouge events, lateral and oblique lateral-axial pipe/soil interaction events, and II) large deformation lateral pipe/soil interaction events in cohesionless soil. The two-phase approach was developed to address the identified technology gaps, which is the motivational basis, and take advantage of an opportunity to conduct large-scale pipe/soil interaction tests at the Queen's GeoEngineering Center in cohesionless soil. Outcomes from the test program include contour plots of localized shear strain, produced using the Particle Image Velocimetry (PIV) technique, that were used in the verification of numerical modelling procedures for pipe/soil interaction events advanced in this thesis. The objectives for each research phase are summarized below.

Phase I: Free-field ice gouging, pipe/soil and coupled ice/soil/pipeline interaction in cohesive soil

- compilation and critical literature review on data characterizing ice gouge events for field conditions (e.g. geographic location, water depth, gouge geometry, probable ice feature type, soil type and soil strength parameters), physical modelling studies and numerical simulation investigations,

- compilation and critical literature review on physical modelling studies and numerical simulation investigations for lateral and oblique lateral-axial pipeline/soil interaction events,
- development and refinement of constitutive models for ice gouge and pipe/soil interaction events,
- development and verification of free-field ice gouge model using available centrifuge test data,
- assessment of the effects of oblique lateral-axial pipe movement, using continuum FE modelling procedures, to determine oblique failure envelopes,
- development of a simulation tool for coupled ice/soil/pipeline interaction in cohesive soil, and
- conduct a performance assessment between structural and continuum FE modelling procedures for ice gouge load effects on buried pipelines.

Phase II: Lateral pipe/soil interaction in cohesionless soil

- compilation and critical review of granular soil behaviour and assessment of available test data for plane strain and triaxial testing conditions;
- establish the requirements to refine the soil constitutive models for improving the computational simulations of large deformation soil/structure interaction events;
- establish procedures for translating soil strength parameters obtained from laboratory tests (e.g. direct shear, triaxial test) for use in constitutive models and numerical simulations (e.g. plane strain, 3D conditions);

- refinements to the soil constitutive model algorithms, via user subroutines, that account for the characterization of elastic soil response and progressive mobilization of soil strength parameters (e.g. friction angle, dilation angle) as a function of a deformation measure (e.g. plastic shear strain) and mean effective stress;
- compilation and critical review of available physical test data for lateral pipe/soil interaction in granular soils to assess the effects of soil density, burial depth ratio and pipe diameter on the ultimate soil resistance and corresponding mobilization distance to assess guideline recommendations and provide a comparison baseline for the large scale physical testing program conducted at Queen's University; and
- development and validation of a numerical simulation tool that is readily extendable to the more complex ice/soil/pipeline interaction scenario (3D capable numerical and constitutive formulation), based on the numerical simulation of the recently acquired Queen's dataset for pipe/soil interaction in cohesionless material.

1.3 Thesis Organization

The background information and motivation that drives this thesis study is addressed in further detail through the literature review (Chapter 2). The literature review has four main subheadings; the first two subsections are related to Phase I (cohesive soil) described above and explore conventional design of buried pipelines in geohazard areas, previous physical and numerical studies related to free-field ice gouging, lateral and oblique pipe/soil interaction, and coupled and decoupled ice/soil/pipeline interaction. The

Phase II (cohesionless soil) objectives required a detailed review of cohesionless soil behavior. A review of constitutive modelling relationships for granular materials, as determined from laboratory test (triaxial compression and direct shear) data, was conducted and applicable models are identified and outlined. This is followed by an overview of analytical models, and previous physical and numerical studies of lateral pipe/soil interaction in dry sand.

The constitutive models utilized for estimating cohesive and cohesionless soil behavior are introduced in Chapter 3. First, the constitutive model implemented for simulating undrained events in cohesive soil is described; the methodology associated with incorporating varying shear strength and elasticity profiles with soil depth is put forth. The Mohr-Coulomb constitutive model enhancements using a user defined field subroutine to account for mobilized friction and dilation angles with plastic deviatoric strain, and variation of peak properties with mean effective stress are also described. A review is also provided on existing laboratory test data for the synthetic olivine sand used in the large-scale lateral pipe/soil physical testing program conducted at Queen's University. The modified constitutive model parameters for synthetic olivine are formulated based on the existing data.

The following chapter (Chapter 4) describes the development of FE models used for the various study applications including free-field, coupled and decoupled ice gouge events, and lateral and oblique pipe/soil interaction events. The CEL FE method is used primarily due to its large deformation modelling capability that is required for ice/soil/pipeline interaction simulation. The CEL FE method is introduced at the

beginning of the chapter. The FE model for each application is described; some of the applications have overlapping aspects (e.g. application of the geostatic stress field), however, the models are separated for clarity.

Based on technical gaps identified in the literature study, a large-scale physical testing program to study lateral pipe/soil interaction in sand was designed and executed at the Queen's University GeoEngineering Centre; the literature review findings and the present study test program results are summarized in Chapter 5. Test data compiled in the literature study is summarized in Appendix A, Table 9.1. Present study data analysis was conducted on the variation of peak horizontal bearing capacity factor, and the corresponding pipe displacement, with burial depth ratio and soil density. Lower (loose conditions) and upper (dense conditions) bound equations to define the lateral soil spring resistance curves are proposed based on the test data, as a function of the H/D ratio. The proposed equations can be used in preliminary FEA studies to provide bounding envelopes on the buried pipe/soil interaction response.

The progression of the literature review, constitutive and numerical model development is culminated in Chapter 6 whereby the integrated framework is applied to simulating large deformation pipe/soil interaction events in cohesive and cohesionless soils. The following briefly outlines the constitutive and finite element model applications:

- The free-field ice gouge FE model is validated against centrifuge test data with improved keel reaction force and subgouge soil deformations realized when realistic soil conditions are incorporated;

- Lateral pipe/soil interaction is simulated to verify the numerical model predictions against existing engineering guidelines and previous numerical model results.
- The lateral-axial soil reaction response envelope is assessed using undrained interface behavior showing that the maximum axial resistance is controlled by the mobilized frictional interface shear strength related to the clay sensitivity.
- The coupled ice/soil/pipeline interaction is simulated to provide a comparative assessment of the performance of decoupled structural models. This builds on previous work that used the decoupled subgouge soil deformation field not accounting for the pipe obstruction influence on the subgouge soil flow. This ties together the free-field ice gouge and orthogonal pipe/soil interaction FEA models developed, and applied in the previous subsections, in a case study example of the decoupled and coupled approaches to assessing pipeline response to ice gouge events. The results and outcomes from this application subsection were published in a special edition of the Canadian Geotechnical Journal on Pipeline Geotechnics (Pike and Kenny, 2016).
- In the final application subsection, the modified Mohr-Coulomb constitutive model and CEL FE model for lateral pipe/soil interaction is utilized to simulate the Queen's large-scale physical test results in dense sand. The results indicate the improved force-displacement and strain localization response when strain hardening and softening are incorporated.

Finally, conclusions are drawn from the work and recommendations for further research and development are put forth. Several publications were published over the course of study; eight (8) conference papers and two (2) journal manuscripts. The first page of each paper is provided Appendices E and F. Including the first page only limits the size of this document while providing an abstract to guide the reader.

2 Literature Review

2.1 Context

A comprehensive review of the current knowledge base on pipe/soil interaction and ice gouge events, with a focus on large deformation ground movement, is presented. The literature review explores the use of empirical and analytical solutions, laboratory testing, physical modelling and numerical methods that frame the context and motivation for the investigations conducted in this thesis. Confidence in advancing finite element procedures to simulate the complex, nonlinear coupled ice gouge/pipe/soil interaction events requires an understanding of parameters influencing soil constitutive behaviour, subgouge soil deformation and failure mechanisms during free-field ice gouge events, and large deformation pipe/soil interaction events, as a subset of the fully coupled ice gouge problem. These aspects are addressed in the following subsections.

This thesis considers large deformation pipe/soil interaction events in both cohesive and cohesionless soils to address the development of finite element tools for suitable application to areas with natural soil variability. The first half of the literature review examines the knowledge base for ice gouging, pipe/soil interaction and coupled ice/soil/pipe interaction in cohesive soil. The remainder of the review focuses on a review of cohesionless soil behavior and pipe/soil interaction in dry granular soil. The cohesive soil behavior is primarily a function of the undrained shear strength and elastic modulus, whereas cohesionless soil behavior is relatively complex and must consider stress level and relative density effects, and strain hardening and softening in order to capture realistic

soil behavior. For this reason, a separate subsection has been added that focuses on cohesionless soil behavior alone, as it has important implications for the numerical pipe/soil interaction analysis conducted later in the thesis.

2.2 Ice Gouging in Cohesive Soil

Through numerical modelling, examination of relic ice gouges and centrifuge testing, the Pressure Ridge Ice Scour Experiment (PRISE) – a joint industry project led by C-CORE – showed that significant soil displacements can occur beneath the base of gouging ice features (Woodworth-Lynas et al., 1996). This implied that avoiding direct pipeline contact with gouging features may not be sufficient to maintain pipeline integrity, as the large subgouge soil deformations could damage the pipeline. Hence, ice gouging demands trenches of sufficient depths to protect pipelines and other seabed facilities from loads associated with ice keel contacts and subgouge soil deformations (see Figure 2.1). These concepts were understood, in principle, before quantification, primarily through physical modelling, which demonstrated the potential significance of subgouge soil deformations on buried pipelines (Palmer, 1990). Design trenches are a sensitive decision in terms of hydrocarbon field development economics; hence, the rationale for selecting trench depths must be well understood. Subgouge soil deformations are a critical and complex issue that requires careful consideration of expected gouge characteristics, ice keel shape, seabed sediment type and soil stratification, and ice keel properties.

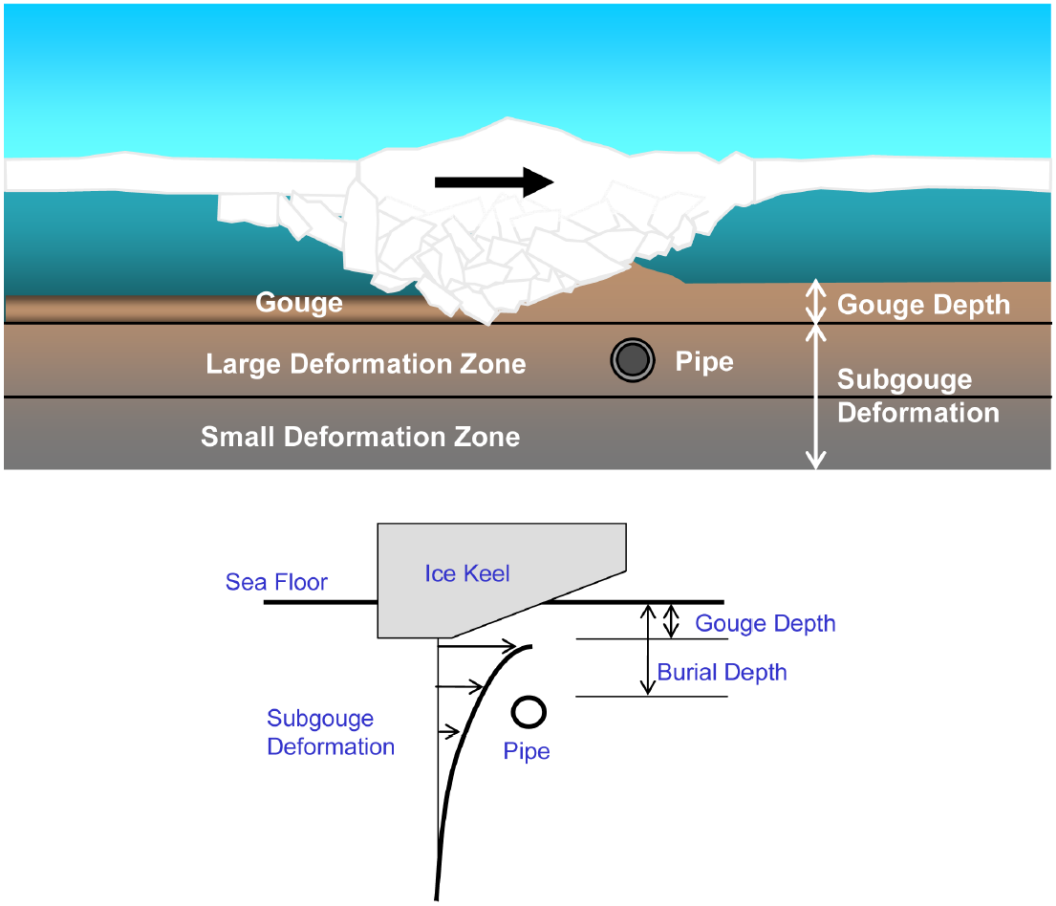

Figure 2.1. Seafloor gouging by ice keel and subgouge deformation (Lele et al., 2013)

2.2.1 Physical Model Testing of Ice Gouging

The original intent of the PRISE program was to validate FE ice gouge models using the centrifuge dataset and subsequently explore the effect of parameter variation on the subgouge soil deformation field using FE modelling as an independent tool. However, the Lagrangian based FE models, available at that time, were plagued by convergence issues and could not reach simulated steady-state gouging conditions necessary to extract the subgouge soil deformation field. Hence, based on a limited number of centrifuge tests

using prismatic indenters with a keel attack angle of 15 to 30 degrees, semi-empirical equations were developed to predict the subgouge soil deformation field in clay (Woodworth-Lynas et al., 1996).

The maximum lateral subgouge soil deformation at a coordinate corresponding to the gouge centreline (i.e. coordinate system origin) at the gouge depth was defined as:

$$u(0,0,0) = 0.6\sqrt{BD} \tag{2.1}$$

where the coordinates x, y, z are the gouge direction, the transverse lateral gouge direction and the transverse vertical gouge direction measured from the base of the keel (i.e. total depth – gouge depth), and B and D are the gouge breadth (width) and depth. The vertical subgouge attenuation function is defined by:

$$\frac{u(0,0,z)}{u(0,0,0)} = \exp\left(-\frac{2z}{3D}\right) \tag{2.2}$$

At a particular subgouge depth z (i.e. from the base of the keel, positive downwards), the transverse lateral subgouge soil deformation field is defined as:

$$\frac{u(0,y,z)}{u(0,0,z)} \begin{cases} = 1 \text{ if } y/B < 0.25 \\ = 0.5[1+\cos(2y/B-0.5)\pi] \text{ if } 0.25 < y/B < 0.75 \\ = 0 \text{ if } y/B > 0.75 \end{cases} \tag{2.3}$$

Equations (2.1) to (2.3) can be used to define a three-dimensional representation of the subgouge soil displacement field. Figure 2.2 shows an example of the deformation field (half-symmetry about the gouge centerline) for B = 10 and D = 2 in clay.

The current design practice for offshore buried pipelines in areas subject to ice gouging follows an empirical decoupled (i.e. ice/soil and pipe/soil interactions treated

separately) approach. As described in Lanan et al. (2001, 2011) for the Northstar offshore arctic pipeline design, the subgouge soil displacement field derived from the PRISE experiments (Woodworth-Lynas et al., 1996) described above was utilized.

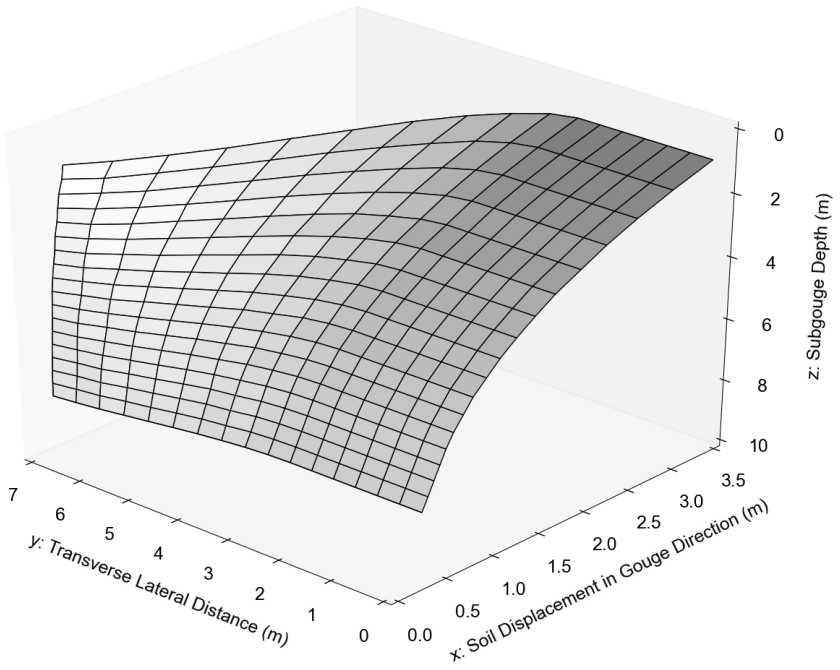

Figure 2.2. Three-dimensional schematic of subgouge soil displacement field

The issue of subgouge soil deformations has been the subject of study by several research groups that have approached the subject using reduced scale centrifuge testing (e.g. Woodworth-Lynas et al., 1996; Hynes, 1996; Lach, 1996; Schoonbeek and Allersma, 2006; Yang, 2009), 1g small-scale (e.g. 2013, Giuliani) and medium-scale laboratory testing (e.g. Been et al., 2008), and large-scale field testing (Sancio et al., 2011). Even more groups have used various numerical tools to simulate the ice gouge

problem in the following, non-exhaustive list of references including Yang and Poorooshasb (1997), Konuk et al., (2005), Kenny et al., (2007), Abdalla et al., (2009), Phillips and Barrett, (2010), Eskandari et al., (2012), Pike and Kenny (2011a), Pike et al., (2011b), Pike and Kenny (2012a,b), Panico et al., (2012), Peek and Nobahar, (2012), El-Gebaly et al., (2012), and Liferov et al., (2014).

The PRISE empirical equations (Woodworth-Lynas et al., 1996) provide conservative (high) estimates of subgouge soil displacements based on physical modelling. As discussed by Been et al. (2008, 2013), the estimates do not account for other parameters, which have been established in studies conducted after conclusion of PRISE, known to influence the behaviour:

- Soil strength and stiffness that has a significant influence on the extent and magnitude of subgouge soil deformations;
- Gouge geometry where the test data for the gouge width to depth ratios was greater than 6, however, the displacements scale with the square root of width and do not have any upper limit as defined in Equation (2.1);
- Angle of attack where the tests were carried out with shallow keel angles (15 and 30°), and the keel angle does not appear as a variable in the relationships but has a significant effect on the magnitude and extent of subgouge soil deformations, soil failure mechanisms and clearing processes.

Lach (1996) conducted a series of 9 centrifuge tests in clay using a smooth surface prismatic indenter with a keel angle of 15° for 8/9 tests (one test at 25°). The model

prototype width was 10 m for 8/9 tests (one test at 5 m). The steady-state gouge depth ranged from 0.4 to 2.2 m with an average magnitude of 1.2 m for the complete range of tests performed; the overall sample height was 18 m. The parameters are illustrated in the following Figure 2.3; note the depth beneath the base of the keel is considered positive downwards and is commonly referred to as the subgouge depth.

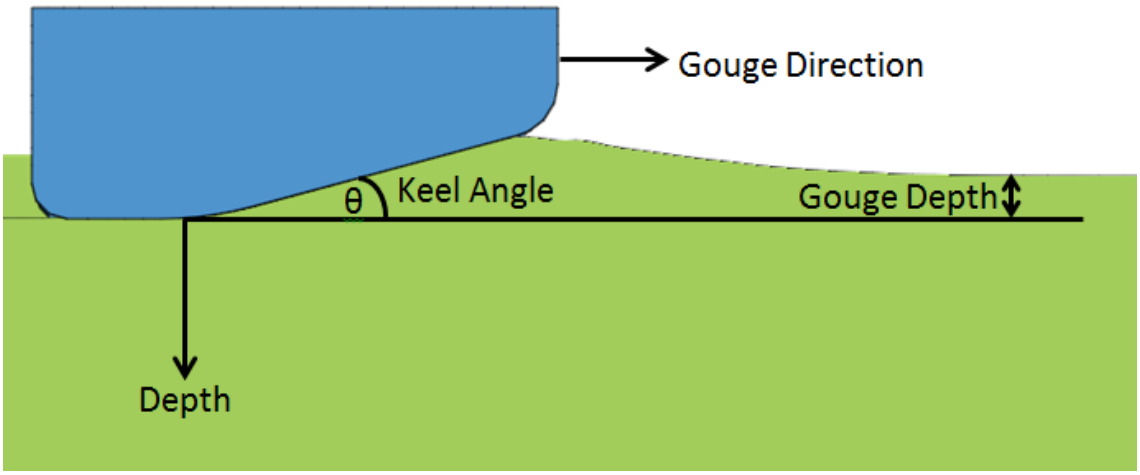

Figure 2.3. Definition of gouge parameters

Based on the test matrix examined by Lach (1996), the average steady-state horizontal and vertical keel reaction force ranged from 2.1 to 6.0 MN, and 6.0 to 17.6 MN, respectively. The vertical/horizontal force ratio ranged between 1.9 and 3.9, with an average value 3.0. The keel reaction forces in clay per unit keel width are shown to increase approximately linearly with gouge depth, as shown in Figure 2.4. The majority of the data points are for tests conducted with a 15° keel, with only one test at 25°. However, the clay test bed was relatively soft; typically about 17.5 kPa at the gouge depth

level. Hence, it is difficult to draw general conclusions without more test data over a broader range of conditions.

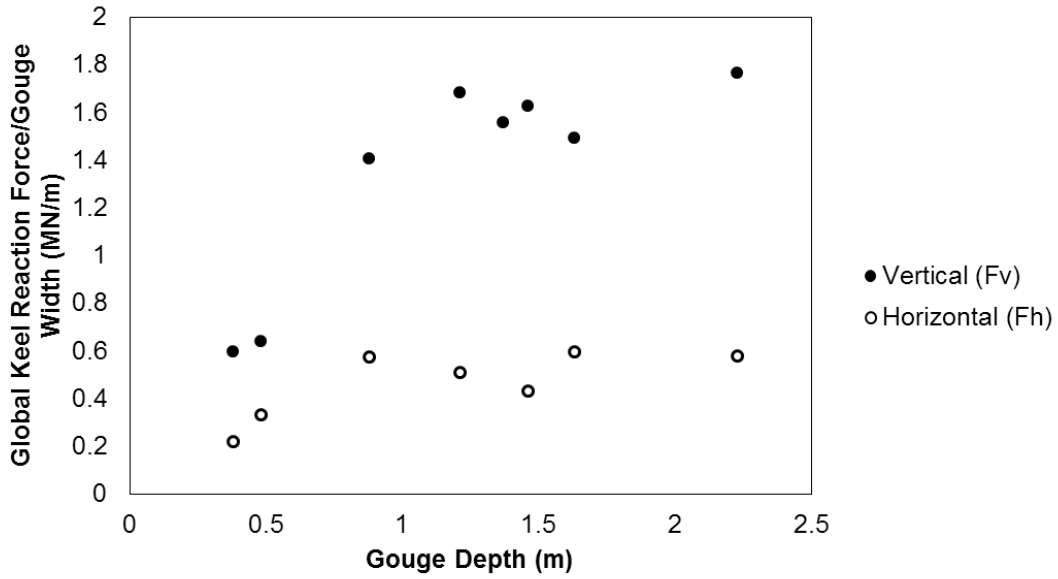

Figure 2.4. Steady-state keel reaction forces in clay centrifuge tests (after Lach, 1996)

The subgouge soil deformations for these tests (Lach, 1996) are plotted in Figure 2.5. The subgouge depth is normalized with the gouge depth for each test, and the horizontal soil displacement is normalized with the square root of the gouge width (or breadth), B, multiplied by the gouge depth, D; the $\sqrt{BD}$ normalization was suggested by Woodworth-Lynas et al. (1996) and is used to calculate the lateral soil displacement due to gouging in clays using the "PRISE engineering equation". The PRISE equation is plotted for reference, showing that it provides a conservative bound to the dataset.

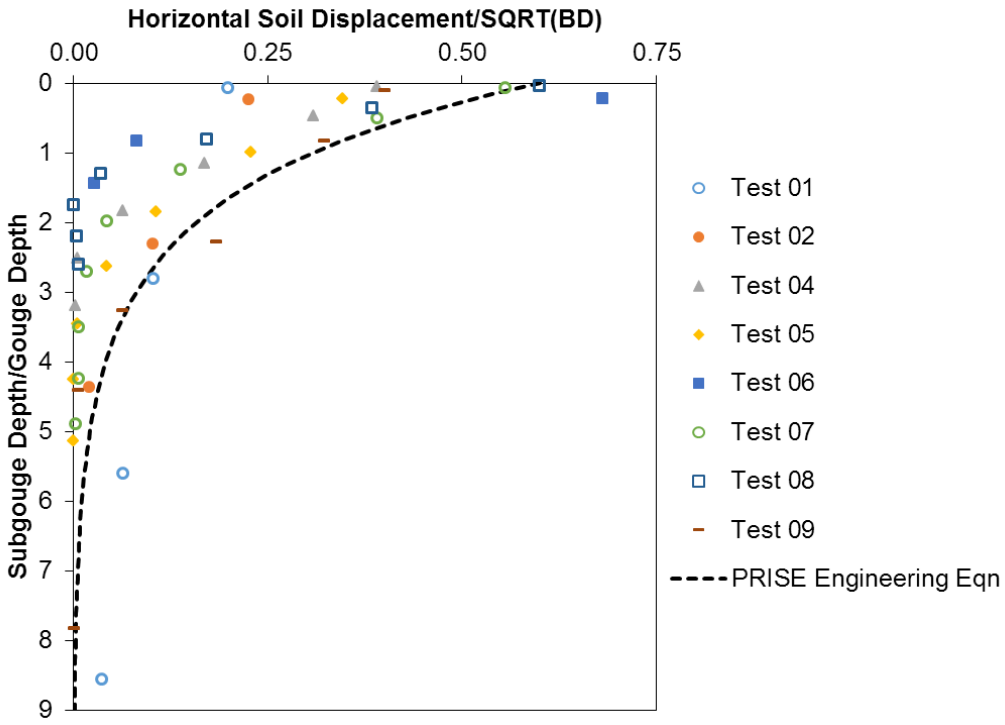

Figure 2.5. Centrifuge subgouge soil deformation data (Lach, 1996) and PRISE engineering equation

Been et al. (2008) conducted medium scale indenter tests in clay (s_u varied from 20 to 45 kPa) with gouge depths up to about 0.3 m, varying keel angle (15, 30, 45 degrees), and constant keel width (1.5 m) and shape. Empirical lateral subgouge soil displacement equations were developed considering the keel angle (α), soil rigidity index ($I_r = G/s_u$) and gouge depth (D_g).

Since soil clearing mechanisms vary depending on the keel angle (see Figure 2.6), which ultimately influences the subgouge soil deformation field, separate "tentative" equations defining the centreline lateral subgouge soil deformation were developed for relatively steep (30° and 45°) and shallow (15°) keel angles. While not included in the

empirical relationships, it was noted that the gouge width should be examined for its effect on the subgouge soil deformation profile; many of the deepest gouges are relatively narrow (Been et al., 2008). Related to work done for the Kashagan field project in the North Caspian, Been et al. (2013) presented additional sets of equations defining the subgouge soil displacement fields in soft and stiff clays.

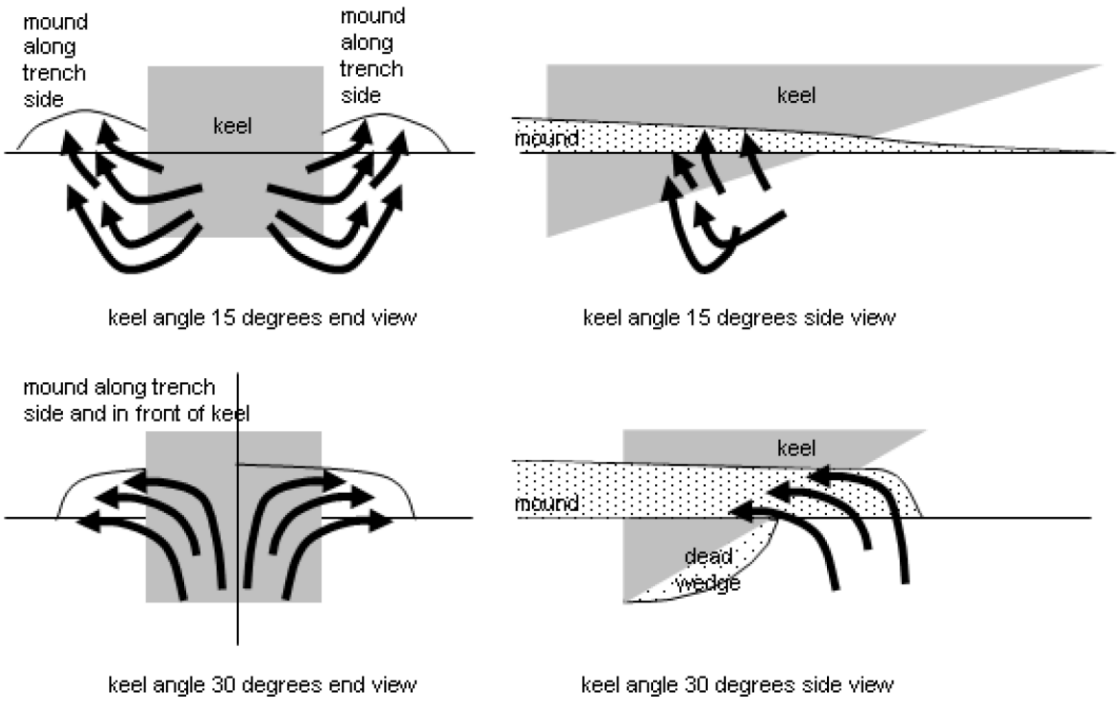

Figure 2.6. Soil particle trajectories during ice gouging in clay (Been et al., 2008)

2.2.2 Numerical Simulation of Ice Gouging

For the numerical modelling of pipe/soil interaction events, the soil behaviour is generally defined by discrete orthogonal springs (e.g. Figure 2.7) defining the

force/displacement response in the lateral, axial, vertical uplift and vertical bearing directions. The spring curves are defined using available guidelines for the design of buried pipes (ASCE, 1984; ALA, 2001; PRCI, 2009).

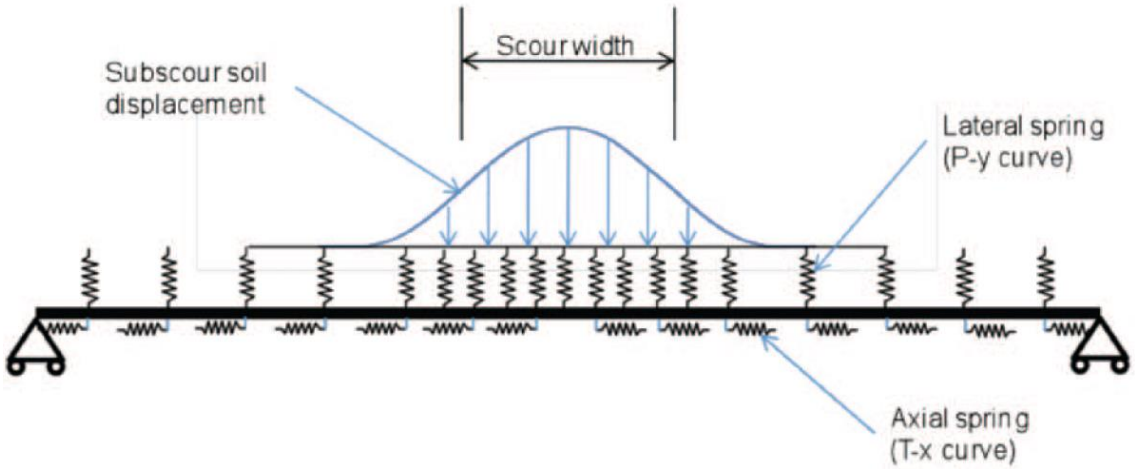

Figure 2.7. Winkler spring model for soil/pipeline structural analysis (Been et al., 2011)

There are several idealizations and assumptions in the decoupled approach that are considered limitations:

- Directional Load Coupling: There is no interaction between the vertical, lateral and axial springs used to represent the soil; i.e. there is no directional soil spring coupling. For example, when the pipe moves at some angle in the lateral-axial plane, it has been shown that the axial interaction force increases for small angles of coupled lateral movement (Pike and Kenny, 2012c).

- Continuum or “Slice-to-Slice” Coupling: There is no interaction between soil springs at different locations along the length of the pipeline. The force in a spring relies only on the displacement at a point, and is not influenced by adjacent springs; Peek and Nobahar (2012) call this “slice-to-slice” coupling.
- Superposition Errors: The superposition assumption leads to a conflict, or error, where the imposed subgouge soil deformations are based on the free-field subgouge soil displacement field. The pipe, however, does not follow the exact movement of the soil particles due relative differences in stiffness and the buried pipe obstructs or influences the subgouge displacement/plastic strain field (e.g. Konuk et al., 2005; Pike et al., 2011b).
- Geometric Nonlinearity: Further reductions in the available soil resistance to pipe motion may be caused by the removal of material in the vicinity of the pipeline. As discussed by Peek and Nobahar (2012), this should also be part of the superposition error as it arises from the nonlinear soil response, to which superposition does not apply.
- Soil Material Nonlinearity: Peek and Nobahar (2012) discuss that since the ice gouging process involves severe soil strains, the soil strength to resist pipeline motion may decrease due to strain softening during the ice gouge process, as opposed to the subset pipe/soil interaction scenario used to derive the soil springs where the ice gouging stresses and strains are not present. In comparing the 3D continuum response to the structural model, this effect would likely only be evident if the reduction of shear strength (be it undrained shear strength for

cohesive materials, or friction softening for granular materials) with incremental plastic shear strain were accounted for in the constitutive soil behaviour.

- Beam Mechanical Response: Conventional pipe elements do not allow for section ovalization due to bending, which can lead to differences in the curvature response in comparison with continuum models, and thus leads to potential differences in the predicted pipe strain response.

Konuk et al. (2006) evaluated the adequacy of the Winkler-type model for simulating the pipe/soil response during an ice gouge event. The approach involved decoupling the ice gouge event using an idealized beam/spring model, representing the pipe/soil interaction, subject to an imposed subgouge soil displacement field. The horizontal soil spring resistance versus displacement relationship was defined for undrained shear strengths of 10 kPa and 50 kPa. The 3D pipe response attained from the ALE numerical model was compared with the Winkler-type model results. The subgouge soil displacement field applied in the Winkler-type model were derived from two sources: 1) the free-field deformations as predicted by the ALE simulation and 2) the PRISE engineering equation. However, the soil properties used in the ALE simulation did not correlate with the cohesive soil properties used to generate the soil spring load-deformation relationships used in the Winkler-type beam/spring model.

Nevertheless, the analysis suggests that the PRISE model is conservative, which is consistent with outcomes from other research studies (e.g. Abdalla et al, 2009; Peek and Nobahar, 2012). Konuk (2009) suggested that the Winkler-type approach involves a

larger level of conservatism and uncertainty than usually assumed by design engineers for the reasons outlined above. The study results indicated the Winkler-type model might result in significantly greater burial depths in comparison with continuum analysis to establish the same pipe strain magnitude for each simulation technique.

Peek and Nobahar (2012) conducted a similar study comparing continuum and structural models investigating the effects of subgouge soil displacements on buried pipelines in clay assuming undrained loading conditions. The structural model inputs were derived as follows: a) the subgouge soil displacement was determined by running a free-field simulation with the 3D coupled (ABAQUS/Explicit ALE) model; and b) the spring force/displacement curves were derived for the vertical uplift and bearing, and lateral directions via 3D coupled simulations of rigid pipe movement in the respective directions. These inputs were then applied to the uncoupled structural model to assess the pipeline response. Peek and Nobahar (2012) reasoned that neither slice-to-slice nor directional coupling could result in the resulting discrepancy (peak strains about 200% higher in the structural model); the superposition error, as discussed above, was cited as the main cause of the difference. However, the prescribed soil displacements in the decoupled model, based on 3D free-field simulations, are not consistent with the strain field in the 3D coupled model that is influenced by the pipe that obstructs the soil flow.

In an attempt to reduce the structural model conservatism and uncertainty, Lele et al. (2011) studied ice/soil/pipe interaction in granular and cohesive soils whereby the soil spring curves ("continuum springs") and the free-field subgouge soil deformations were developed using the 3D coupled (ABAQUS/Explicit CEL) model. The pipeline strain

demand as a function of the burial depth/gouge depth ratio (in sand) using the decoupled approach was assessed. In one case presented, the longitudinal strains from the continuum-spring approach were in closer agreement with the 3D continuum results than the decoupled (i.e. empirical subgouge soil deformation and soil resistance) approach. However, with increasing burial depth, the continuum-spring approach predicted increasing strain demand in contrast with the continuum model. It was found that the strain demand actually increased with burial depth (Fig. 3 in ref.), contrary to realistic expectation. However, keeping the gouge depth constant, the strain demand was in fact shown to reduce with burial depth (Fig. 11 in ref.); though the results were very conservative in comparison to the continuum model.

Been et al. (2011) put forth an interesting discussion surrounding the strength of clay backfill and its effect on the pipeline strain demand. Using the decoupled structural modelling approach for 254 mm (10″) and 762 mm (30″) pipeline diameters it was shown that pipeline axial strains remain below 1% when buried in a soft clay (s_u = 8 kPa) where the strain levels were based on the critical gouge width at which strains are a maximum. Also, depending on the pipeline diameter, strains did not increase significantly (or at all) beyond lateral pipe displacements of 1 to 2 m. There are several noteworthy discussion points in Been et al. (2011):

- The limiting loads on a pipeline are directly proportional to the undrained shear strength of the clay; hence, soft backfill conditions provide a potential simple solution to mitigate load transfer effects;

- Increased tolerable pipe strain levels would allow for higher backfill strengths, higher operating pressures and temperatures, and reduced pipe wall thickness;
- Categorically considering soil types and the subsequent influence on gouge depth and subgouge soil deformation can lead to reduced number of analysis cases and reduced conservatism; this leads back to considering the soil strength as a parameter that limits the gouge depth and influences the subgouge soil deformation profile.

2.3 Pipe/Soil Interaction in Cohesive Soil

2.3.1 Overview

During large deformation ground movement events, such as ice gouging, oblique pipeline/soil interaction may occur due to non-orthogonal crossing angles of the geohazard and pipeline curvature in response to the ground deformation field (Kenny et al., 2007). Recent studies have shown the conventional approach for structural based beam/spring models that assumes independence, or uncoupled behaviour, between orthogonal soil springs may be conservative (e.g. Nobahar et al., 2007a,b; Pike and Kenny, 2016). The pipeline trajectory may exhibit a complex pattern that evolves in response to the development of subgouge soil displacement field, failure mechanisms and clearing processes (Kenny et al., 2007; Pike et al., 2011b). To develop confidence in the numerical simulation procedures for coupled ice gouge events, the soil continuum response must be calibrated to account for the large soil deformations and strain, and 3D pipeline/soil interaction event that may be influenced by contact mechanics and path

dependent response. Physical and numerical modelling data for simple loading conditions (e.g. lateral loading of rigid pipeline) and for more complex scenarios, such as oblique loading, can be used to achieve this goal.

As discussed in Section 1.1, in conventional engineering design practice for buried pipelines, the pipeline-soil system is represented by a simplified finite element model comprised of a structural beam (for the pipeline), and directional springs to approximate soil reaction forces in the axial (longitudinal), transverse horizontal (lateral), transverse vertical (uplift and bearing) directions. Each spring has an associated load-deformation curve representing the behaviour of the soil in the respective direction. The nonlinear load-deformation curve may be approximated by a bilinear (elastic-perfectly plastic) or multi-linear (usually hyperbolic) relationship. The soil reaction force, or load (per unit length), is generally assumed to remain constant once a maximum value has been reached (ASCE, 1984; ALA, 2001; PRCI, 2009).

Guidelines for buried pipe design (e.g. ASCE, 1984; ALA, 2001; PRCI, 2009) provide equations for defining soil spring curves that are based on laboratory and field experimental tests, and numerical studies on pipe/soil interaction, as well as related geotechnical approaches for piles, embedded anchor plates and strip footings. A review of these studies is given throughout this thesis, with an emphasis on pipe/soil investigations, as the related approaches (e.g. pile loading) are covered implicitly.

The soil reaction force is related to the soil strength, unit weight and burial depth. The burial depth (H) is generally defined as the depth of soil to the pipe springline (or centerline) and is usually normalized by the pipe diameter; although, some studies use the

pipeline cover depth or the embedment depth in this ratio. In this thesis, the pipe springline shall be used, except where otherwise noted. The burial depth ratio is defined as the ratio of burial depth to pipeline diameter, H/D (Figure 2.8).

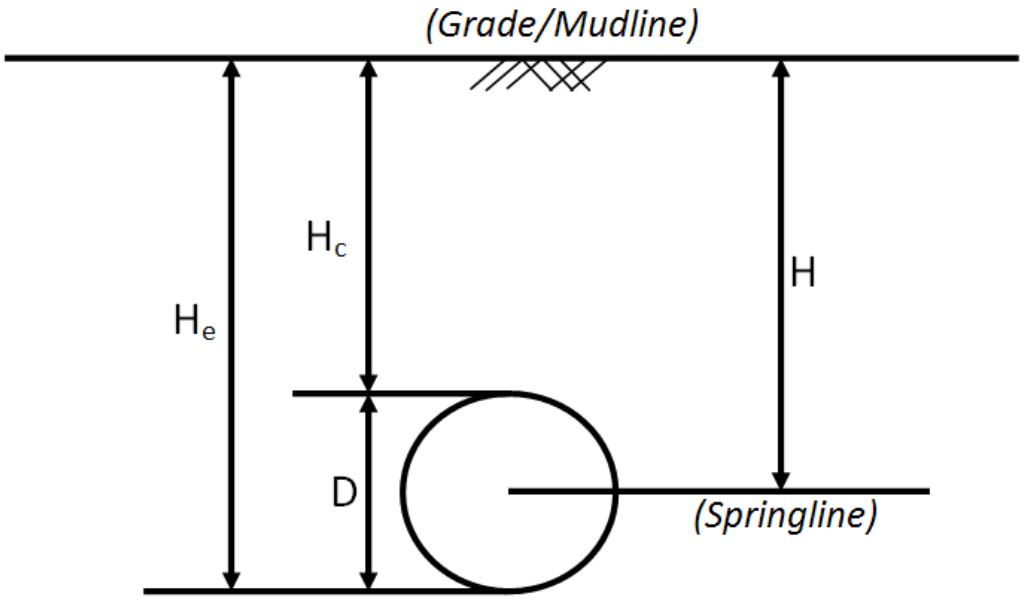

Figure 2.8. Buried pipe nomenclature definitions

It has been observed that dense sand and stiff clay exhibit similar load-displacement behaviour, however, the equations used in defining soil springs for sand and clay differ according to their respective strength parameters. A similar observation holds true for the comparison between loose sand and soft clay. While these equations and the conventional modelling framework in general may serve as a useful tool in preliminary design of buried pipelines, there are several drawbacks that should not be overlooked:

- Soil yield and displacement values;

- Soil strength reduction from peak to residual is not accounted for;
- Soil is assumed to be uniform, i.e. trench effects not accounted for;
- Soil springs are independent and the effect of shear stress between adjacent soil springs is not accounted for.

These aspects of pipe/soil interaction and the influence on the pipe mechanical response are discussed in detail in PRCI (2009).

2.3.2 Lateral Bearing Interaction

As discussed in various publications (e.g. Rizkalla et al., 1992; Poorooshasb et al., 1994), there are several aspects of lateral pipe/soil interaction that present modelling complexities. The rate of pipe movement must be considered as it will govern the type of soil strength mobilized to be either drained or undrained. The rate of pipe movement will be rapid in case of pressure and temperature loading and catastrophic ground movement, and slow in case of typical creeping landslide loads. As the pipeline moves laterally, the pipe/soil interface is engaged, soil deformation occur that may be accompanied by strain hardening or softening behaviour. Trailing the pipeline, varying mechanisms can occur such as separation and local soil unloading or suction caused by negative pore pressure. Further complexity is introduced by the presence of two distinct materials: backfill material and in-situ undisturbed material, and modelling the interface between them. It is also important to consider the type of backfill material, and the strength of which can increase with consolidation over time.

In 1991, Nova Gas Transmission Limited (NGTL) began an experimental research program using centrifuge modelling to study the load transfer behaviour of buried

pipelines subjected to lateral soil movement in cohesive soil. Two phases of testing were conducted; Phase I and Phase II are described by (Rizkalla et al., 1992; Poorooshasb et al., 1994) and Paulin et al. (1995), respectively. The Phase I study demonstrated that the centrifuge method was suitable for lateral loading of pipelines; however, there were issues with interpretation of the horizontal bearing capacity factors related to limited control of the shear strength and desiccation of the soil. Phase II of the study investigated the geometric effects of pipeline soil cover, trench width and displacement rate on the horizontal bearing capacity factors. Reanalysis of the Phase I data was also conducted based on improved understanding of the soil conditions at the time of testing (Paulin et al., 1995).

As discussed by Poorooshasb et al. (1994), the Committee on Gas and Liquid Fuel Lifelines (CGL) concluded that pertinent data on laterally displaced pipelines in clay indicate a trend towards increased levels of P_u until H/D reaches a value of 6. The CGL (ASCE, 1984) suggests that Hansen's (1961) bearing capacity model can be used to estimate P_u in clay. Centrifuge testing of lateral pipeline movement in clay conducted by Poorooshasb et al. (1994) concluded that loads predicted by the state of practice (Hansen, 1961; ASCE, 1984) were about half of those measured in the test program. Similarly, they found that the Rowe and Davis (1982) factors assuming "immediate breakaway" conditions significantly underestimate the loads transferred to the pipe. Several cases exhibited close agreement with the "no separation" condition, however, the authors explained several reasons why the development of such a condition was unlikely, and

ultimately suggested that the ASCE (1984) guidelines may significantly underestimate the magnitude of ground movement loads being transferred to a buried pipeline.

Paulin et al. (1995) explained that the horizontal bearing capacity factors from the Phase I tests conducted by Rizkalla et al. (1992) and Poorooshasb et al. (1994) were incorrectly interpreted for the following reasons: 1) desiccation of the soil had occurred that restrained the surface movement yielding high interaction forces, and 2) the interpreted shear strength at the pipe springline was under-predicted. Lessons learned from the Phase I tests were used to design and execute the Phase II tests which are described by Paulin et al. (1995). The tests were designed to assess the effects of trench width, burial depth, pipe/soil interaction rate, preconsolidation pressure, and backfill type. The test results indicated that the trench width had little or no effect on the interaction, the soil resistance increased with increasing burial depth, and the displacement rate had a significant effect on the loads transferred to the pipeline by the soil. Paulin et al. (1995) indicated that the rate result is significant because if the current state-of-practice is based on the assumption that there is an undrained interaction between pipe and soil, then it could significantly underestimate the load transferred to the pipeline.

For tests with rapid pipe displacement (undrained), the interaction factors followed Rowe and Davis' (1982) immediate breakaway curve for $H/D < 2$, and for deeper burial depths, the results were bound by Rowe and Davis' curve and Hansen's (1961) slightly increasing curve. For tests in which the pipe displacement rate caused a drained soil response, the interaction factors exceeded Rowe and Davis' (1982) "no

separation" interaction curve, however, since the drained condition applies, the Rowe and Davis method does not apply.

Wantland et al. (1979) conducted two phases of lateral pipe/soil tests in clay. The first phase was conducted in the field with 6.25 m long pipe sections embedded in underconsolidated, highly plastic clay. The pipe embedment in phase one did not exceed the pipe diameter, hence, the results will not be discussed in this report. Phase two was conducted in the laboratory with burial depth to diameter ratios typically greater than one (16 of 20 tests), and an open trench configuration (i.e. no backfill). Two pipe diameters, 38 mm and 75 mm were each displaced at rates of 1.2 mm/min and 0.36 mm/min.

From the test results, Wantland et al. (1979) developed a relationship between the displacement corresponding to the failure load (y_f) and the trench depth (H_e). The failure load was taken as the load value at the point of intersection of the tangents of the two linear portions of the force-displacement curve. This relationship (normalized to pipeline diameter, D) was accompanied by an observed transition in the failure mechanisms with increasing burial depth. The shallow pipes appear to fail by surface sliding, whereby the soil continuously builds up in front of the pipe, hence the resistance continues to build and failure is not observed. At intermediate depths, the soil is mobilized in a passive wedge, requiring less displacement to fail. Soil in front of deeply buried pipes fails through a flow-around mechanism requiring larger mobilization displacement. Wantland et al. (1979) noted that the upper limit of N_{ch} appears to be 5 to 6 and does not appear to be influenced by pipe diameter.

Oliveira et al. (2010) developed a simple analytical model to compute N_{ch} based on the pattern of displacements during small-scale lateral pipeline-soil interaction tests. Equation (2.4) is based on shallow failure mechanism and therefore is recommended for H/D ratios up to 4.5. The predicted N_{ch} values compare very closely with Hansen's (1961) model.

$$N_{ch} = 5 \tan^{-1}\left(\frac{H + 0.5D}{D}\right) \tag{2.4}$$

For cohesive soils with no internal angle of friction, the horizontal bearing capacity factor can be defined as (ASCE, 1984; ALA, 2001):

$$N_{ch} = \frac{P_u}{s_u D} \tag{2.5}$$

where P_u is the ultimate lateral soil resistance per unit length, s_u is the backfill undrained soil shear strength and D is the nominal outside pipeline diameter.

Phillips et al. (2004b) developed an expression for a modified lateral bearing interaction factor to account for the change in the potential energy of the passive wedge for shallow H/D ratios. Phillips et al. (2004b) discussed the variation in interaction factor with burial depth related to a change in failure mechanism. For shallow burial (H/D less than approximately 3), the mechanism involves a passive earth failure wedge extending to the soil surface. For deeper burial, there is negligible surface expression and the soil flows around the pipe. Hence, for shallow burial, part of the pipe resistance results from the lifting of the weight of soil within the passive failure mechanism, while for deeper burial, there is little net resistance from such soil displacement. Considering this transition,

Phillips et al. (2004a) recommended the following relationship for N_{ch} based on work done by Rowe and Davis (1982):

$$N_{ch} = min\left(N_{ch}^{*} + \beta\frac{\gamma H}{s_u}, N_{ch}^{max}\right) \tag{2.6}$$

where N_{ch}^{*} is the interaction factor associated with soil strength and $\beta\,\gamma H/s_u$ is the factor to account for the soil weight relative to the vertical stress level at the pipe springline. N_{ch}^{max} is the upper limit for the lateral interaction factor associated with deep burial.

The variation of the individual contributions with burial depth and normalized vertical stress level are provided by Phillips et al. (2004b). To separately distinguish the interaction factor associated with soil strength, finite element analyses were repeated with and without soil weight. The interaction factors determined separately were additive to obtain the total interaction factor. The upper limit, N_{ch}^{max}, was found to be about 11. A value of β=0.85 was found to provide the best fit to the FE results.

This approach has been adopted in the PRCI (2009) guidelines. The displacement corresponding to ultimate soil resistance (y_u) for stiff to soft clay (as well as dense to loose sand) is recommended as:

$$y_u = 0.04\left(H + \frac{D}{2}\right) \leq 0.10 \text{ to } 0.15D \tag{2.7}$$

Phillips et al. (2004a) conducted a series of lateral pipe/soil centrifuge tests in clay with undrained conditions. The effects of trench width, burial depth, backfill material, and trench wall inclination angle were studied in the test program, which comprised 20 tests. The lateral interaction factors were compared against those obtained from Hansen (1961) and Rowe and Davis' (1982) models, and Equation (2.6). The test measurements were

slightly less than those from Rowe and Davis (1982) down to H/D = 1.5, and slightly more than those from Hansen (1961) for H/D greater than 2. The measurements were better predicted by Equation (2.6), as it accounts for the contribution of soil weight for shallow burial.

2.3.3 Oblique Lateral/Axial Interaction

The ultimate axial soil resistance (T_u) is comprised of frictional and cohesive components (ALA, 2001; PRCI, 2009) expressed by:

$$T_u = \pi D H \gamma' \left(\frac{1 + K_o}{2}\right) tan\delta + \alpha \pi D s_u \tag{2.8}$$

where $\delta = f\phi'$ is the pipe/soil interface angle of friction, and α is the adhesion factor. The frictional component (first term) refers to a drained soil response that is associated with slow pipe loading rates. The cohesive term is referenced to undrained soil response under rapid pipe loading rates. The first term follows effective stress analysis and has been termed the β method, while the second is based on total stress state and is referred to as the α method. Values of the friction factor (*f*) for different materials in contact with frictional soils are provided in available guidelines (ALA, 2001; PRCI, 2009). Lower and upper bound adhesion factors as a function of undrained shear strength are also provided.

As discussed by Cathie et al. (2005), for cohesive soils, a decision has to be made regarding drained or undrained behaviour; in general, engineering design practices consider drained or undrained conditions, thus simplifying the equation to a single term. Oliphant and Macanochie (2007) recommend comparing the degree of consolidation at a time, *t*, or the duration of pipeline loading, in order to determine whether or not drained or

undrained conditions are applicable. The time required to achieve a certain level of consolidation can be approximated using one-dimensional consolidation theory.

In large scale axial pipe/soil interaction tests, Paulin et al. (1998) found that the adhesion factors back-calculated from the current experimental data are grossly overestimated by suggestions in the literature and are in better agreement with Rizkalla et al. (1996). The relatively high values observed in the field may be partly due to slight axial misalignment, which can significantly increase the axial resistance as shown by Phillips et al. (2004a). As discussed by C-CORE (2008), high α values can also result from high pore water suctions and cementation effects adhering soil to the pipe.

Centrifuge modelling and numerical simulations using ABAQUS/Standard have shown the axial force increases with modest changes in the oblique angle up to approximately 15 degrees relative to the longitudinal pipe axis (Phillips et al., 2004a). This phenomenon is due to the increased normal pressure acting on the projected inclined pipe surface. The relative angle between the pipe and soil affects the local failure mechanisms and thus limit loads. The axial resistance is controlled by surface traction at low angles of attack and the soil failure mechanisms is dominated by shear through the soil mass at higher angles approaching pure lateral bearing.

Phillips et al. (2004a) conducted 3D continuum FEA of oblique lateral-axial pipe/soil interaction in cohesive soil, assuming undrained conditions, using ABAQUS/Standard. The constitutive model was J_2 plasticity using total stress parameters with the von Mises yield criterion. The pipe/soil contact interface, however, was modelled using drained parameters; a drained friction angle of $\delta = 20°$ was used, without

limiting the interface shear stress. A design equation for oblique lateral-axial pipeline loading in clay was proposed as:

$$N_p^2 + 3N_t^2 = N_{p0}^2 \tag{2.9}$$

where N_p and N_t are the ultimate lateral and axial interaction forces, respectively, and N_{p0} represents the ultimate lateral interaction force for the pure lateral condition.

Seo et al. (2011) also analyzed oblique lateral-axial pipe movements in cohesive soil, showing good correspondence with Phillips et al. (2004b). Numerical simulations were conducted using LS-DYNA, and similarly, the pipe/soil interface contact was treated with an interface friction angle of 25°, without limiting the interface shear stress.

In a total stress analysis of cohesive material, it may be more realistic to adopt an interface shear stress limit that does not permit the contact interface shear stress to surpass the undrained shear strength of the underlying soil. In the case of highly sensitive clays that are prevalent in areas of heavy reworking, remoulding of the soil at the pipe/soil interface can reduce the axial restraint on the pipeline. The shear stress limit in a total stress analysis of pipe/soil interaction in undrained clay should therefore be a function of the clay sensitivity. Oliphant and Maconochie (2007) discuss methodology to determine whether undrained or drained conditions apply depending on the duration of pipeline loading and consolidation properties of the soil, and how to treat the axial soil resistance in each case.

C-CORE (2008) performed 3D continuum FEA and centrifuge model testing for lateral-axial pipe movement in cohesive and cohesionless soils. For the numerical analysis of the interaction in clay, the interface behaviour was assumed to be purely

adhesive, whereby the axial soil resistance was limited by the interface shear stress limit, τ_{max}. In order to mobilize τ_{max}, an unrealistically high interface friction coefficient, $\mu = 5.0$, was applied. The friction parameters produced a vertical cut-off to the lateral-axial interaction diagram for oblique angles less than 20°. This was due to the high initial peak axial resistance that was predicted due to the high interface friction coefficient.

2.4 Cohesionless Soil Behaviour

This section is focused on cohesionless soil behaviour as there are complex aspects (e.g. stress level and density dependence, strain hardening/softening) of the behaviour that are especially relevant to shallow buried pipe/soil interaction in dense sand. Compared to undrained analysis of cohesive soils, the behaviour of cohesionless soils is relatively complex and required an in-depth review to introduce facets of the behavior that shaped the development of the modified Mohr-Coulomb model described in Section 3.2.2.

Dense sand exhibits uniform deformation behaviour until a bifurcation point is reached where a shear band develops and the deformation pattern transitions from uniform response to localized strain patterns (Vermeer and de Borst, 1984). The effect of varying strain is particularly important for dense sands because the peak friction angle may be mobilized at only one point on the failure surface at peak load. At other points on the failure surface, the mobilized shearing resistance is less, and the average mobilized shear resistance, therefore, is smaller than peak at large scales. Walters and Thomas (1982) demonstrated that elasto-plastic finite element analyses with strain softening can be used to model shear zone development in sand. In order to model initial and

subsequent shear zone development, variable non-associated flow rules to control dilatancy were required.

It is important to understand the effects of pressure, related to overburden stress and embedment depth for buried pipelines, and relative density, influenced by trench backfill consolidation (compaction) procedures, on the behaviour of granular materials. In addition, it is practical to understand the differences in soil parameters derived from specific laboratory test methods that are influenced by low pressure and high relative density conditions.

The triaxial compression (TXC) and direct shear (DS) testing methods are common procedures used to evaluate the constitutive behaviour of soils. However, the need for plane strain (PS) parameters often arises in geotechnical engineering practice for various applications such as pipe/soil interaction (O'Rourke, 2010), strip footings, long embankments with constant cross section and most retaining structures (Ramamurthy & Tokhi, 1981). The lack of availability of plane strain testing equipment, however, has led to the development of relationships to estimate PS parameters using the results of TXC (e.g. Ramamurthy & Tokhi, 1981; Shimobe & Moroto, 1983; Schanz & Vermeer, 1996; Hanna, 2001; Nanda & Patra, 2015) and DS testing (e.g. Davis, 1968; Rowe, 1969; Lings and Dietz, 2004) that are more readily available.

Several studies have demonstrated the differences between the stress-strain response between PS and TXC testing (e.g. Lee, 1970; Ahmed, 1972; Al-Hussaini, 1973; Marachi et al., 1981; Hanna, 2001; Alshibli et al., 2003; Nanda & Patra, 2015) in terms of peak shear strength and corresponding strain mobilization. In comparison with TXC test

results, PS test conditions typically result in higher frictional shear strength mobilized at a relatively small shear strain magnitudes. This is due to particle restriction in the intermediate principal stress direction and a greater susceptibility to develop strain localization, particularly for soils with high relative density (compaction) and low confining pressure (shallow embedment). This is a significant consideration when developing constitutive parameters and models to analyze geomechanics problems that exhibit plane strain conditions.

Figure 2.9 illustrates the typical variation of deviatoric stress and volumetric strain with respect to axial strain on a plane strain simulation test on dense sand. The soil response can be divided into four characteristic phases:

1. Quasielastic behaviour (OA): Up to point A the soil deforms quasi-elastically. Some nonlinearity is observed, but without dilation. Point A defines the transition between compression and volumetric expansion of the soil.
2. Plastic behaviour (AB): From point A to B the soil yields, enters the plastic region, and dilates. Peak conditions are reached at point B.
3. Softening behaviour (BD): From point B to D the soil experiences softening. Softening is completed at point D, and the deviatoric stress and volumetric strain remain constant with further axial strain.
4. Residual behaviour (DE): Shearing is accumulated along the developed shear bands.

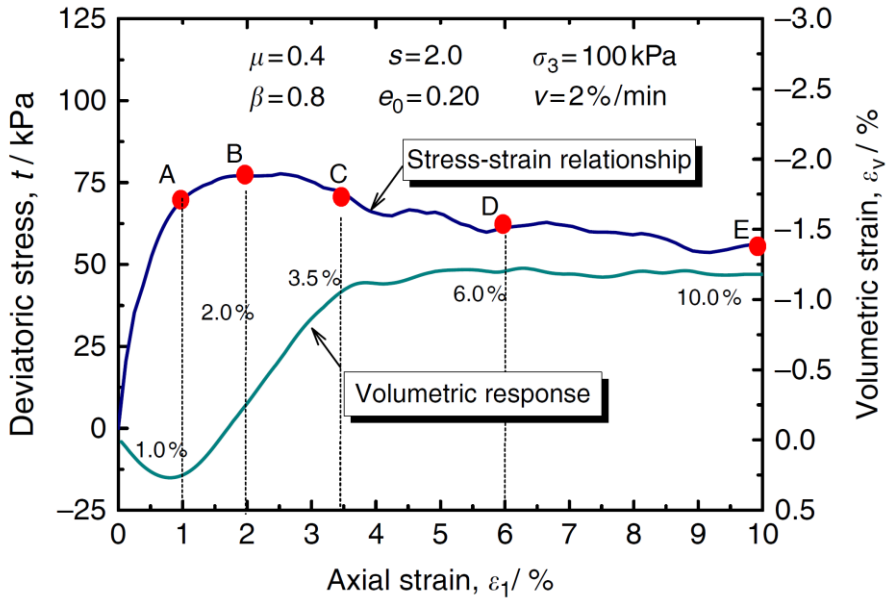

Figure 2.9. Typical variation of plane strain stress ratio and volume change for a dense sand specimen (Jiang & Zhang, 2015)

Common geotechnical parameters that define granular soil plasticity are the peak and critical state friction angles, and the dilation angle (ϕ'_p, ϕ'_{cv} and ψ, respectively). Equations linking these three variables are generally termed "flow rules". Early research by Rowe (1962, 1969) formed the basis for considering the role of dilation in the peak friction angle observed in excess of the critical state. In terms of mobilized dilation angle, mobilized friction angle and critical state friction angle, Rowe's (1962, 1969) equation for plane strain can be written as:

$$\sin \phi'^{ps} = \frac{\sin \phi'_{cv} + \sin \psi}{1 + \sin \phi'_{cv} \sin \psi} \tag{2.10}$$

Bolton (1986) proposed the following flow rule for plane strain conditions,

$$\phi'^{ps}_{p} - \phi'_{cv} = 0.8\psi_p \quad (2.11)$$

on the basis that Rowe's (1962) stress-dilatancy theory produces a curve that has approximately 80% of the slope of the linear relationship:

$$\phi'^{ps}_{p} - \phi'_{cv} = \psi_p \quad (2.12)$$

Hence, the acceptance of Rowe's (1962) theory is inherent in Bolton's (1986) plane strain flow rule.

Under triaxial compression testing conditions, the following flow rule can be inferred from Bolton (1986):

$$\phi'^{tx}_{p} - \phi'_{cv} = 0.48\psi_p \quad (2.13)$$

This is a mean representative value for a wide range of different sand types. However, the coefficient for triaxial compression has been shown to vary depending on the type of sand considered (e.g. Guo and Su, 2007; Chakraborty and Salgado, 2010). The coefficient is also dependent on the analyst's interpretation of the critical state friction angle.

2.4.1 Peak Friction Angle

The peak friction angle increases with reducing pressure and increasing relative density, where several studies (e.g. Clark, 1998; Lancelot et al., 2006; Lau and Bolton, 2011) have demonstrated a linear relationship between the peak friction angle and the logarithm of mean effective stress. Bolton's (1986) relative dilatancy index ($0 < I_R < 4$) was proposed to estimate peak dilation and effective friction angle as an empirical function of relative density, D_r, and mean effective pressure, p'.

$$I_R = D_r\left(Q - \ln(p')\right) - R \quad (2.14)$$

where,

$$\phi'^{ps}_{p} - \phi'_{cv} = A_{\psi} I_R \quad (2.15)$$

Bolton's (1986) analysis found that under plane strain conditions, A_ψ = 5, and in triaxial compression, A_ψ = 3, provided a good fit with test data compiled for 17 different sands. The parameters Q and R are empirical fitting parameters in the relative dilatancy equation proposed by Bolton (1986) with suggested values Q = 10 and R = 1 based on curve fitting to data from a range of sands. Chakraborty and Salgado (2010) demonstrated that Q and R can be modified to improve correspondence with experimental data for a specific sand. They found that Q increases logarithmically with increasing confining stress when R = 1 for Toyoura sand.

The parameter p' corresponds to the mean effective stress at to failure, i.e. corresponding to the peak friction angle. In response to comments regarding stress level effects on Toyoura sand, Bolton (1987) later updated the relative dilatancy index equation to account for mean effective stresses greater than, and less than 150 kPa.

In the following Sections 2.4.1.1 and 2.4.1.2, review and analysis of publicly available plane strain and triaxial compression test data is presented.

2.4.1.1 Review and Analysis of Plane Strain Test Data

To assess the effect of confining stress and relative density on peak friction angle and volumetric response for plane strain tests on sand, and orient the reader in terms of an expected range of parameters, a review of existing literature containing plane strain test data was conducted and the results were compiled and analyzed. The review gleaned a broad range of test data considering varying mineral compositions (e.g. Quartz, Silica,

Feldspar), grain shapes (e.g. R - rounded, SR - subrounded, SA - subangular, A - angular), relative density, and confining pressure. The sand characteristics are summarized in Appendix D, Table 9.4.

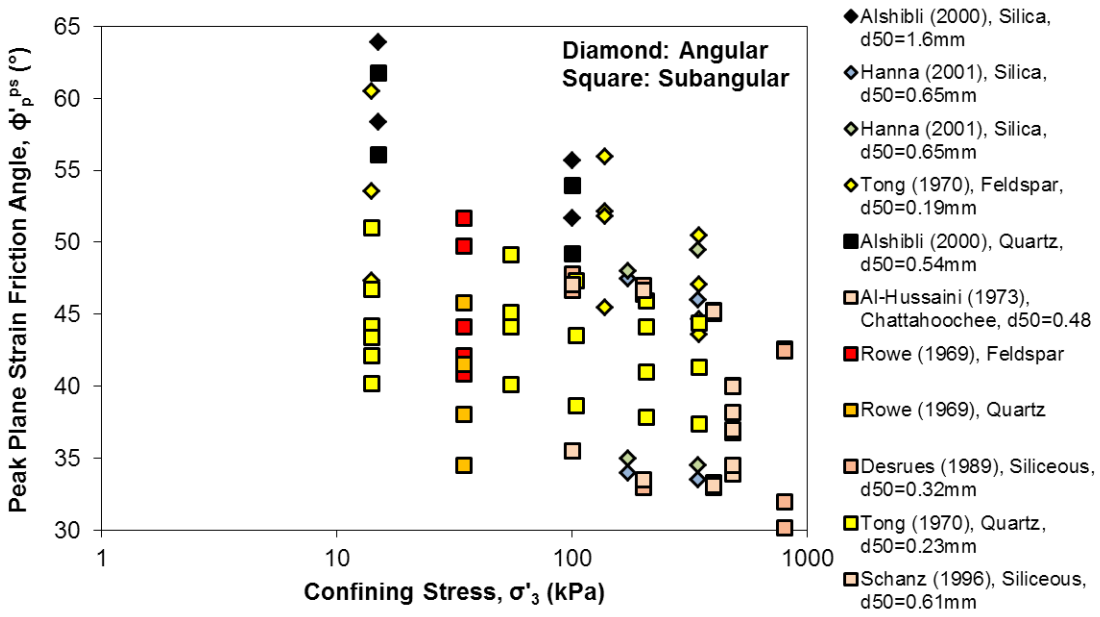

Figure 2.10. Peak plane strain friction angle vs. confining pressure for sands

In order to separate the data for ease of visibility, the sands were divided into two groups: 1) subangular or angular, and 2) rounded or subrounded. The plane strain friction angles for each group were plotted against the confining pressure in Figure 2.10 and Figure 2.11. The data is presented over the entire range of relative density. The figures show a clear trend of increasing plane strain friction angle with reduced confining pressure. Subangular to angular particle shapes mobilize greater frictional resistance,

especially at low confining pressure. The lower bound frictional response is for the spherical glass ballotini material.

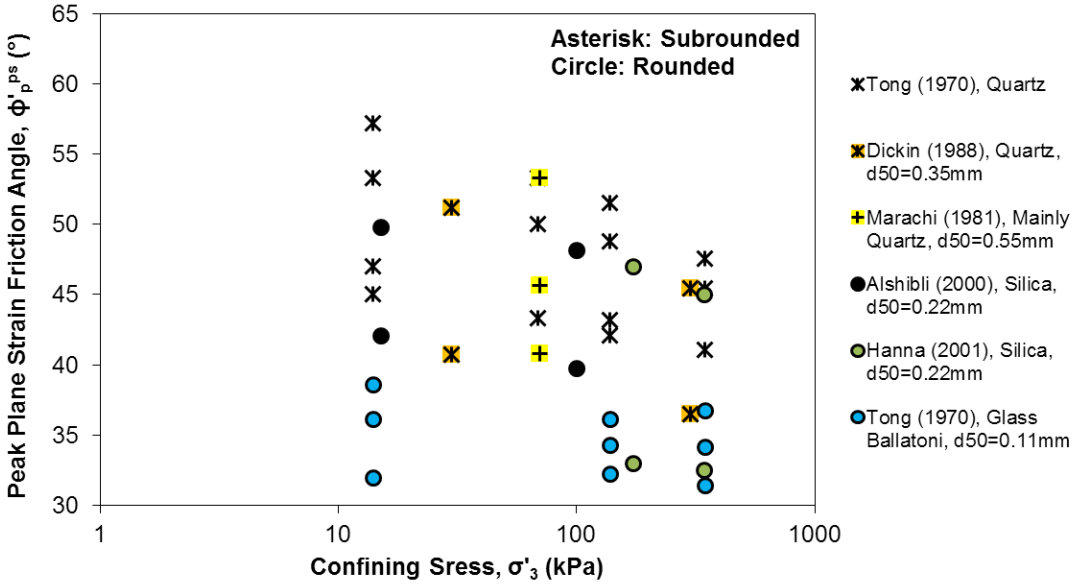

Figure 2.11. Plane strain friction angle vs. confining pressure for sands

2.4.1.2 Review and Analysis of Triaxial Test Data

There is a large available database of consolidated, drained triaxial compression test data on cohesionless soil presented by Jefferies & Been (2006). In this study, supplemental data is added from the studies by Cornforth (1973), and Vaid and Sasitharan (1991), which are summarized in Appendix E, Table 9.5. The mean grain size, D50, fines content, maximum and minimum void ratios, specific gravity, and fundamental critical state parameters are reported where available. The sand samples include laboratory standard sands, natural sands (e.g. offshore seabed, riverbed) and tailings sands.

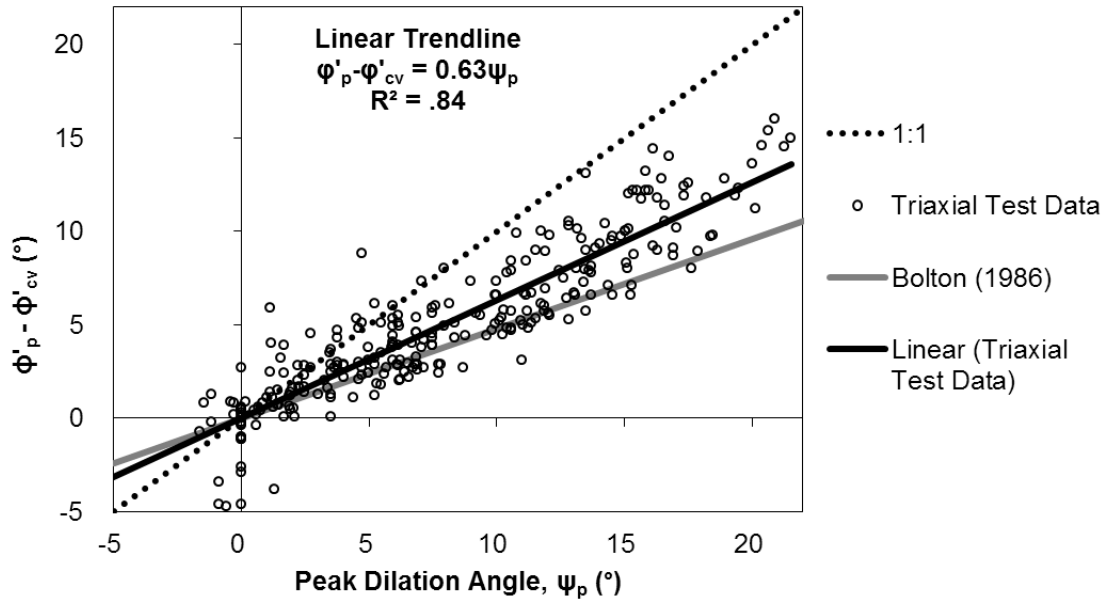

Figure 2.12. ϕ'_p-ϕ'_{cv} vs. ψ_p for triaxial test dataset

An analysis of the dataset was conducted to compare against the triaxial compression flow rule inferred from Bolton (1986). The effective mean pressure at failure, p′, has an overall range of 40 to 4000 kPa. As shown above in Figure 2.12, the linear best fit line gives an estimate:

$$\phi'^{tx}_p - \phi'_{cv} = 0.63\psi_p \tag{2.16}$$

A similar relationship was determined for Toyoura sand by Chakraborty and Salgado (2010) and for Ottawa sand by Guo and Su (2007).

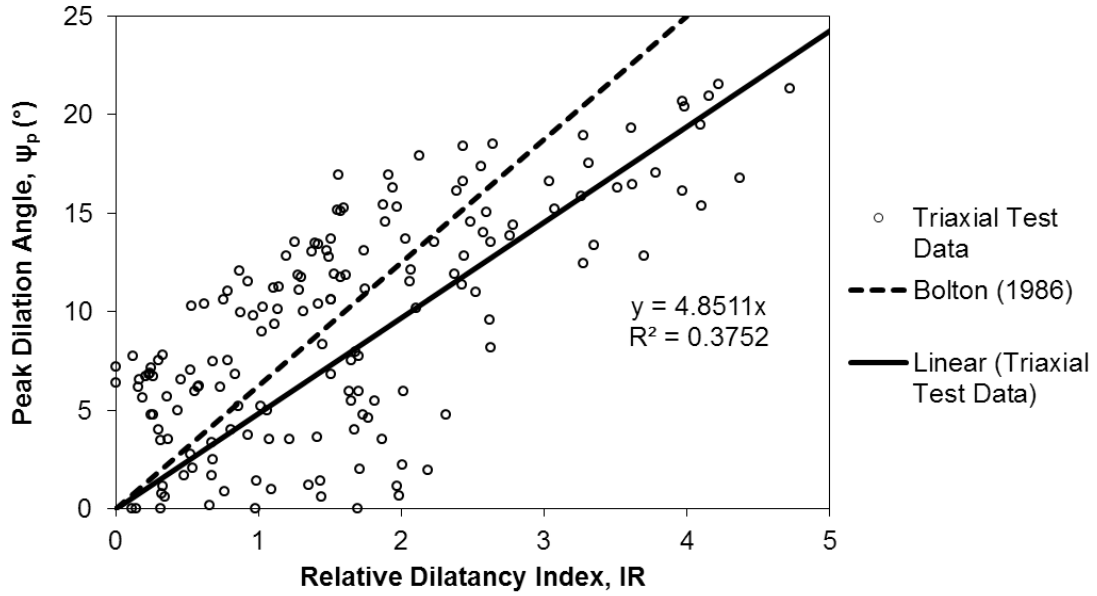

Figure 2.13. Peak dilation angle vs. relative dilatancy index

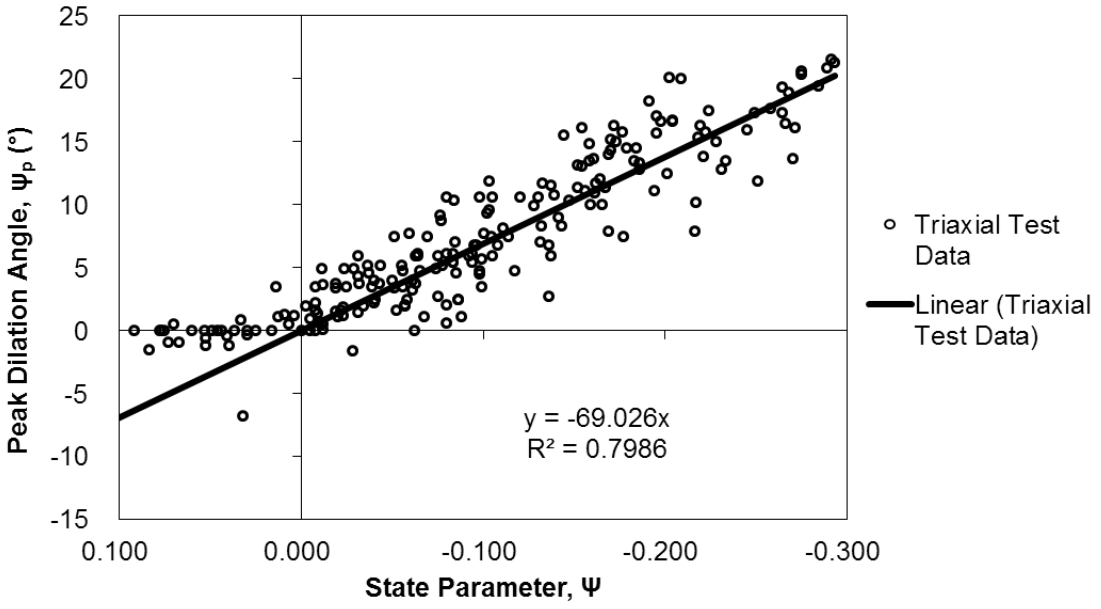

Figure 2.14. Peak dilation angle vs. state parameter

Figure 2.13 shows the relationship between dilation angle and the empirical relative dilatancy index, I_R, proposed by Bolton (1986). The dilation angle showed a weak correlation with I_R, where the data was highly scattered. The state parameter (Ψ) approach proposed by Been and Jefferies (1985) provides a more reliable prediction of the dilation angle (Figure 2.14). Both approaches consider the effects of void ratio and pressure, however, Bolton's (1986) approach is empirical while the state parameter (Ψ) is a measurable quantity.

To further examine the applicability of the relative dilatancy index for predicting triaxial compression test parameters, the test dataset was divided into four relative density ranges ($0.0 < D_r \leq 0.25$, $0.25 < D_r \leq 0.5$, $0.5 < D_r \leq 0.75$, $0.75 < D_r \leq 1.0$). The $\phi'_p{}^{tx} - \phi'_{cv}$ values were then plotted against the mean effective stress and compared to Bolton's (1986) empirical curves at the bounds of each range of relative density (Figure 2.15 to Figure 2.18). Bolton's (1986) curves were plotted with and without limiting the relative dilatancy index ($0 < I_R < 4$); the updated recommendation in Bolton (1987) was also plotted.

The data for $0.75 < D_r \leq 1.0$ is in reasonable agreement with Bolton's (1986) empirical approach. The data for $0.5 < D_r \leq 0.75$ shows significant scatter, though Bolton's (1986) relationship provides an appropriate mean response as there is approximately equal amounts of data above and below the bounds, with a cluster contained inside and at the bounds. The data for $0.25 < D_r \leq 0.5$ is reasonably confined by the bounds. The data for $0.0 < D_r \leq 0.25$ is not confined by the bounds as each value of the dataset lies at, or above Bolton's (1986) line at $D_r = 0.25$.

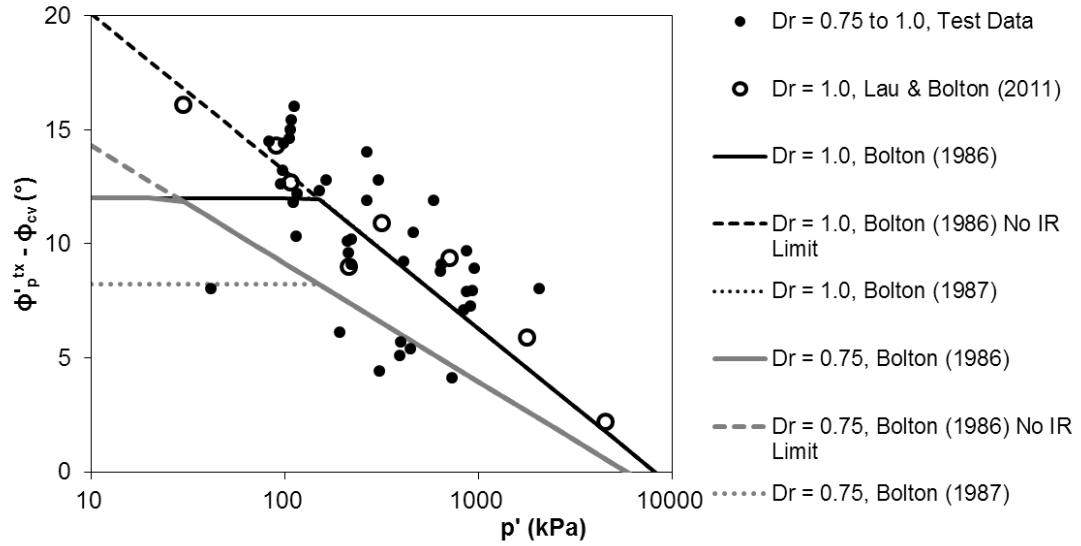

Figure 2.15. $\phi'^{tx}_p - \phi'_{cv}$ vs. p' ($0.75 < Dr \leq 1.0$)

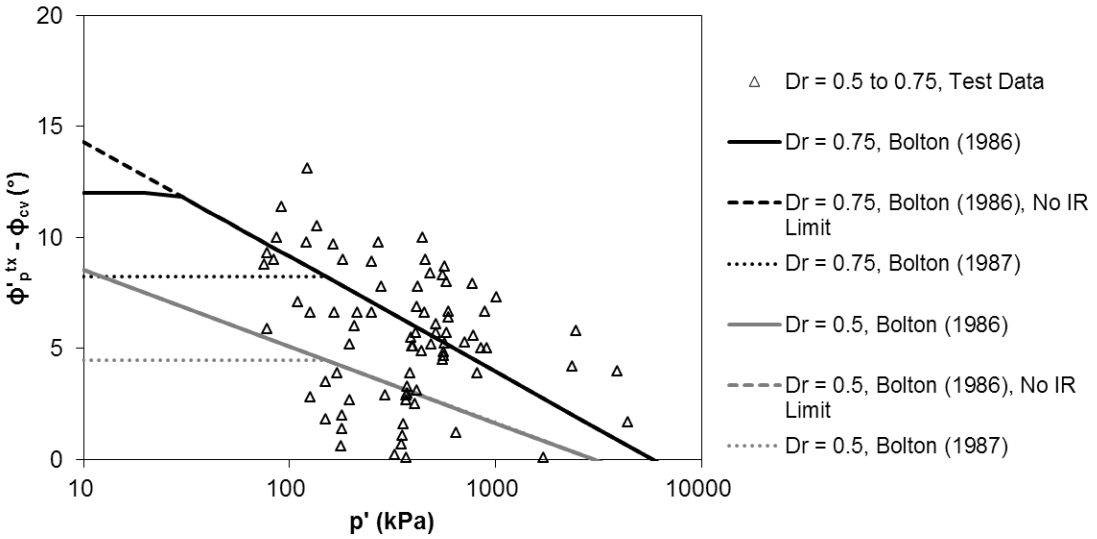

Figure 2.16. $\phi'^{tx}_p - \phi'_{cv}$ vs. p' ($0.5 < Dr \leq 0.75$)

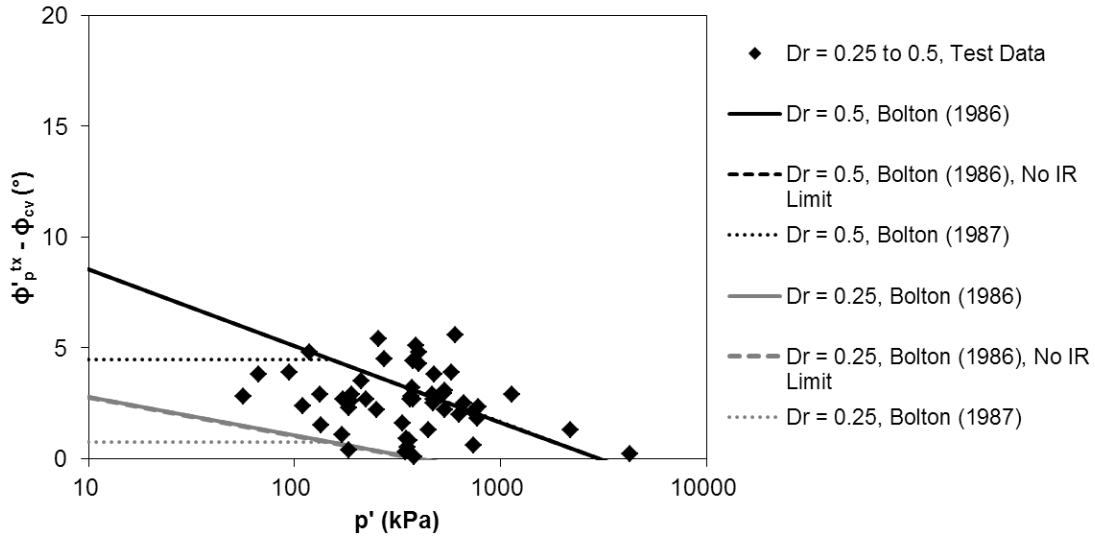

Figure 2.17. $\phi'^{tx}_p - \phi'_{cv}$ vs. p' (0.25 < Dr ≤ 0.5)

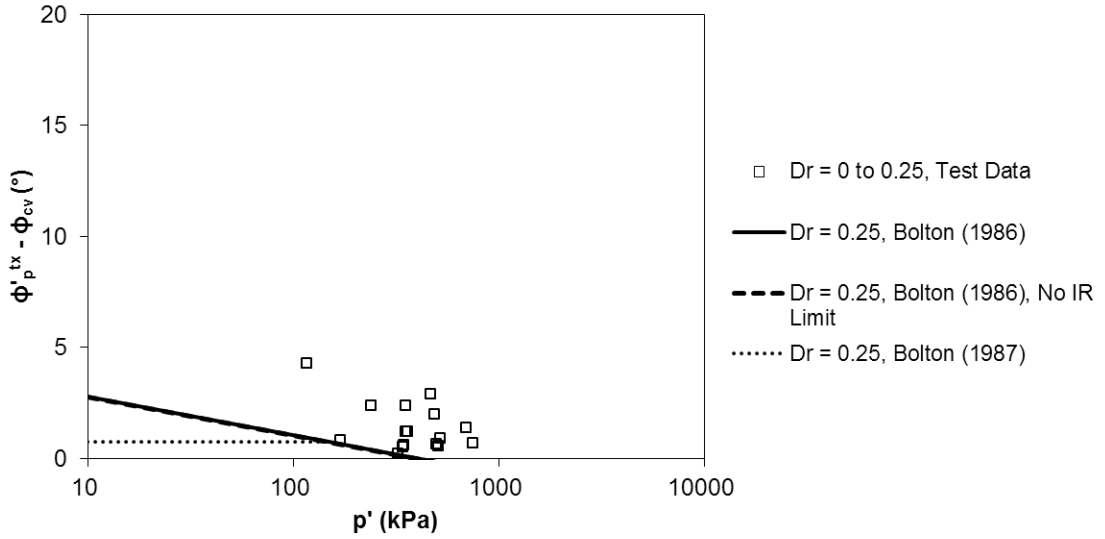

Figure 2.18. $\phi'^{tx}_p - \phi'_{cv}$ vs. p' (0.0 < Dr ≤ 0.25)

In summary, the data shows that Bolton's (1986) empirical approach is best suited for dense to very dense sands and loses predictive capability for loose samples at $D_r < 0.25$.

2.4.1.3 Comparison of Strength Parameters from Plane Strain and Triaxial Tests

As discussed above, the need for plane strain parameters often arises in practical geotechnical engineering applications, however, laboratory test data and equipment availability to determine plane strain parameters are limited. There is then a requirement to translate constitutive parameters (e.g. effective friction angle) from triaxial or direct shear test datasets to plane strain appropriate values. In general, for example, the peak effective friction angle is higher is plane strain compared to direct shear and triaxial compression. Hence, neglecting to account for this effect can lead to an inability to match numerical predictions (e.g. using parameters derived from triaxial compression tests) with data attained from physical tests conducted under plane strain conditions. Furthermore, non-plane strain parameters will provide a conservative (i.e. less soil resistance) numerical response that does not represent physical conditions. This subsection explores the differences between triaxial and plane strain parameters and provides methodology to convert from triaxial compression to plane strain parameters.

Several researchers have conducted plane strain and triaxial compression tests on different types of sand over a range of relative densities and confining pressures (e.g. Lee, 1970; Cornforth, 1973; Al-Hussaini, 1973; Thornton, 1974; Marachi et al., 1981; Hanna, 2001; Alshibli et al., 2003). Some important observations relating the behaviour of soil samples under plane strain and triaxial compression can be summarized:

- ϕ'^{ps} is typically greater than ϕ'^{tx} (converging at the loosest state);
- ϕ'^{ps}_{p} and ϕ'^{tx}_{p} reduce with decreasing relative density;
- ϕ'^{ps}_{p} and ϕ'^{tx}_{p} reduce with increasing confining pressure;
- $\phi'^{ps}_{p} - \phi'^{tx}_{p}$ reduces with decreasing relative density;
- $\phi'^{ps}_{p} - \phi'^{tx}_{p}$ reduces with increasing confining pressure;
- $\phi'^{ps}_{p} - \phi'^{tx}_{p}$ increases with increasing ϕ'^{tx}_{p};
- ϕ'^{ps}_{p} is consistently mobilized at smaller axial strain than ϕ'^{tx}_{p};
- the residual friction angle was also mobilized at smaller axial strain for plane strain tests;
- for both tests, the axial strain corresponding to peak strength reduced with increasing relative density;
- for both tests, the axial strain corresponding to peak strength reduced with decreasing confining pressure.

As discussed by Ramamurthy & Tokhi (1981), the relatively high strength found in plane strain conditions is due to restricted movement of particles in the intermediate principal stress direction as compared to axisymmetric conditions. Desrues & Hammad (1989) found that plane strain specimens were subject to failure characterized by distinct shear bands accompanied by strain softening depending on the relative density and pressure level. Specimens tested under triaxial compression conditions were found to bulge uniformly near peak stress and subsequently developed complex multiple

symmetrical radial shear bands with continued strain (Alshibli et al., 2003). Other researchers also noted the existence of shear banding in specimens tested in triaxial compression (Peters et al., 1988; Peric et al., 1992).

The stability behaviour and failure mechanisms, which influence the mobilization of shear strength with strain, are quite different for plane strain and triaxial tests (Peters et al., 1988). The peak stress ratio generally corresponds with the onset of localization (e.g. Desrues & Hammad, 1989; Wanatowski & Chu, 2007); hence, the peak friction angle is mobilized at relatively small axial strains for plane strain tests conducted on dense samples at low confining stress.

In general, for application of triaxial test results to the analysis of plane strain conditions, it can be summarized that peak strength determined from triaxial testing will be most conservative at low confining pressure and high relative density. Marachi et al. (1981) found $\phi'^{ps}_{p} - \phi'^{tx}_{p}$ up to 8° for relatively dense Monterey No. 20 sand tested at 70 kPa confining pressure. For dense uniform-size glass spheres, Leussink & Wittke (1964) found differences as high as 11° at 70 kPa. Cornforth (1973) found that $\phi'^{ps}_{p} - \phi'^{tx}_{p}$ can range from 0.5 to 5° for loose to dense Brasted sand at approximately 275 kPa confining pressure. Al-Hussaini (1973) also found $\phi'^{ps}_{p} - \phi'^{tx}_{p}$ within this range (1 to 3°) for Chattahoochee River sand at 480 kPa. Tong (1970) notes differences up to 13° under dense, low pressure conditions. For silica sands with varying uniformity coefficient, Ahmed (1972) found a maximum difference between the two tests of about 8° at 100 kPa, reducing to a negligible deviation at 1400 kPa. Wanatowski & Chu (2007) found the difference between plane strain and triaxial compression friction angles to be as much as

11° for dense (D_r = 65%) samples of Changi sand under mean effective stresses (p') ranging from 36 to 300 kPa. Based on the above data review, the maximum difference between the plane strain and triaxial compression peak friction angles are plotted against confining pressure in Figure 2.19. From this brief review, it is apparent that $\phi'^{ps}_p - \phi'^{tx}_p$ is pressure and density dependent and dense samples tested at low confining pressures can reach values up to about 14°.

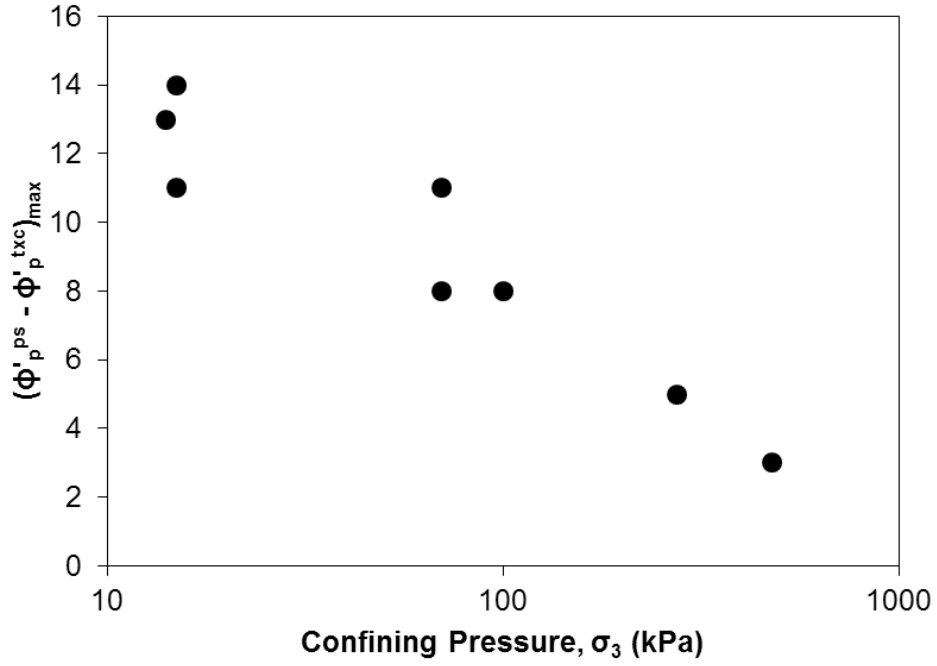

Figure 2.19. Difference between plane strain and triaxial compression friction angle vs. confining pressure

In general, it has been found in cases of plane strain and triaxial compression testing that the axial strain corresponding to mobilization of the peak friction angle

decreases with confining pressure (e.g. PS – Desrues & Hammad, 1989; TXC - Hsu, 2005). It has also been shown that the axial strain at failure is consistently less under plane strain rather than axisymmetric conditions. Lee (1970) reported that the ratio of axial strain at failure between plane strain and triaxial compression test results can be less than 0.5. Results presented by Marachi et al. (1981) for Monterey sand indicate ratios of 0.48 to 0.64 for dense to loose samples at 70 kPa; similar values were found at 550 kPa. Al-Hussaini (1973) found a ratio of about 0.85 to 0.9 for dense to loose Chattahoochee River sand tested at a confining pressure of 480 kPa. Hanna (2001) found average ratios of about 0.3 to 0.35 for three different sands tested at 172 and 344 kPa; minimum values were approximately 0.2. For the well graded angular sand tested by Hanna (2001), the ratio apparently reduced with confining pressure, while the dependency was not evident for the other sands. Correlations between the axial strain at failure for PS and TXC conditions with relative density was not evident from the analysis conducted.

2.4.1.4 Determining Plane Strain Parameters from Triaxial Test Results

As discussed by Schanz and Vermeer (1996), Bolton's (1986) plane strain and triaxial relationships can be rearranged to express ϕ'^{ps}_{p} as a function of ϕ'^{tx}_{p}, or vice versa:

$$\phi'^{ps}_{p} = \frac{1}{3}\left(5\phi'^{tx}_{p} - 2\phi'_{cv}\right) \tag{2.17}$$

Schanz and Vermeer (1996) presented data supporting this relationship. This expression was also supported by data presented by Cox (2008) for silica sand over a range of relative densities, where it provided a reliable estimate of ϕ'^{ps}_{p}. Hanna (2001) derived an

approach based on Rowe's (1969) stress-dilatancy relationship that related values K, D and ϕ'_{cv} from triaxial tests to estimate the plane strain effective friction angle:

$$\tan \phi'^{ps}_{p} \cos \phi_{cv} = \frac{(KD-1)\sqrt{12D-3D^2}}{4KD-KD^2+3D} \tag{2.18}$$

where K and D are defined based on triaxial data.

A present study derivation considered using Rowe's (1969) stress-stress dilatancy theory and Horne's (1965) equation relating the interparticle and critical state friction angle, which can be shown to give:

$$\frac{R^{ps}}{R^{tx}} = \frac{tan^2\left(45+{\phi'_{cv}}/{2}\right)}{tan^2\left(45+0.5\phi_{\mu}(D-1)+0.5\phi'_{cv}(2-D)\right)} \tag{2.19}$$

This relationship satisfies Rowe's (1969) dilatancy index bounds (D = 1 to 2) and accounts for intermediate values assuming linear interpolation. Hanna's (2001) proposed methods can result in ϕ_f not satisfying the bounds proposed by Rowe (1969). Applied to the dataset compiled by Hanna (2001), the absolute mean percent errors for glass ballotini, River Mersey and Brasted sand are 3.4%, 3.0% and 1.8% respectively; in comparison, Equation (2.17) results in percent errors 8.3%, 4.2% and 2.2%. Furthermore, the linear empirical equation proposed by Shimobe & Moroto (1997):

$$\phi'^{ps}_{p} = 1.265\phi'^{txc}_{p} - 6.71 \tag{2.20}$$

provides accuracy in the same range, with mean percent errors 1.4%, 3.7% and 2.9%. The greatest difference in the predictions is for the glass ballotini material. For the natural sands (River Mersey and Brasted sands) Equation (2.19) provides the closest

approximation and involves less empiricism; however, either approach is reasonably accurate for the natural sands considered.

2.4.2 Critical State Friction Angle

Some researchers have suggested that the critical state friction angle (ϕ'_{cv}) is primarily related to mineralogy and shape, as opposed to relative density and confining stress (Bolton, 1986; Sadrekarimi and Olson, 2011). Bolton (1986) assumes a unique ϕ'_{cv} for plane strain and triaxial conditions. Schanz and Vermeer (1996) suggest that this is true for Hostun sand, and Cornforth (1973) provides supporting evidence for Brasted River sand.

However, based on available data for Toyoura sand, Chakraborty and Salgado (2010) assumed that the value of was 36° for plane strain conditions and 32.8° for triaxial compression. They stated that ϕ'_{cv} can be 3 to 5° higher in plane strain conditions than in triaxial, and is related to the stress path difference rather than changes in initial density or confining pressure. Tong (1970) suggested that ϕ'_{cv} is generally 1 to 2° higher in plane strain than triaxial compression. Shimobe and Miyamori (1991) indicated the difference to be in the range of 2 to 3°, and Wanatowski and Chu (2007) also found the difference to be within this range.

There is also evidence showing that both the dilatancy rate and the critical state friction angle may reduce with confining pressure (e.g. Tong, 1970; Chu, 1995), suggesting that stress level affects both the structural and frictional components of shear strength. The interparticle friction is reduced as the load per particle on the sand grains increases with mean pressure, leading to a decrease in the value of ϕ_μ and subsequently

ϕ'_{cv}. As shown in Figure 2.20, this is prevalent especially in the quartz River Welland and River Mersey sands, whereby the critical state friction angle is about 3° higher at 14 kPa than at 345 kPa.

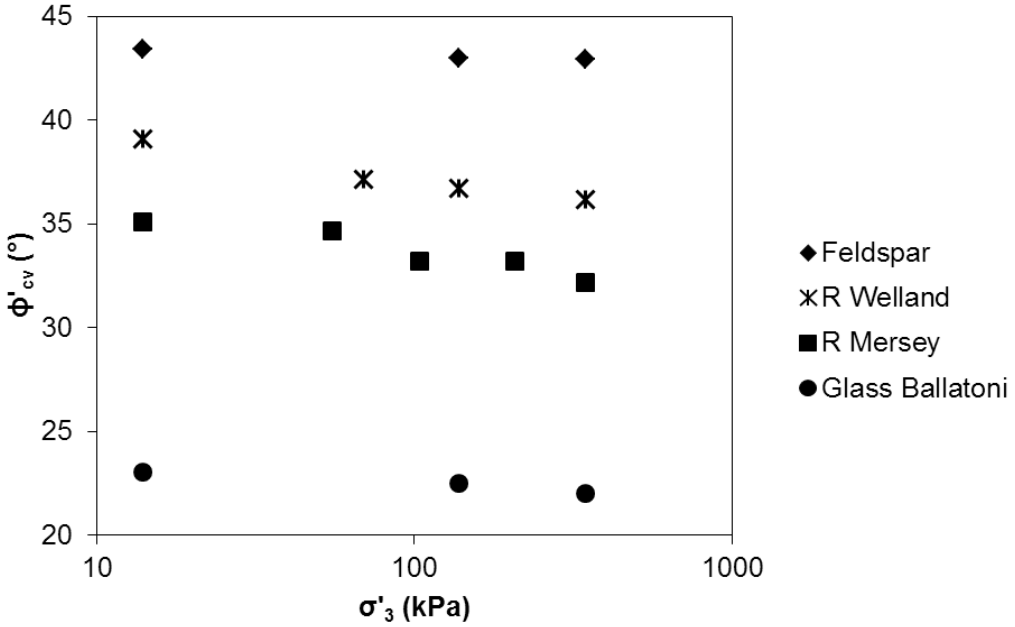

Figure 2.20. Critical state friction angle vs. confining stress for plane strain tests on various sands (after Tong, 1970)

Chu (1995) suggested that while a unique critical state curve may exist, the critical state friction angle for Sydney sand (uniformly graded quartz sand with d_{50} = 0.3 mm) is not constant, but an effective mean stress level dependent parameter; particularly in the low stress range. Chu (1995) points to other examples in the literature where similar behaviour is observed (Castro, 1969; Wu, 1990). For a clean, uniform Silica sand with d_{50} = 0.22 mm, Zhu (1998) observed that the peak and critical state friction angle decreased

linearly with stress in a semi-log scale plot, where the confining pressure ranged from 25 to 2500 kPa.

2.4.2.1 Influence of Particle Shape

The grain shape is more completely defined in terms of roundness (cf. angularity) and sphericity (R and S); within each angularity band grains may have high, medium or low sphericity (Figure 2.21). Cho et al. (2006) showed that the critical state friction angle is more sensitive to roundness than sphericity. The shift in the critical state friction angle is supported by data presented by Cho et al. (2006), as shown in Figure 2.22.

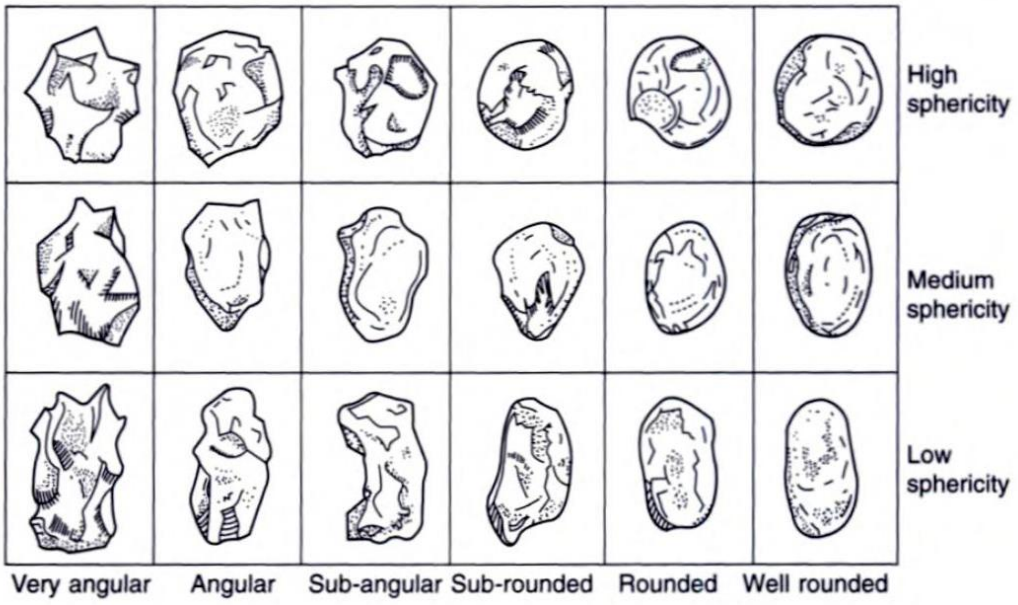

Figure 2.21. Classification of grain shapes (Foseco, 2000)

By comparing the shear strength and volumetric response of spherical glass ballotini and angular crushed glass at the same low confining pressure (14 kPa) and void

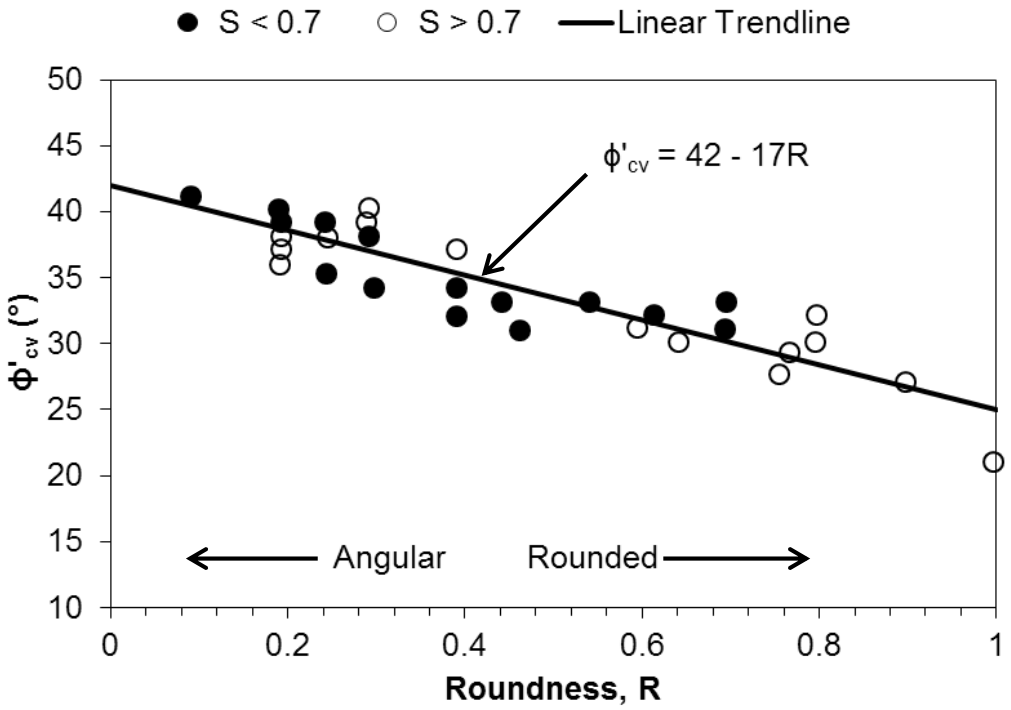

Figure 2.22. Effect of particle shape on critical state friction angle (after Cho et al., 2006)

ratio, Tong (1970) demonstrated the effect of particle shape for two materials having the same basic material properties. The resulting maximum plane strain friction angles were 38.6° and 57.6° for glass ballotini and crushed glass. This indicates that a change in particle shape towards angularity causes an increase in the shearing strength (Tong, 1970). It was suggested that the increase is caused mainly by an increase in interparticle friction rather than an increase in the dilation angle, as the maximum dilatancy factor was not significantly different, while the critical state friction angle doubled from 23° to 46°.

Guo and Su (2007) found Rowe's friction angle, ϕ_f, to be higher than ϕ'_{cv} for rounded Ottawa sand, but higher than ϕ'_{cv} for angular crushed limestone owing to

interparticle locking induced by particle angularity. Suggestions were made to modify the stress-dilatancy relations to take into account the interparticle locking associated with particle angularity. As discussed above, Rowe's friction angle $\phi_f = \phi'_{cv}$ for plane strain conditions and $\phi_\mu \leq \phi_f \leq \phi'_{cv}$ for triaxial tests. However, based on triaxial tests on rounded Ottawa sand (Sand O) and angular crushed limestone (Sand L), Guo and Su (2007) suggest that $\phi_f > \phi'_{cv}$ is possible in for angular soils leading to higher peak friction angles due to particle interlocking. This might help explain high peak friction angles in plane strain conditions for angular soils such as feldspar due to particle interlocking and restraint of the out of plane principal stress. Evidence was provided for the sands tested under triaxial compression conditions as illustrated in Figure 2.23.

As the simplified flow rules by Bolton (1986) utilize the critical state friction angle, these conflicting reports tend to confuse the subject of constant volume friction angle and subsequently estimating the peak friction angle under plane strain and triaxial testing conditions. However, this perceived disconnect, or change in what one would expect to be a unique parameter, can be explained by considering Rowe's friction angle (ϕ_f) as an alternative; this allows for approximate consideration of interparticle locking depending on particle shape. The suggested approach based on Rowe's (1962) stress-dilatancy theory updated to account for $\phi_f > \phi'_{cv}$ affected by interparticle locking is illustrated in Figure 2.24.

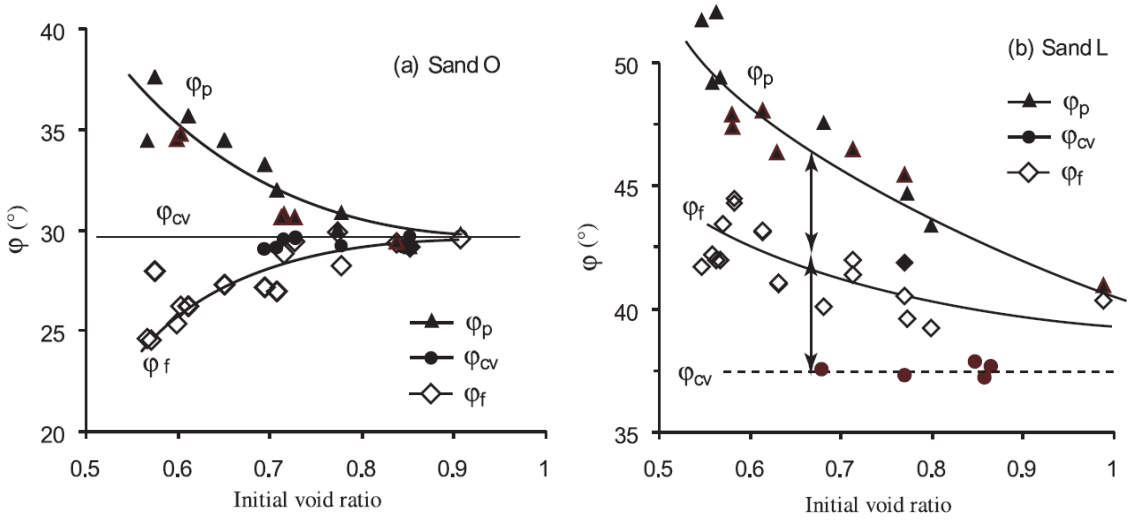

Figure 2.23. Measured shear strength of Ottawa sand and crushed limestone vs. void ratio at σ'_3 = 100 kPa (Guo & Su, 2007)

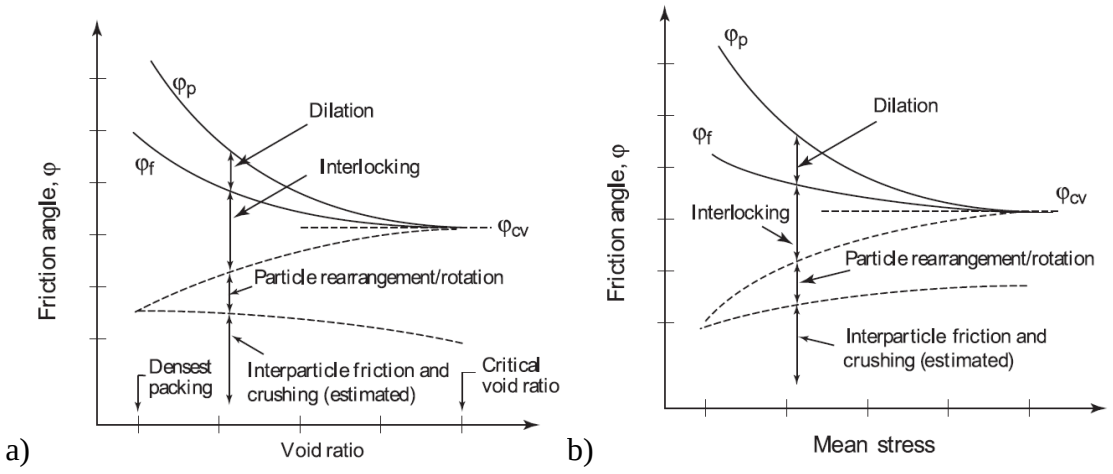

Figure 2.24. An alternative conceptual model for shear resistance of granular materials (Guo & Su, 2007)

2.4.3 Dilation Angle

Vermeer and de Borst (1984) derived the following equation to estimate the angle of dilation from laboratory test data that is valid for plane strain and triaxial testing conditions:

$$\sin\psi = -\frac{\dot{\varepsilon}_v/\dot{\varepsilon}_1}{2 - \dot{\varepsilon}_v/\dot{\varepsilon}_1} \tag{2.21}$$

where, $\dot{\varepsilon}_v = \dot{\varepsilon}_1 + \dot{\varepsilon}_2 + \dot{\varepsilon}_3$. It is important to note that compressive volumetric strains are considered positive, and hence dilation rates are usually negative corresponding to expansion at peak stress conditions. If compressive volumetric strains are considered negative (as they often are), then the first minus sign in Equation (2.21) should be removed.

As discussed by Schanz and Vermeer (1996), since Equation (2.21) applies to triaxial and plane strain test conditions, it follows that the same dilatancy angle is measured in both conditions. Bolton's (1986) analysis confirms that both tests result in the same peak ratio of volumetric to axial strain. Rowe (1969) indicated that D = 1 for sand in the loosest state, and 2 for sand in the densest state, for both plane-strain and triaxial conditions; these bounds are confirmed by several sources for a range of sand types (e.g. Rowe, 1969; Cornforth, 1973; Bolton, 1986; Vaid and Sasitharan, 1991; Hanna, 2001).

Another common definition of the dilation angle is based on the Mohr circle of strains:

$$\sin\psi = -\frac{\dot{\varepsilon}_v}{\dot{\varepsilon}_1 - \dot{\varepsilon}_3} \tag{2.22}$$

An equation for the dilation angle under plane strain conditions ($\dot{\varepsilon}_2^p = 0$) can be deduced from Equation (2.21) or (2.22):

$$\sin\psi = -\frac{\dot{\varepsilon}_1 + \dot{\varepsilon}_3}{\dot{\varepsilon}_1 - \dot{\varepsilon}_3} \tag{2.23}$$

Vaid and Sasitharan (1991) used Equation (2.23) to develop the following expression for the dilation angle under triaxial compression conditions using $\dot{\varepsilon}_3 = (\dot{\varepsilon}_v - \dot{\varepsilon}_1)/2$, giving:

$$\sin\psi = \frac{2}{1 - \frac{3}{\dot{\varepsilon}_v/\dot{\varepsilon}_1}} \tag{2.24}$$

The resulting equations for triaxial compression conditions lead to different estimates of mobilized dilation angle, especially for highly dilatant soils. At the densest state, using Rowe's suggested maximum dilatancy factor D = 2, Equation (2.21) would estimate $\psi_p = 19.5$ while Equation (2.24) predicts $\psi_p = 30.0$. This shows that the interpretation of the dilation angle from triaxial test data is not unique in the literature and potentially significant discrepancies in the predicted dilation angles can occur. This is evident in a number of studies (e.g. Vaid and Sasitharan, 1991; Yang and Li, 2004; Wanatowski and Chu, 2007) where the triaxial compression flow rule coefficient is relatively low (~0.3) compared to a value of 0.48 based on Bolton's (1986) study. Present study reanalysis of the data in these studies using Equation (2.21) finds a coefficient closer to that inferred from Bolton (1986).

2.4.4 Mobilization of Frictional Strength and Dilation

The previous sections dealt with estimating the peak effective friction and dilation angles from laboratory test data. To incorporate strain dependent behaviour such as hardening and softening, it is necessary to define the mobilization of peak and residual, or critical state, as a function of shear strain. In the built-in Mohr-Coulomb in Abaqus, the failure criterion is elastic until a stress condition satisfies the failure criterion and then remains perfectly plastic with increased shear strain. Studies that have used modified Mohr-Coulomb models incorporating friction hardening and/or softening using linear or nonlinear relationships are discussed in the following subsections. The strain-hardening and softening behaviour can be implemented in ABAQUS/Standard or ABAQUS/Explicit through a user defined field, USDFLD or VUSDFLD, respectively.

2.4.4.1 Linear Friction and Dilation Softening

As discussed by Anastasopolous et al. (2007), several researchers have successfully modelled fault rupture propagation in cohesionless soil using an elasto-plastic constitutive model with Mohr-Coulomb failure criterion and strain softening. Anastasopoulos et al. (2007) proposed a model for strain softening behaviour by reducing the mobilized friction (ϕ'_{mob}) and dilation angle (ψ_{mob}) with an increase in plastic deviatoric (octahedral) shear strain (γ^p_{dev}), as shown in Figure 2.25.

Anastasopolous et al. (2007) introduced a procedure to estimate the plastic shear strain at which softening is complete (γ_f^p) based on direct shear test data. The yield shear strain and the peak shear strain are calculated using Equations (2.25) and (2.26) assuming

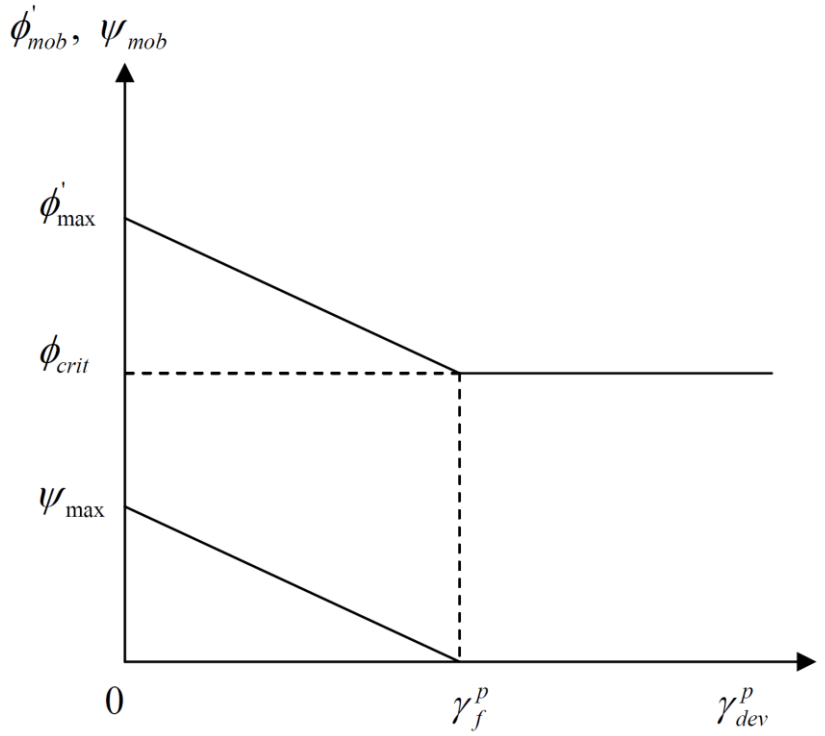

Figure 2.25. Variation of friction angle and dilation angle (Anastasopoulos et al., 2007)

that the shear zone thickness is the same as the sample thickness, H. This approach assumes the shear strain is uniformly distributed prior to the shear band formation at peak stress.

$$\gamma_y = \frac{\delta x_y}{H} \tag{2.25}$$

$$\gamma_p = \frac{\delta x_p}{H} \tag{2.26}$$

where δx_y and δx_p are the horizontal shear displacement at the onset of yield and at peak shear stress. The plastic shear strain at peak conditions is therefore given by:

$$\gamma_p^p = \frac{\delta x_p - \delta x_y}{H} \tag{2.27}$$

Once the shear band is initiated, a two-block shearing model (Shibuya et al., 1997) assumes that all plastic shear deformation takes place within the shear band while the rest of the soil body remains elastic. Assuming the width of the shear band, d_b, is a multiple of the mean sand particle size, N_b*d_{50}, the plastic shear strain at which softening is completed can be expressed by:

$$\gamma_f^p = \gamma_p^p + \frac{\delta x_f - \delta x_p}{N_b d_{50}} \tag{2.28}$$

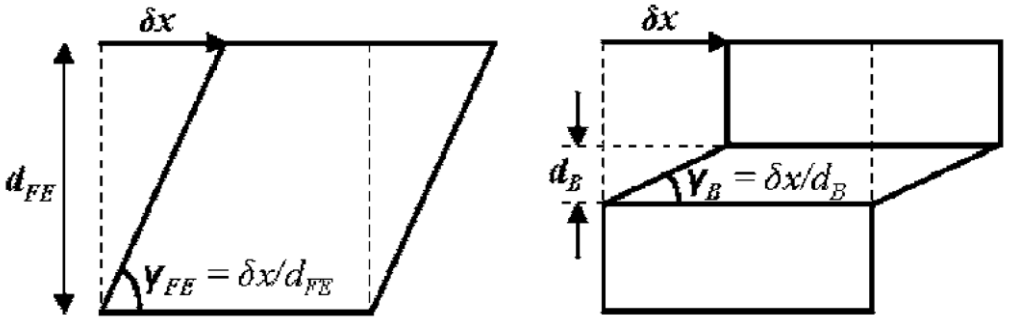

Figure 2.26. Idealized simple shear conditions: left) finite element computed shear strain, right) post-peak shear strain along the shear band (Anastasoploulos et al., 2007)

As discussed by Anastasopoulos et al. (2007), the use of the finite element method in combination with strain softening constitutive models may lead to mesh-dependent solutions. To address this issue, Anastasopoulos et al. (2007) proposed an approximate simplified scaling method. The key assumption in the proposed method is that the shear localization can take place along one element; hence, the width of the shear band will be

equal to the edge length of the element, d_{FE}, for four-node elements. Therefore, d_{FE} should be chosen such that it is equal to the width of the real shear band, d_B ($\approx 16d_{50}$).

Assuming simple shear conditions (above Figure 2.26), for a given shear displacement δx the shear strain in one finite element, γ_{FE}, will be:

$$\gamma_{FE} \approx \frac{\delta x}{d_{FE}} \tag{2.29}$$

Prior to development of the shear band, Equation (2.29) is a reasonable assumption, however, after the shear band forms, the real shear strain will be considerably larger:

$$\gamma_B \approx \frac{\delta x}{d_B} \tag{2.30}$$

The ratio between γ_B and γ_{FE}, λ, can be expressed as:

$$\lambda = \frac{\gamma_B}{\gamma_{FE}} = \frac{\delta x / d_B}{\delta x / d_{FE}} = \frac{d_{FE}}{d_B} \tag{2.31}$$

Since γ_y and γ_p are not involved in shear band formation (i.e. are not influenced by scale effects), the γ_f^p compatible with the actual shear strain is given by the following:

$$\gamma_f^p = \gamma_p^p + \frac{\delta x_f - \delta x_p}{d_B}\frac{d_B}{d_{FE}} = \gamma_p^p + \frac{\delta x_f - \delta x_p}{d_{FE}} \tag{2.32}$$

Hence, this suggests that for $d_{FE} = d_B$ ($d_B/d_{FE} = 1$) the large displacement shear strain directly from the direct shear test is appropriate as input to the FE model, i.e. no scaling takes place. It follows then that scale effects can be avoided by selecting an element size equivalent to the approximate shear band thickness. It is not practical to utilize element sizes $d_{FE} < d_B$, however for $d_{FE} > d_B$ we should be cautious of how the scaling effects may influence the results. Essentially, the amount of strain that occurs from the peak state to

the start of the residual state, or the amount of softening strain, is scaled to account for the relative size of the finite element to the shear band thickness.

2.4.4.2 Nonlinear Hardening and Softening

Vermeer and de Borst (1984) proposed the following equation to approximate nonlinear hardening of the mobilized friction angle as a function of accumulated plastic strain. It is assumed that the mobilized friction angle will increase from 0.0° to ϕ'_p when ε_p^p is reached.

$$\sin \phi'_m = 2 \frac{\sqrt{\left(\varepsilon^p \varepsilon_p^p\right)}}{\varepsilon^p + \varepsilon_p^p} \sin \phi'_p \tag{2.33}$$

To accommodate an initial friction angle corresponding to the beginning of plastic response, ϕ'_o, the equation can be modified accordingly:

$$\phi'_m = \phi'_o + \sin\left(\frac{2\sqrt{\varepsilon^p \varepsilon_p^p}}{\varepsilon^p + \varepsilon_p^p}\right) \sin\left(\phi'_p - \phi'_o\right) \tag{2.34}$$

During post-peak softening, the mobilized friction angle can be expressed by the following (Vermeer and de Borst, 1984; Hsu and Liao, 1998):

$$\phi'_m = \phi'_{cv} + \left(\phi'_p - \phi'_{cv}\right) \times exp\left[-\left(\frac{\varepsilon^p - \varepsilon_p^p}{\varepsilon_c^p}\right)^2\right] \tag{2.35}$$

where ε_c^p is the strain softening parameter; the softening curve has a reflection point when,

$$\varepsilon^p = \varepsilon_p^p + \varepsilon_c^p / \sqrt{2} \tag{2.36}$$

as illustrated in Figure 2.27.

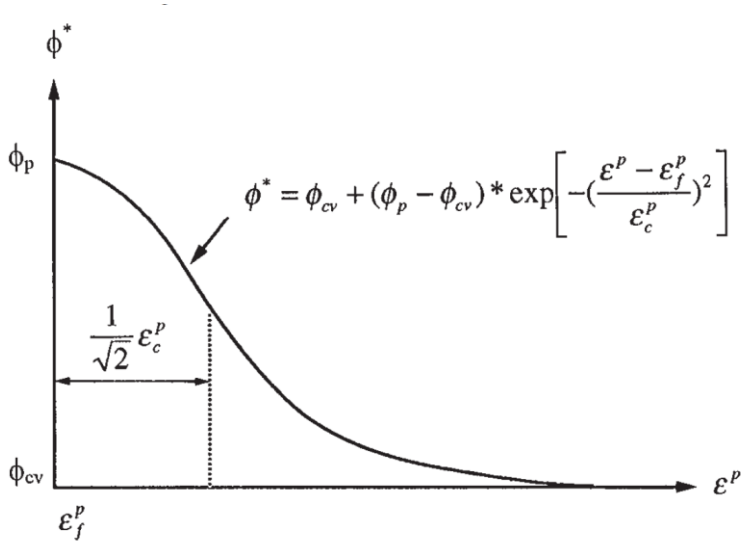

Figure 2.27. Strain softening reflection point (Hsu and Liao, 1998)

Vermeer and de Borst (1984) recommended using Rowe's (1962) stress-dilatancy equation to relate the mobilized dilation angle, ψ_{mob}, to the mobilized effective friction angle:

$$\sin\psi_{mob} = \frac{\sin\phi'_{mob} - \sin\phi'_{cv}}{1 - \sin\phi'_{mob}\sin\phi'_{cv}} \tag{2.37}$$

It is important to note that the Mohr-Coulomb model available in most FE software, such as Abaqus, does not allow for definition of negative dilation angles. Hence, for values of $\phi'_{mob} < \phi'_{cv}$ leading to negative dilation angles, ψ_{mob} should be set to zero with any initial contraction accounted for by the Poisson's Ratio, ν.

Another approach is to define dilation hardening and softening as a function of ψ_p and ε_p, respectively, using the following expressions:

$$\sin\psi_{mob} = \frac{2\sqrt{\varepsilon^p \varepsilon_p^p}}{\varepsilon^p + \varepsilon_p^p}\sin\psi_p \tag{2.38}$$

$$\psi_{mob} = \psi_p exp\left[-\left(\frac{\varepsilon^p - \varepsilon_p^p}{\varepsilon_c^p}\right)^2\right] \tag{2.39}$$

It is also important to note that peak strengths are mobilized at relatively smaller strain levels for dense sands under low confining pressures; hence, the plastic shear strain corresponding to peak friction angle can be expressed as a function of both the relative dilatancy and confining pressure, as shown by Hsu and Liao (1998). Recent work in pipe/soil interaction has adopted the above approach to model lateral pipe/soil interaction in dry dense sand (Roy et al. 2015).

2.5 Pipe/Soil Interaction in Cohesionless Soil

This section provides a comprehensive review of physical lateral pipe/soil interaction tests in dry sand that have been conducted, and summarizes the publicly available test data. Additional large-scale testing was conducted in a collaborative research and development program between Memorial University, Queen's University and the Wood Group. The details of the test results are presented in Burnett (2015), and a summary is provided herein. The current guideline recommendations for ultimate lateral soil resistance and the corresponding pipe displacement are also summarized.

The American Society of Civil Engineers (ASCE) subcommittee on pipe/soil interaction, and task committee on thrust restraint design of buried pipelines have presented recent papers dealing with lateral pipe/soil interaction (e.g. Shumaker, 2011;

Rajah, 2014). In (Shumaker, 2011), it was discussed that the use of 3D FE methods to design for pipe/soil interaction problems through the use of load-displacement considerations is prohibitive in most typical applications due to the user skill required to overcome modelling complexity. However, the use of these tools provides thorough capability to consider more complex aspects of pipe/soil interaction such as unusual geometries (e.g. trench configurations, soil stratigraphy) and soil properties (e.g. strain hardening/softening, density and pressure dependence through user subroutines or user materials). Advanced FE simulation tools have allowed significant advancement in the understanding of pipe/soil interaction behaviour and are a key component in the development of improved design methodologies. In (Shumaker, 2011), the ASCE encouraged research groups to conduct more gold-standard full-scale or large-scale tests for soil-structure interaction in order to validate finite element as well as simpler analysis tools.

2.5.1 Review of Previous Physical Tests

There is a significant amount of physical test data available in the literature to help establish peak lateral soil forces per unit length of buried pipeline in dry sand. A comprehensive review compiled approximately 150 data points across a range of sand type, initial sand density, pipeline diameter (D), and burial depth ratio (H/D). Of the data gathered, the majority of the tests were conducted at 1g, while only 12 of the tests were conducted at centrifuge scale with a prototype D = 1.0 m (Dickin, 1988). The references contributing to the dataset and the general soil characteristics are provided in Appendix C, Table 9.3.

Early studies, in the 1960's through 1980's, on pipe/soil interaction events sought analogous behaviour with other buried structures including vertical anchors and piles in soil through comparison of theoretical formulations and physical test results. For example, Trautmann (1983) showed that Ovesen's (1964) approach for vertical anchor slabs provided good correspondence with his large-scale test data. Furthermore, the ALA (2001) guidelines adopted Hansen's (1961) relationships for lateral motion of rigid piles that have been shown to be very conservative relative to physical test results by Trautmann (1983). More recent guidelines by PRCI (2009) make recommendations for the lateral bearing factor based on verified numerical simulation results by Yimsiri et al. (2004) against the physical tests conducted by Trautmann (1983). Given that there is a sufficient amount of data contributing to the state-of-the-art for lateral pipe/soil interaction physical tests in sand, analogous datasets are not included in this paper.

In general, physical pipe/soil interaction experiments are designed to (a) to study the pipe/soil interaction (b) to reveal the failure mechanisms at shallow and large depths of embedment (c) determine the load-displacement (P-y) curves; and (d) to investigate the influence of such parameters as depth, embedment ratio, pipe diameter, and soil density. Where available, the following data has been compiled and is provided in Appendix A, Table 9.1: peak dimensionless force, H/D ratio, external pipe diameter, diameter to thickness ratio (D/t), dry unit weight of soil, relative density, and friction angle including the laboratory testing method. This study focuses on test results in dry sand, and the reader is referred to Robert (2010) for insight on the effects of moisture content on the

pipe/soil interaction response. The reader is referred to the source papers for details, while a brief overview of this dataset is summarized in the following bulleted points:

- Audibert & Nyman (1975) conducted a series of physical model tests using three model pipelines with diameters of 25 mm, 60 mm and 111 mm tested in loose and dense sand with cover depth ratio ranging from 1 to 24.
- Trautmann (1983) conducted a testing program comprising 30 lateral pipe/soil interaction tests using pipelines with 102 mm and 324 mm diameters buried in dry sand at H/D ratios of 1.5, 3.5, 5.5, 8.0, and 11.0. Three sand densities (14.8 kN/m^3, 16.4 kN/m^3, 17.7 kN/m^3) corresponding to loose, medium and dense sand were used in the testing program.
- Dickin (1988) conducted centrifuge tests on buried pipes and vertical anchor plates to test the underlying assumption that plates and pipes behave similarly in lateral pull tests. The tests were conducted using a 1 m prototype pipe under loose and dense conditions at H/D ratios from 0.5 to 8.5.
- Hsu (1993) conducted a large number of lateral pipe/soil interaction tests to study the effects of sand density, pipe diameter, pipe burial depth, and relative pipe velocity on the pipe lateral soil restraint. Pipes with diameters ranging from a minimum of 38 mm (1.5") to 229 mm (9") were used and the pipe loading rate ranged from 0.001 to 0.2 pipe diameters per second. The H/D ratio was varied from 0.5 to 20 depending on the pipe diameter. In the study by Hsu (1993), the embedment (H_e) depth (i.e. cover depth) rather than the springline depth is used. In this thesis, pipe burial depth ratio and normalized forces have been adjusted to

be consistent with the springline burial depth. The results from Hsu's (1993) tests for loading rates on the lower end of the range are presented in this paper. Hsu et al. (2001) conducted a further study on lateral-axial oblique pipeline motion in loose sand at shallow burial depths (H/D = 1 to 3) for pipe diameters 152.4, 228.6 and 304.8 mm.

- Calvetti et al. (2004) provided results for lateral pipe/soil interaction tests using small (20 and 50 mm) tubes with square and circular cross sections. The tests were performed in loose sand with H/D ratios from about 1.5 to 7.0. The experimental results were shown to match Hansen's (1961) model assuming a friction angle equal to 35°.
- Turner (2004) tested the effect of moisture content in sand on the lateral soil resistance against pipe movement. The 119 mm pipe was buried at H/D ratios from 6 to 20 in two different sands with varying density and moisture content.
- Karimian et al. (2006) presented load-displacement results for three lateral pipe/soil interaction tests in Fraser River sand for diameters 324 and 457 mm at H/D = 2.75 and 1.92, respectively. Each test used the same initial soil density, with relative density equal to approximately 70%.
- Sakanoue (2008) presented two lateral pipe/soil interaction tests conducted in loose and dense conditions in Chiba sand. The 100 mm diameter pipe was buried to a H/D ratio of 6.5. Results of discrete element analyses were also presented.
- Robert (2010) described large-scale lateral pipe/soil interaction tests conducted at Cornell University and at the Pipeline Engineering Research Laboratory (PERL)

owned by Tokyo Gas. The tests were conducted in dry sands at a H/D ratio ranging from 5.3 to 5.7 with pipe diameters ranging from 0.115 m to 0.124 m. Further tests were conducted at varying levels of moisture content, and the reader is referred to Robert (2010) for details.

- Wijiwickreme et al. (2014) described the lateral physical pipe/soil interaction tests conducted as part of Monroy's (2013) broader research effort that included oblique loading test cases. The tests were conducted in three different types of granular material (Fraser River sand with 4% moisture content, road mulch and crushed limestone) at shallow H/D ratios from 1.6 to 1.9 using 406 mm and 457 mm pipelines.

2.5.2 Failure Mechanisms

For model tests of lateral pipe/soil interaction in sand, Audibert & Nyman (1975) described the general soil failure mechanisms, visible through plexiglass wall, for tests with cover depths less than or equal to 6 pipe diameters. In all test cases, a well-defined soil wedge was visible. The overall soil wedge was comprised of three distinct zones: (1) an almost vertical active zone towards the back of the model pipe, (2) a soil wall above the pipe that extended to the soil surface and (3) a passive wedge bound by a logarithmic spiral in front of the pipe. With increasing cover depth, the front limit of the soil wall tilted forward into another logarithmic spiral. For extreme cover depths, a punching mechanism extending two to three diameters in loose sand, and approximately one diameter in dense sand, was observed. At shallow embedment conditions, noticeable

surface heave was present; however, there were no visible signs of disturbance at the surface for deep conditions. These failure mechanisms are illustrated in Figure 2.28.

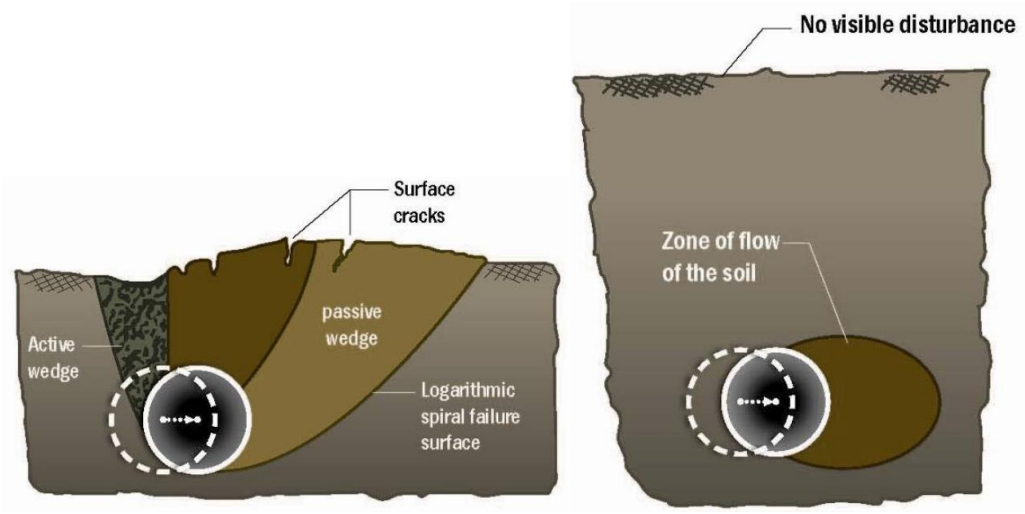

Figure 2.28. Depiction of shallow (left) and deep (right) failure modes for pipes (Rajah, 2014)

Trautmann and O'Rourke (1985) found similar soil displacement patterns for shallow and deep embedment conditions. For shallow burial, the passive and active zones mentioned above were noted, as well as the 'soil wall' that was characterized as the zone of complex displacements. The test results showed that the transition from the shallow to deep failure mechanism occurred for loose and medium dense sand at H/D greater than or equal to 8. For dense sand, at the deepest test burial depth, a transition was not observed. The deep burial failure mechanism for medium dense sand was interpreted as a displacement pattern localized in a region extending about 4D to 5D in front of the pipe and 3D above the pipe; the passive shear surface was not visible at the surface in contrast to shallower tests.

As discussed by Burnett (2015), the PIV technique, initially developed by White et al. (2003), was used to measure soil displacement through the transparent sidewall, capturing the development of soil failure mechanisms during the lateral pipe/soil interaction tests. Both incremental displacement and shear strain fields were plotted at particular intervals of pipe displacement. The typical shallow burial failure mechanisms observed by Burnett (2015) are in line with previous work and are illustrated in Figure 2.29.

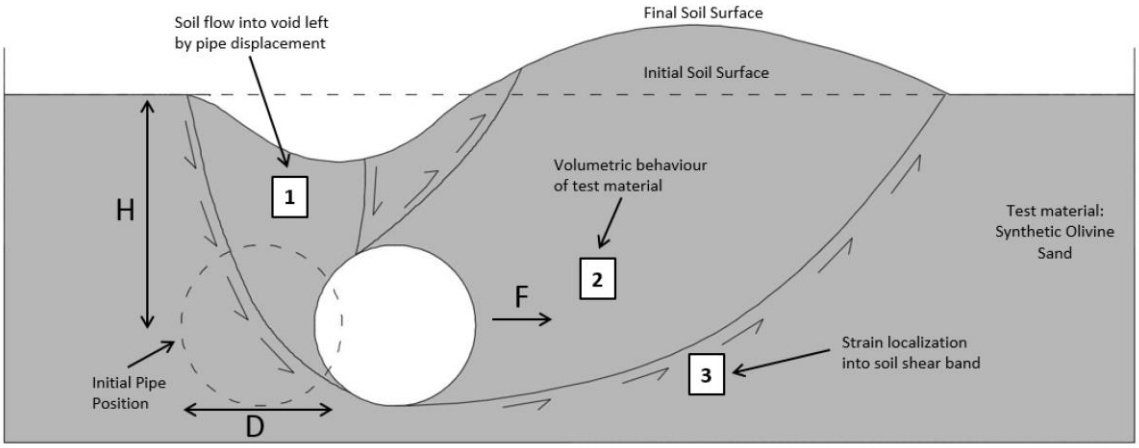

Figure 2.29. Shallow burial soil failure mechanisms (Burnett, 2015)

2.5.3 Summary of Guideline Recommendations

Design guidelines for buried pipes have utilized results from physical testing programs to provide engineering recommendations on the force-displacement spring curves. The spring curves are used define the soil resistance against pipe movement per unit length for use in structural finite element models. Based on tests performed with

buried pipes in dry, uniform sand conducted by Audibert & Nyman (1975, 1977) and Trautmann (1983), the following hyperbolic expression relating the lateral force per unit length, P, and the horizontal pipe displacement, y, has been shown to approximate the force (soil resistance) – displacement response up to the ultimate soil resistance:

$$P = \frac{y}{A' + B'y} \tag{2.40}$$

where:

$$A' = \frac{0.15 y_u}{P_u} \tag{2.41}$$

$$B' = \frac{0.85}{P_u} \tag{2.42}$$

The following formula is used to determine ultimate lateral soil resistance for granular soils:

$$P_u = N_{qh} \gamma' H D \tag{2.43}$$

where γ' is the effective soil unit weight, H is the centerline pipeline depth, D is the external pipeline diameter, and N_{qh} is the horizontal bearing capacity factor. For dry or saturated sands and gravels, and for partially saturated gravels and coarse sand, the ASCE (1984) recommends N_{qh} based on the design curves prepared by Trautmann and O'Rourke (1985). The ASCE (1984) recommends using the Hansen (1961) model for most conditions of pipeline burial in cohesionless sands and gravels when greater conservatism is required. Conservatism in this context can interpreted as predicting the ultimate lateral soil resistance to be 50% to 100% higher compared to Trautmann and O'Rourke's (1985) curves. In the context of buried pipe design however, it is generally

accepted that conservatism implies lower soil resistance that may increase pipe strain due to local buckling. The ALA (2001) guidelines recommend Hansen's (1961) curves as a generic approach for the lateral force-displacement relationship.

Recent guidelines presented by PRCI (2009) recommend N_{qh} curves based on FEA model results presented by Yimsiri et al. (2004); the FEA results were calibrated against Trautmann's (1983) physical test data. The validated numerical tools aided the extension of the design curves to deeper burial depths (Yimsiri et al., 2004). PRCI (2009) provides the following relationship for the lateral bearing capacity factor:

$$N_{qh} = \mathrm{a} + \mathrm{b}\frac{H}{D} \tag{2.44}$$

where a and b are defined for a range of friction angles and burial depths as summarized in Table 2.1.

Table 2.1. Parameters to determine lateral bearing capacity factor (PRCI, 2009)

ϕ'	H/D Range	a	b	Max. N_{qh}
35	0.5 to 12	4	0.92	15
40	0.5 to 6	5	1.43	23
	6 to 15	8	1.00	
45	0.5 to 7	5	2.17	30
	7 to 15	10	1.33	

Interpolation was recommended for values between 35° and 45°, however, a minimum value fixed at 35° was suggested even if soil tests indicate lower ϕ' values (PRCI, 2009). This recommendation is in accordance with the ASCE (1984) guideline

that advises caution when dealing with extremely loose soil (ϕ' = 30°). Physical tests (e.g. Trautmann, 1983) have shown that densification of the soil occurs as the pipeline moves laterally, resulting in a higher acting friction angle.

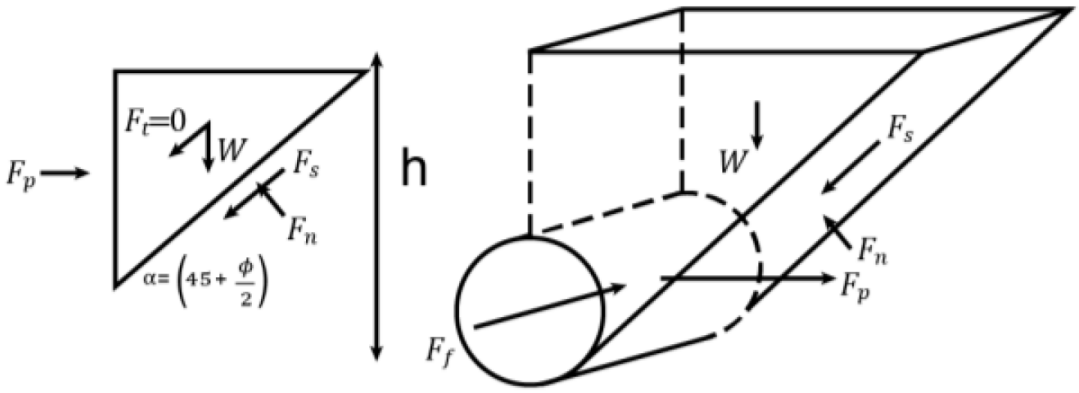

Figure 2.30. Force diagram for passive wedge failure in sands (Rajah, 2014)

Rajah (2014) discussed a P-y curve approach for piles in sands that can be adopted for pipes considering the force diagrams of the passive wedge (Figure 2.30) and flow-around failure mechanisms. For the passive wedge (shallow burial) failure mechanism, the ultimate force acting on a pipe is obtained by considering the equilibrium of forces in the horizontal and vertical directions, and resolving for F_p giving:

$$F_{p1} = \frac{\gamma(H + 0.707D)^2}{2} \tan^2\left(45 + \frac{\phi'}{2}\right) \quad (2.45)$$

where γ is the soil unit weight. For the deep burial condition, the possible ultimate lateral force acting on the pipe from the flow-around failure is given by:

$$F_{p2} = \gamma(H + 0.707D)\left(\frac{1 + \tan\phi'}{1 - \tan\phi'}\right)^4 \quad (2.46)$$

Hence it is suggested that the ultimate lateral resistance acting on the pipe, P_u, can be estimated as the minimum of F_{p1} and F_{p2}; however, Equation (2.46) appears to be limited to $\phi' < 45°$. O'Rourke and Liu (2012) also present equations for shallow and deep burial conditions that can be used to estimate the lateral soil resistance, help explain laboratory test results and illustrate the influence of burial depth; though it is noted by the authors that the equations are not necessarily recommended for use in practice. O'Rourke and Liu's (2012) equation for shallow burial can be simplified to:

$$F_p = \frac{\gamma(H + 0.5D)^2}{2} \tan^2\left(45 + \frac{\phi'}{2}\right) \tag{2.47}$$

which is very similar to Equation (2.45) but leads to a smaller estimate of the ultimate lateral resistance (e.g. 77% at H/D = 1; 95% at H/D = 7). Equation (2.45) provides a similar response to Trautmann and O'Rourke (1985) before deviating beyond H/D = 3, as shown in Figure 2.31.

As discussed above, the ALA (2001) guidelines based on Hansen (1961) predict higher lateral bearing factors. The ASCE (1984) guideline recommended using Hansen's (1961) curves to conservatively estimate horizontal soil forces for most conditions of pipeline burial in cohesionless sands and gravels. This refers to the effects of partial saturation that may lead to increased shear strength relative to dry or saturated states. However, it is the author's opinion that the effects of partial saturation should not be relied on to provide increased shear strength. Furthermore, Robert (2010) found that increased strength due to partially saturated conditions did not exist in one set of experiments (in "Cornell sand"), while increased strength was observed in another set of experiments (in "Tokyo Gas sand"). Robert (2010) discovered that this was due to the

presence of fine particles in the Tokyo Gas sand that caused macroscopic suction and apparent cohesion by microscopic meniscus formation; the latter effect was limited in the Cornell sand.

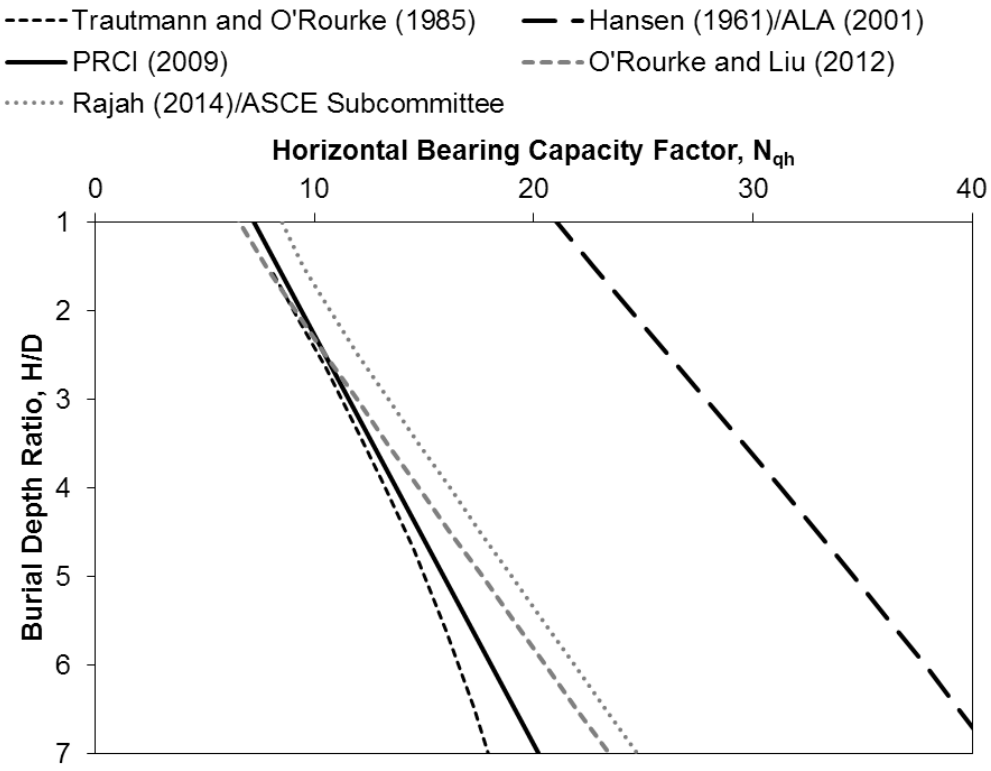

Figure 2.31. Peak normalized lateral force vs. H/D ratio at ϕ = 45° based on guidelines and analytical equations

The ASCE (1984) guideline suggests the following for ultimate displacement based on sand density:

$$y_u = \begin{cases} 0.07 \text{ to } 0.10(H + D/2) & \text{for loose sand} \\ 0.03 \text{ to } 0.05(H + D/2) & \text{for medium sand} \\ 0.02 \text{ to } 0.03(H + D/2) & \text{for dense sand} \end{cases} \quad (2.48)$$

The ALA (2001) and PRCI (2009) define the ultimate displacement by:

$$y_u = 0.04\left(H + \frac{D}{2}\right) \leq 0.10 \text{ to } 0.15D \tag{2.49}$$

for dense to loose sands.

2.5.4 Previous Numerical Studies

Popescu et al. (2002) conducted 2D, nonlinear FEA of large scale tests of lateral loading of a rigid pipe for dense and loose sands using ABAQUS/Standard. To describe the constitutive behaviour of sand, a Mohr-Coulomb model with non-associated plasticity was used. The soil was discretized using quadratic finite elements with 8 nodes and reduced integration (i.e. CPE8R element in Abaqus). The pipe/soil interface friction was taken as $\mu = \tan(0.6\phi')$. Nobahar et al. (2001) describe the procedure used to estimate hardening/softening behaviour of dense sands and hardening of loose sands, based on results of direct shear box laboratory soil tests performed by others. The deformation moduli variation in the elastic range was implemented as shown by Popescu et al. (2002). A non-associated Mohr-Coulomb model was implemented in ABAQUS/Standard that was customized to account for progressive mobilization of soil shear strength parameters during large shear deformations. The modified model also relates the variation of the dilation angle with mobilized friction angle, according to Rowe's (1962) stress dilatancy relation. It was shown that the soil constitutive model could satisfactorily simulate the observed phenomena involved in large relative pipe/soil displacements. However, the material parameter variation with shear strain had to be recalibrated based on the pipe diameter and H/D ratio to account for the effect of pressure on peak strength parameters.

Yoshizaki and Sakanoue (2004) compared their numerical results using finite element methods against the recommended ASCE (1984) guidelines. A two-dimensional (2D) model was developed using ABAQUS/Standard to evaluate the pipe/soil interaction in the lateral direction. The Mohr-Coulomb constitutive soil model was used to model very dense sand conditions. Yoshizaki and Sakanoue (2004) showed that their numerical results agreed reasonably well with the ASCE (1984) guidelines for maximum dimensionless force and displacement. However, with displacement greater than that corresponding to the maximum force, the numerical results for dense sand exhibited a decrease in soil resistance, as observed experimentally by Trautmann and O'Rourke (1985). The observed softening obtained numerically is likely due to a reduction in resistance with upward pipe movement, as the Mohr-Coulomb model is not capable of capturing the softening response.

Yimsiri et al. (2004) implemented the Nor-Sand constitutive model in Abaqus, originally developed by Jefferies (1993), to compare against the experimental data of Trautmann et al. (1985) for lateral and upward tests in sands. The Mohr-Coulomb model was also used as a basis for comparison of the force-displacement response. When using the Nor-Sand model, the force-displacement relationships were more consistent with the experimental data; stiffer in the elastic region and captured strain softening behaviour. The FE analyses predicted the ultimate force due to lateral pipe loading reasonably well for medium and dense sands, with little variation due to differences in the soil constitutive model used in the analysis.

Design charts for lateral and upward pipe movements were proposed based on ultimate loads determined from numerical analysis using the Mohr-Coulomb failure load criterion. Critical embedment depths at which the dimensionless forces become constant are also proposed. The numerical results indicated that the limiting values of N_{qh} for friction angles of 35, 40 and 45 degrees were 14, 22, and 30 with corresponding embedment depths of 12, 15 and 16, respectively. PRCI (2009) guidelines recommend lateral bearing factors based in part on the numerical results presented by Yimsiri et al. (2004).

Guo and Stolle (2005) analyzed the effects of incorporating pressure dependent soil properties on lateral pipe/soil interaction. The maximum dimensionless force is shown to increase with H/D ratio when the soil friction angle and dilatancy are considered independent of soil pressure. However, when pressure dependency is invoked, different trends are observed. At shallower depths, the soil has a higher effective friction angle due to lower confinement pressure, resulting in higher N_{qh}. With increasing H/D ratio, N_{qh} tends to increase, however the decrease in soil friction angle causes N_{qh} to reduce simultaneously. The combined effect is such that N_{qh} decreases initially and then increases with variation of H/D. Guo and Stolle (2005) also showed that including a pressure dependent elastic-modulus significantly decreased the pipe displacement required to fully mobilize the soil resistance. Guo and Stolle (2005) conducted a parametric study to establish N_{qh} as a function of pipe diameter and H/D ratio.

Guo and Stolle (2005) developed a 2D plane strain FE model to analyze lateral pipe/soil interaction in dry sands. The Mohr-Coulomb model was used, with strain

hardening and softening achieved by coupling the friction angle with plastic shear strain. The dilation angle was kept constant for the majority of the analyses. The force-displacement response up to peak loading was not very sensitive to the hardening characteristics; however, post-peak behaviour was shown to be heavily dependent on strain softening of the friction angle. Guo and Stolle (2005) tested the mesh sensitivity on load-displacement relationships and found that using coarse and fine meshes, the response up to peak load was nearly identical, with a discrepancy observed only after the peak. Since only the ultimate soil resistance was of interest in the study, the effect of mesh size was neglected.

Large-scale lateral pipe/soil physical tests were conducted by Karimian et al. (2006) in a large sand chamber available at the University of British Columbia. In addition, 2D numerical analysis using the finite-difference code FLAC was conducted to compare against the experimental dataset. Burial depth ratios of 1.92 and 2.75 were tested with two different pipe sizes, 324 mm and 457 mm. The average density of the sand was 1600 kg/m^3, corresponding to a relative density (D_r) of about 70%. The experimental results showed that the peak load was reached within the first 100 mm of pipe displacement and remained essentially constant with further displacement. For the numerical simulations, the interface dilation angle was accounted for in addition to the interface friction angle. Two constitutive models were used to calibrate the numerical load-displacement response: a bi-linear Mohr-Coulomb model, and a hyperbolic nonlinear model (Duncan and Chang, 1970). The hyperbolic nonlinear model, which accounts for stress dependency of material stiffness and peak friction angle, better

predicted the experimental load-displacement curve; however, it was found to be very sensitive to the failure ratio parameter, as described by Karimian et al. (2006).

Badv and Daryani (2010) used the finite-difference software FLAC to develop a model for lateral and vertical pipe/soil interaction in sand. The constitutive behaviour was based on the Mohr-Coulomb model with the added capability to harden or soften the cohesion, friction angle, dilation angle, and tensile strength after the onset of plastic yield. The numerical model was calibrated against the experimental work of Trautmann (1983). The calibrated model was then used to perform sensitivity analysis examining the effects of pipe diameter (scale effect), burial depth and sand density. It was found that the bearing capacity factor in the lateral direction was a function of the pipe diameter. The results showed that for the same burial depth ratio, a pipe with a smaller diameter has a larger bearing capacity factor; negligible change in the bearing capacity was predicted in the vertical direction. It was not indicated if varying soil failure mechanisms played a role in the lateral bearing factor relationship with pipe diameter. The bearing capacity factor was shown to increase with H/D at shallow conditions, however, due to the local failure mechanism, the bearing capacity factor was assumed to remain constant for deep conditions in both lateral and vertical directions.

Jung (2011) conducted 2D plane strain FEA of pipe/soil interaction for lateral, vertical upward and vertical bearing cases. The FE analyses were calibrated against data from Trautmann (1983), Turner (2004) and Olson (2009). For the constitutive soil model, a modified Mohr-Coulomb plasticity model was used. The finite element mesh was constructed such that the refined part of the mesh had a characteristic element size of 12

mm. This thickness compared favorably with shear band thicknesses of 8 to 20d_{50}, where d_{50} is the median grain size, which equaled about 0.6 mm, as reported by Olson (2009). The geostatic loads were applied under K_o=1 conditions after sensitivity analysis showed a negligible variation in peak dimensionless force by about 1% while varying K_o from 0.5 to 2. In comparison to the large scale lateral test results of Trautmann (1983) and Olson (2009) for dry and partially saturated sand, the numerical predictions obtained by Jung (2011) generally over-predicted the dimensionless peak force by a small, but conservative, margin of 2 – 7%.

Robert (2010) performed extensive two dimensional (2D) finite element analysis (FEA) of pipe/soil interaction in dry and unsaturated sand. Two material models were used within the study, including Modified Mohr-Coulomb (MMC) and Unsaturated NorSand (UNS), and exhibited favorable simulation outcomes in comparison with element tests and large-scale pipe/soil interaction tests. The MMC model is a Mohr-Coulomb model that captures strain-softening by incorporating the reduction of mobilized friction, dilation and cohesion with an increase in plastic deviatoric strain. The UNS model is a modified version of the original critical state-based Norsand model described by Jefferies and Been (2006) that incorporates cohesion and dilation enhancements for unsaturated granular materials.

The UNS model requires one set of model input parameters to simulate sand behaviour over a range of void ratios, confining stresses, and water saturations, whereas the MMC model requires a different set of parameters depending on its initial soil density, water saturation and pipe embedment depth (Robert, 2010). The UNS model is

therefore relatively versatile, however, when comparing the level of laboratory testing to determine parameters, and programming effort to implement the model in a user-subroutine, the MMC model is far less involved. Hence, the MMC model is a viable option that involves relatively low technical execution risk, has parameters that are easily understood and derived simply from direct shear or simple shear testing and has been shown to reproduce desired mechanical features of dense granular materials under dry, saturated and unsaturated conditions (e.g. Anastasopoulos et al., 2007; Robert, 2010; Jung, 2011; Pike et al., 2014a,b; Roy et al., 2016).

The MMC model was adopted by the author in (Pike et al., 2013; Pike et al., 2014a, b) for lateral pipe/soil interaction. Pike et al. (2013) examined the effect of element size on the numerical force-displacement response, showing that the regularization technique to scale the critical plastic deviatoric strain was successful from characteristic element sizes ranging from 9 to 25 mm. The modified Mohr-Coulomb simulation results for lateral pipe/soil interaction were compared against results using the built-in Mohr-Coulomb model. In contrast, the Mohr-Coulomb results attained a constant peak load, while the modified Mohr-Coulomb model was able to capture post-peak softening in the force-displacement response.

The method was used in both ALE and CEL FE applications, showing consistency in the force-displacement response for lateral pipe displacements to about 0.4D. The CEL method was shown to accommodate pipeline displacement beyond the limits of ALE that was affected by mesh distortion issues. To verify the numerical and constitutive procedures, FEA was conducted to simulate physical lateral pipe/soil interaction tests

reported by Trautmann (1983) in very dense soil conditions at H/D ratios 3.5, 5.5 and 8. The analysis results showed good correspondence with the physical force-displacement test data in terms of the peak load (+/- 5%) and softening branch. The shallow burial failure mechanisms observed by Trautmann (1983), including the passive and active wedges and distinct shear band mechanisms, were also captured in the simulation (Pike et al., 2014a,b).

The application of strain softening/hardening and low stress level effects on peak strength parameters is further explored in this thesis through CEL simulations (Section 6.4) of the large-scale lateral physical tests conducted at Queen's University (Section 5.1).

3 Constitutive Models

In this chapter, the constitutive models utilized to simulate undrained loading in cohesive soil and effective stress analysis in cohesionless soil are introduced and developed. The constitutive models are described in their basic form, followed by the present study enhancements that are implemented to account for realistic soil behavior. For undrained behavior of clay this involves methodology to incorporate varying shear strength and stiffness parameters with depth. For cohesionless soils, mobilized effective friction and dilation angles with plastic deviatoric strain, and variation of the peak friction angle with mean effective stress, are implemented using a user defined field (VUSDFLD) user subroutine.

3.1 Constitutive Model for Undrained Cohesive Soil

The interpretation of shear modulus and undrained shear strength from test data (i.e. from cone penetration testing or self-bored pressuremeter) relies mostly on a bilinear, elastic perfectly-plastic simplification, whilst nonlinear behaviour is prevalent in real soils (Konrad & Law, 1987). In numerical modelling of clays, in the absence of more detailed data, it is reasonable to adopt this assumption and apply available interpreted geotechnical properties in a logical and coherent manner using an elastic perfectly-plastic constitutive soil model. The study by Palmer et al. (1990) supports this assumption and approach.

The undrained shear strength of cohesive soils may be determined by laboratory testing methods on fully saturated soil samples, such as the unconsolidated-undrained (UU) triaxial test, and the unconfined compression (UC) test. In UU tests, the confining

pressure (σ_3) is applied to the sample without permitting drainage of the soil specimen. The test specimen is then sheared to failure by application of deviator stress, σ_d, expressed by:

$$\sigma_d = \sigma_1 - \sigma_3 \tag{3.1}$$

As illustrated in Figure 3.1, the deviator stress at failure is effectively independent of the applied confining pressure. For undrained conditions, in the deviatoric plane, the von Mises, Tresca and Mohr-Coulomb failure theories can be used (Figure 3.2). The Mohr-Coulomb failure envelope is a horizontal line ($\phi' = 0$ conditions) in the meridional plane, and the undrained shear strength can be expressed by:

$$s_u = \frac{\sigma_1 - \sigma_3}{2} \tag{3.2}$$

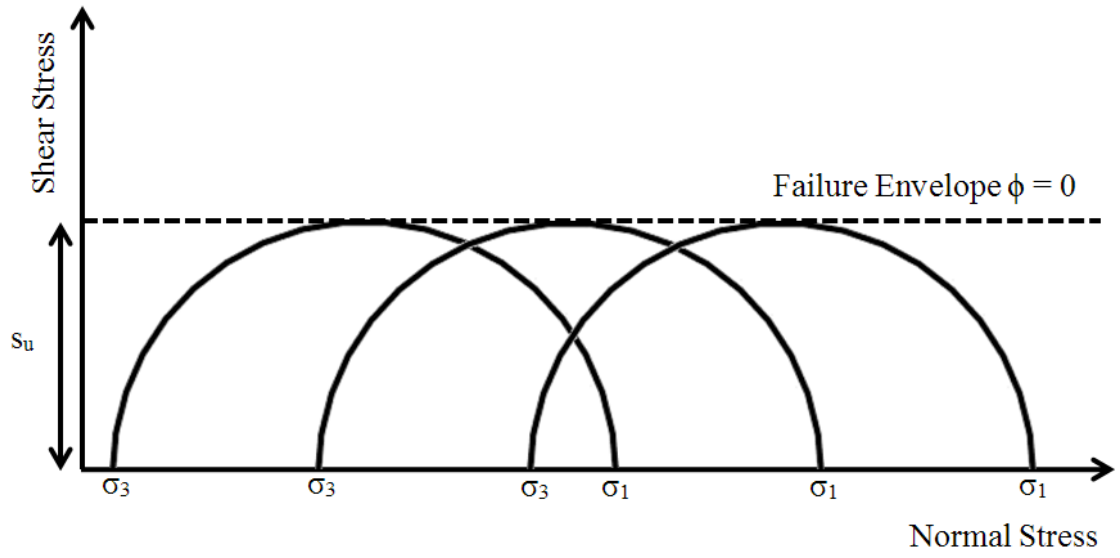

Figure 3.1. Undrained shear strength obtained from unconsolidated-undrained triaxial tests on fully saturated cohesive soil (after Das, 2002)

In principal stress space (Figure 3.2), the Mohr-Coulomb failure envelope is defined by a conical prism having infinite length and reduces to the Tresca yield surface, which has the shape of a six-sided prism having infinite length, when $\phi' = 0$. The von Mises failure surface is defined by a circular cylinder of infinite length in principal stress space and represents a smooth approximation of the Tresca failure surface. In the deviatoric (π) plane, the Tresca failure envelope is a hexagon whereas the von Mises failure envelope is a circle giving equal weighting to all three principal stresses. The Tresca and von Mises models are elastic, perfectly-plastic models expressed in terms of total stress.

The von Mises circle circumscribes and intersects the Tresca yield surface under triaxial stress conditions, whereas the inscribed surface is tangent to the Tresca yield surface under plane strain conditions. For triaxial stress conditions the von Mises yield stress,

$$\sigma_y = 2s_u \tag{3.3}$$

and under plane strain conditions,

$$\sigma_y = \sqrt{3}s_u \tag{3.4}$$

For a triaxial stress state, the yield stress predicted by the von Mises circle and Tresca hexagon are identical. In other stress states, the circumscribed von Mises circle will slightly overestimate the Tresca yield stress to a maximum factor of 1.15 (i.e. $2/\sqrt{3}$).

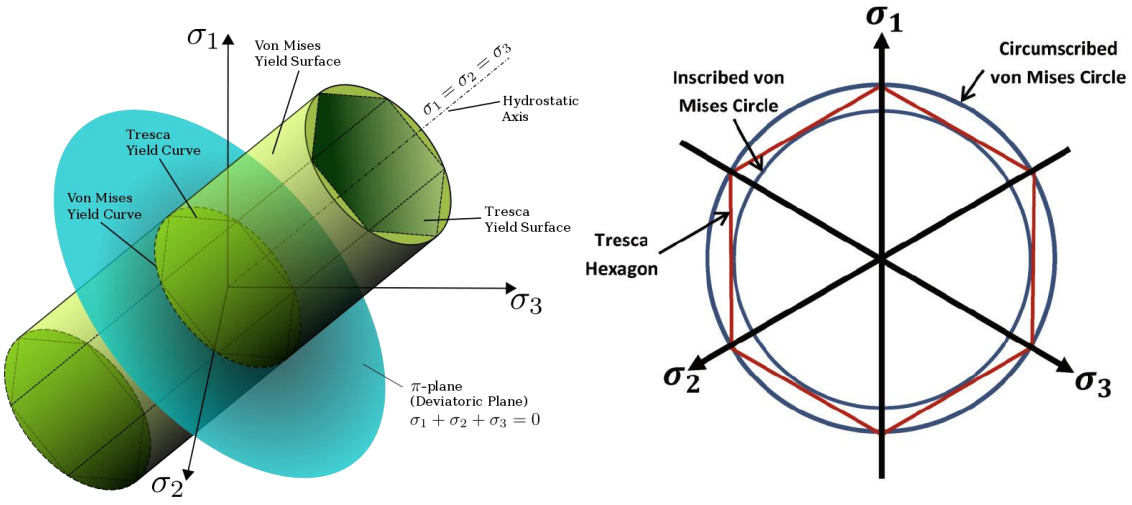

Figure 3.2. Schematic representation of Tresca and von Mises failure surfaces (Left: Wikipedia, 2016; Right: Tho et al., 2013)

To implement the von Mises and Tresca yield surfaces in Abaqus, the input deck templates are provided in Table 3.1. The undrained elastic modulus, E_u, is typically assumed to be a multiple of the undrained shear strength, as discussed further in the subsection below. The Poisson's ratio is typically taken close to 0.5 (e.g. ν = 0.49 to 0.499) to simulate incompressibility, where perfect plasticity (i.e. ν = 0.5) is avoided to prevent a zero (i.e. 1-2ν) denominator in the elasticity formulation.

In the von Mises option, the undrained shear strength is not specified directly, rather the yield stress depending on the assumption of triaxial compression or plane strain conditions is provided; the plastic strain corresponding to yield is zero (0.0) as the response is elastic inside the failure surface. In the Tresca option, the undrained shear strength is specified directly in place of the cohesion yield stress, with a corresponding

value of zero (0.0) plastic strain. The additional line entry TEMP can be used to specify pseudo-depth dependent parameters, as discussed in the following subsection.

Table 3.1. Sample input deck material templates for undrained behaviour

von Mises Yield Surface	**Tresca Yield Surface**
*DENSITY	*DENSITY
Mass Density	Mass Density
*ELASTIC	*ELASTIC
E, ν, TEMP	E, ν, TEMP
*PLASTIC	*MOHR COULOMB
Yield Stress, Plastic Strain, TEMP	$\phi' = 0$, $\psi = 0$
	*MOHR COULOMB HARDENING
	Cohesion Yield Stress, Absolute Value of Corresponding Plastic Strain, TEMP

3.1.1 Constitutive Model Enhancements

The undrained shear strength, as measured in the field (e.g. from cone penetration testing or self-bored pressuremeter) or physical models, is typically not a uniformly distributed, homogeneous property. For the ice gouge centrifuge tests conducted by Lach (1996), the undrained shear strength was estimated based on an empirical relationship with the moisture content that was measured using an in-flight vane shear test. The variability of undrained shear strength (s_u) and overconsolidation ratio (OCR) with depth (Figure 3.3), for speswhite kaolin clay were shown to be consistent with Beaufort Sea clays (Lach, 1996; Figure 6.18).

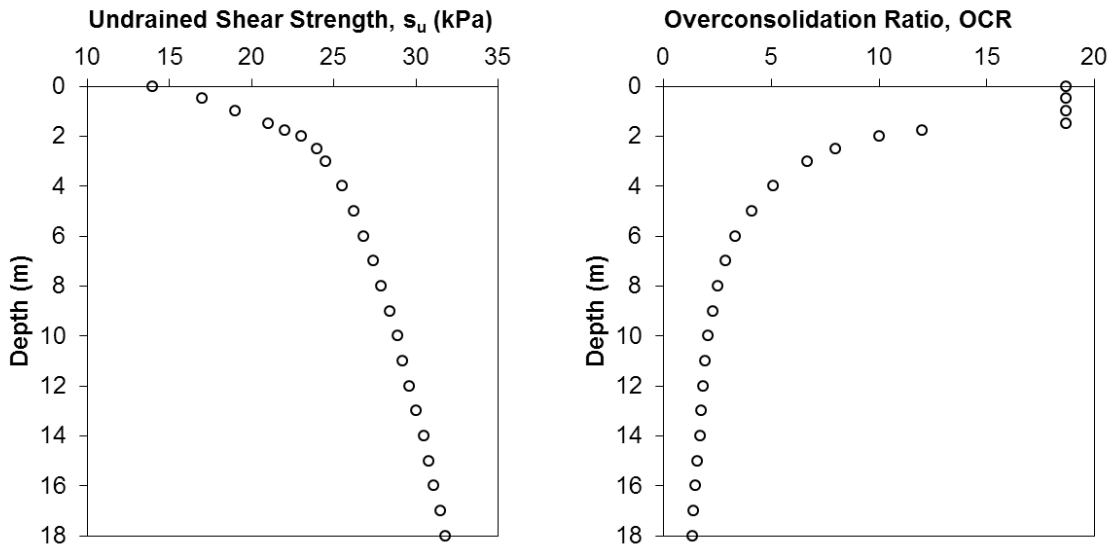

Figure 3.3. Undrained shear strength and overconsolidation profile (after Lach, 1996)

With knowledge of the OCR and shear strength profiles, and the plasticity index (PI), the shear modulus, G_{50}, was approximated via the rigidity index (I_r) using the following relationship provided by Mayne (2007):

$$I_r = \frac{e^{(137-PI)/23}}{\left(1 + ln(1 + (OCR - 1)^{3.2}/26)\right)^{0.8}} \tag{3.5}$$

where,

$$I_r = \frac{G_{50}}{s_u} \tag{3.6}$$

The rigidity index (I_r) has been shown to increase with decreasing plasticity index and overconsolidation ratio per the above Equation (3.5) and Figure 3.4. In a study by Kenny et al. (2007), the use of I_r as a befitting parameter in the prediction of subgouge

soil displacements was presented. Based on physical model tests in clay, Been et al. (2008) provided semi-empirical subgouge soil deformation equations for shallow (15°) and steep angle (30 and 45°) keels that require I_r as an input parameter.

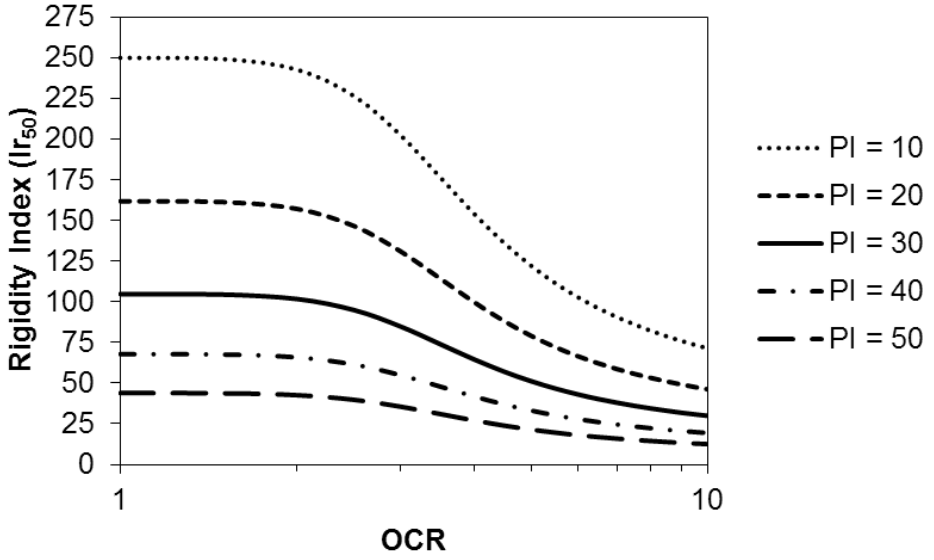

Figure 3.4. Rigidity index vs. overconsolidation ratio (after Keaveny and Mitchell, 1986)

Since undrained conditions are assumed, Poisson's ratio, ν, is taken as 0.5, the undrained Young's modulus, E_{u50}, is defined by:

$$E_{u50} = 3G_{50} \tag{3.7}$$

Based on this, a relationship for E_{u50} as a function of depth can be obtained. For large deformation problems, selecting a stiffness ratio at an intermediate stress level (e.g. G_{50}) may be used to account for the complex variation in moduli with mobilized strain (Robertson & Campanella, 1983; Konrad & Law, 1987; Schnaid et al., 1997).

In FE modelling using Abaqus, the nonlinear yield stress and elastic profiles were defined in tabular format with temperature (i.e. pseudo-depth) dependency. Using temperature as a dummy variable is a versatile modelling approach that is relatively easy to implement in comparison with the development of a user subroutine. Furthermore, parameters related to depth such as the effective vertical stress (e.g. proxy parameter for confining stress) can be implemented to define the variation in state parameters (e.g. elastic modulus for granular materials).

The temperature field is applied using an analytical expression that defines the temperature as a function of the model coordinates. The z coordinate is used in the depth direction (positive downwards) with the origin at the soil surface, hence, the temperature expression is simply defined by:

$$TEMP = Z \tag{3.8}$$

For example, Figure 3.5 shows the temperature contour ranging from 0 to 18, corresponding to the surface at 0 m depth extending to the base of the soil test box at 18 m.

The variation of the elastic modulus (E) and undrained shear strength (s_u) is incorporated within the numerical modelling procedures developed in this thesis (e.g. Section 6.1.3). An example of the elastic and plastic material properties supplied in the input file is provided in Table 3.2 for plane strain conditions. These parameters relate to elastic, perfectly plastic undrained soil behaviour with a von Mises yield stress. By default, the temperature dependent parameters are linearly interpolated for intermediate

values within the range specified (i.e. 0 to 18 in this example case) but are extrapolated as constant values outside the range specified.

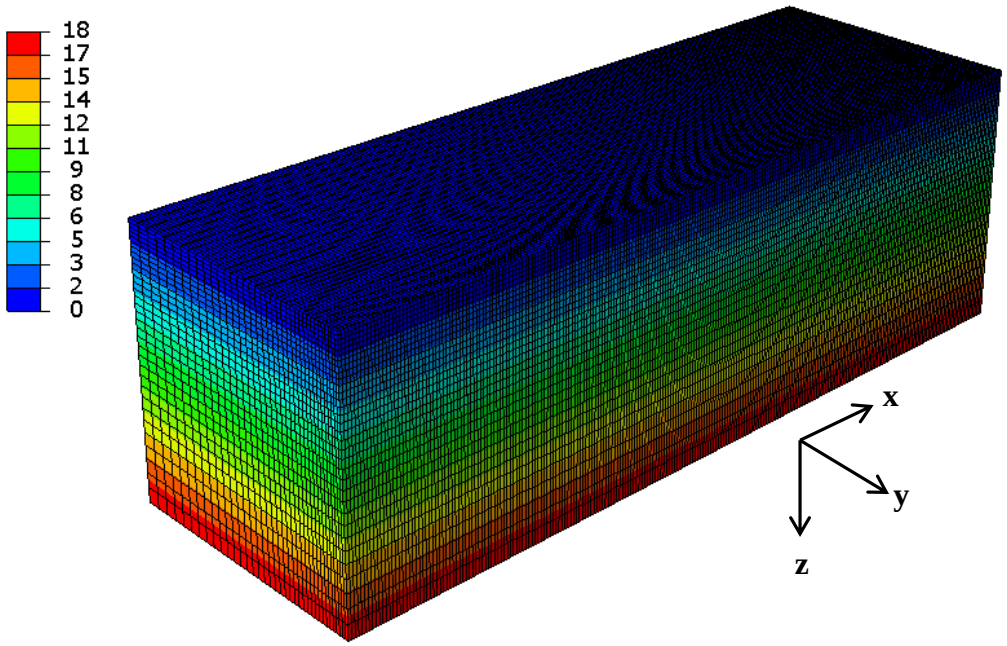

Figure 3.5. Temperature profile output for pseudo-depth dependency

Table 3.2. Abaqus input parameters for varying E and s_u profiles

*ELASTIC (E, ν, TEMP = DEPTH)	*PLASTIC ($\sigma_y = \sqrt{3}s_u$, 0, TEMP = DEPTH)
894737.2, 0.499, 0	24248.7, 0, 0
1086466.6, 0.499, 0.5	29444.9, 0, 0.5
1214286.2, 0.499, 1	32909.0, 0, 1
1342105.9, 0.499, 1.5	36373.1, 0, 1.5
1711650.6, 0.499, 1.75	38105.1, 0, 1.75
1975583.3, 0.499, 2	39837.2, 0, 2
2374528.8, 0.499, 2.5	41569.2, 0, 2.5
2767146.4, 0.499, 3	42435.2, 0, 3
3679683.9, 0.499, 4	44167.3, 0, 4
4738721.9, 0.499, 5	45379.7, 0, 5
5944212.9, 0.499, 6	46419.0, 0, 6
6846479.4, 0.499, 7	47458.2, 0, 7
7535839.2, 0.499, 8	48324.2, 0, 8
8008078.3, 0.499, 9	49190.2, 0, 9
8362068.0, 0.499, 10	50056.3, 0, 10
8571398.7, 0.499, 11	50575.9, 0, 11
8753403.4, 0.499, 12	51268.7, 0, 12
8923422.0, 0.499, 13	51961.5, 0, 13
9093602.5, 0.499, 14	52827.5, 0, 14
9217568.6, 0.499, 15	53347.2, 0, 15
9331783.5, 0.499, 16	53866.8, 0, 16
9467871.0, 0.499, 17	54559.6, 0, 17
9563473.4, 0.499, 18	55079.2, 0, 18

3.2 Constitutive Model for Cohesionless Soil

As the Mohr-Coulomb parameters are density and pressure dependent, this study examines the significance of relative density and stress level on estimates of peak effective friction angle and dilation angle, as obtained from plane strain (PS) and triaxial (TXC) testing conditions. A discussion is also presented regarding the estimate of elastic parameters as a function of stress level and relative density.

To simulate nonlinear soil behaviour considering strain softening and hardening, a review of the critical state friction angle, and methods to simulate the mobilization of peak and critical state values of the friction and dilation angles with shear strain are presented.

Finally, a user-defined subroutine that implements these aspects is shown to accurately simulate the response of triaxial compression test data. Furthermore, it is demonstrated that accounting for nonlinear strain hardening and softening in the constitutive model can provide accurate predictions of triaxial test data (e.g. deviatoric stress and volumetric strain response with axial strain). The available built-in Mohr-Coulomb constitutive model, within Abaqus, cannot capture the post-peak shear stress response due to friction softening, nor can it limit the volumetric expansion with increased axial strain due to dilation softening. Consequently, the user subroutine is essential for capturing realistic soil behaviour.

3.2.1 The Mohr-Coulomb Model

For cohesionless granular materials, the Mohr-Coulomb model predicts an elastic perfectly plastic deviatoric stress response with axial strain. The initial slope of the

volumetric vs. axial strain response depends on the Poisson's ratio and corresponds to the elastic deviatoric stress – axial strain response, while upon yielding the soil dilates per the dilation angle. With a constant dilation angle, the material continues to dilate with increased strain. In the following subsections, the yield and plastic potential functions are introduced, and an illustrative example is provided that demonstrates the response of the built-in Mohr-Coulomb model.

To illustrate the enhancements, developed within this study, to the Mohr-Coulomb constitutive model, a further demonstration of the model output based on triaxial element test results is presented. The modified Mohr-Coulomb (MMC) constitutive model, which is discussed in further detail in Section 3.2.2, is an important outcome from the thesis investigations. In addition, a significant contribution to engineering practice is advanced through the development of a robust yet simple and practical modelling algorithms used in the numerical the simulation of pipe/soil interaction problems.

3.2.1.1 Yield Function

The Mohr-Coulomb failure criterion has been widely adopted to determine the effective friction angle for granular materials. The Abaqus Mohr-Coulomb plasticity model uses the classical Mohr-Coulomb yield function (Figure 3.6). The Mohr-Coulomb failure criterion can be expressed as:

$$\tau_f = c' + \sigma'_{nf} \tan \phi' \qquad (3.9)$$

where τ_f and σ'_{nf} are the shear and normal stresses on the failure plane. This equation can be rewritten as:

$$\sigma'_1 - \sigma'_3 = 2c' \cos\phi' + (\sigma'_1 + \sigma'_3) \sin\phi' \tag{3.10}$$

which is adopted as the yield function:

$$f = \sigma'_1 - \sigma'_3 - 2c' \cos\phi' - (\sigma'_1 + \sigma'_3) \sin\phi' \tag{3.11}$$

For cohesionless materials the yield function can be expressed as:

$$f = (\sigma'_1 - \sigma'_3) - (\sigma'_1 + \sigma'_3) \sin\phi' \tag{3.12}$$

and, for cohesionless soils, the effective friction angle can be determined from:

$$\sin\phi' = \frac{(\sigma'_1 - \sigma'_3)}{(\sigma'_1 + \sigma'_3)} \tag{3.13}$$

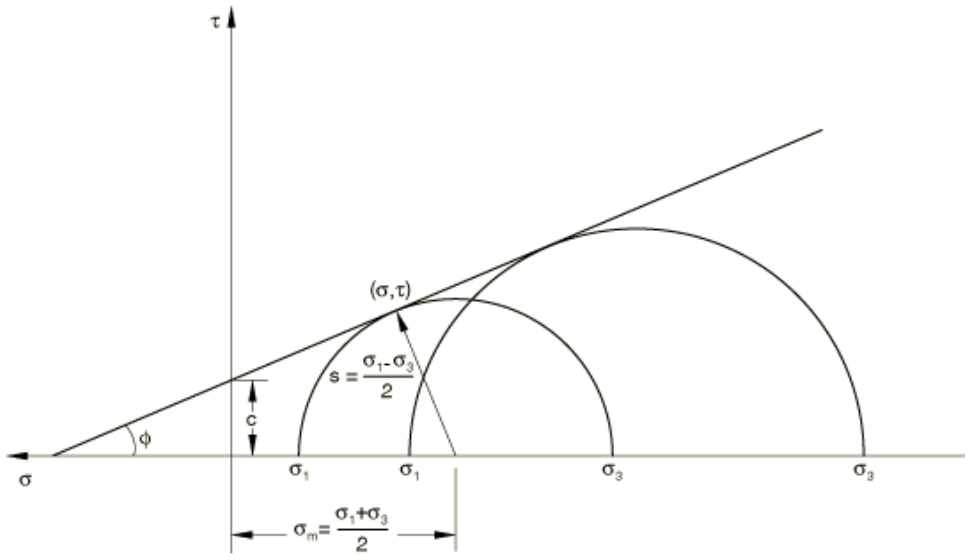

Figure 3.6. Mohr-Coulomb yield surface in the meridional plane (Abaqus, 2016)

For application to general stress states, the yield function can be rewritten in terms of stress invariants and the deviatoric polar angle. Further details are provided in the Abaqus (2016) theory guide, and Potts and Zdravkovic (1999).

3.2.1.2 Plastic Potential Function

The plastic potential function (also termed flow potential) is a means of specifying the direction of plastic straining at every stress state (Potts and Zdravkovic, 1999). If the plastic potential function, g, is assumed to be the same as the yield function (i.e. f = g), the flow rule defining the plastic strain rate is said to be associated. A non-associated flow rule assumes f ≠ g. The Mohr-Coulomb plasticity model available in Abaqus (2016) uses a non-associated flow rule with a smooth flow potential that has a hyperbolic shape in the meridional stress plane and a piecewise elliptic shape in the deviatoric stress plane. The non-associated flow potential function takes a similar form as the yield function, but with ϕ' replaced by ψ.

An associated flow rule essentially assumes that $\phi' = \psi$, which leads to unrealistic plastic volumetric strains and continued dilation with increasing plastic strain. Real soil behaviour tells us that soils eventually reach a critical state whereby the dilation angle reduces to zero (i.e. plastic shearing of the soil continues without volumetric expansion). A non-associated flow rule is an improvement, in that it allows control of the dilation generated by specifying the dilation angle. However, the model still predicts increasing volumetric strains, regardless of how far the soil is sheared. To remedy this problem, the dilation angle can be varied with plastic strain.

3.2.1.3 Sensitivity Analysis

The elastic perfectly-plastic Mohr-Coulomb model available in the Abaqus FE software requires five basic input parameters:

1. Elastic Modulus, E;

2. Poisson's Ratio, ν;
3. Effective Cohesion Intercept, c';
4. Effective Friction Angle, ϕ';
5. Dilation Angle, ψ.

A parametric study (Table 3.3) was conducted, with a variation in the elastic modulus, Poisson's ratio and dilation angle for a constant friction angle and confining stress state, to illustrate the effect of the Mohr-Coulomb parameters on the material response for triaxial compression test conditions. The sensitivity values are selected for demonstration purposes. The elastic moduli are representative for mean stress conditions at shallow burial depths. The predicted deviatoric stress and volumetric strain state with respect to the mobilized axial strain, across the range of parameters examined, are presented in Figure 3.7.

Table 3.3. Basic Mohr-Coulomb parameters for triaxial element test

Case	E (MPa)	ν	ϕ'	ψ	σ'_3 (kPa)
1	3.62	0.4	41.9	15.5	31.1
2	**7.24**	0.4	41.9	15.5	31.1
3	3.62	**0.2**	41.9	15.5	31.1
4	3.62	0.4	41.9	**7.75**	31.1

Cases 1, 3 and 4 are conducted at the same elastic modulus and hence yield at the same level of axial strain, while Case 2 uses a higher modulus and hence yields at a

smaller strain level. Cases 1, 2 and 4 are conducted at the same Poisson's ratio and hence have the same initial compression slope, while Case 3 has a lower value and hence experiences higher compression in the elastic region. Each case has the same friction angle and subsequently the sample yields at the same level of deviatoric stress. Finally, cases 1, 2 and 3 have the same dilation angle, and therefore have the same dilatancy rate ($d\varepsilon_v/d\varepsilon_1$), while the influence of a lower dilation angle resulting in a more gradual slope results for cases 4. This provides a basis to understand the effects of the built-in model Mohr-Coulomb model upon which more realistic soil behaviour can be incorporated using user-subroutines that allow variation of the main parameters with increasing strain level.

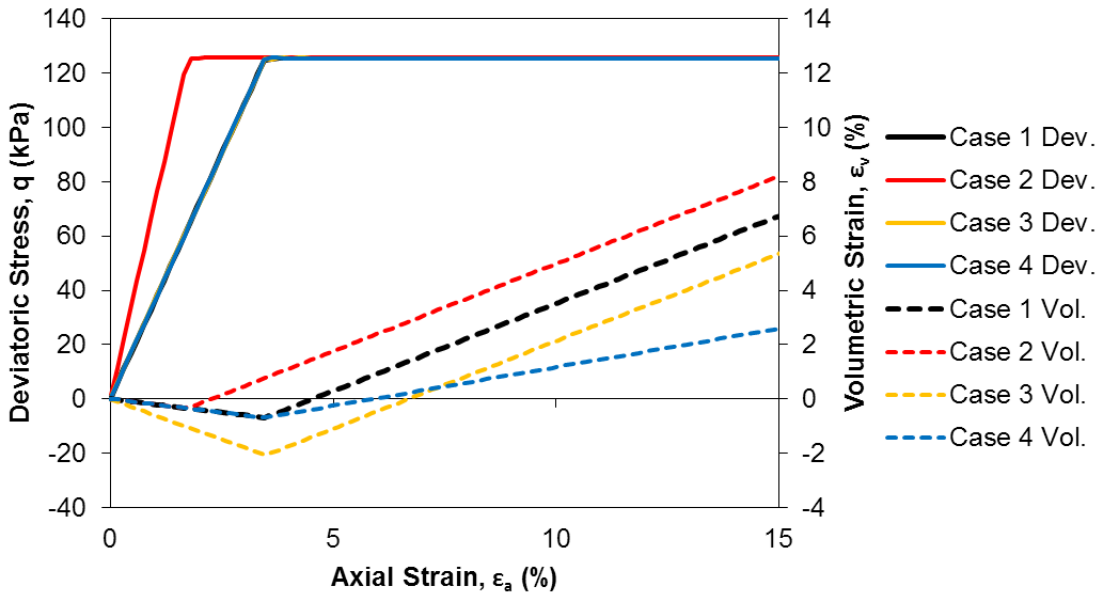

Figure 3.7. Mohr-Coulomb parameter effects

3.2.2 Constitutive Model Enhancements

3.2.2.1 Overview

The built-in Mohr-Coulomb constitutive model, within the Abaqus simulation framework, does not account for some characteristics of realistic soil behaviour that are of practical importance when modelling large deformation, pipe/soil interaction events. By default, the state parameters, including Elastic modulus, Poisson's ratio, effective friction angle and dilation angle, assume constant values and cannot account for a variation in these parameters with the mobilized stress or strain response.

This will constrain the numerical modelling prediction with respect to calibrating the constitutive model to capture specific characteristics of the soil mechanical behaviour. For example, the effects of strain hardening and strain softening on the mobilization of peak and residual shear strength with increasing strain are not captured. The modelling procedures could be calibrated with physical data to match the initial elastic and peak strength response but provide relatively weaker correspondence with the residual strength or critical state parameters. In terms of the volumetric response, after a small initial compression, dense samples expand in volume (or dilate) before continuing to shear without further volume change. The dilation effect increases with sample density, and decreases with increasing confining pressure. This helps explain the reduction of peak effective friction angle with increasing confining pressure, i.e. since dilation is restricted due to high confining pressure, the effect is a reduction in the peak effective friction angle.

This study addresses the enhancement of the Mohr-Coulomb constitutive model, to simulate large deformation, large strain pipe/soil interaction problems and overcome the inherent limitations of the built-in Mohr-Coulomb (MC) model. The refined modified Mohr-Coulomb (MMC) provides a basis to account for the variation of the state variables (i.e. effective friction angle and dilation angle) as a function of field variables (i.e. mean effective stress, deviatoric strain). Details of this enhancement to the built-in MC constitutive model are presented in the following subsections.

3.2.2.2 Elastic Behaviour

The basic Mohr-Coulomb model approximates the soil response as linear elastic until the stresses in the soil exceed the yield surface. The model uses a constant elastic modulus to approximate the nonlinear stress-strain behaviour of the soil before yield, and thus provides a simplified equivalent representation of the soil response. The elastic modulus, E, may be applied as a constant or as a function of depth through a dummy temperature field; the latter case is used in this study for applications to pipe/soil interaction in cohesionless.

Lapos and Moore (2002) expressed the initial elastic modulus of synthetic olivine sand with Janbu (1963) parameters, K and n, per the following equation:

$$\frac{\mathrm{E_i}}{p_0} = \mathrm{K}\left(\frac{\sigma_3}{p_0}\right)^n \tag{3.14}$$

where p_0 is atmospheric pressure (101.3 kPa), K and n are constant for a particular density level and σ_3 is the effective confining stress.

Use of the initial tangent modulus is appropriate when strain softening is accounted for through variance of the strength parameter (e.g. mobilized friction angle) with plastic strain. Other approaches that do not account for strength softening consider a reduced elastic modulus to approximate the force displacement response by equalizing the amount of over- and under-prediction associated with the initial slope linear simplification (e.g. Figure 3.8). Jung (2011) used the K_{70} approach (Trautmann, 1983) to calibrate an equation for $E_{70\text{-}H}$ as a function of the soil density and effective stress vertical stress at the pipe centerline through iterative FE pipe/soil interaction simulations; Trautmann (1983) and Olson (2009) physical datasets formed the comparison basis.

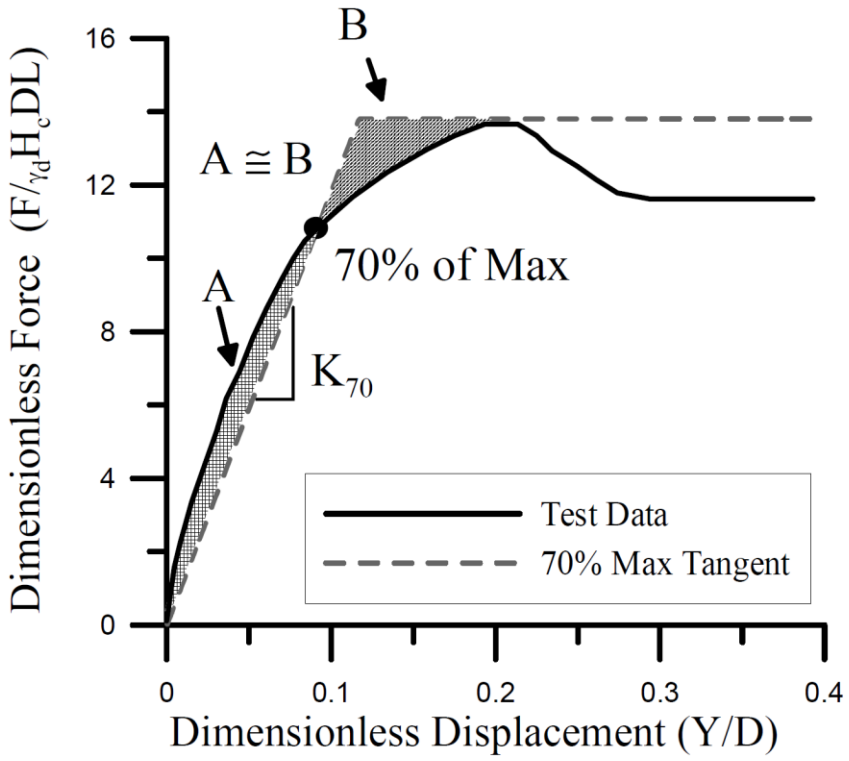

Figure 3.8. K_{70} approach of bilinear model for dimensionless force-displacement curve (Jung, 2011)

Similar to above (Section 3.1.1), implementation of the elastic Janbu (1963) parameters, or other expressions of elastic variance with stress, can be achieved simply and effectively in Abaqus using temperature dependent properties. This is achieved by introducing a temperature field as an initial condition; the temperature field can be incorporated such that the distribution of temperatures equates exactly to the vertical coordinates. Hence, the elastic properties are related to depth, which is easily related to the effective vertical stress at the pipe centerline that can act as a proxy for the effective confining stress.

The Poisson's ratio defines the initial compression response of soil specimens. For samples tested at low confining pressure and high relative density, the volumetric strain response shows that specimens compress very little before dilation occurs at small axial strain levels. This relates to higher ν values for dense sands at low confining pressure compared to loose samples at high confining pressures. Hsu & Liao (1998) account for this through calibrated empirical relationships for elastic and bulk modulus (E and K) that are a function of relative density and effective mean pressure that result in higher values of Poisson's ratio for samples that are relatively dense tested at relatively low confining pressure. The empirically calibrated relationships to estimate the elastic and bulk moduli for I-Lan sand are as follows (Hsu, 2005):

$$E = (70 + 200D_r)p_0(\sigma_3/p_0)^{0.8} \tag{3.15}$$

$$K = (11 + 110D_r)p_0(\sigma_3/p_0)^{0.2} \tag{3.16}$$

where P_a is the atmospheric reference pressure in kPa. Hence, knowing E and K, the Poisson's ratio can be solved, making it a function of relative density and pressure level.

Lee (1970) addressed the differences in the elastic regime response for plane strain and triaxial compression tests. Based on an ideal elastic isotropic material, Lee (1970) derived expressions for equivalent elastic modulus and Poisson's ratio for plane strain conditions (E_p and ν_p). Based on the analysis of triaxial test data E_p and ν_p can be expressed as:

$$E_p = \frac{E}{1-\nu^2} \tag{3.17}$$

$$\nu_p = \frac{\nu}{1-\nu} \tag{3.18}$$

where E and ν are the elastic modulus and Poisson's ratio determined from triaxial test results.

3.2.2.3 Pressure Dependency

As discussed in Section 2.4.1, peak friction (e.g. Figure 3.9) and dilation angles exhibit stress dependency effects that are especially amplified under conditions of low pressure and high relative density. It is important to consider these effects related to simulating pipe/soil interaction in granular material, as pipe burial depths are generally shallow enough that low stress conditions apply. For example, the effective vertical stress at the pipe centerline for a 254 mm diameter pipeline at H/D = 3 in dense sand would be approximately 12 kPa. This is in the range of very low stress conditions with limited literature on the behaviour of granular material at this stress range.

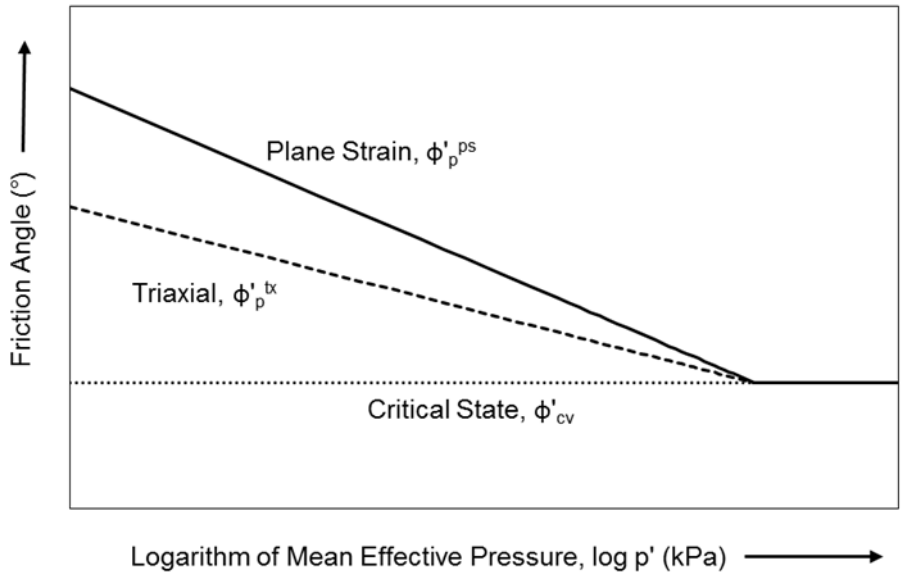

Figure 3.9. Friction angle dependency on mean effective pressure (after Lau and Bolton, 2011)

The mean effective stress is defined by:

$$p' = -\frac{1}{3}(\sigma_{11} + \sigma_{22} + \sigma_{33}) \tag{3.19}$$

The dependency of the friction angle on the mean effective stress is generally defined for the peak friction angle, and therefore p' must correspond to the stress conditions at failure. There are existing generic empirical relationships that can help predict friction and dilation angle variation with mean effective stress, p' (e.g. Bolton, 1986 as discussed in Section 2.4.1). However, the stress dependency can be tailored for specific materials based on the results of laboratory tests (e.g. Hsu and Liao, 1998; Zhu, 1998).

3.2.2.4 Strain Dependency

As discussed in Section 2.4, realistic soil behaviour for dense sand is characterized by strain hardening and softening. In addition to appropriate selection of the peak and constant volume friction angle, and peak dilation angle, depending on the stress and density level, it is also important to address how these strength parameters are mobilized as a function of some strain measure, as was discussed in Section 2.4.4.

In the current study, it was important to consider a general framework that could be applied to both 2D and 3D model scenarios where the developed numerical tools could be applied to complex coupled interaction scenarios such as ice/soil/pipeline interaction (e.g. application to cohesive soils in Section 6.3).

The octahedral (deviatoric) strain was used in the present study as it involves all six components of the strain tensor and hence can be applied to 3D simulations. Since the deviatoric strain is not an existing output variable in Abaqus, a user subroutine (VUSDFLD) for use with ABAQUS/Explicit was developed to calculate the incremental plastic deviatoric strain (γ_{dev}^{p}) as a solution dependent variable (SDV).

The general 3D state of strain can be transformed into two scalars, a volumetric component, and a deviatoric component. The total strain energy of the general system is the same as the sum of the strain energies resulting from individual application of the dilatational and deviatoric strains. Performing this split, requires transformation of the general state of strain onto the octahedral planes, which are the 8 planes forming equal angles with each of the principal strain directions, and results in the octahedral normal strain (dilatational component),

$$\epsilon_n = \frac{1}{3}(\epsilon_{11} + \epsilon_{22} + \epsilon_{33}) \tag{3.20}$$

which describes the volume change, and the octahedral shear strain (deviatoric component),

$$\gamma_{dev} = \frac{2}{3}\sqrt{(\epsilon_{11} - \epsilon_{22})^2 + (\epsilon_{11} - \epsilon_{33})^2 + (\epsilon_{22} - \epsilon_{33})^2 + 6(\epsilon_{12}^2 + \epsilon_{13}^2 + \epsilon_{23}^2)} \tag{3.21}$$

which is the maximum value of the shear strain on any plane. Both of these components are independent of the orientation of the coordinate system. The shear strain components, in the user subroutine VUSDFLD (ABAQUS/Explicit), are stored as tensor components and not engineering components; as defined in the user subroutine USDFLD for use in ABAQUS/Standard.

The accumulated plastic strain, ε_p, is commonly used in relation to shear and volumetric response in triaxial tests (Hsu and Liao, 1998), and is defined as:

$$\epsilon_p = \frac{2}{3}\left(\epsilon_a^p - \epsilon_r^p\right) = \epsilon_a^p - \frac{1}{3}\epsilon_v^p \tag{3.22}$$

where ϵ_a^p (ϵ_{11}^p), ϵ_r^p ($\epsilon_{33}^p = \epsilon_{22}^p$) and ϵ_v^p are the axial, radial and volumetric plastic strains. The octahedral shear strain under triaxial testing conditions can be simplified to:

$$\gamma_{dev} = \frac{2}{3}\sqrt{(\epsilon_{\mathrm{a}} - \epsilon_{\mathrm{r}})^2 + (\epsilon_{\mathrm{a}} - \epsilon_{\mathrm{r}})^2} = \frac{2\sqrt{2}}{3}(\epsilon_a - \epsilon_r) = \sqrt{2}\epsilon_p \tag{3.23}$$

3.2.2.5 Subroutine Implementation

In this study, a user-defined field variable subroutine for ABAQUS/Explicit (VUSDFLD) was developed to incrementally update the mean effective stress and deviatoric strain values through correspondence with predefined tabular entries

expressing the relationship between the effective friction angle, dilation angle and mobilized strain magnitude for a series of effective mean stress (p') values (see flowchart in Figure 3.10). During each increment of the numerical simulation, each of the six plastic strain variables (PE11, PE22, PE33, PE12, PE13, PE23) are read into the subroutine and are used to calculate the octahedral shear strain per Equation (3.21). Similarly, the mean effective stress is calculated using the normal stress components (S11, S22, S33) of the stress tensor per Equation (3.19). The friction and dilation angle values are interpolated based on the current value of the octahedral shear strain and mean effective stress.

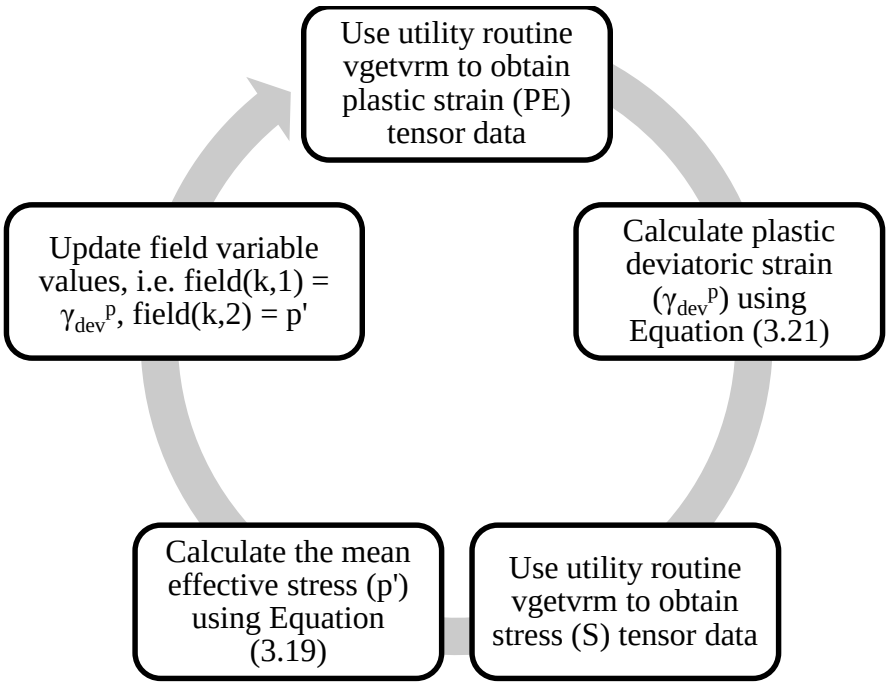

Figure 3.10. VUSDFLD subroutine flowchart for updating field variables

In this study two field variables were used, hence the friction and dilation angle response surfaces can be plotted in three-dimensions (e.g. Figure 3.11). There are two important aspects of this methodology to consider: 1. the field variable dependency should be specified for the range of expected values as 2. the dependent variables are linearly interpolated for intermediate values of the field variables but are held constant outside the range specified at the upper and lower bounds.

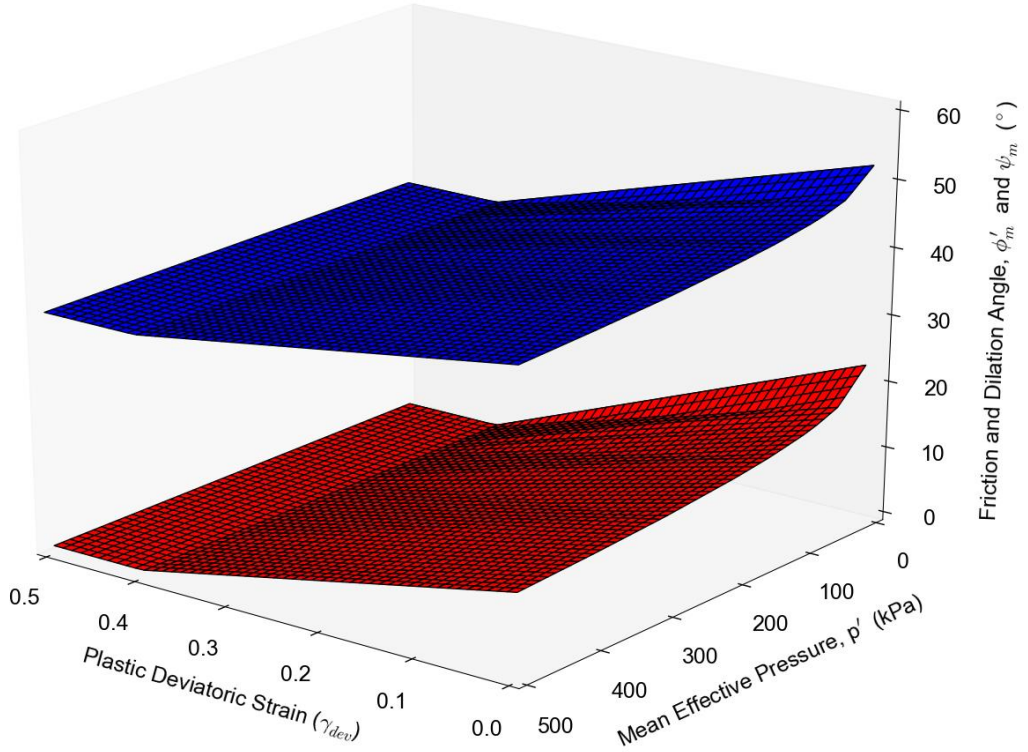

Figure 3.11. Three-dimensional representation of stress and strain dependent friction and dilation angles

To demonstrate the subroutine and verify correct input/output operations, triaxial element tests (Table 3.4) were conducted for a range of confining pressure. The peak

friction angle, elastic modulus, and Poisson's ratio values are based on the triaxial compression test data presented by (Clark, 1998; Zhu, 1998) for very dense (D_r = 90%) samples of silica sand. The pressure dependent friction angle can be expressed by:

$$\phi'^{tx}_{p} = -4.97 \log p' + 57.44 \tag{3.24}$$

The linear softening model (Section 2.4.4.1) is used for ease of demonstration, and the material is assumed to fully soften once the plastic deviatoric strain reaches 0.4. The present model also assumes that the critical state friction angle is constant. The specification of the MMC model in the analysis input file is presented in Table 3.5. The strain dependent curves for respective p' values can be supplied to account for more realistic features of soil behavior including nonlinear hardening and softening, and pressure dependent strain levels for peak and residual conditions.

The results presented in Figure 3.12 indicate that the correct friction angle is determined using the implemented VUSDFLD subroutine, along the p' axis, based on Equation (3.24). For each respective case, the friction angle reaches a peak value corresponding to the peak mean effective stress, and then softens to the critical state friction angle. The results in Figure 3.13 indicate that the deviatoric stress (q) is fully softened at the specified value γ_{dev}^{p} = 0.4, and remains constant with increased plastic deviatoric strain.

Table 3.4. Triaxial element test cases to demonstrate VUSDFLD subroutine

Case	Confining Pressure, σ_3 (kPa)	Elastic Modulus, E_i (MPa)	Poisson's Ratio, ν
1	10	9.0	0.42
2	100	44.0	0.34
3	250	80.0	0.29

Table 3.5. Modified Mohr-Coulomb Input Deck Template (Case 1)

```
*MATERIAL, NAME=SOIL
*USER DEFINED FIELD
*DEPVAR
2
1, STRAIN_OCT, "Octahedral shear strain"
2, PRESSURE_MEAN, "Mean Effective Pressure"
*DENSITY
1600.0
*ELASTIC
9340000, 0.42
*MOHR COULOMB, DEPENDENCIES=2
52.5, 23.0, , 0, 10000
35, 0, , 0.4, 10000
49.0, 18.4, ,0 , 50000
35, 0, , 0.4, 50000
48.0, 17.1, ,0 , 80000
35, 0, , 0.4, 80000
47.5, 16.4, , 0, 100000
35, 0, , 0.4, 100000
46.6, 15.3, , 0, 150000
35, 0, , 0.4, 150000
46, 14.5, , 0, 200000
35, 0, , 0.4, 200000
45.1, 13.3, , 0, 300000
35, 0, , 0.4, 300000
44.5, 12.5, , 0, 400000
35, 0, , 0.4, 400000
44.0, 11.9, , 0, 500000
35, 0, , 0.4, 500000
42.5, 9.9, , 0, 1000000
35, 0, , 0.4, 1000000
*MOHR COULOMB HARDENING
 100.0, 0.
```

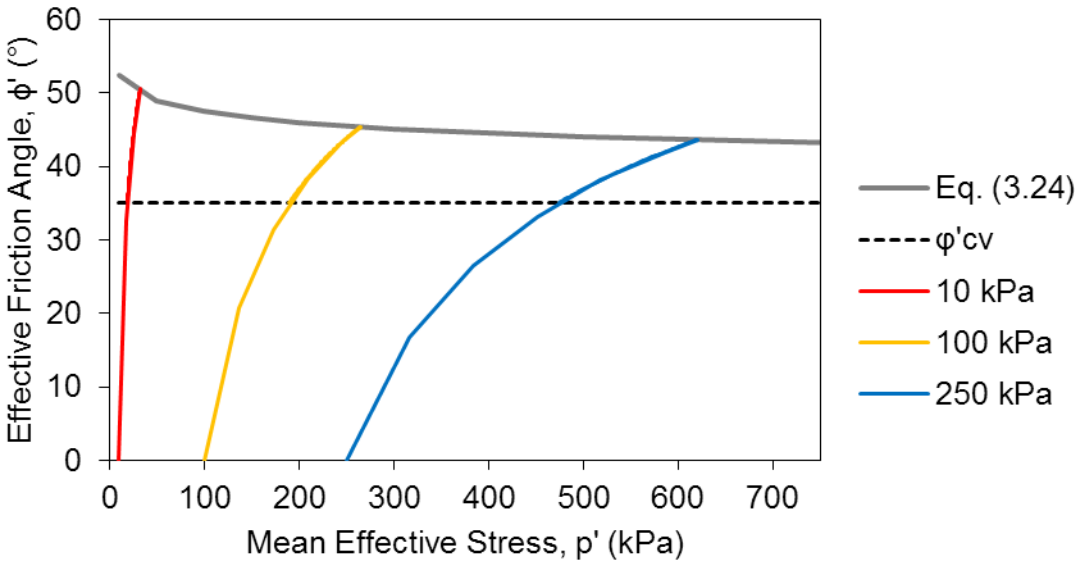

Figure 3.12. Effective friction angle vs. mean effective stress response

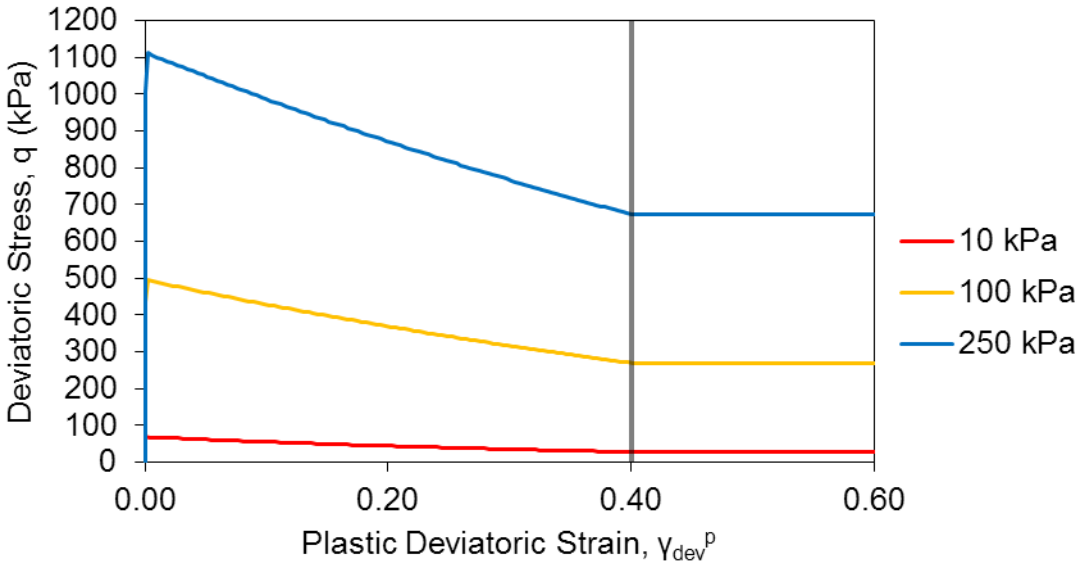

Figure 3.13. Deviatoric stress vs. deviatoric strain response

3.2.3 Characterization and Behaviour of Synthetic Olivine

This subsection provides a detailed overview of the general characteristics and mechanical behaviour of the synthetic olivine material used in the large scale pipe/soil interaction physical tests that were conducted at the Queen's University GeoEngineering Center (see Section 5.1 below).

As discussed by Lapos and Moore (2002) health concerns have meant discontinued use of silica-based materials in the GeoEngineering Center at Queen's University. The replacement material was Olimag synthetic olivine sand, an angular material typically used for sand-blasting. Owing to its chemical and mineral composition, synthetic olivine is a non-toxic material with less than 1% free silica (Olimag Inc., 2016).

A certain level of image contrast variation (image texture) is required to accurately determine soil displacements using PIV analysis. Synthetic olivine material has been shown to have beneficial image texture properties for PIV analysis (Dutton, 2012). In a comparison study of PIV results capturing the compression behaviour of loose sands under a shallow foundation, Dutton (2012) showed that uniformly colored quartz sand was prone to erroneous results, while the colorful synthetic olivine was not.

As discussed in Section 2.4, the results of triaxial tests do not transfer directly to plane strain conditions; friction angles are generally higher and the mobilization of peak and residual friction angles occurs over smaller levels of strain due to greater susceptibility for strain localization and confinement in the intermediate principal stress direction. Without plane strain test data to enable direct determination of the parameters

for plane strain analysis, the parameters were developed based on the collective information available for synthetic olivine sand used in the physical testing program.

3.2.3.1 Physical Characteristics

The specific gravity of synthetic olivine, G_s = 3.1, was determined as part of the present study; Lapos and Moore (2002) stated G_s = 3.2. The high specific gravity is particularly suited for sand blasting as the relatively heavy granular particles provide high energy particle impact and abrasiveness. Based on recent sieve analysis conducted by Burnett (2015), the sand can be classified as poorly graded with a coefficient of uniformity C_u = 1.98 and coefficient of curvature C_c = 1.10, and a mean grain size, $d_{50} \approx$ 0.74 mm (Figure 3.14).

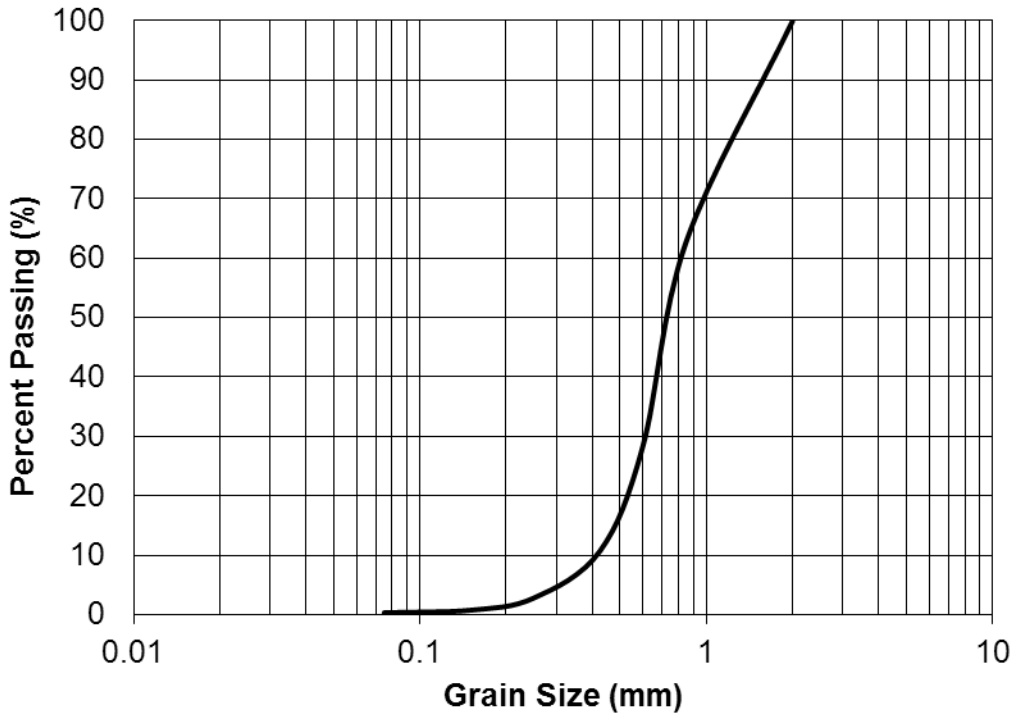

Figure 3.14. Synthetic olivine gradation (Burnett, 2015)

3.2.3.2 Material Strength and Volumetric Response

Previous studies to characterize the behaviour of synthetic olivine were conducted by Lapos and Moore (2002). Tests were conducted on loose and dense samples in triaxial compression and direct shear. Analysis of the triaxial test data shows an increase in the friction angle with reducing confining pressure, reaching about 55° at 20 kPa.

Almahakeri (2013) studied the stability of buried steel and glass fibre reinforced polymer (GFRP) pipes under lateral ground movement by conducting large-scale physical tests in synthetic olivine. Triaxial compression tests were conducted at low confining pressures of 18.8, 33 and 44 kPa to assess the Mohr-Coulomb soil parameters. The peak and residual friction angles, and the dilation angle were provided as 53°, 45° and 16° based on extrapolation of the test data to the extreme low initial confining stress range (0.8 kPa to 3 kPa) expected during the physical tests. Following Bolton's (1986) flow rule for plane strain conditions, this would result in a peak plane strain friction angle of $\phi'_p{}^{ps}$ = 45 + 0.8(16) = 58°.

At a relative density D_r = 86% (γ_d = 15.7 kN/m^3) El-Amam et al. (2004a,b) found the peak direct shear friction angle, $\phi'_p{}^{ds}$, was approximately 51° on average (maximum 52.5°) at low normal pressures (6 to 20 kPa); the residual friction angle was found to be 46° and the peak dilation angle was 15°. The peak plane strain friction angle was calibrated using numerical simulations of the direct shear tests using plane strain elements and was found to be $\phi'_p{}^{ps}$ = 58°. Applying Bolton's (1986) flow rule for plane strain conditions gives $\phi'_p{}^{ps}$ = 46 + 0.8(15) = 58°, which is in accordance with the numerical findings. These properties were used in several subsequent studies (e.g. Bathurst et al.,

2007a,b; Zarnani & Bathurst, 2008,2009). The plane strain parameters determined by El-Amam et al. (2004a,b) are in close agreement with Almahakeri (2013).

Direct shear tests conducted by the author confirm the high values of peak friction angle at low normal pressures 16 and 32 kPa. However, further testing is recommended to address the differences in the friction angle estimates in the recent literature, as discussed. The new plane strain testing equipment at Memorial University can be utilized as a key component in this future work.

3.2.3.3 Initial Elastic Response

Lapos and Moore (2002) provided Janbu parameters for the initial elastic modulus (in kPa) with *K* and *n* values of 190 and 0.98, and 340 and 0.81 for loose and dense conditions, respectively. Almahakeri (2013) estimated parameters K = 326 and n = 0.86 for the dense condition. The relatively high exponent (*n*), which was found close to unity in comparison with 0.5 for most sands, indicates the elastic response is heavily pressure dependent (Lapos and Moore, 2002).

3.2.3.4 Constitutive Model

Based on the triaxial test results provided by Lapos and Moore (2002), a relationship between ϕ'^{tx}_{p} and p' was determined in the present study and is expressed by the following Equation (3.25):

$$\phi'^{tx}_{p} = -12.73 \log p' + 78.8 \qquad (3.25)$$

This type of relationship is a convenient means of expressing the friction angle dependency on the mean effective stress at a particular density level; Han et al. (2014) provided equations of the same form for five different sands.

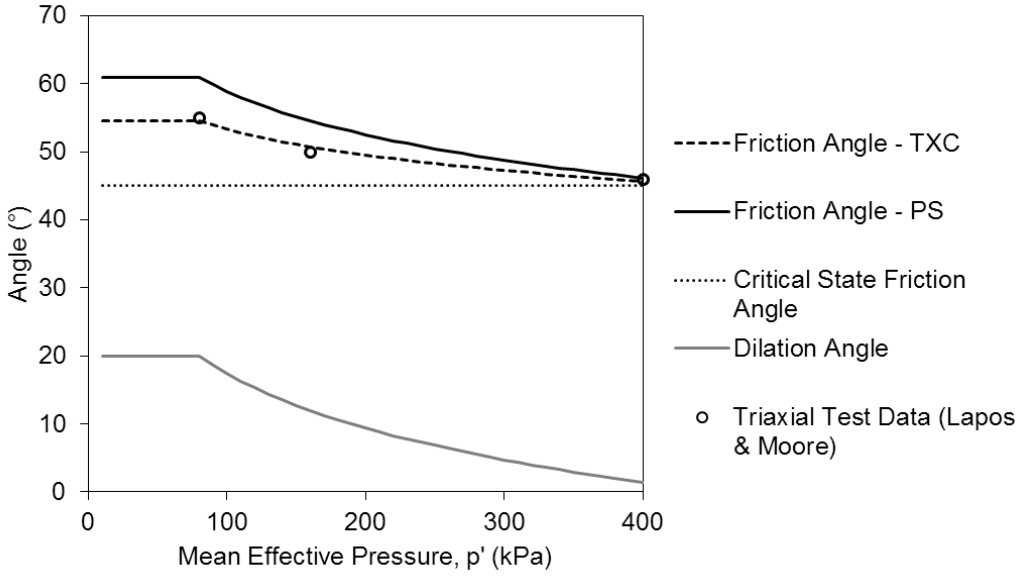

Figure 3.15. Triaxial and plane strain friction angle and dilation angle variance with mean effective stress

The present study assumed that the critical state friction angle was $\phi'_{cv} = 45°$ consistent with Almahakeri (2013). The dilation angle variation was estimated using Bolton's (1986) flow rule for triaxial compression conditions, where ψ is a function if $\phi'_p{}^{tx}$ and ϕ'_{cv}. The $\phi'_p{}^{tx}$ values were then translated to plane strain, $\phi'_p{}^{ps}$, using Bolton's flow rule for plane strain conditions, where $\phi'_p{}^{ps}$ is a function of ψ and ϕ'_{cv}. The friction and dilation angle variation with mean effective stress is plotted above in Figure 3.15. The dilation angle was limited to a maximum of 20° based on Rowe's (1962)

recommended range of the dilatancy factor (D) combined with Equation (2.21), observed test data presented in Section 2.4.1.2, and data summarized by Andersen and Schjetne (2013).

The nonlinear hardening and softening model described in Section 2.4.4.2 was used to approximate the mobilization of effective friction and dilation angles with respect to deviatoric strain. Considering the interaction effects of the pressure and strain level, a three-dimensional plot of the mobilized friction and dilation angles is presented in Figure 3.16.

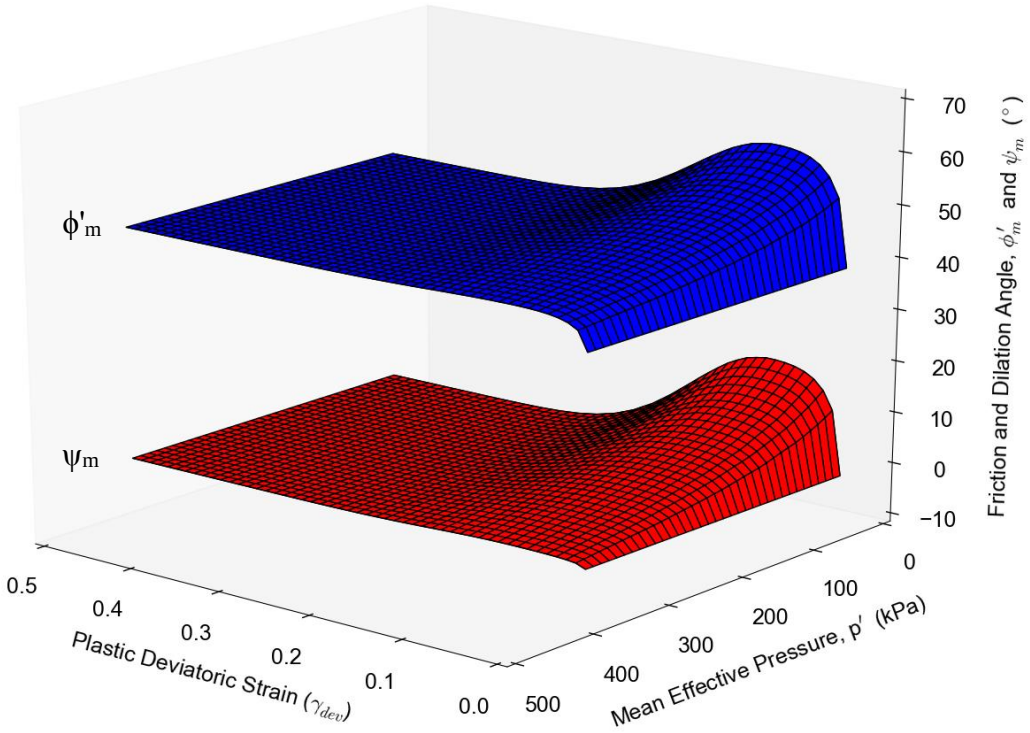

Figure 3.16. Mobilized Friction and Dilation Angles

Finite element simulations of triaxial tests were conducted to assess the constitutive model performance against the test data in terms of predicting the peak strength over a range of confining pressure. As shown in the below Figure 3.17, the elastic regime, strain softening and peak deviatoric stress is matched very closely with the triaxial test data at confining pressures 20 kPa and 50 kPa.

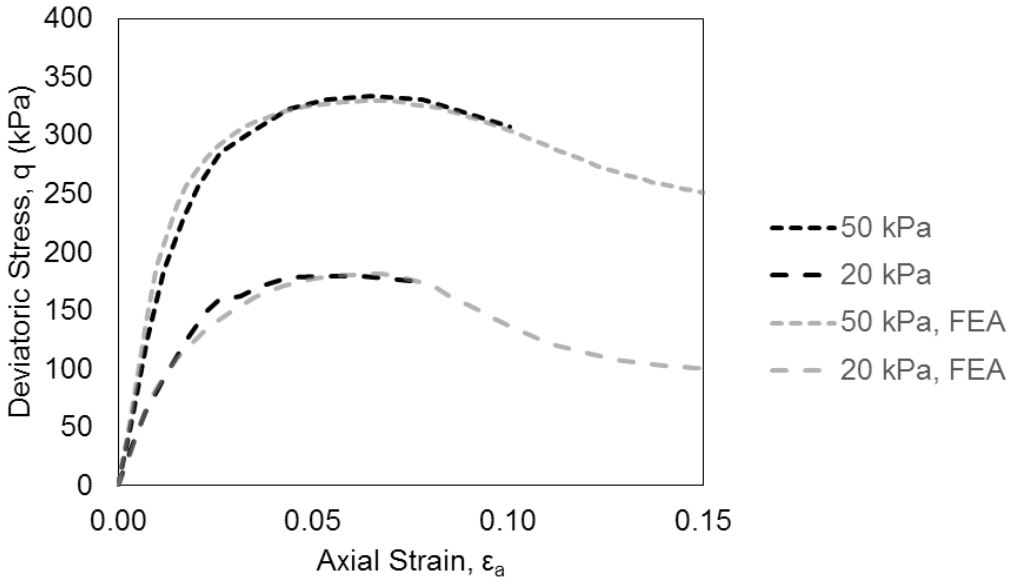

Figure 3.17. Deviatoric stress response for varying σ'3; test data vs. FEA prediction (data from Lapos and Moore, 2002)

3.3 Summary

This chapter covered in detail many important aspects relating to the behaviour of granular material. A detailed review of relationships linking the shear stress and volume change (flow rules) was provided, and the influence of mean effective stress and density on the peak friction and dilation angles was addressed. The available flow rules were summarized for plane strain, triaxial and direct shear test conditions. A significant amount of publicly available plane strain and triaxial test data was compiled in order to analyze the influence of confining stress, relative density and particle shape on the peak soil shear strength and volumetric response. For the plane strain dataset, the influence of particle angularity was shown to affect the interparticle friction and in turn the peak friction angle. The triaxial test dataset was used to assess Bolton's (1986) dilatancy index in terms of predicting the peak friction angle; it was shown that the dilatancy index is better suited for dense to very dense samples. However, it was shown that in general, the state parameter is a better predictor for $\phi'_p{}^{tx} - \phi'_{cv}$ and ψ_p.

As discussed above, the need for plane strain parameters often arises often in geotechnical practice; however, direct shear and triaxial test equipment is more commonly utilized to characterize the soil behaviour. On this basis, a detailed overview is provided that can aid the reader in translating to plane strain parameters using either triaxial or direct shear test results. An equation for estimating plane strain parameters from triaxial compression data was developed using Rowe's (1962) stress-dilatancy theory, and performed well, though for a limited dataset.

A detailed discussion surrounding the critical state friction angle, ϕ'_{cv} was provided. When applying the flow rule and plane strain translation equations described above, the ϕ'_{cv} value influences the peak and post-peak soil stress-strain behaviour. Instead of relying on a singular prediction of ϕ'_{cv}, the approach based on Rowe's (1962) stress-dilatancy theory updated to account for $\phi_f > \phi'_{cv}$ affected by interparticle locking is suggested.

Having predicted the critical state friction angle, and the peak friction and dilation angles, it is necessary to define how the values are mobilized with increasing strain; the methods for doing so are summarized. Finally, a subroutine (VUSDFLD) developed for varying friction and dilation angles with increasing plastic deviatoric strain for 3D applications was tested against available triaxial test data, over a range of confining pressure, to verify its operation. Accounting for nonlinear hardening and softening was shown to capture realistic shear and volumetric soil response, whereas the built-in elastic-perfectly plastic fails to capture post-peak friction softening and suppression of volumetric expansion.

4 Development of Finite Element Models

Finite element models were developed using different analysis solvers (e.g. ABAQUS/Standard and Explicit) and formulations (e.g. Winkler beam-spring, CEL, ALE) to study free-field ice gouging, decoupled and coupled ice/soil/pipe interaction, and orthogonal and oblique pipe/soil interaction; as summarized in the following Table 4.1. The respective finite element models are described in this chapter. In particular, the element types, initial conditions (i.e. predefined fields), boundary conditions (e.g. displacement, velocity), treatment of interface contact, and analysis steps are outlined. While there is overlap in some aspects of the modelling procedures (e.g. geostatic stresses are applied using the same methodology for each application), each application is addressed separately to provide clarity for the reader.

As the finite element mesh sensitivity results form part of the analysis outcomes, the mesh sensitivity studies are contained within the model application sections in Chapter 6.

Table 4.1. Summary of finite element model solver and formulation applications

Application	Solver	Formulation
Free-field ice gouging	ABAQUS/Explicit	CEL
Orthogonal pipe/soil interaction	ABAQUS/Explicit	CEL
Oblique pipe/soil interaction	ABAQUS/Explicit	ALE
Decoupled ice/soil/pipe interaction	ABAQUS/Standard	Winkler Beam-Spring
Coupled ice/soil/pipe interaction	ABAQUS/Explicit	CEL

The CEL formulation provides a robust modelling framework for large deformation, highly non-linear geotechnical problems (Qui et al., 2011; Pike et al., 2013; Tho et al., 2013; Fallah et al., 2015). The CEL method is widely used in this thesis, and is briefly introduced in the following Section 4.1.

4.1 Coupled Eulerian Lagrangian Finite Element Modelling

4.1.1 Introduction

The traditional Lagrangian finite element method is ill-suited for geomechanics problems involving severe soil deformations. The Lagrangian description of material motion is such that the movement of the continuum is a function of the material coordinates and time, and the nodes of the mesh move with the material. For applications involving extreme deformation this leads to mesh distortion, degradation of solution performance and convergence issues.

In the Eulerian framework, continuum movement is a function of the spatial coordinate and time whereby the material can move freely through the fixed Eulerian mesh. In ABAQUS/Explicit, the material is tracked through the Eulerian mesh by computing its Eulerian volume fraction (EVF) within each element. This is known as the volume-of-fluid method, as described by Benson and Okazawa (2004a). Eulerian elements may be full of material, or may be partially or completely void of material. If a material completely fills an element, EVF = 1, or if the element is completely void of material, EVF = 0 (Abaqus, 2016). The Eulerian element (EC3D8R) is an extension of the conventional Lagrangian based eight-node brick element with reduced integration.

4.1.2 Initializing Eulerian Material

The Eulerian material assignment is applied as an initial condition based on assigning the volume fraction to the geometric region within the Eulerian part that initially contains Eulerian material. Depending on the geometry, this can be accomplished using one of two field types: 1. the uniform field can be used for simple geometry or 2. the discrete field can be used for complex geometry. The discrete field is created using the volume fraction tool. A reference part is created that provides a geometric representation of the initial Eulerian domain. Within the material assignment dialogue, the Eulerian instance is first selected, followed by the reference part. A volume fraction field is then generated by the software to define the initial volume of material.

The Eulerian material assignment is further described by application in the following Sections 4.2 and 4.2.5.

4.1.3 Eulerian-Lagrangian Contact

The Eulerian-Lagrangian contact formulation is based on an enhanced immersed boundary method. The Lagrangian body occupies void space within the Eulerian mesh and the Eulerian-Lagrangian contact interface is tracked automatically. This removes the need for a mesh design that conforms to the outer surface of the Lagrangian part. Abaqus (2016) suggests that a simple regular grid of Eulerian elements often yields the best accuracy.

The Coupled Eulerian Lagrangian method available in ABAQUS/Explicit permits the interaction of Lagrangian bodies (rigid or deformable) with Eulerian materials. The Eulerian material boundary must be computed during each time increment and generally

does not correspond to an element boundary. Instead, the interface reconstruction algorithm (i.e. volume-of-fluid method) approximates the material boundaries within an element as simple planar facets. Since the approximated material surface may be discontinuous between adjacent elements, fine mesh resolution is required to delineate complex geometries. Abaqus (2016) recommends a simple rectangular grid of elements that does not conform to the shape of the Eulerian materials. The material shape can be represented within the Eulerian mesh using a combination of fully and partially filled elements surrounded by void regions.

Eulerian-Lagrangian contact constraints are enforced using a penalty method, where the default penalty stiffness parameter is automatically maximized subject to stability limits.

4.1.4 Solution Advection

The CEL method uses an explicit time integration scheme. As stated in the Abaqus (2016) user's manual, the Eulerian time incrementation algorithm uses a traditional Lagrangian phase, followed by an Eulerian phase, known as "Lagrange-plus-remap", based on the work of Benson (1997). During the Lagrangian phase the elements deform with the material. In the Eulerian phase, the deformation is suspended, elements with significant deformation are automatically remeshed, and the material flow between neighboring elements is computed; this process is illustrated in Figure 4.1. The state variables are transferred between elements by an advection algorithm.

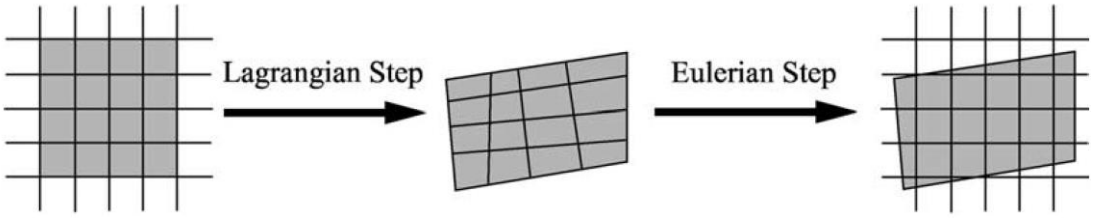

Figure 4.1. Operator split for Eulerian formulation (Benson and Okazawa, 2004b)

This briefly covers some aspects of the CEL method. A full description of the details is beyond the scope of this thesis; the reader is referred to the Abaqus (2016) theory and user manuals for further details.

4.2 Free-field Ice Gouging

This section describes the development of a CEL FE model for free-field ice gouging. As discussed in the literature (e.g. Abdalla et al., 2009; Phillips et al., 2010), early attempts to model the ice gouge phenomenon using Lagrangian-based continuum models were unsuccessful due to mesh distortion and convergence issues. The CEL method has emerged as the state-of-the-art modelling framework as it can accommodate the severe soil deformations that occur during the gouging process, can accommodate contact with both rigid and deformable lagrangian bodies, and provides a more robust and less restricted solution than the ALE method.

4.2.1 Element Selection

The model ice keel is meshed using Lagrangian, 8-node, reduced integration, continuum brick elements (C3D8R). However, the keel is treated as a rigid body using a

rigid body tie constraint tied to a reference point. The soil is modelled using three-dimensional, 8-node Eulerian elements (EC3D8R). Eulerian elements are useful for simulations involving material that undergoes extreme deformation, up to and including fluid flow. The underlying mechanical response formulation of the EC3D8R element is based on the C3D8R element with extensions to allow multiple materials and to support the Eulerian transport phase (Abaqus, 2016). The mesh design and sensitivity study is presented in Section 6.1.1.

4.2.2 Initial Conditions

The following initial conditions are specified as predefined fields and are established before the analysis begins.

4.2.2.1 Geostatic

The procedure used to establish the geostatic stress field was based on Abaqus' (2016) recommended approach for explicit analysis (see benchmark "Pressure on infinite geostatic medium"). The initial geostatic stress field was defined using initial conditions (i.e. *INITIAL CONDITIONS, TYPE=STRESS, GEOSTATIC). The dedicated geostatic analysis step available in ABAQUS/Standard, is not available in ABAQUS/Explicit. Instead, the gravitational (self-weight) load was applied in the first analysis step over a short duration of 5 milliseconds. This approach was effective in maintaining the state of stress defined in the initial conditions, and is an efficient solution in terms of analysis time.

4.2.2.2 Material Assignment

The region of the Eulerian mesh initially containing the soil material was defined using the initial condition, type "material assignment". Since the geometry of the soil test box is simply rectangular, the uniform field option was used to define the region initially containing soil (i.e. EVF_VOID = 0); by default the void space was also assigned (EVF_VOID = 1).

4.2.2.3 Temperature

Initial temperature conditions are also applied to the Eulerian mesh. The temperature is a dummy parameter set equal to the soil depth that is used to define depth dependent material parameters (e.g. yield stress, elastic modulus), as described above in Section 3.1.1.

4.2.3 Boundary Conditions

The keel displacement boundary conditions are applied at the reference point that controls the global keel kinematics. In steps 2 and 3 noted below, all degrees of freedom are constrained except for the prescribed motion. The keel is moved at a constant rate of 1.0 m/s.

As shown in Figure 4.2, the soil test box boundary conditions were defined using velocity-based constraints at each external face. The velocity normal to each face was set to zero to simulate the sides of the centrifuge test box. The model took advantage of half-symmetry about the centerline of the gouge. The void region above the initial soil surface

is established with sufficient height to allow the flow of soil into the void space without extending beyond the void ceiling. The model dimensions are indicated in Section 6.1.1.

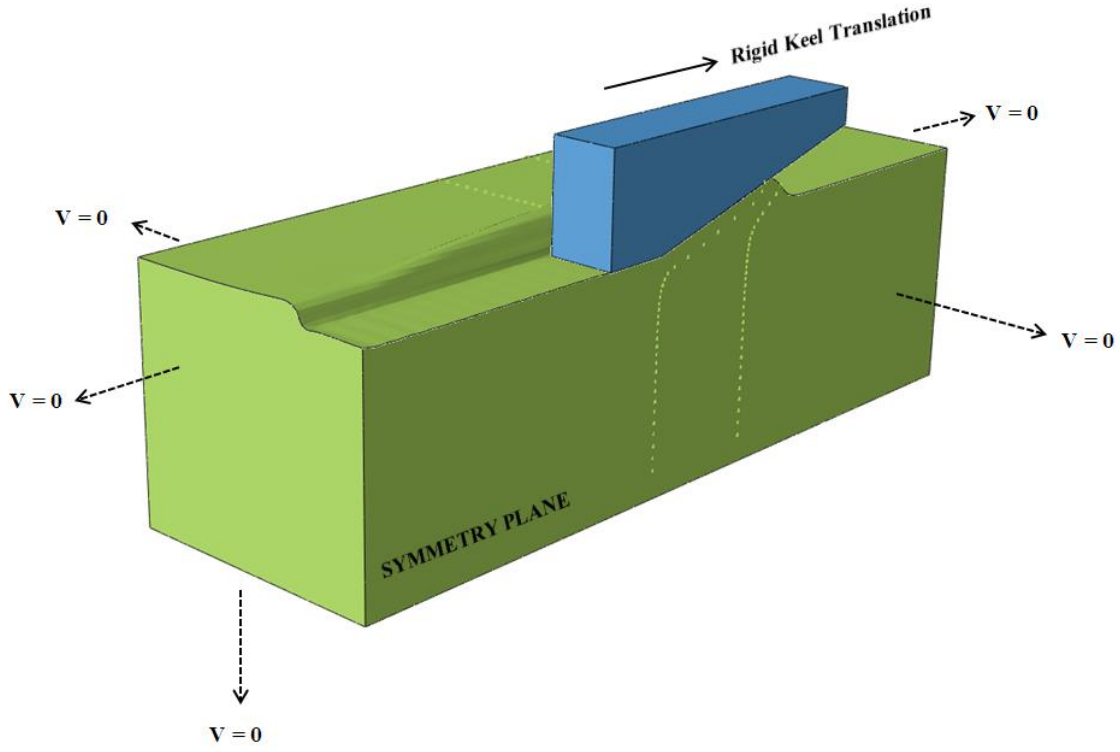

Figure 4.2. Free-field ice gouge model boundary conditions

4.2.4 Keel/Soil Contact

Contact between the model ice keel and the Eulerian soil material is established with the general contact option. Since there are only two interacting surfaces, a global interaction property is defined, and the software automatically finds the interacting contacting surfaces. If there are multiple bodies interacting with the Eulerian material,

and more than one interaction property must be defined, this can be achieved using individual property assignments.

The default normal contact behaviour was utilized that specifies hard contact, allowing separation after contact. The tangential behaviour was enforced using a penalty-based formulation that required specification of the Coulomb friction coefficient. There is also an optional shear stress limit that controls the maximum allowable interface shear stress.

Applying an interface shear stress limit (τ_{max}), as a fraction of the undrained shear strength (s_u), is typical in total stress analysis when undrained interface behaviour is assumed (e.g. Peek and Nobahar, 2012; Hikooei, 2013). When modelling clay, the interface friction is generaly assumed to be adhesive with no relative sliding before reaching the interface shear stress limit; i.e. rigid-perfectly plastic interface behaviour.

4.2.5 Analysis Steps

In the present study, the analysis for simulating free-field ice gouge centrifuge tests is conducted in three steps:

1. the geostatic soil stress state is established;
2. the model ice keel is depressed into the soil such that the base of the keel reaches the gouge depth level based on the prescribed (or achieved) steady-state gouge depth in the centrifuge test;
3. the model ice keel is translated in the gouge direction at a constant velocity.

4.3 Orthogonal Pipe/Soil Interaction

For pipe/soil interaction, use of the ALE method has shown that the numerical solution degrades after about 0.4D to 0.6D pipe movement due to a combination of mesh compression in front of the pipe and mesh rotation behind the pipe (Pike and Kenny, 2012c). The CEL method does not suffer this drawback as the soil is allowed to flow through the fixed Eulerian mesh. Pike et al. (2013) showed good correspondence between ALE and CEL simulations for pipe/soil interaction up to about 0.4D for built-in and modified Mohr-Coulomb models. Pike et al. (2014) used the ALE method to simulate physical pipe/soil interaction test data by Trautmann (1983) and showed excellent correspondence between the numerical and physical force-displacement response for a range of burial depths.

Three-dimensional continuum finite element modelling procedures were developed to model lateral pipe/soil interaction in cohesive and cohesionless soils using ABAQUS/Explicit. Models were developed using the Coupled Eulerian Lagrangian (CEL) technique. The use of the CEL technique that allows simulation of relatively large pipe displacements is a contribution to the study of pipe/soil interaction.

4.3.1 Element Selection

The pipeline was modelled using the Lagrangian based solid, 8-node linear brick element (C3D8R). The pipeline elements were made rigid using a rigid body tie to a reference point. The pipeline lateral displacement was applied at the reference point, controlling the rigid body pipeline kinematics.

4.3.2 Initial Conditions

The following initial conditions are predefined fields that are established before the analysis begins.

4.3.2.1 Geostatic

Refer to Section 4.2.2.1.

4.3.2.2 Material Assignment

The region of the Eulerian mesh initially containing the soil material was defined using the initial condition, type “material assignment”. Since the geometry of the soil test box is not uniform (i.e. has a hole in it containing the pipe), the discrete field option was used to define the region initially containing soil (i.e. EVF_VOID = 0); by default the void space was also assigned (EVF_VOID = 1). The discrete field is created using the “Volume Fraction Tool” that utilizes a reference part representing the shape of the initial soil. The reference part is instanced in the assembly and aligned geometrically to overlap the Eulerian part. Using the “Volume Fraction Tool”, the Eulerian part is first selected, followed by the reference part. The software then computes the element volume fractions; the elements defining the space filled by the pipeline may be only partially full of material. The components of this process are shown below in Figure 4.3; the Eulerian instance and the reference part are shown in exploded view, when in reality the coordinates would overlap.

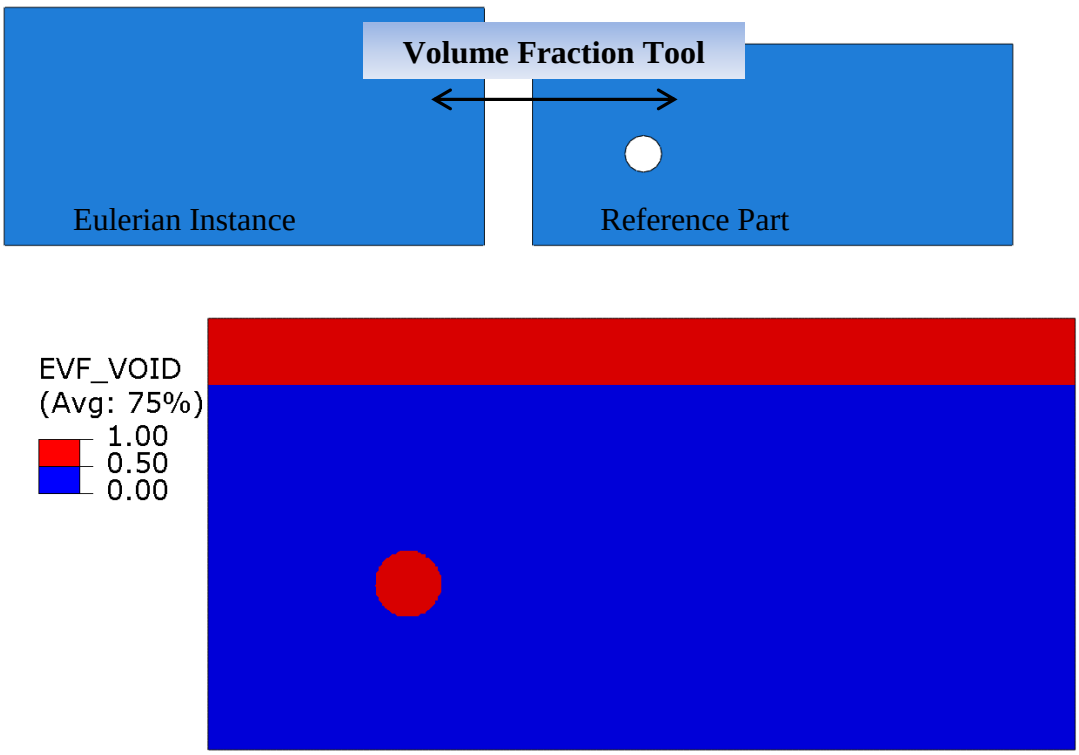

Figure 4.3. Illustration of the volume fraction tool used in the CEL method

4.3.2.3 Temperature

The dummy temperature field is applied as described above in Section 4.2.2.3, and is used for specification of depth dependent elastic properties; e.g. in Section 6.4.

4.3.3 Boundary Conditions

The model boundary conditions were defined to represent two-dimensional plane strain conditions that were consistent with the physical model tests. It is important to note that plane strain elements were not used, rather 3D elements with plane-strain boundary

conditions. The development of 3D tools allows for extension of the plane-strain models to more complex interaction scenarios having built confidence in the model subset.

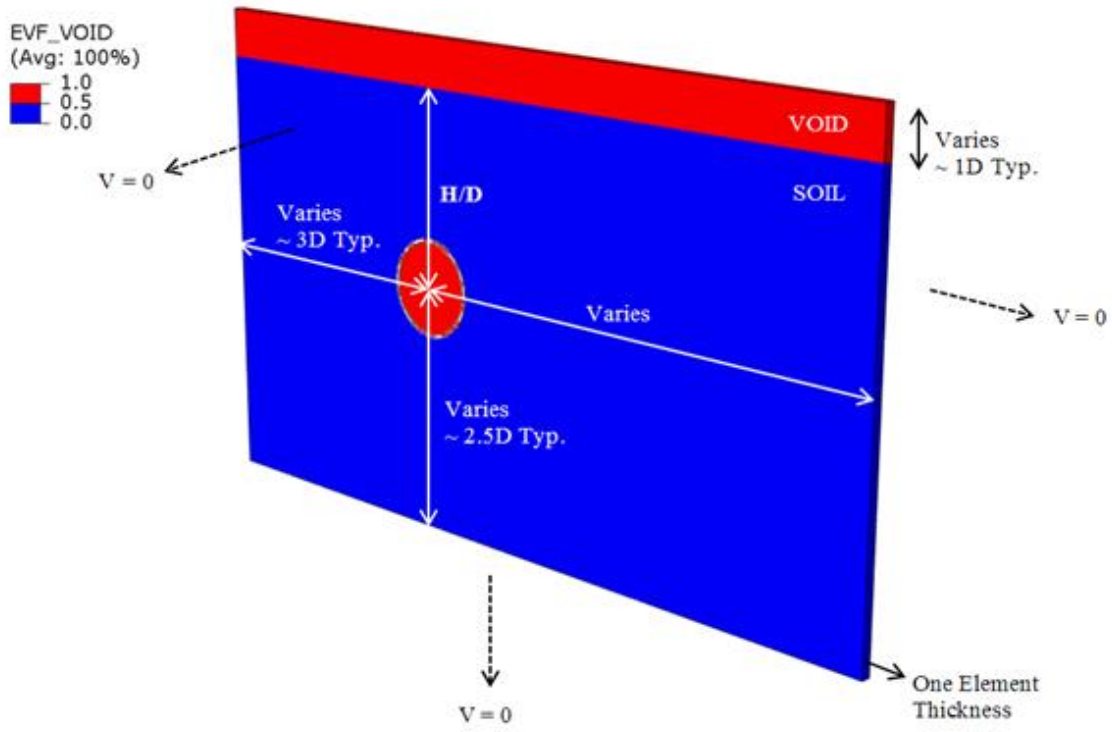

Figure 4.4. Orthogonal pipe/soil interaction model dimensions and boundary conditions

The model boundaries were extended in lateral and vertical directions to avoid boundary effects. The distance from the pipe to the boundaries varies based on the application and is noted for specific applications in Chapter 6. The velocity normal to each face of the model was set to zero. For two-dimensional (2D) applications (e.g. plane strain), Abaqus (2016) recommends using a model thickness of one element. A typical model setup is illustrated in Figure 4.4.

4.3.4 Pipe/Soil Contact

The pipeline/soil interface contact was modelled using the general contact option available in ABAQUS/Explicit. The pipe/soil contact interface was defined by the Coulomb interface friction model with penalty method used to account for the effects of relative pipe penetration and over-closure. Estimating the friction coefficient is performed on the basis of the pipe coating, and is discussed further in the applications described in Section 6.4.1.

For undrained analysis of pipe/soil interaction with cohesive soils, surface based contact was enforced using the Coulomb friction model, with a friction coefficient of 1.0 and maximum interface shear stress, τ_{max}, equal to a fraction (typ. $\tau_{max} = 0.5s_u$) of the undrained shear strength.

4.3.5 Analysis Steps

The lateral pipe/soil interaction analysis is conducted in two steps:

1. gravity is applied to the whole model to establish the initial stress state based on the soil unit weight, while the pipe is fixed in position;
2. the pipeline is moved laterally as a rigid body free to move in the vertical direction with rotations fixed. Gravity is applied to the whole model, with the pipe assumed to be in the empty condition (consistent with the physical tests).

4.4 Oblique Pipe/Soil Interaction

To model oblique lateral-axial pipe/soil interaction, a 3D continuum ALE FE model was developed using ABAQUS/Explicit. In Abaqus versions prior to 6.13, issues

with the frictional interface model in ABAQUS/Explicit CEL were identified affecting activation of the shear stress limit (Pike and Kenny, 2012b). Due to this software limitation, the Arbitrary Lagrangian Eulerian (ALE) method was utilized that was shown to properly capture the effects of the shear stress limit.

The suite of analyses conducted for lateral-axial pipe movement were conducted when the contact issue existed, and were not repeated using the CEL method.

4.4.1 Element Selection

The soil was modelled using eight-node reduced-integration brick elements, C3D8R. The pipeline was treated as a rigid body (tied to a reference point) and was modelled using shell (S4R) elements.

4.4.2 Initial Conditions

4.4.2.1 Geostatic

Refer to Section 4.2.2.1.

4.4.3 Boundary Conditions

The model dimensions and typical mesh resolution are shown in Figure 2.4. Zero velocity boundary conditions (similar to above Figure 4.2) are imposed perpendicular to each face of the model soil box, except for the top face. The pipeline is moved at varying translation angles (θ) from purely axial (0°) to purely lateral (90°) in order to capture the effect of the oblique angle (Figure 4.6) on the lateral (i.e. horizontal) and axial bearing capacity factors. The pipeline is moved at a constant velocity equal to 0.1 m/s.

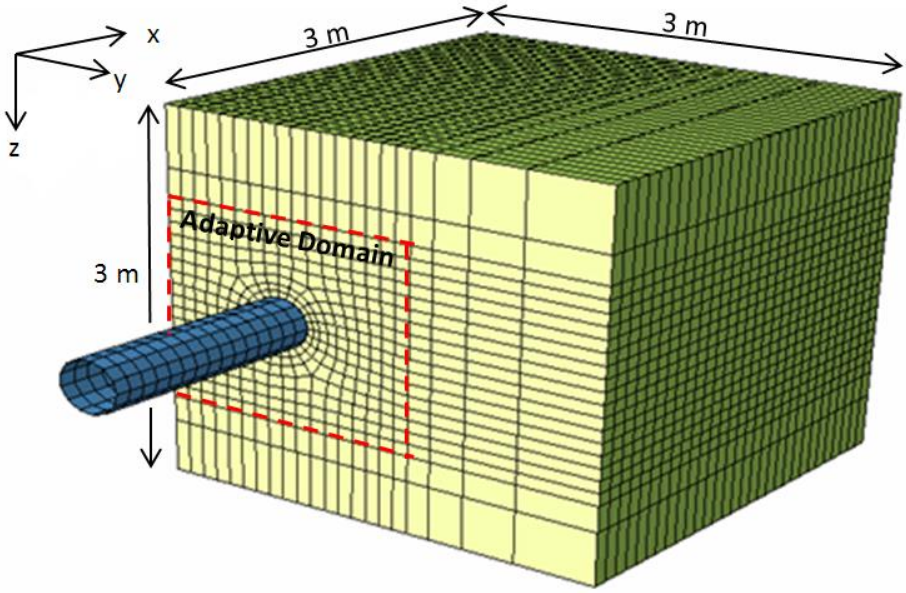

Figure 4.5. ALE pipe/soil interaction model

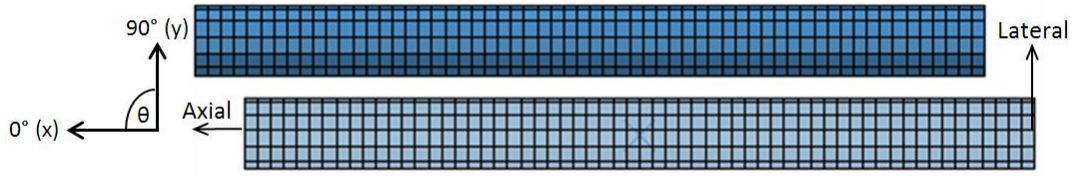

Figure 4.6. Lateral-axial oblique pipeline movement

4.4.4 Pipe/Soil Contact

The contact pair option was used with the pipeline defined as the master surface and the soil as the slave surface. Penalty-based tangential friction was applied with definition of the friction coefficient and shear stress limit, τ_{max}.

4.5 Decoupled Ice/Soil/Pipeline Interaction

As discussed above in Section 2.2, the conventional approach to assess the pipeline mechanical response to subgouge soil deformations involves a decoupled structural model approach whereby the empirical horizontal subgouge soil displacement field is applied to spring nodes attached to pipe (specially formulated beam elements) elements. The performance of the decoupled approach is assessed compared to the fully coupled CEL continuum model described in the following Section 4.6 in application Section 6.3. Typical output of the decoupled structural model longitudinal strain is shown in the following Figure 4.7; note that the wireframe pipe elements have been rendered to show the 3D shape, and only the lateral soil springs are shown for clarity. The model is half-symmetric at the gouge centerline corresponding to the point of maximum axial compressive strain in the below figure.

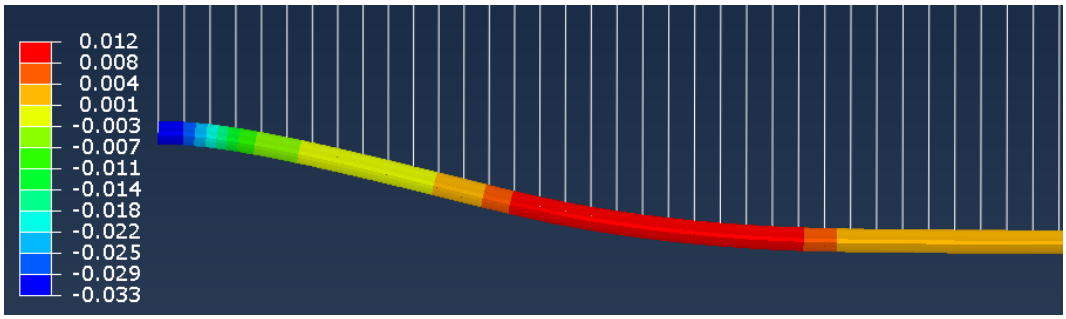

Figure 4.7. Longitudinal pipe logarithmic strain due to subgouge soil displacement

4.5.1 Element Selection

The structural beam/spring model was discretized using PIPE31H and SPRINGA elements within the ABAQUS/Standard modelling framework. The PIPE31H element is a 2-node linear hybrid structural beam element defined by three displacement and three rotational degrees of freedom per node. Additional variables account for the effects of internal pressure and thermal expansion. The SPRINGA element is defined by a force-displacement curve that acts along an axis defined by two nodes; the spring behaviour can be linear or nonlinear. In the analyses conducted in this thesis, the spring curves were defined as piecewise nonlinear, with further details presented in Section 6.3.2. The pipeline was discretized with a constant pipe element length of approximately one pipe diameter, as recommended in available guidelines for buried pipeline design (e.g. PRCI, 2009).

4.5.2 Boundary Conditions

A symmetry boundary condition was specified at the ice gouge centerline that corresponds to the pipe mid-length. The far end of the pipe was pinned. The spring nodes are connected to the pipe nodes, and the far ends of the spring nodes are fixed.

4.5.3 Analysis Steps

The analysis was conducted in three steps with application of:

1) the internal pipe pressure;
2) the differential temperature, and;

3) the subgouge soil deformation field by displacing the spring nodes connected to the pipe.

4.6 Coupled Ice/Soil/Pipeline Interaction

The coupled ice/soil/pipeline interaction model blends aspects of the free-field ice gouge model (Section 4.2) and pipe/soil interaction model (Section 4.3). The pipeline is placed in the Eulerian domain at the appropriate H/D ratio, and the volume fraction tool is used to define the initial soil and void volumes (Section 4.3.2.2). The mesh is refined in the region surrounding the pipeline to ensure contact is resolved at the pipe/soil interface (Figure 4.8) throughout the simulation. The mesh size requirement for buried pipe/soil interaction in cohesive soil is established in Section 6.2.1.1 and is used to develop the coupled interaction model.

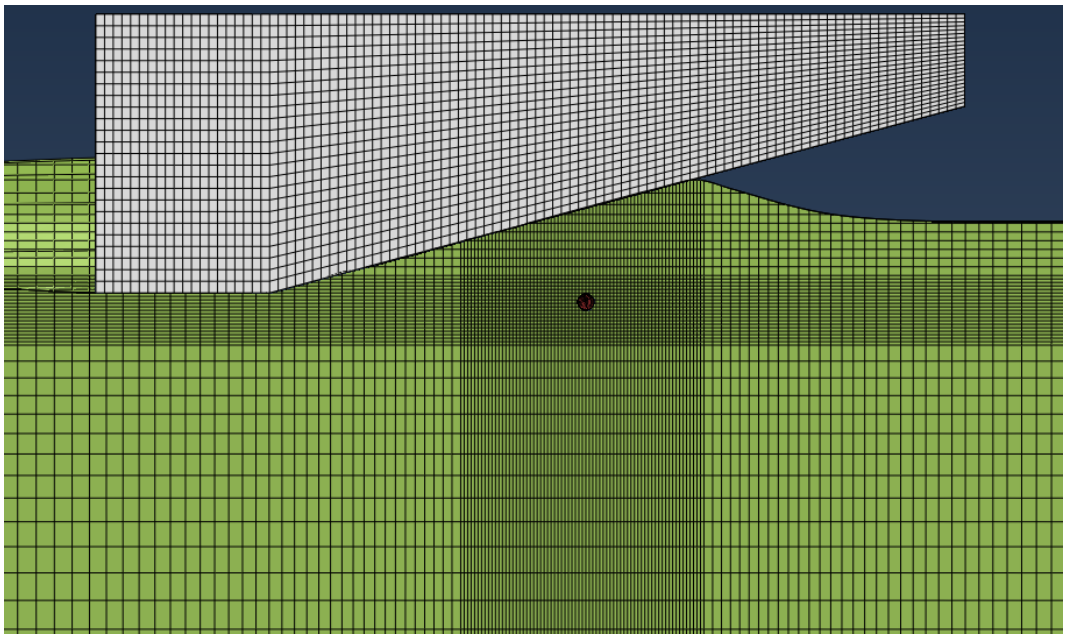

Figure 4.8. Coupled ice/soil/pipeline model mesh design

The extension of the free-field ice gouge and orthogonal pipe/soil interaction models to couple the ice keel/soil and pipe/soil interactions require some unique model features that are covered in the following subsection. In particular, since the size of the Eulerian material domain is limited to reduce analysis run times, while pipeline lengths must be extended to properly account for axial feed-in effects, the pipe/soil interaction must be extended with an adjoining structural beam/spring model that is connected to the continuum model. This is illustrated in the following Figure 4.9 where the soil springs have been removed for clarity.

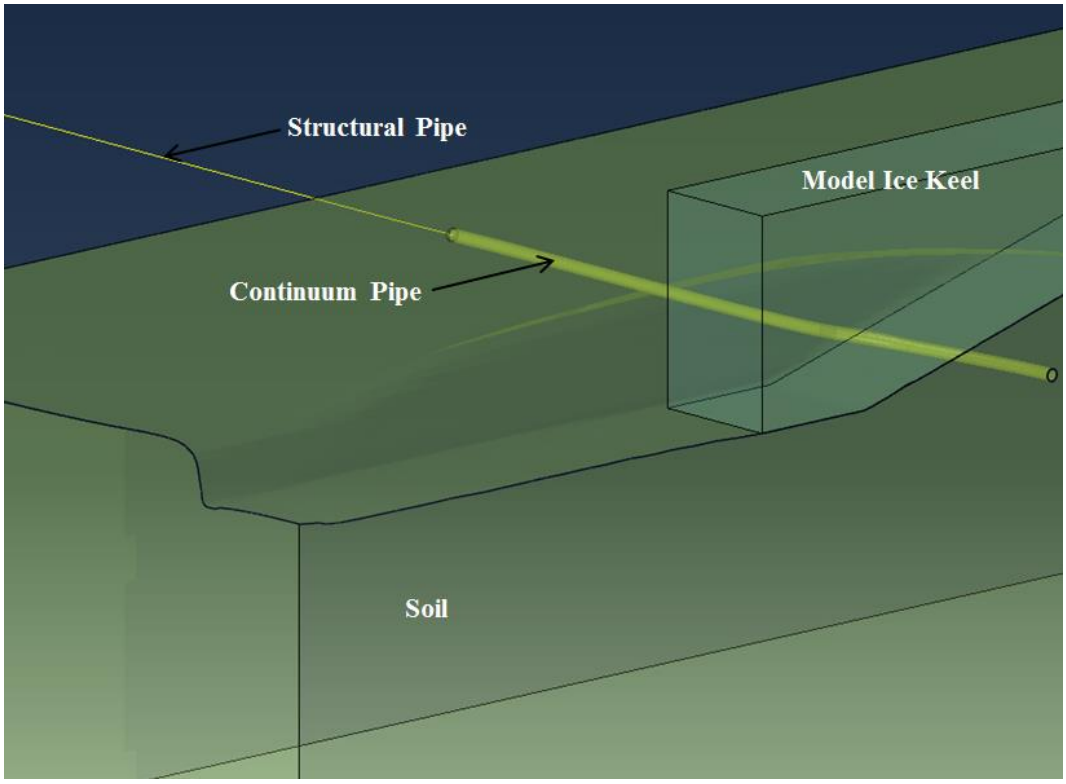

Figure 4.9. Coupled ice/soil/pipeline interaction model

4.6.1 Element Selection

As discussed above in Section 4.2.1, the Eulerian element EC3D8R is used to model the soil material. The continuum pipe is discretized using 4-node, reduced integration shell elements (S4R) based on shell theory with shear deformations, and five integration points across the wall thickness. The pipe structural model comprises PIPE31H elements that are typically discretized with element lengths equal to one pipe diameter and connected to SPRINGA elements (see above Section 4.5.1). The soil spring elements are normal to the pipeline longitudinal axis and define the lateral, axial and vertical soil spring force-displacement relationships, along three mutually perpendicular axes, based on guideline recommendations or tailored FEA, as presented later in Section 6.3.2.3.

4.6.2 Structural Model Extension

The continuum-structural pipe model connection is established using distributing coupling. At the coordinate defining the connection point at the boundary of the Eulerian domain, the structural pipe node is connected to all nodes defining the perimeter of the continuum pipe model. There are some limitations using this method as discussed in the next subsection. However, where the response at the connection point involves mainly longitudinal transfer of stress and displacement, the effect is minimal on the local bending response that is concentrated at the gouge centerline.

4.6.3 Analysis Steps

The analysis is conducted in four steps:

1) the geostatic stress state is established in the soil;
2) the keel is lowered to the prescribed gouge depth while the internal pressure is applied to the shell (S4R) elements and an equivalent temperature change is applied to the structural (PIPE31) elements (this is due to internal software limitations when defining a coupled constraint where the effects of internal pressure are not transferred to the structural elements);
3) the change in temperature is applied to both structural and continuum pipeline models, and;
4) the keel is displaced in the gouge direction.

5 Physical Model Testing of Lateral Pipe/Soil Interaction in Cohesionless Soil

5.1 Large-Scale Lateral Pipe-Soil Interaction Physical Testing Program

As part of the current study, a series of large-scale tests were conducted at the Queen's University GeoEngineering Centre in Kingston, Ontario. The test program was investigating geotechnical loads and soil failure mechanisms during large-scale, lateral pipe/soil interaction tests, which was a collaborative research effort among the partners including the Wood Group, Memorial University of Newfoundland and Queen's University. The principal highly qualified personnel (HQP) involved were M.Sc. (Engineering) candidate Alexander Burnett (Queen's University) and the author, PhD (Engineering) candidate Kenton Pike (Memorial University). The author was involved throughout the test program and was on site, for approximately 6 weeks, as a visiting researcher at Queen's University and was directly involved in the test design, set-up, execution and analysis. The test program objectives were:

- to conduct large-scale physical pipe/soil interaction tests in dry sand across a range of pipeline diameter, burial depth ratio and soil density;
- to record the soil failure mechanism processes by capturing high quality digital images of the lateral pipe/soil interaction test using glass viewing panes; and
- to use digital image correlation techniques (DIC) to post-process the images generating displacement and strain field plots at incremental stages of pipe

displacement and subsequently examine the influence of each of the test parameters, and

- to improve the current understanding of soil deformation through continuous monitoring methods (i.e. DIC) for large lateral pipe displacement..

5.1.1 Candidate Contribution to Testing Program

The collaborating HQP Burnett provides a description of the test program and contributions in his M.Sc. thesis (Burnett, 2015). The major contributions provided by the author (Kenton Pike) in this study, accomplished directly on-site as visiting researcher and remotely, can be summarized as:

- to conduct literature review and preliminary FEA for advising on the test pit configuration, effects of boundary conditions and interface contact mechanisms, and expected pipe displacement response across the range of test parameter examined;
- to assist in the design and fabrication of test apparatus and instrumentation used for the pipe (i.e. end-caps, load cell placement) and test bed (i.e. density pans, placement of sensors);
- to assist in preparation of the test bed and quality control with respect to expected conditions and repeatability (e.g. specific gravity, monitor and control of soil placement density), and test pit excavation; and
- to compare the physical test results with existing published test data and relevant engineering guidelines on pipe/soil interaction;

- to perform a series of laboratory tests (e.g. direct shear, triaxial compression) on the test sand, over a range of confining pressure and density, to characterize the soil strength and volumetric response behaviour ;
- to calibrate constitutive models against the laboratory test data to determine the soil model parameters; and
- to develop large deformation finite element analysis tools to simulate the physical tests with a reasonable level of accuracy in terms of force-displacement response and soil failure mechanisms, i.e. strain localization.

5.1.2 Testing Program and Results Summary

Two test pipes were used with external diameters (D) of 254 mm and 609.6 mm having diameter to thickness ratios (D/t) of 40 and 64, respectively. The tests were conducted under loose ($\gamma_d \approx 14.7$ kN/m^3) and dense ($\gamma_d \approx 15.6$ kN/m^3) conditions at burial depth ratios (H/D) of 1.0, 3.0, and 7.0. Density control was achieved in each test with standard deviations from 0.8% to 1.6% for relatively loose conditions, and 2.0% to 2.6% for dense conditions. Based on density control attained by Trautmann (1983) of about 1.0% for CU filter sand, observations for the present study are consistent. A summary of the tests conducted is provided in Table 5.1.

The test set-up is illustrated in Figure 5.1, and details pertaining to the displacement and load instrumentation hardware, and image capturing hardware and software are provided by Burnett (2015). The test configuration simulates plane strain boundary conditions with the pipe ends (fitted with Teflon end-caps to minimize frictional resistance) and surrounding sand visible through the transparent sidewalls that

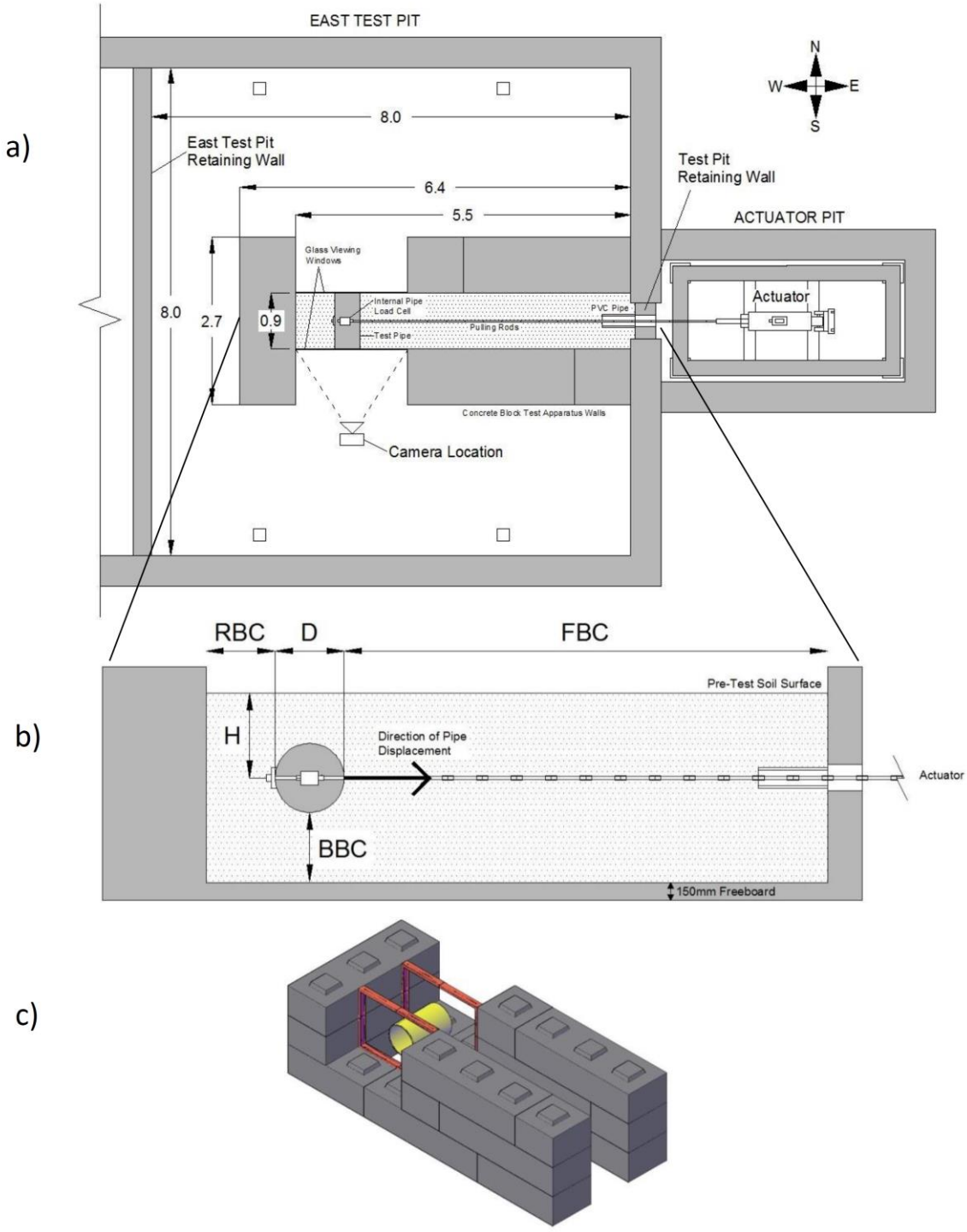

Figure 5.1. Test set up with the a) plan view (all dimensions in m) b) elevation view (definition of boundary conditions) c) 3-D oblique view (Burnett, 2015)

Table 5.1. Summary of Queen's large scale lateral pipe/soil interaction test series

Test ID	D (mm)	H/D	No. Density Measurements	Mean γ_d (kN/m^3)	S.D. (kN/m^3)	Coeff. of Variation (%)
04	254	3.0	24	14.73	0.19	1.3
05	254	1.0	15	15.66	0.37	2.4
06	254	1.0	15	14.72	0.14	1.0
07	254	1.0	15	15.46	0.34	2.2
08	254	1.0	15	15.40	0.31	2.0
09	254	1.0	15	14.72	0.23	1.6
10	254	3.0	23	14.56	0.18	1.2
11	254	3.0	24	15.43	0.39	2.5
12	609.6	1.0	18	15.57	0.41	2.6
13	609.6	1.0	21	14.60	0.25	1.4
14	609.6	1.0	13	15.22	0.35	2.3
15	609.6	1.0	7	14.55	0.11	0.8
21	254	7.0	10	14.83	0.22	1.5

allow for image capturing and analysis. The force-displacement response, pipe trajectory and soil failure mechanisms are captured during the tests to provide detailed data records on pipe/soil interaction processes. Past research (e.g. Audibert and Nyman, 1975; Trautmann, 1983; Turner, 2004) provided observed soil displacement fields, however, the utilization of particle image velocimetry (PIV) techniques by Burnett (2015) marks the first time that incremental displacement and shear strain plots have been captured for large-scale lateral pipe/soil interaction tests.

The pulling force and pipe displacement were recorded during each test to help characterize the peak and residual normalized forces and corresponding mobilization distances that are typically used to develop soil spring relationships. The direct (raw) force-displacement data for the dense and loose tests is provided in Figure 5.2. The dense tests exhibited a clear peak soil resistance force that was mobilized at a lateral displacement of approximately 0.1D. The loose test cases showed a more gradual mobilization of the soil resistance, and the force-displacement curve began to flatten after about 0.2D to 0.3D pipe movement at H/D ratios 1 and 3. The single case at H/D = 7 in loose sand was approaching asymptotic behaviour after 1.0D pipe displacement, which marked the end of the test corresponding to the available stroke of the pulling rod.

The peak dimensionless forces were corrected to account for the sidewall friction forces experienced by the ends of the pipe, as discussed by Burnett (2015). The resulting corrected dimensionless forces were compared against existing guideline recommendations in Figure 5.3. Under dense conditions, at H/D = 1.0, some of the test results show excessive forces in comparison with the guideline curves. However, the

guideline curves are generalized for friction angle increments that potentially do not apply to the test data; i.e. the peak friction angle has been shown to increase at very low stress levels that influences the peak soil resistance against lateral pipe movement (Pike et al., 2014; Roy et al., 2015). The loose tests are shown to correspond with the PRCI (2009) line based on an assumed 40° effective friction angle.

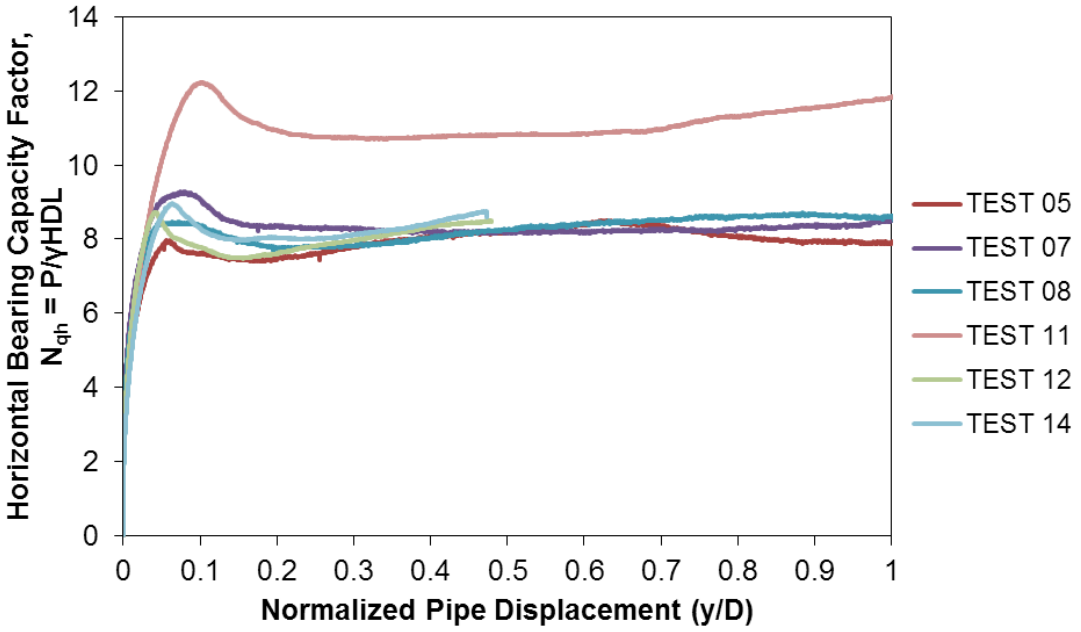

a)

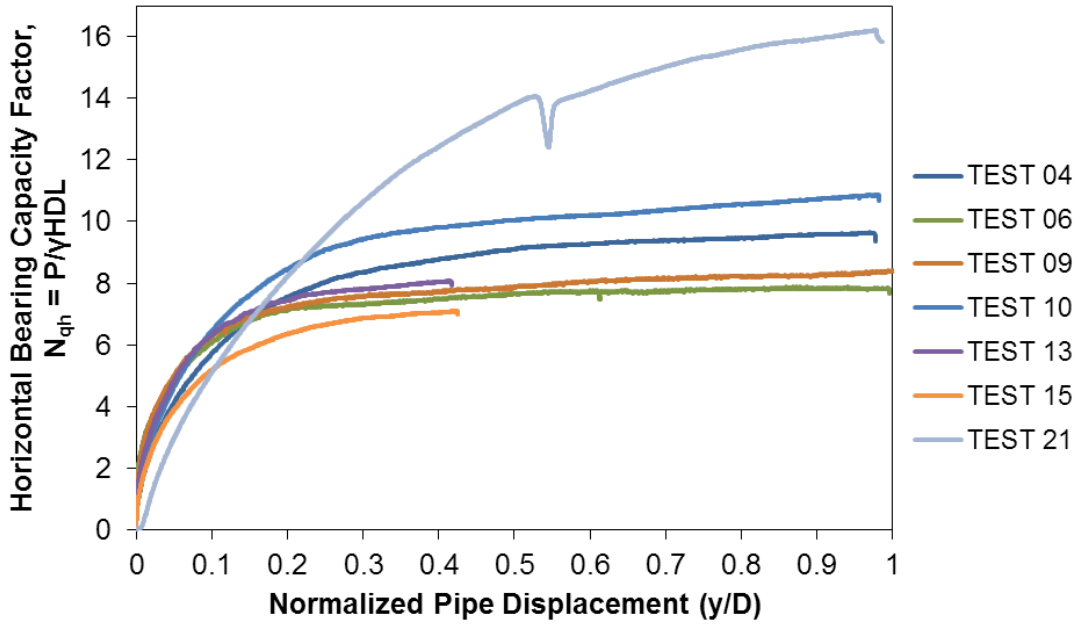

b)

Figure 5.2. Uncorrected normalized force-displacement data a) dense b) loose

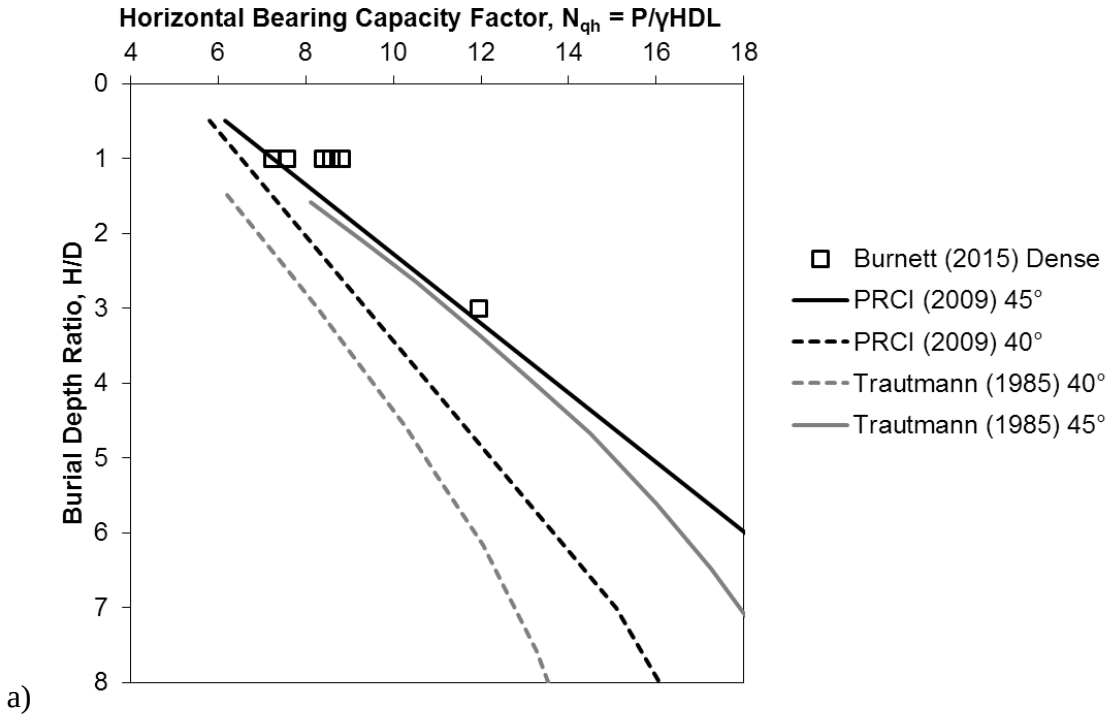

a)

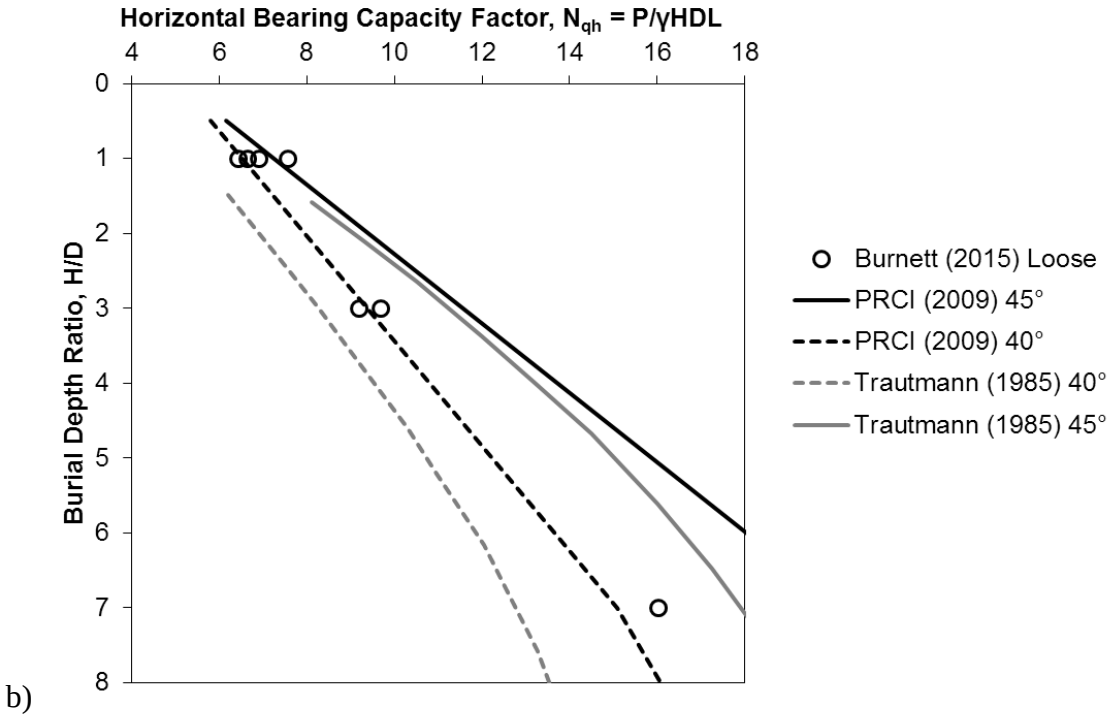

b)

Figure 5.3. Dimensionless forces compared against guideline curves a) dense b) loose

5.2 Analysis of Physical Test Data

A detailed analysis was conducted, on the public domain test database as reviewed in Section 2.5.1, to examine the effects of pipe diameter, burial depth ratio, soil density and strength on the normalized ultimate load and corresponding pipe displacement. Data were collected for a total of approximately 150 physical lateral pipe/soil interaction tests, as summarized in Appendix A, Table 9.1. For each contributing dataset, the soil type, specific gravity, maximum and minimum void ratio, and grading characteristics are summarized in Appendix C, Table 9.3. Based on this data compilation and analysis, new equations defining the ultimate soil resistance and displacement response in loose and dense conditions are proposed in Sections 5.2.2 and 5.2.3. The updated equations can be used to provide bounds on the soil response due to potential variation of sand density, or strength.

A histogram showing the distribution of external pipeline diameter is provided below in Figure 5.4. About 45% of the compiled dataset is for tests with a pipeline diameter less than 100 mm (approximately 25 to 75 mm or 1 to 3 inch). Approximately 29% of the data is for pipeline diameters from 100 mm to 150 mm (4 to 6 inch) and the remaining 26% ranges from 250 mm to 610 mm (10 to 24 inch).

Practical ranges for offshore oil and gas fields are 100 mm to 305 mm (4 to 12 inch) for gathering lines (i.e. flowlines) and as large as 914 mm (36 inch) for trunklines that transport hydrocarbons to shore. Similarly, Canada's underground oil and gas pipeline network is comprised of 100 to 305 mm (4 to 12 inch) gathering lines and transmission pipelines up to 1.2 m (48 inch) in diameter; about 50% of the transmission

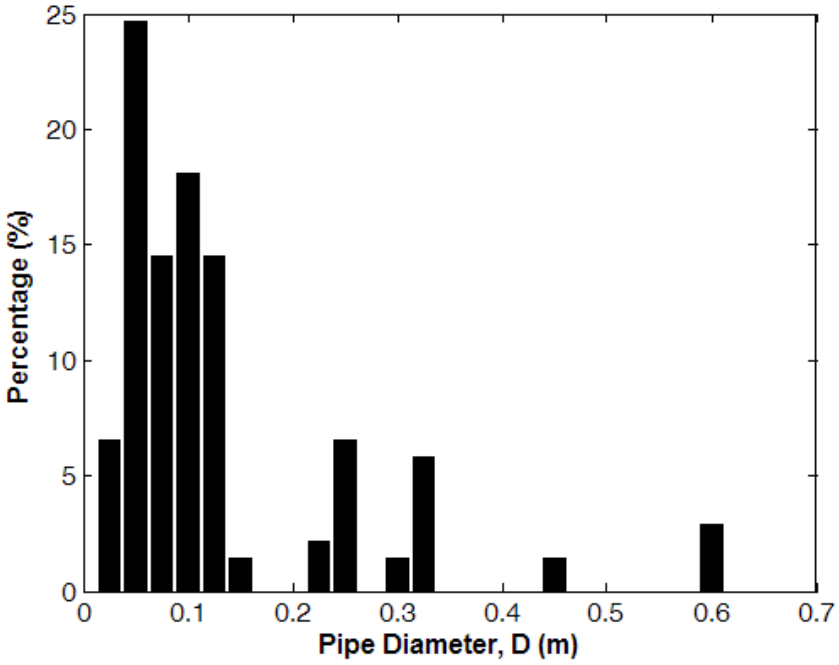

Figure 5.4. Distribution of pipe diameters for lateral pipe/soil interaction tests

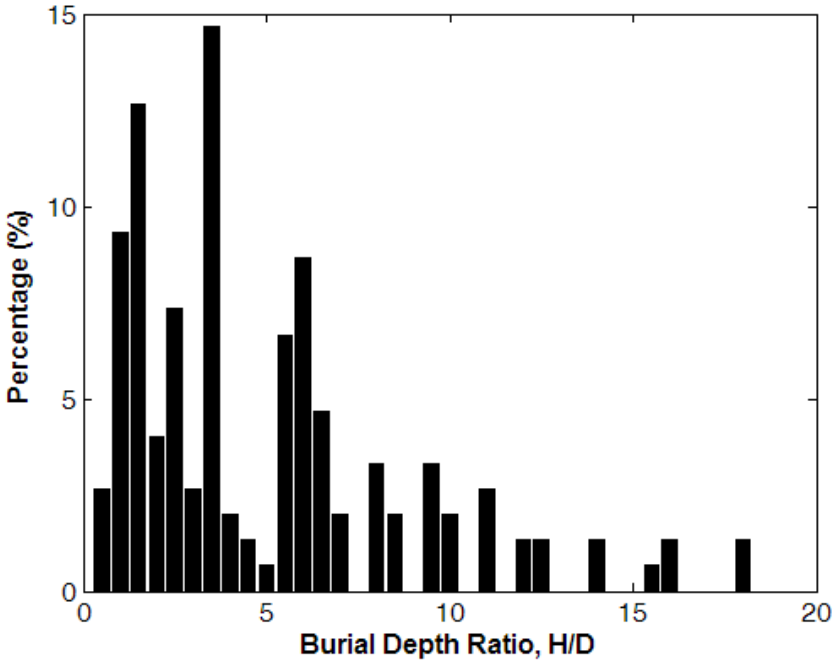

Figure 5.5. Distribution of H/D ratio for lateral pipe/soil interaction tests

lines are 457 mm (18 inch) or larger, and about 33% are 254 mm (10 inch) or smaller (CEPA, 2015).

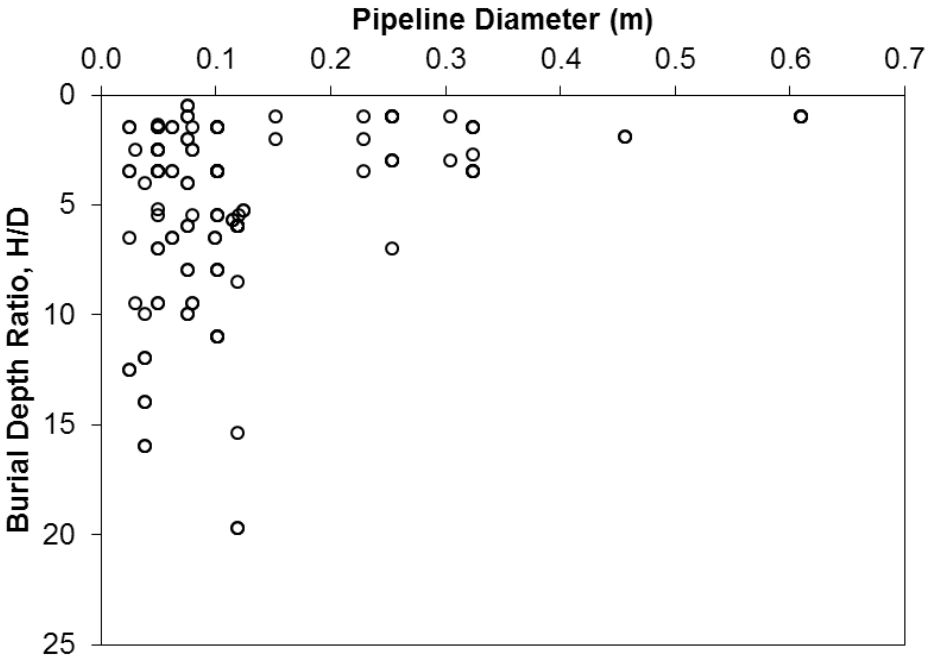

Figure 5.6. Pipeline diameter vs. H/D ratio for lateral pipe/soil interaction tests

The need for more testing at deep burial conditions to provide a basis to validate numerical simulations and delineate design curves is evident in the distribution of H/D ratios for the test dataset shown in Figure 5.5; although large H/D ratios are less common in practice. Large H/D ratios (e.g. H/D > 10) can occur for onshore pipelines where smaller diameter pipelines may have a minimum depth of cover requirement (e.g. minimum 1.2 m) in certain areas, e.g. inland water body crossings (CEPA, 2013). However, for offshore applications, even for protection against ice gouging, pipelines have been installed with a cover depth of about a depth of 2.13 m (7 ft.), corresponding

to H/D ≈ 8 (Lanan et al., 2001). Approximately 88% of the available physical test data is for H/D < 10, and 60% of the dataset is for H/D ratios less than or equal to 3.5. Furthermore, as shown in Figure 5.6, the tests conducted at deep burial levels (say H/D > 8) are for small pipeline diameters D = 25 to 75 mm.

5.2.1 Pipe Diameter and Model Scale Effects

In consideration of the wide range of test pipe diameters, this Section provides some discussion on the potential effects that the diameter range may have on the pipe/soil interaction response. Wood (2002) summarized that potential scale effects result from a) the thickness of ruptures or dilation bands, which is a function of particle size, and b) the mobilization length associated with changing rates of dilation (i.e. the reduction from peak to critical state conditions), which is a function of the relative displacement across the shear band. For scale models, one should ensure that the results can be applied to full-scale events, or ensure that adjustments are made accordingly, such that similitude is achieved. As discussed by Randolph and House (2001), it is generally accepted that a minimum structural dimension 20 to 30 times the mean particle size (B/d_{50} ratio) is sufficient to avoid scaling effects. However, it has been shown that this threshold cannot be applied as a general rule, and the required ratio can be higher especially where discrete rupture surfaces are formed, with dilation followed by strain-softening. For pile-soil interface tests, Foray et al. (1998) showed a minimum ratio of 20 was needed between the pile diameter and the width of the shear band along the interface for similitude with full-scale tests; hence assuming shear band widths are approximately $10d_{50,}$ then a ratio of

about $200d_{50}$ is required. This result was echoed and confirmed by Balachowski (2006) for highly dilative or contractive soil within the interface.

According to Garnier et al. (2007), to ensure grain size effects are avoided in centrifuge testing, the ratio of the structural dimension to the mean grain size B/d_{50} should be greater than 48 for pull-out of anchor plates, greater than 45 to 60 for the response of piles to lateral loads, greater than 50 for circular footings on granular soil (Toyosawa et al., 2013), and greater than 50 to 100 for the development of shear band patterns. Since the failure mechanisms for shallow embedded pipelines are governed by similar failure mechanisms as anchor pull-out tests and lateral pile loading, that involve strain localization in the form of shear bands, physical tests should target an absolute minimum ratio $D/d_{50} = 60$. These guidelines are for centrifuge scale experiments where appropriate scales are applied to match prototype pipe diameter and soil stress level. At 1g conditions, pressure dependent soil strength will have a greater effect on increasing the normalized soil resistance at shallow burial conditions.

A study by Guo and Stolle (2005) observed the lateral bearing interaction force decreased with increasing pipe diameter for a constant burial depth (H/D). A significant increase was highlighted in the lateral bearing interaction factor for smaller pipe diameter (e.g. < 50 mm) where the interaction factor may be 2 times the corresponding factor for a 330 mm diameter pipe. However, for practical ranges of energy pipeline diameters, say 150 mm to 1200 mm, then the expected variation in the lateral bearing factor, estimated by Guo and Stolle (2005), would be 12 to 10. This is a relatively minor variation (~ 20%)

in the interaction factor, due to pipe size effects, that is more consistent with the physical evidence.

The comprised physical dataset was compartmented into tests conducted under loose (Figure 5.7) and dense (Figure 5.8) conditions in order to assess the effect of pipe diameter on the lateral bearing factor variation with burial depth ratio. In the loose state, it is evident for the Trautmann (1983) data that the lateral bearing factor actually increases with pipe diameter by about 10% at H/D = 1.5, and about 40 % at H/D = 3.5. The dataset belonging to Hsu (1993) for D = 76.2 mm shows less soil resistance than Trautmann's (1983) data at 102 mm and 324 mm, as well as Hsu's (2001) data at 152.4 mm and 228.6 mm; the data for D = 38.1 mm provides a reasonable extension to the D = 76.2 mm data at deep burial depths.

This is in contrast to the relationship proposed by Guo and Stolle (2005). However, the data representing Audibert and Nyman (1975) at D = 25 mm shows significantly larger values, while the data for D = 62 mm shifts more towards Trautmann's (1983) data. The bearing factors for Calvetti et al. (2004) and diPrisco and Galli (2006) at D = 50 mm are more in line with, and even exceed Audibert and Nyman's (1975) data at D = 25 mm. Small diameters 25 mm (Audibert and Nyman, 1975) and 38.1 mm to 76.2 mm (Hsu, 1993) essentially lead to results that provide an upper and lower bound failure envelope, in a dataset having a maximum value of 324 mm. Hence, the trend that depicts decreasing bearing factors with increasing pipe diameter is not abundantly clear for the loose condition based on the currently compiled dataset.

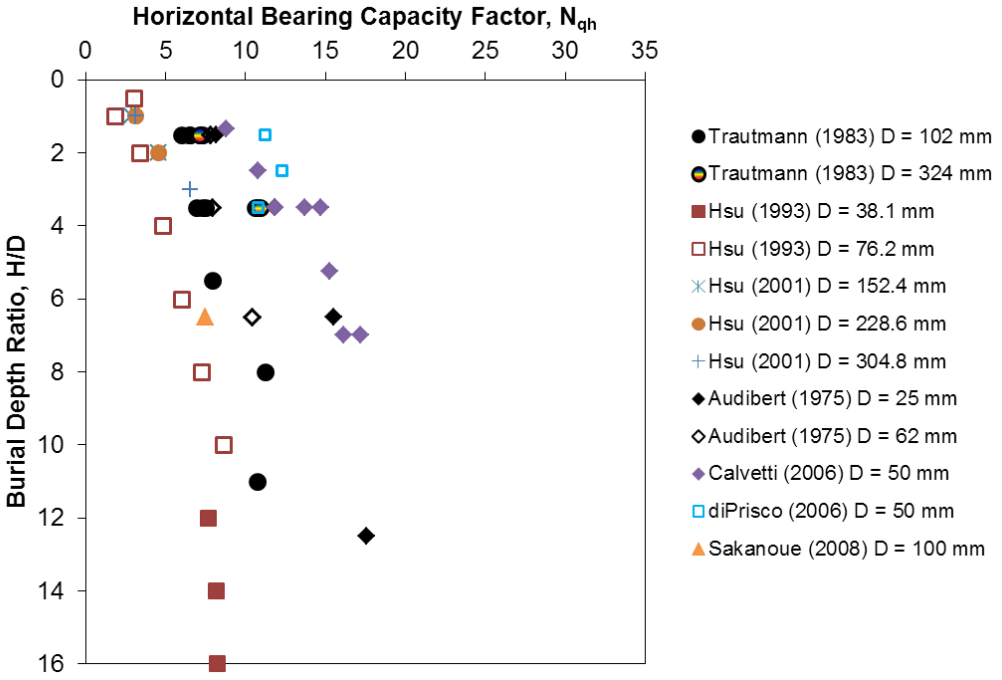

Figure 5.7. N_{qh} vs. H/D with varying D (loose conditions)

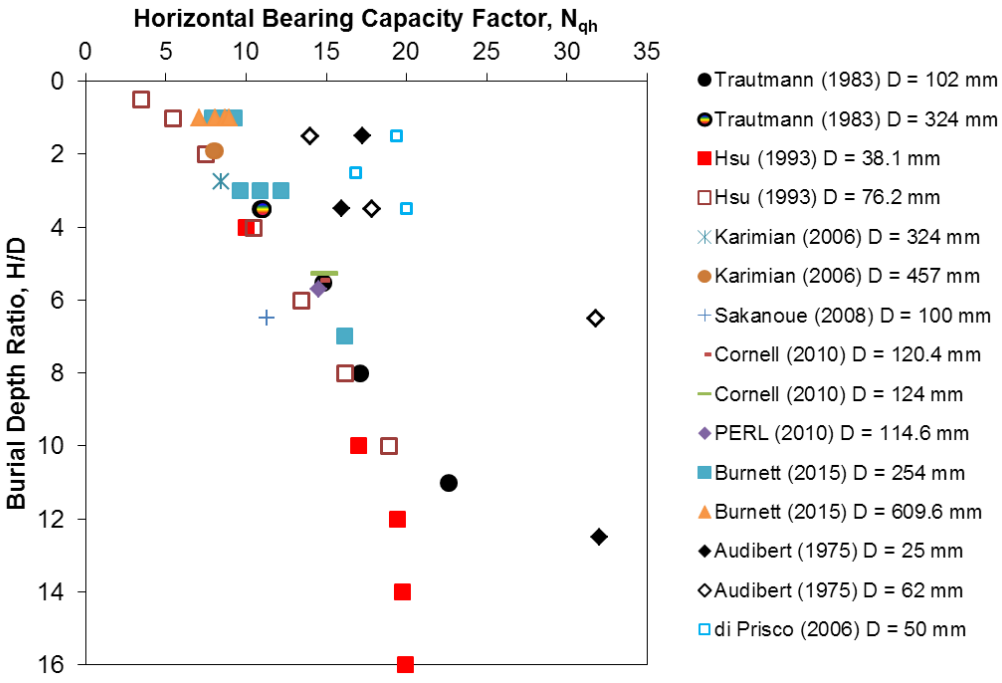

Figure 5.8. N_{qh} vs. H/D for varying D (dense conditions)

A histogram of the diameter to mean grain size ratio (D/d_{50}) related to the compiled physical test dataset is provided below in Figure 5.9. The minimum D/d_{50} ratio for the Audibert and Nyman (1975) test results is approximately 38 (D = 25 mm), which is less than recommended as discussed above. The minimum D/d_{50} ratio for Hsu's (1993) tests is approximately 65 (D = 38.1 mm) to 129 (D = 76.2 mm) which perhaps permits localization patterns that are closer to prototype conditions. However, this does not explain the results presented by Calvetti et al. (2004) or diPrisco and Galli (2006) that were conducted with $D/d_{50} \approx 143$.

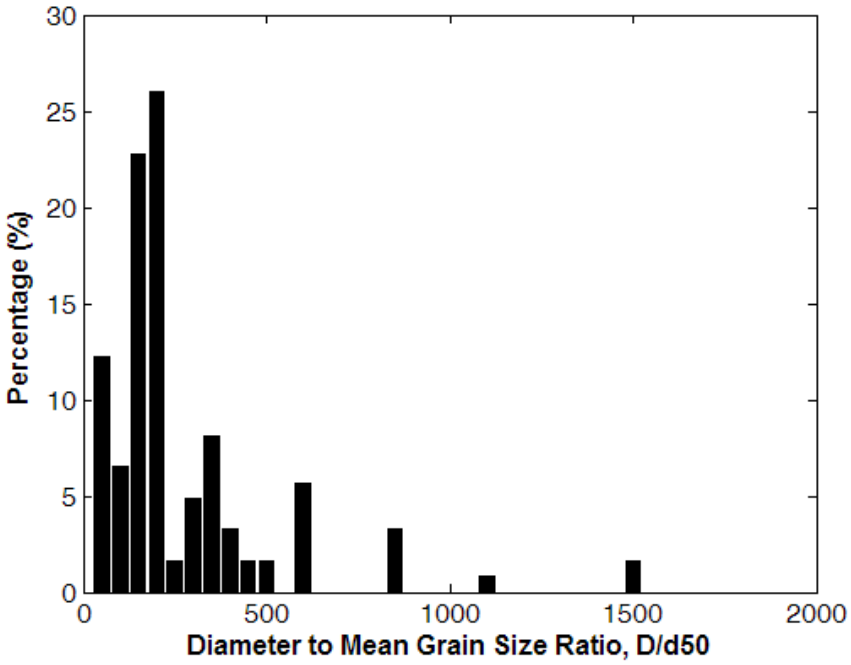

Figure 5.9. Distribution of D/d_{50} ratio for lateral pipe/soil interaction tests

There remains considerable uncertainty on the factors that influence the horizontal bearing capacity factor. The pipe diameter scale effect as proposed by Guo and Stolle

(2005) suggests that the bearing factor scales down for small pipe diameters; however, there is contradicting evidence in the physical test data that requires further investigation. For example, Hsu's (2001) for small pipe diameters (38.1 mm) is either less than, or consistent with the data for larger diameters, while Calvetti's (2006) data (50 mm) shows a much higher bearing factor range. These issues are related to shallow burial of small diameter pipes that can be influenced by increased friction angle at low confining pressure, and differences in the strain localization that may be influenced by the diameter to grain size ratio. These aspects require further study for application of test data from small scale tests to practical scale problems.

5.2.2 Recommendation for Ultimate Lateral Soil Resistance

Guo and Stolle (2005) compiled a dataset for lateral plate anchor and pipe movement physical tests in loose and dense sand. For the purposes of sorting the dataset, the loose condition was defined as sand having a friction angle less than 35°, and for the dense condition, greater than 35°. A similar analysis was conducted in the present study or the compiled lateral pipe/soil interaction test dataset; the test data are plotted below in Figure 5.10 and Figure 5.11 for loose and dense soil test conditions. The lateral bearing factor design curves proposed by Trautmann and O'Rourke (1985) - denoted T & O - and by PRCI (2009) are also plotted.

In the loose condition, PRCI (2009) recommends that the lower bound design curve be defined by the 35° friction angle line. However, the design curve defined by Trautmann and O'Rourke (1985) for 30° is in line with the lower bound envelope of the test data. This has potential significance in that the lateral soil resistance could be over-

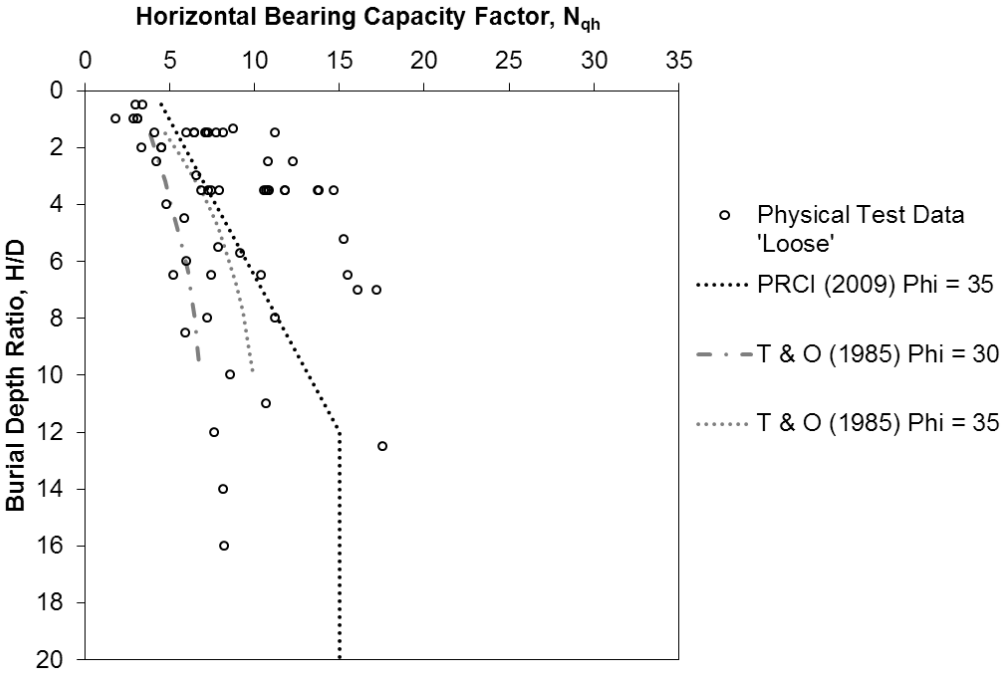

Figure 5.10. N_{qh} vs. H/D (loose conditions)

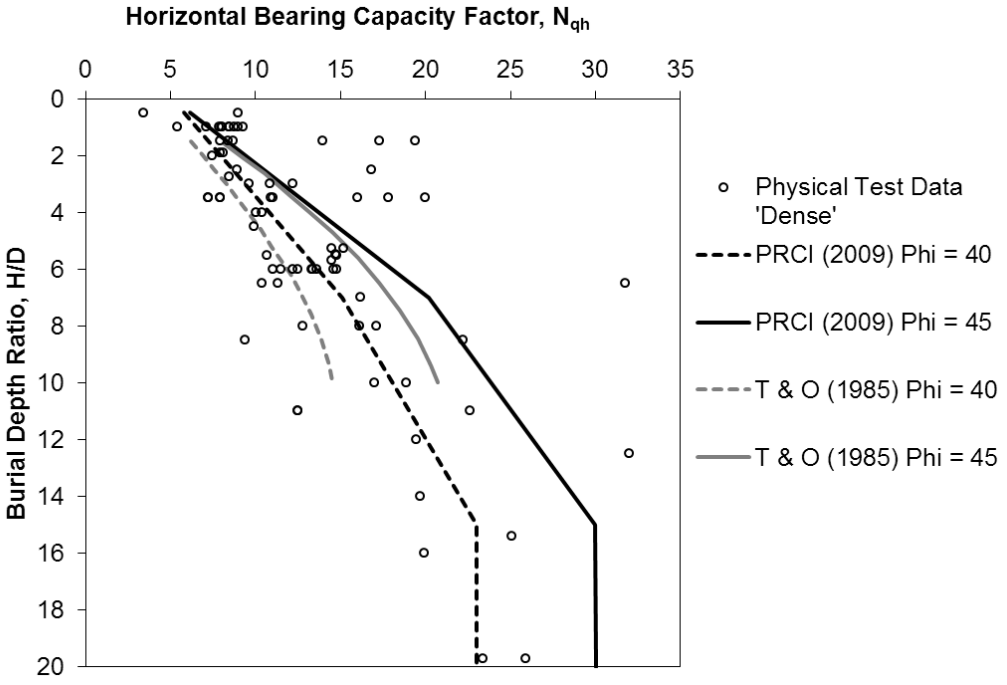

Figure 5.11. N_{qh} vs. H/D ratio (dense conditions)

estimated leading to less resistance to lateral buckling of buried pipelines in loose cohesionless backfill.

In general for the overall range of soil density, the lateral soil resistance is shown to increase with H/D ratio and soil strength. The data for deep burial conditions is sparsely populated with tests using small diameter pipelines. Though further physical testing at deep burial is recommended, it appears that the normalized ultimate lateral resistance fully transitions to the deep burial flow mechanism, or remains constant, at H/D > 10 to 12. For both loose and dense conditions, there is a significant spread in the range of normalized ultimate resistance, especially at shallow H/D ratios < 4.

Guo and Stolle (2005) explained this discrepancy through examining the relationship between normalized lateral soil resistance and pipe diameter. It was shown that the lateral bearing factor increases with decreasing pipe diameter, highlighting the importance of cautious application of results from small scale laboratory tests conducted at 1g with small diameter pipes (e.g. 25 mm).

It should be noted that the test results summarized in Appendix A, Table 9.1 are for dry sand conditions only. Tests conducted by Monroy (2013) were mentioned in the literature review, but are not included in the data compilation due to the moisture content (4%); however, the results in moist Fraser River sand are consistent with earlier tests conducted by Karimian et al. (2006) in dry Fraser River sand using the same pipe diameter, D = 457 mm, and burial depth ratio H/D = 1.9 (i.e. $N_{qh} \approx 8$ in both cases).

It is often the case in design situations that there is limited data available to make accurate predictions of the strength of granular backfill materials over a range of relative

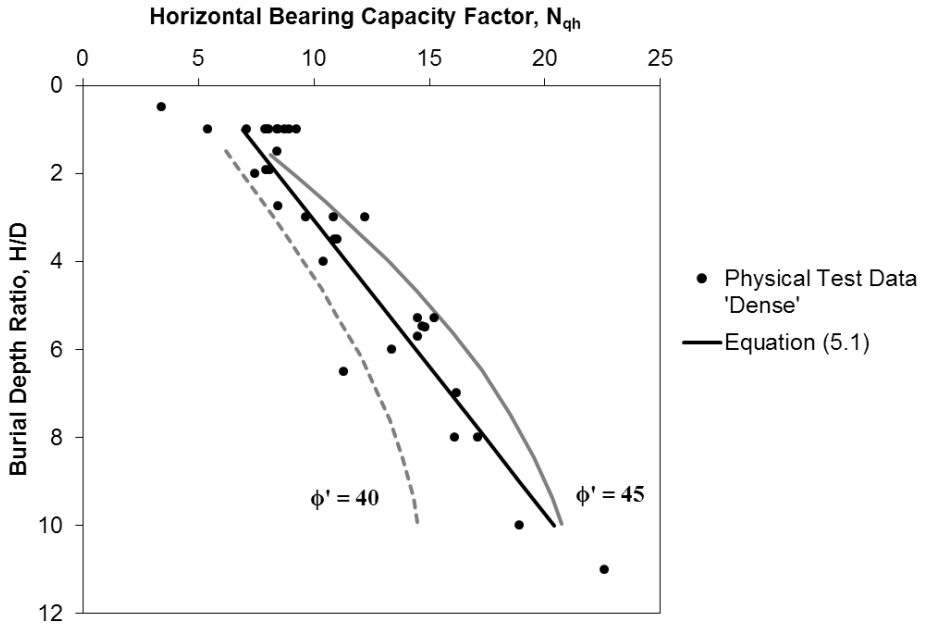

Figure 5.12. Lateral pipe/soil interaction test data in dense conditions for D > 75 mm

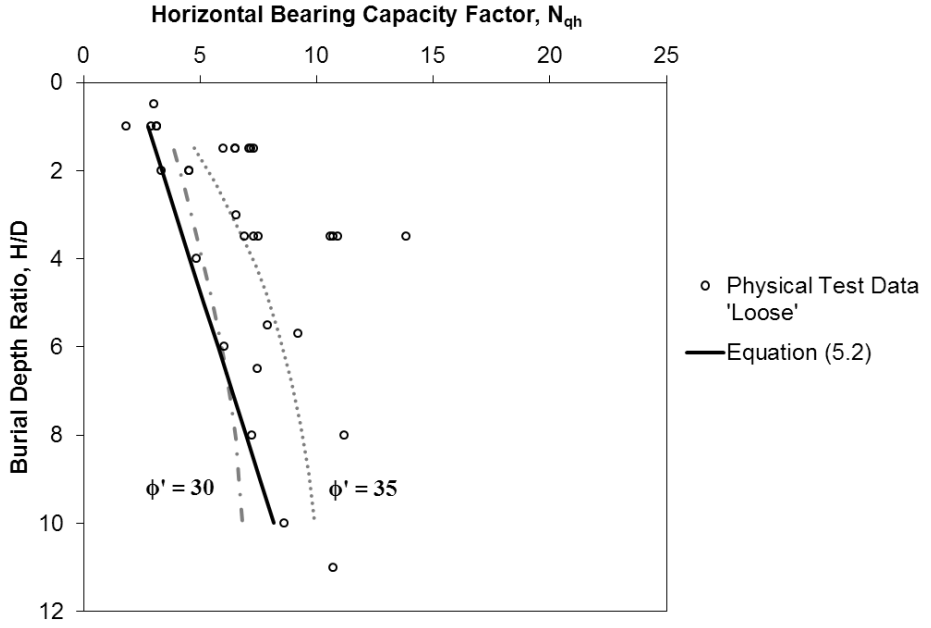

Figure 5.13. Lateral pipe/soil interaction test data in loose conditions for D > 75 mm

density and pressure. Where there is uncertainty in the quantitative measure of soil strength, qualitatively assuming loose and dense conditions to perform an upper and lower bound sensitivity study on buried pipeline response to operational loading can be an effective means of enveloping the system response.

Due to the uncertainty surrounding pipe diameter and stress level effects, it is recommended that tests using pipe diameters less than 3 inches (~ 75 mm) be omitted from the pipe/soil interaction test dataset conducted at 1g. In terms of best practice recommendations, this helps reduce potential scale effects discussed above and tends toward alignment with practical energy transport pipeline diameters.

As shown in Figure 5.12, the physical test data for dense conditions can be approximated using a linear best fit relationship expressed by Equation (5.1). The resulting equation is statistically significant ($R^2 \approx 89\%$) and intersects Trautmann and O'Rourke's (1985) recommended design curve for very dense ($\phi' = 45°$) conditions.

$$N_{qh(UB)} = 1.5\left(\frac{H}{D} + 3.6\right) \tag{5.1}$$

The data for loose conditions shows more scatter, likely due to densification of the soil in front of the pipeline during testing. However, a lower bound approximation expressed by Equation (5.2) can be applied to conservatively account for loose backfill conditions, as shown in Figure 5.13. The upper and lower bound equations are recommended for $H/D \leq 10$.

$$N_{qh(LB)} = 0.6\left(\frac{H}{D} + 3.6\right) \quad (5.2)$$

5.2.3 Recommendation for Ultimate Lateral Displacement

The pipe displacement corresponding to the ultimate lateral resistance (y_u) was also compiled for the physical test dataset where attainable. Similarly, the data was separated in to loose and dense conditions to examine the relationship between the ultimate lateral displacement, soil density and burial depth. As discussed above, guidelines (ALA, 2001; PRCI, 2009) provide recommendations for estimating y_u as a function of H/D and D. The guideline recommendation is plotted along with the test data in the same format in Figure 5.14. The guideline suggestion $y_u/(H+D/2) = 0.04$ is shown to provide a reasonable prediction for the dense test data, but underestimates the data for the loose condition.

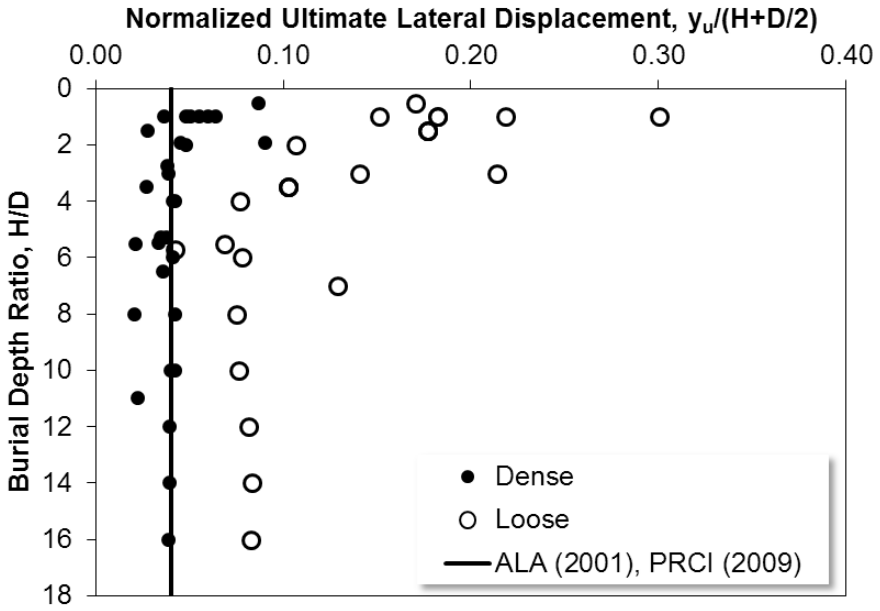

Figure 5.14. Normalized pipe displacement vs. guideline recommendation

Presenting the data in an alternative format provides a clear relationship for loose and dense conditions that shows pipe displacement normalized with pipe diameter (y_u/D) increasing with the H/D ratio (Figure 5.15). This leads to empirical expressions for y_u as a function of the pipe diameter and H/D ratio for both loose and dense conditions, as expressed by Equations (5.3) and (5.4), respectively. Alternatively (as suggested above for the ultimate lateral resistance), this provides an estimate of the lower (LB) and upper bound (UB) y_u for qualitatively loose and dense granular backfill materials (where lower and upper are in reference to the lateral soil resistance).

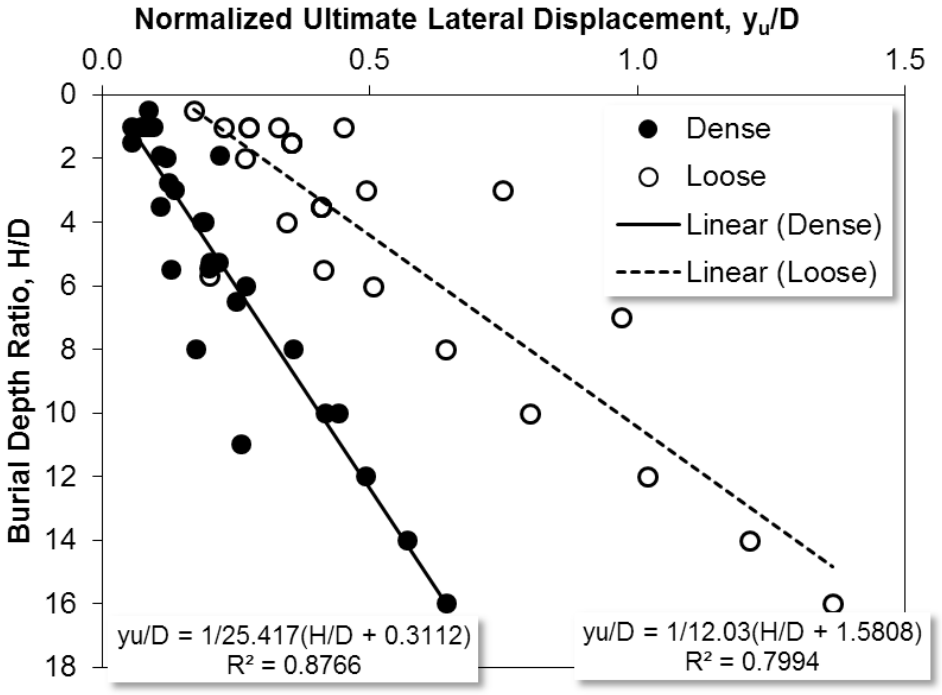

Figure 5.15. Normalized pipe displacement vs. H/D ratio

$$y_{u(LB)} = \frac{\mathrm{D}}{12.0}\left(\frac{H}{D} + 1.58\right) \tag{5.3}$$

$$y_{u(UB)} = \frac{D}{25.4}\left(\frac{H}{D} + 0.31\right) \tag{5.4}$$

Combining the lower and upper bound estimates for ultimate lateral soil resistance and corresponding displacement, bilinear (or hyperbolic) soil springs can be developed for use with structural beam-spring models.

5.3 Summary

This chapter examined existing data for physical lateral pipe/soil interaction tests conducted in dry sand conducted by several different research groups using a range of sand types and placement densities, pipe diameters and H/D ratios. The comprehensive data mining exercise revealed an extensive test dataset available in the public domain. However, a gap in the available data for deep burial conditions was identified; likely reflecting the limits of laboratory soil test pit depths.

The results of a new large-scale lateral pipe/soil interaction testing program conducted through a collaborative research and development effort between the Memorial University of Newfoundland and Labrador, Queen's University and the Wood Group were presented in summary form; for further detail the reader is referred to Burnett (2015). The test results follow the general data trends, though the bearing factors for typical loose ($\phi' \approx 35°$) and dense ($\phi' \approx 45°$) conditions are higher than the proposed guideline curves at the shallowest burial depth ratio H/D = 1.0. This may be attributed to

the effects of the low confining stress and the angular shape of the synthetic olivine sand particles that can increase the interparticle friction and ultimately, the peak friction angle.

The guideline recommendations discussed in Section 2.5.3 are based partially on estimates of the soil friction angle for granular materials. The bearing factor curves proposed by Trautmann (1983) are based on effective friction angle measured from direct shear tests. However, different laboratory soil testing methods can lead to different estimates of the friction angle, especially at low confining pressure and high relative density. These aspects of granular soil behaviour were discussed in Section 2.4.

In the present Chapter, general recommendations are provided for the ultimate lateral soil resistance and corresponding pipe displacement that provide upper and lower bound estimates based on the physical test data. Equations for the ultimate displacement are suggested that improve upon the existing guideline recommendations, especially considering the response of loose sands. These bounds can be used to assess the sensitivity of the pipe response to the soil force-displacement response in structural pipe/soil interaction modelling for shallow buried pipes. In light of the typical site variation of soil properties, differences in strength between fresh and aged granular backfill, and the uncertainty introduced by varying testing methods, the bounding exercise can be useful in preliminary design and analysis to understand the potential envelope of pipeline response.

The test results were compiled and grouped based on loose or dense conditions to analyze trends in the dataset. The pipe diameter was also considered to assess potential pipe diameter and model scale effects discussed by Guo and Stolle (2005). The data

analysis does not allow for definitive conclusions on the pipe diameter effect, and in general it can be shown that for practical pipe diameters used for hydrocarbon transport the pipe diameter effect can be ignored.

6 Finite Element Model Applications

This Chapter describes the application of the constitutive and finite element models described above in Chapter 3 and Chapter 4, respectively. As outlined in Chapter 1, the present study was conducted in two phases, where Phase I focused on developing the coupled ice/soil/pipeline interaction simulation capability for cohesive soils. The development and verification of the subset ice/soil and soil/pipeline interaction models are described. The coupled simulation tool was then used in a comparative assessment with the conventional structural decoupled modelling approach for ice gouging. The comparison was conducted on a consistent basis whereby the decoupled structural model inputs for the soil spring resistance and imposed subgouge displacements were based on the coupled continuum CEL model results. This is a unique contribution and improvement relative to previous studies that used the decoupled free-field subgouge displacements from empirical or continuum models.

The phase II research and development involved physical and numerical modelling of lateral pipe/soil interaction in sand. The objectives of the numerical model development were to adequately predict the mechanical pipe/soil interaction and strain localization response. The modified Mohr-Coulomb constitutive model described in Section 3.2.2 was used successfully to meet the program objectives described above. The model is easily understood and relatively straightforward to implement in comparison to complex user material subroutines. Furthermore, it captures realistic soil behavior within a constitutive modelling framework for which the parameters can be derived from common laboratory tests.

6.1 Ice Gouging in Cohesive Soil

The following subsections apply the CEL FE free-field ice gouge model described in Section 4.2. Mesh sensitivity is conducted to assess the mesh resolution necessary to achieve convergence in the global keel reaction forces and subgouge soil displacements. The influence of the assumed undrained constitutive model (i.e. plane strain or triaxial compression matching yield stress with von Mises failure surface, or Mohr-Coulomb model with $\phi = 0$ conditions per Section 3.1) on these parameters was also assessed. The influence of implementing a varying undrained shear strength and stiffness profile (Section 3.1.1) was demonstrated, showing improved performance in matching centrifuge test data. This approach is a novel contribution by the author in the field of free-field ice gouge finite element modelling.

6.1.1 Mesh Sensitivity

For the free-field ice gouge simulations, a mesh sensitivity study, as summarized in Table 6.1, was conducted to assess the influence of element size and mesh density on the solution run time and predicted outcomes with respect to ice keel reaction forces and soil displacements. The analysis case results are compared for relative convergence against one another, while further analysis in Section 6.1.3 seeks to verify the numerically predicted results against centrifuge scale test data. The solution run time was observed to be a nonlinear, exponential relationship with the number of elements used in the Eulerian mesh domain. The analyses were conducted using 24 cpus on the Silicon Mechanics cluster located in the Memorial University Engineering building.

Table 6.1. Mesh convergence study for free-field ice gouge simulations

Case	Min. Element Size (m)	Max. Element Size (m)	Number of Eulerian Elements	Run Time
1	1.0	1.0	32,500	5 min.
2	0.5	1.0	126,000	22 min.
3	0.25	1.0	441,600	2 hrs. 18 min.
4	0.125	1.0	1,439,600	16 hrs. 8 min.

A uniform, medium stiff cohesive soil with an undrained shear strength, s_u = 50 kPa was examined in the mesh sensitivity study. The circular von Mises failure surface with yield stress criterion matching the Tresca yield stress in triaxial compression was utilized; hence, the plastic yield stress was assumed as σ_y = 100 kPa. The elastic modulus was assumed as 10 MPa (i.e. 200 s_u) to define an intermediate value for medium plasticity clay. The Poisson's ratio was set at ν = 0.499 to simulate incompressible behaviour. The total unit weight was assumed equal to 19 kN/m^3. A limit was imposed on the allowable keel/soil interface shear stress (τ_{max}) equal to half the undrained shear strength, and the friction coefficient was assumed μ = 1.0 (i.e. stick-slip condition). The limit is imposed to ensure that the interface shear stress does not exceed the strength of the underlying material, which can occur with high normal contact stresses, and also to account for the remoulded strength of the clay due to shearing at the interface.

The keel was displaced downwards to a prescribed gouge depth of 2.0 m and then translated in the gouge direction for 30 m with all other degrees of freedom restrained.

The 2 m gouge depth is selected to coincide with the extreme gouge depth level defined by Blasco et al. (2011) based on gouge records in the Canadian Beaufort Sea. The 2 m gouge depth is also used in the case study on ice/soil/pipeline interaction in the following Section 6.3. The 30 m keel displacement is enforced to reach steady-state gouging conditions, but limit the overall displacement to reduce analysis run times. The analysis results indicated that the keel reaction forces were approximately level after about 20 m of keel displacement. The keel had a half-width of 5 m, a base dimension of 5 m and an attack angle of 15°. An array of tracer particles was situated at a distance of 20 m in the gouge direction to track the subgouge soil deformation. The geometry is illustrated in Figure 6.1.

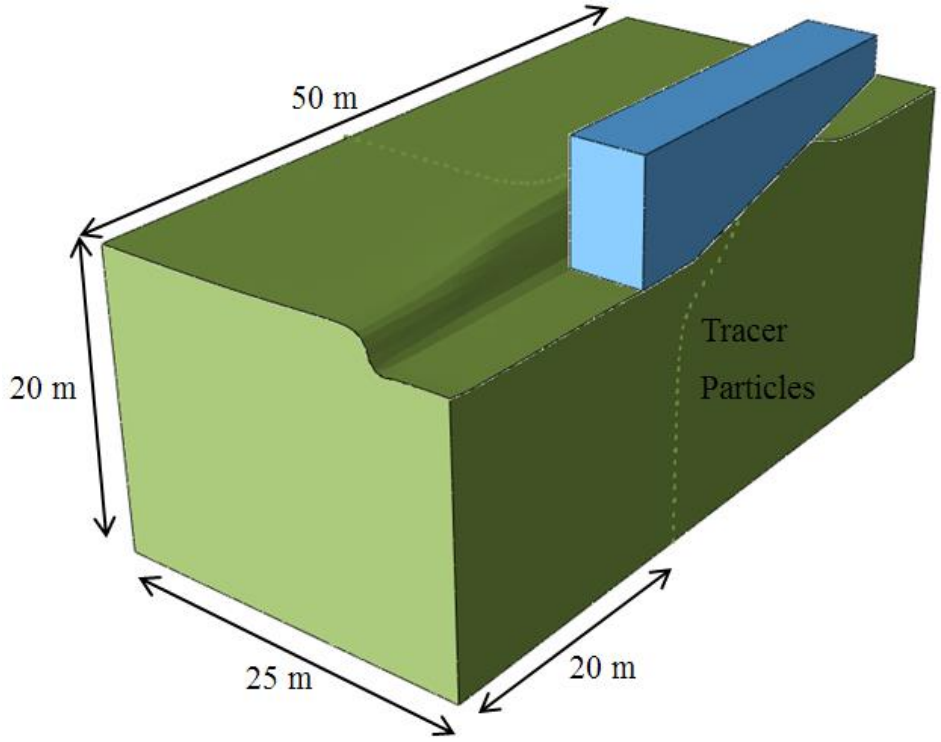

Figure 6.1. Ice gouge simulation geometry schematic

The soil box dimensions, for the Lagrangian and Eulerian space, were 50 m in the gouge direction, 25 m (half-width due to symmetry) in the transverse lateral direction, and 20 m in the transverse vertical direction. The mesh was constructed using single bias meshing in the transverse lateral and vertical gouge directions, whereby the element size was varied from minimum to maximum sizes (Figure 6.2). The element size was also biased at the intersection of the void and soil space from minimum to maximum in the vertical upward and downward directions. The element size was held constant in the gouge motion direction. The minimum element size varied from 1.0 m to 0.125 m, while the maximum element size was kept at 1.0 m for each case. For the mesh convergence study, the total number of Eulerian elements, including elements initially full and void of soil material, ranged from 32,500 to 1,439,600 (Table 6.1). Also, the analysis run times ranged from just 5 minutes to about 16 hours running on 24 CPUs.

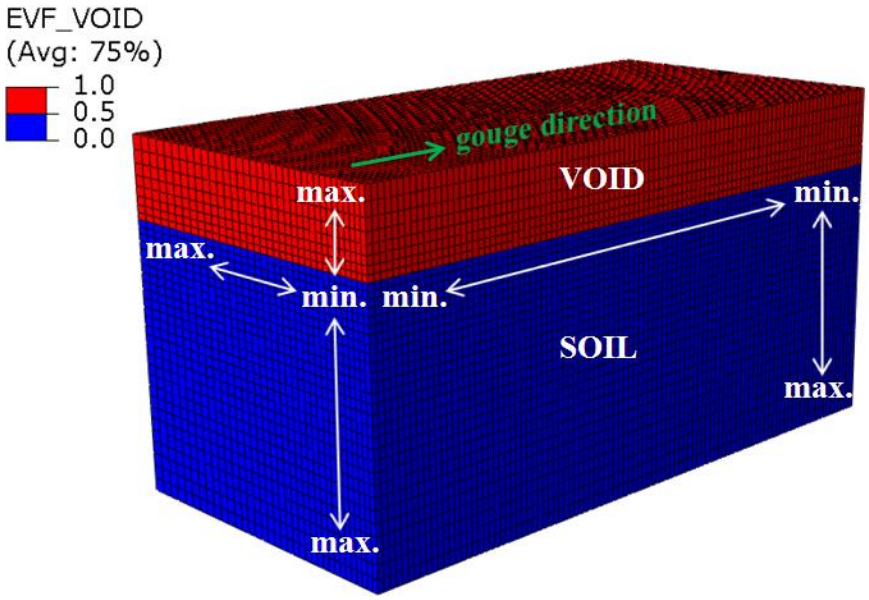

Figure 6.2. Mesh design schematic for ice gouge simulation

6.1.1.1 Horizontal Subgouge Soil Deformation

The horizontal subgouge soil displacement for Cases 1 to 4 were plotted against the depth below the base of the keel (subgouge depth) normalized with the gouge depth. As shown in Figure 6.3, the coarse mesh (Case 1, Table 6.1) provided conservative predictions of the horizontal subgouge soil displacement field. A slightly more refined mesh (Case 2, Table 6.1) provided optimistic predictions on the horizontal subgouge soil displacement field. Increasing mesh refinement (Case 3 and Case 4, Table 6.1) resulted in a converged profile of horizontal subgouge soil displacements.

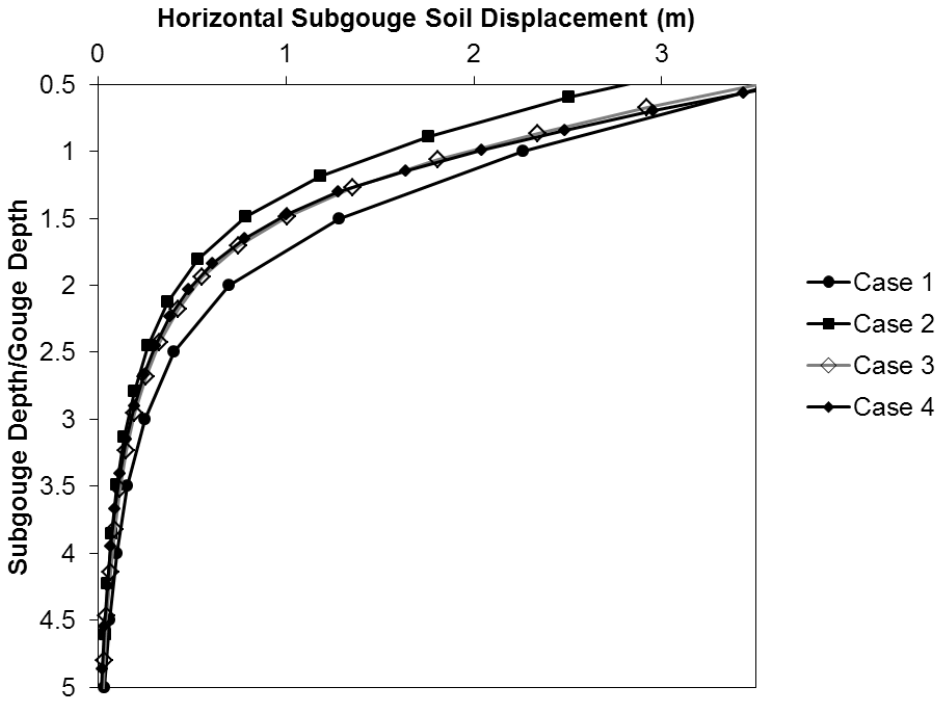

Figure 6.3. Mesh size effect on horizontal subgouge soil displacement

The numerical prediction of the subgouge displacement field is a complex problem that is dependent on the material strength and stiffness, treatment of the interface behavior, element size, and soil box size. The idealized elastic perfectly plastic constitutive relationship influences the gouge clearing mechanisms and formation of the side berms and frontal mound that do not account for surface cracks that occur due to the lack of soil tensile strength. This has an effect on the numerical tool capability to accurately predict the true physical behavior.

Comparatively, Case 3 had more than three (3) times fewer elements, and ran about eight (8) times faster than Case 4, yet the prediction of subgouge displacements was nearly identical between the two analyses. The results suggest, for the parameters examined, then the Case 3 mesh density is adequate to achieve convergence on the horizontal subgouge soil deformation field. The following subsection examines the keel reaction forces.

6.1.1.2 Horizontal and Vertical Keel Reaction Forces

The comparison of the global horizontal and vertical keel reaction forces indicates disparity between the Case 1 and Case 2 predictions (Figure 6.4 and Figure 6.5). As expected, the reaction forces correlate with the magnitude of subgouge soil displacement, where the Case 1 prediction is conservative, while Case 2 predicts comparatively small reaction forces. The Case 1 solution is relatively noisy, especially compared to the Case 3 and Case 4 results. The Case 3 reaction forces are 4 % greater than the Case 4 predictions,

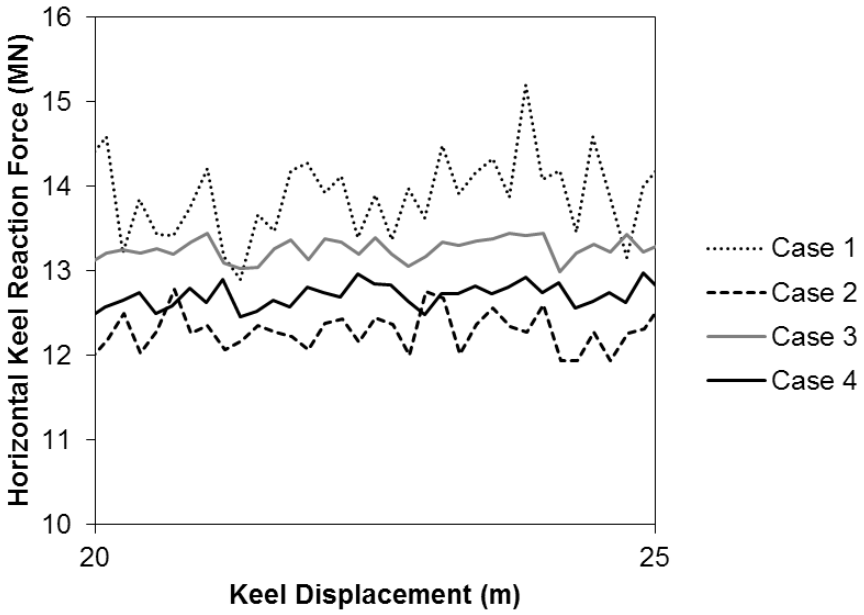

Figure 6.4. Mesh size effect on horizontal keel reaction force

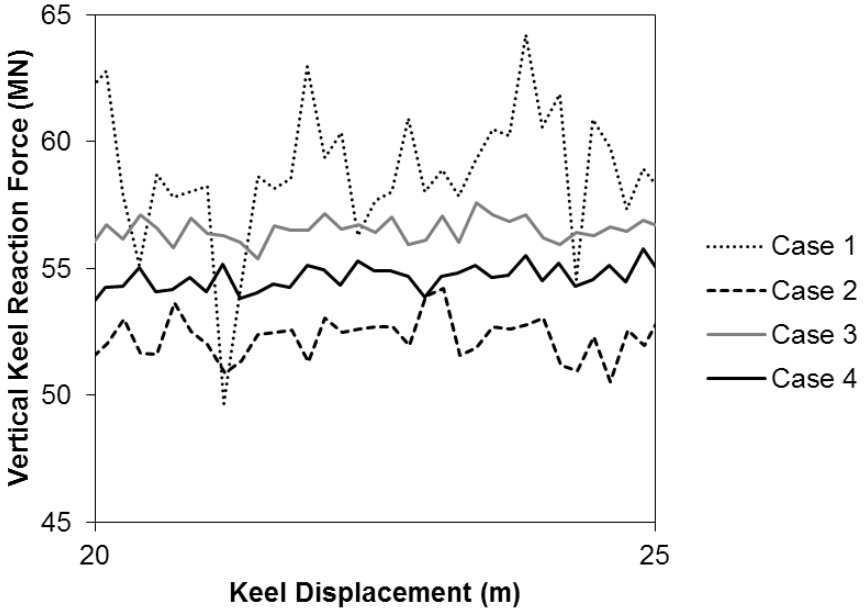

Figure 6.5. Mesh size effect on vertical keel reaction force

whereas the Case 1 reaction force was 1.2 times greater than the Case 2 predictions. Based on these findings, to balance analysis run times and solution accuracy, then the Case 3 mesh density was utilized for CEL FEA free-field ice gouge simulations.

6.1.2 Effect of Undrained Cohesive Constitutive Model

As discussed in Section 3.1, constitutive modelling for total stress analysis of undrained cohesive soil is typically accomplished by one of three methods: 1. using the circular von Mises failure surface with the yield stress criterion defined by matching the Tresca yield surface in triaxial compression, 2. using the von Mises failure surface, intersecting the Tresca yield surface under plane strain conditions, or 3. the Tresca yield surface is used assuming $\phi = 0$ conditions within the Mohr Coulomb model, setting the undrained shear strength directly. These three methods to define the yield strength and surface were evaluated in free-field ice gouge simulations, as summarized in Table 6.2.

Table 6.2. Analysis cases for undrained free-field ice gouging (24 CPUs)

Case	Yield Surface	Yield Stress	Run Time
3a	Circular von Mises	$\sigma_y = 2s_u$	2 hrs. 18 min.
3b	Circular von Mises	$\sigma_y = \sqrt{3}s_u$	2 hrs. 19 min.
3c	Hexagonal Tresca	$c' = s_u$	3 hrs. 16 min.

The Case 3 model described above formed the basis for this comparison study, and hence Case 3 from Table 6.1 is equivalent to Case 3a in Table 6.2. The only

parameters changed in cases 3b and 3c are the constitutive parameters that defined the plastic yield surface. The effects of the assumed constitutive parameters were examined in terms of the horizontal subgouge soil displacement and global keel reaction forces as discussed in the following subsections.

6.1.2.1 Horizontal Subgouge Soil Deformation

The horizontal subgouge soil deformations for Cases 3a, 3b and 3c are compared in the following Figure 6.6.

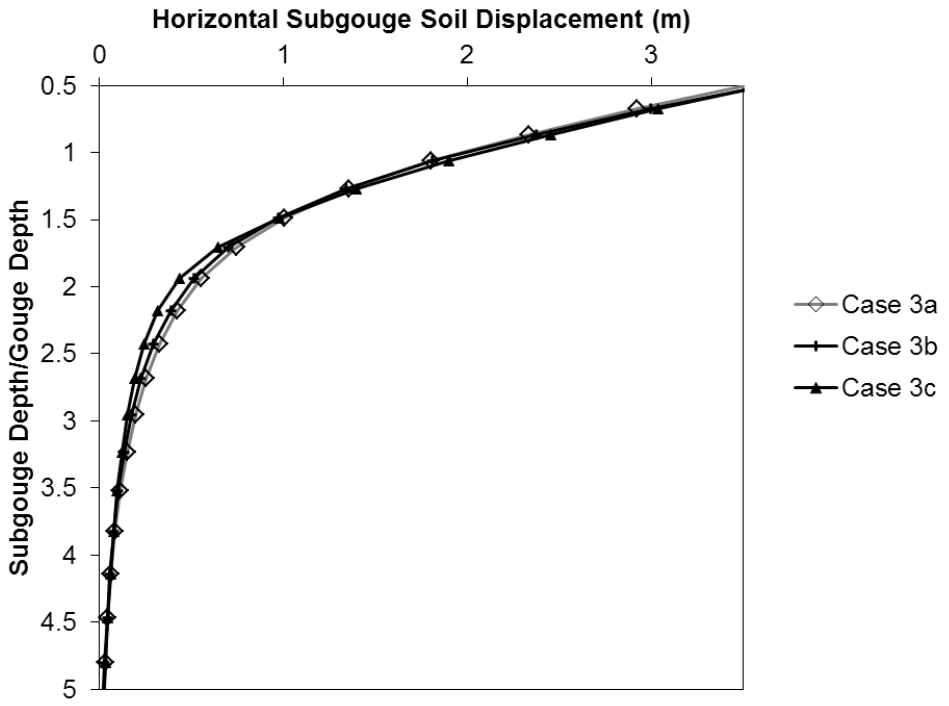

Figure 6.6. Undrained cohesive constitutive model effect on horizontal subgouge soil displacement

The predicted soil deformations are very similar between all three models. This might be explained by the congruency in the interface properties (i.e. similar amount of

interface shear stress to drag the soil forwards) and elastic modulus specified for each analysis case. Also, the horizontal subgouge soil deformations are constrained at the plane of symmetry (i.e. gouge centerline) in an approximate state of plane strain and are similarly influenced by the subduction of forces.

6.1.2.2 Horizontal and Vertical Global Keel Reaction Forces

The horizontal and vertical global keel reaction forces are compared in Figure 6.7 and Figure 6.8. Case 3a, having a higher yield stress than Case 3b predicts higher horizontal and vertical forces. Case 3b, which has a circular yield surface tangent to the Tresca yield surface at plane strain conditions, predicts very close traces of both horizontal and vertical keel reaction forces. This suggests that the elements yielding plastically are doing so under conditions closer to plane strain, rather than under triaxial compression. In any event, the Case 3a force predictions are relatively conservative, albeit by a small amount of about 10% or less.

Based on these findings, either assumption is valid, as some cases of ice gouging, depending on the keel angle, width and geometry may be more towards either plane strain or triaxial compression conditions. The conservative approach in terms of predicting gouge forces is certainly the von Mises failure surface assuming that the yield stress is defined by matching the Tresca hexagon in triaxial compression.

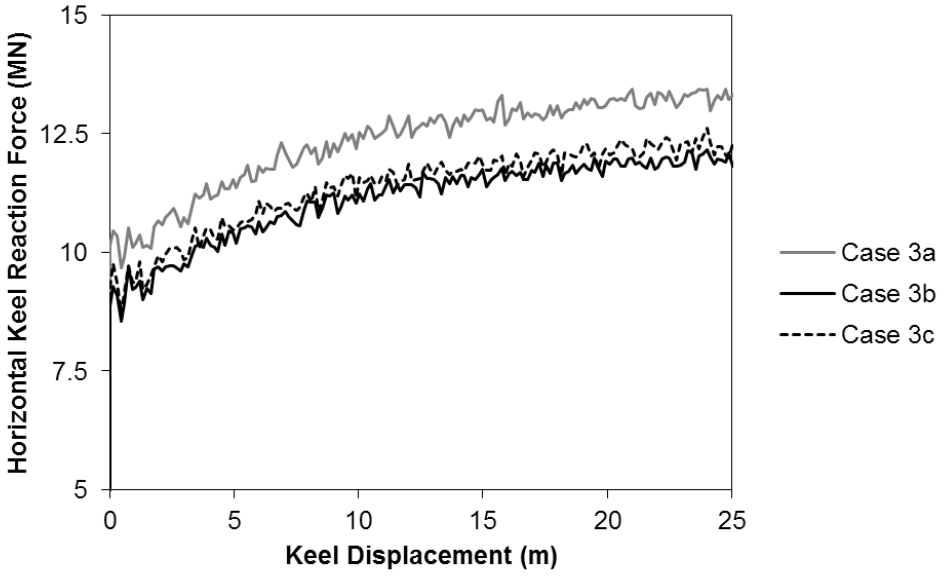

Figure 6.7. Undrained constitutive model effect on horizontal keel reaction forces

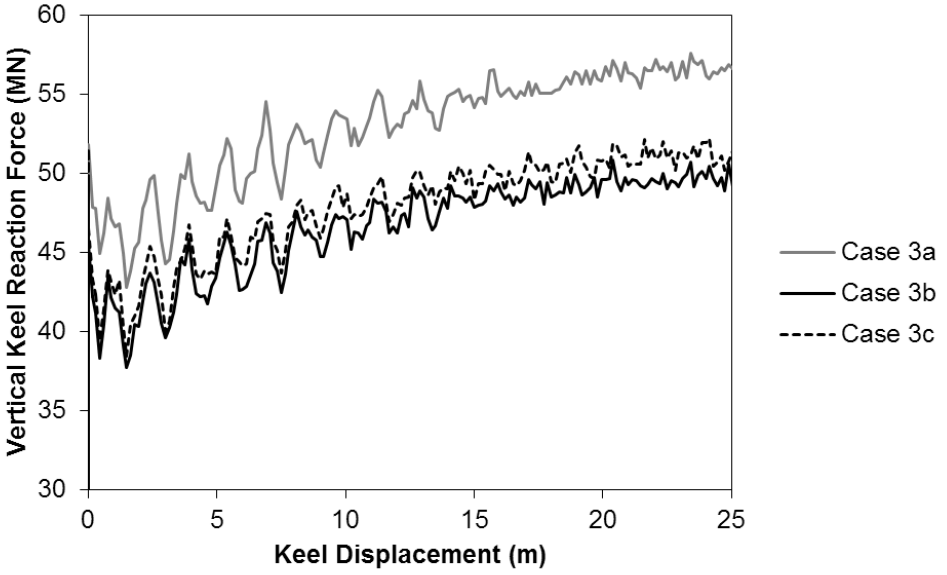

Figure 6.8. Undrained constitutive model effect on vertical keel reaction forces

6.1.3 Verification of Free Field Ice Gouge Analysis

The previous sections dealt with the mesh sensitivity and influence of the undrained constitutive model on the keel reaction forces and horizontal subgouge deformation. This section verifies the numerical tools by comparison with test data from centrifuge scale ice gouge tests conducted by Lach (1996), as described in Section 2.2.1. Lach's (1996) study represents a publicly available dataset providing sufficient experimental input and output data as a basis to verify finite element modelling procedures simulating free-field ice gouge events in cohesive soil. On this basis, the following describes the present study verification and parametric analysis.

In these tests, the "model iceberg" was represented by a rigid body with kinematic freedom to heave and pitch. Test 05 (of 9) was stated as a baseline case to which the effect of soil state, keel angle, width, and buoyant weight of the model iceberg were compared. The 10 m wide model iceberg in test 05 achieved a steady-state gouge depth of 1.21 m. It was deemed that the modelled gouge event was sufficiently rapid for essentially undrained conditions to prevail (Lach et al., 1993).

The s_u and OCR profiles with depth during testing were provided (Figure 6.9) and shown to be similar to Beaufort Sea clays. The OCR profile was achieved by applying a preconsolidation stress to the sample resulting in high overconsolidation in the upper third of the prepared soil bed.

The CEL finite element method described in Section 4.2 was used in developing a prototype numerical model of Test 05 mentioned above. The dimensions of the centrifuge test were scaled accordingly to develop a numerical test bed and model keel at prototype

scale (1.8 m deep, 20 m wide, 60 m long). The keel had an attack angle of 15°, was 10 m wide in the transverse gouge direction and its length at the base was 5 m. The keel was modelled as a rigid indenter fixed in all degrees of freedom but the gouge direction. The indenter was pushed through the soil at a prescribed gouge depth pertaining to steady-state conditions in the centrifuge experiment.

6.1.3.1 Sensitivity Study

A sensitivity study (see Table 6.3) was conducted to examine the influence of the soil constitutive model enhancement described in Section 3.1.1 (varying undrained shear strength and stiffness profiles) on the subgouge soil deformation field and global keel reaction forces. In each of the 10 cases, the circular von Mises failure surface was assumed. Initial cases (1 to 4) were conducted with a constant undrained shear strength corresponding to s_u at the steady-state gouge depth; $s_u \approx 20$ kPa at 1.2 m depth. Cases 1 to 4 varied the elastic modulus ($E = 100\ s_u$ to $300\ s_u$) and interface shear stress limit ($\tau_{max} = 0.5\ s_u$ to $1.0\ s_u$).

Cases 5 to 7 utilized the varying strength and stiffness profile consistent with the in-situ values provided by Lach (1996). In these cases the variable yield stress was based on the von Mises yield stress criterion ($\sqrt{3}\ s_u$). The elastic modulus is varied based on the approach described in Section 3.1.1. The interface shear stress limit was varied from $\tau_{max} = 0.5\ s_u$ to $1.0\ s_u$ and was deactivated in Case 7 where a smooth friction coefficient $\mu = 0.1$ was assumed. Cases 8 to 10 followed similarly, except with the yield stress defined by $\sigma_y = 2\ s_u$. The undrained shear strength and yield stress profiles corresponding to cases 5 to 10 are shown in Figure 6.9.

Table 6.3. Free-field ice gouging constitutive model sensitivity study

Case	Undrained Shear Strength, s_u (kPa)	Yield Stress, σ_y (kPa)	Elastic Modulus, E (kPa)	Interface Shear Stress Limit, τ_{max} (kPa)
1	20.0 (Approx. value at 1.2 m gouge depth level)	$\sqrt{3}*s_u$	$100*s_u$	10.0 (0.5 s_u at 1.2 m gouge depth level)
2	20.0	$\sqrt{3}*s_u$	$100*s_u$	20.0
3	20.0	$\sqrt{3}*s_u$	$300*s_u$	10.0
4	20.0	$\sqrt{3}*s_u$	$300*s_u$	20.0
5	Varying	$\sqrt{3}*s_u$	Varying	10.0
6	Varying	$\sqrt{3}*s_u$	Varying	20.0
7	Varying	$\sqrt{3}*s_u$	Varying	OFF ($\mu = 0.1$)
8	Varying	$2*s_u$	Varying	10.0
9	Varying	$2*s_u$	Varying	20.0
10	Varying	$2*s_u$	Varying	OFF ($\mu = 0.1$)

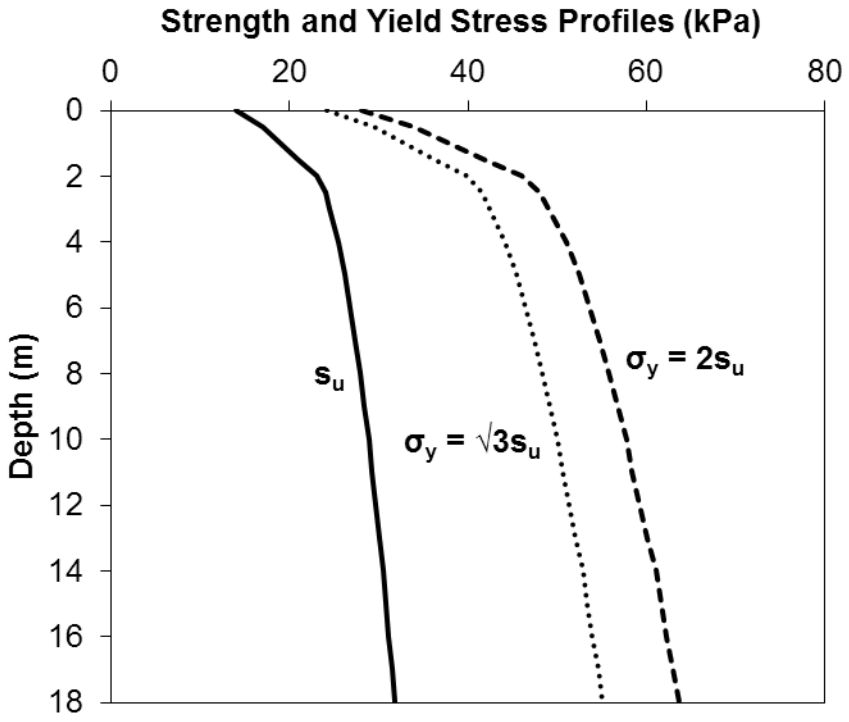

Figure 6.9. Varying undrained shear strength and assumed yield stress profiles

6.1.3.2 Subgouge Soil Deformation

The horizontal and vertical subgouge soil displacements for Cases 1 through 10 above are presented in Figure 6.10 and Figure 6.11. The results are presented in terms of soil displacement in the gouge direction versus normalized depth below the base of the gouging feature, i.e. the depth below the base of the gouge divided by the gouge depth. The numerical results are compared against Lach's (1996) test data and the PRISE engineering equation.

The horizontal subgouge soil deformation is over-predicted for Cases 1 to 4 assuming uniform strength and stiffness. Cases 3 and 4 with increased stiffness show

increased horizontal subgouge soil deformation. Cases 2 and 4 exhibit a tendency to drag the soil in the gouge direction due to the increased keel/soil interface shear stress limit compared to Cases 1 and 3.

Since the constant strength profile does not account for the increase in stiffness and strength with depth, the deformations are larger and fail to attenuate with depth as rapidly in comparison with the varying strength property profile. This demonstrates the importance of incorporating realistic soil profiles with depth (E, s_u) in order to reduce conservatism in the subgouge soil deformation predictions.

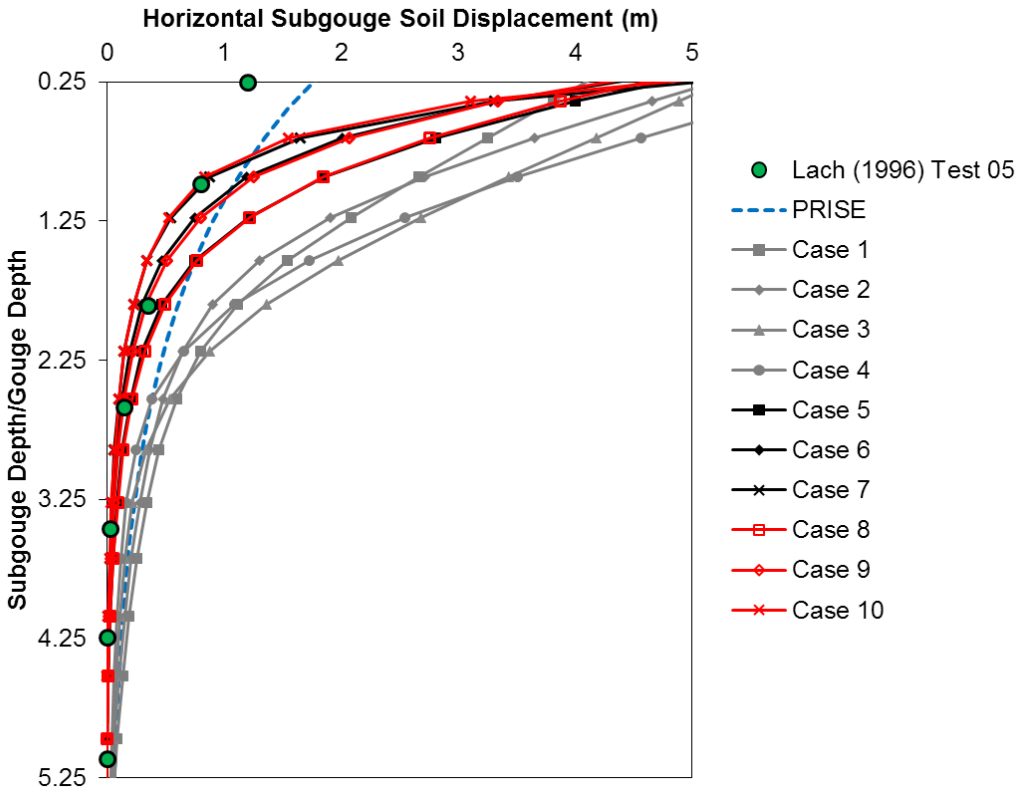

Figure 6.10. Comparison of horizontal subgouge soil deformations

The horizontal subgouge soil deformation is improved when a varying strength profile is considered. It is interesting to note that corresponding pairs of cases (5 and 8, 6 and 9, 7 and 10) show nearly identical traces of subgouge soil deformation, even though the yield stress is 15% higher for cases 8 to 10. Since the stiffness profiles are consistent, the variation in the response is caused by the assumed interface properties. The predicted horizontal subgouge soil displacement profile is improved when the shear stress limit is equal to the shear stress at the gouge depth, and when a smooth interface is assumed.

The agreement between the numerical and centrifuge test data tends to diverge at one gouge depth beneath the base of the keel. This may be explained by a shift from a continuum mechanical response to a localized zone of high shear that is difficult to capture with the current mesh resolution, and constant strain element formulation that causes difficulty in capturing sharp strain gradients. Furthermore, without limiting the tensile capacity in the soil plasticity model, the berms formed during the soil clearing process are higher than observed in the physical tests. This may lead to increased overburden pressure on the soil in front of the keel that can influence the horizontal subgouge soil deformation.

The vertical subgouge soil deformations are shown to follow a similar trend as the test data, but are under-predicted by both the varying and constant shear and stiffness profiles. This response is consistent with that of other researchers (e.g. Phillips and Barrett, 2010). The mismatch on the vertical displacement may be partially related to the assumed elastic constitutive model parameters that simulate incompressible behavior; i.e. the lack of volume change prevents the elements from compressing under the vertical

keel forces. The issue of vertical subgouge soil deformations remains an open area for further development, as current best practice does not apply vertical subgouge soil deformations in structural models for design against ice gouging, which was discussed by Fleet (2000).

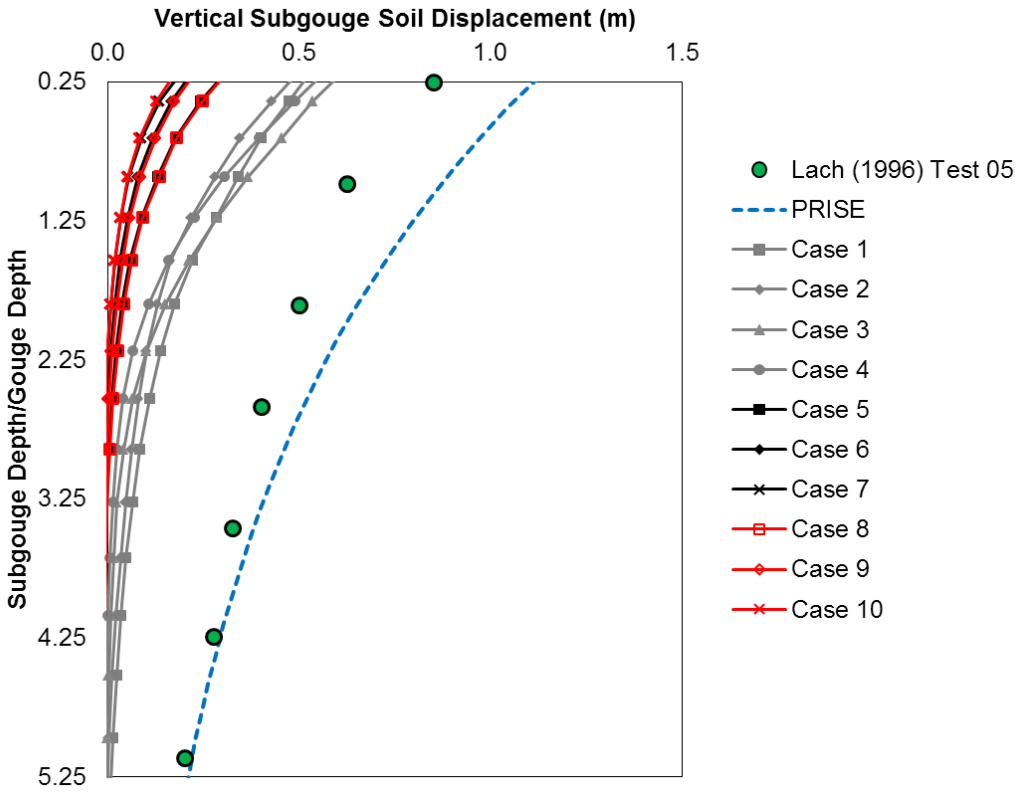

Figure 6.11. Comparison of vertical subgouge soil deformations

Studies using continuum FE modelling have shown the pipe trajectory involves coupled nonlinear horizontal and vertical movements, with rebound after the keel has passed (e.g. Pike et al., 2011b; Konuk and Yu, 2013). Questions remain on the

simultaneous application of free-field vertical and horizontal soil deformations in the structural analysis. The resultant subgouge soil deformation vector based on horizontal and vertical subgouge deformations does not comply with the observed pipe trajectory in the coupled numerical simulation.

6.1.3.3 Keel Reaction Forces

For each analysis case summarized above, the numerically predicted steady-state horizontal and vertical keel reaction forces were normalized against the experimental values (gouge depth = 1.2 m); the results are plotted in Figure 6.12 and Figure 6.13. The following outlines some important observations from this sensitivity study:

- the horizontal and vertical reaction forces exhibit strong dependency on the interface shear stress limit.
- with constant s_u, the horizontal and vertical keel reaction forces increase with E;
- Cases 1 to 4 with constant s_u under-predict the horizontal and vertical gouge force;
- the varying yield stress profile assuming $\sigma_y = 2s_u$ provides improved predictions of the horizontal and vertical reaction forces compared to the varying strength profile with $\sigma_y = \sqrt{3}s_u$, and compared to the constant strength cases;
- the interface shear stress limit τ_{max} = 20 kPa (s_u at gouge depth level) provides improved prediction of the horizontal and vertical reaction forces, in comparison to τ_{max} = 10 kPa (0.5 s_u at gouge depth level);
- increasing τ_{max} increases horizontal force but decreases vertical force;
- increasing yield stress increases the horizontal and vertical reaction force when comparing Case 5 and 8, 6 and 9, 7 and 10.

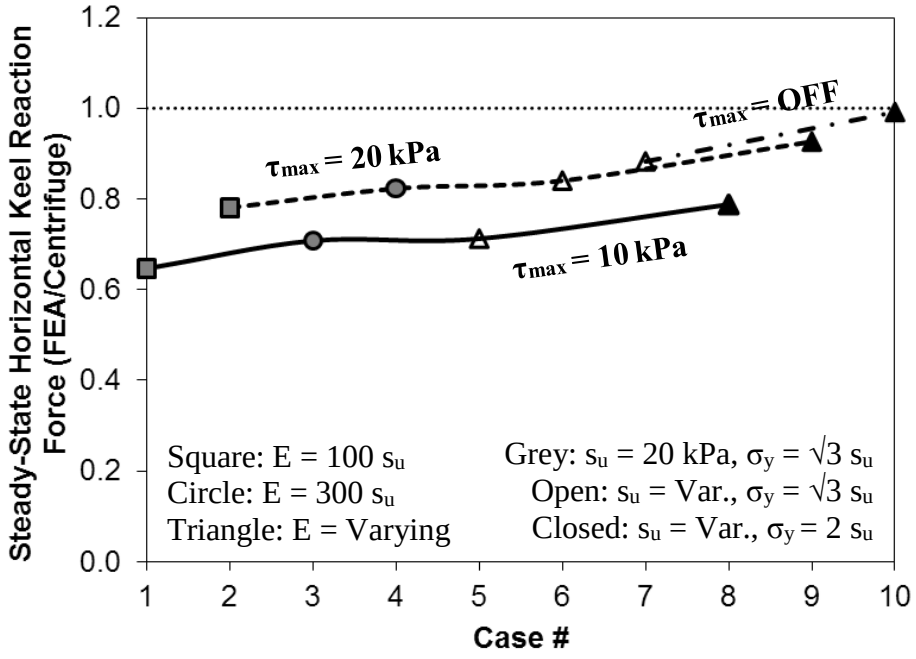

Figure 6.12. Comparison of global horizontal keel reaction forces

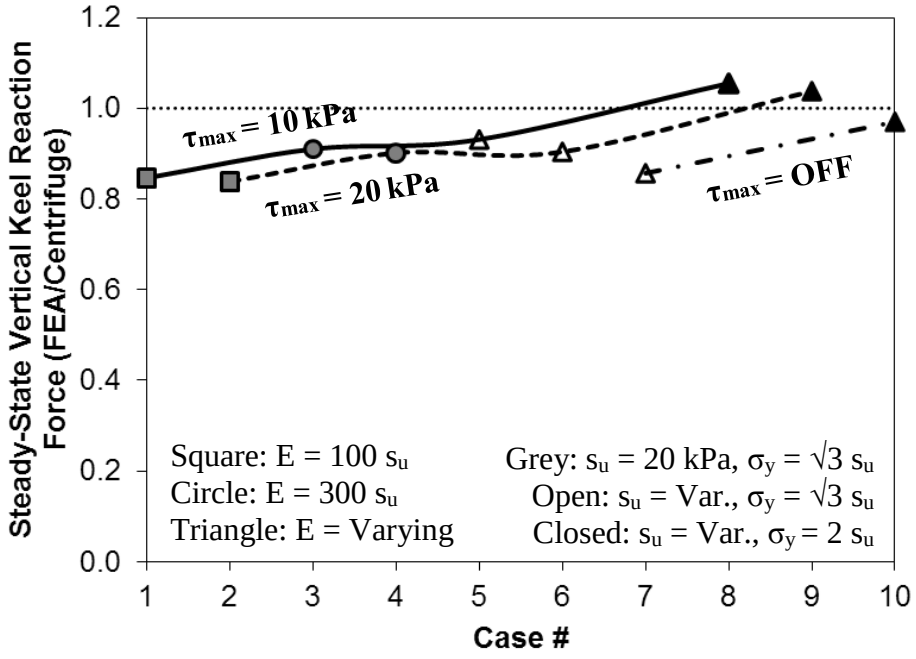

Figure 6.13. Comparison of global vertical keel reaction forces

6.1.3.4 Soil Berm Development

During the gouge process, the soil clearing mechanisms produce a frontal mound and side berms as illustrated in Figure 6.15. Based on centrifuge test data, the berm height as a ratio of gouge depth is shown to decrease with the gouge depth to gouge width ratio (Figure 6.14). Consistent with the present study, Rossiter and Kenny (2012) showed that numerical ice gouge simulations of centrifuge tests in clay resulted in berm heights that were approximately three (3) times higher than the experimental results.

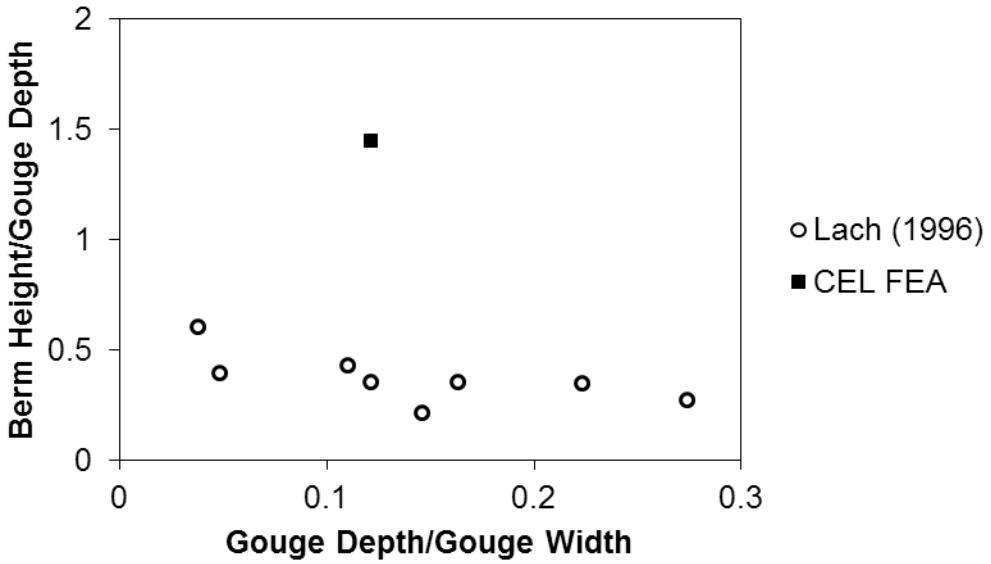

Figure 6.14. Berm height/gouge depth vs. gouge depth/gouge width in clay

This discrepancy may be due to the constitutive model used to approximate undrained clay behaviour. The von Mises failure surface is appropriate for compressive loading; however, it can significantly overestimate the load carrying capacity in tension,

as the tensile stress state was not limited in the CEL model. Given that tensile stresses can develop in the soil as the gouge clearing mechanisms push soil upwards and to the side, it is not surprising that numerical predictions of side berm and frontal mound height are larger than the experimentally observed values. This numerical phenomenon leading to higher predicted berm heights than large-scale physical test results was also observed by Peek et al. (2013).

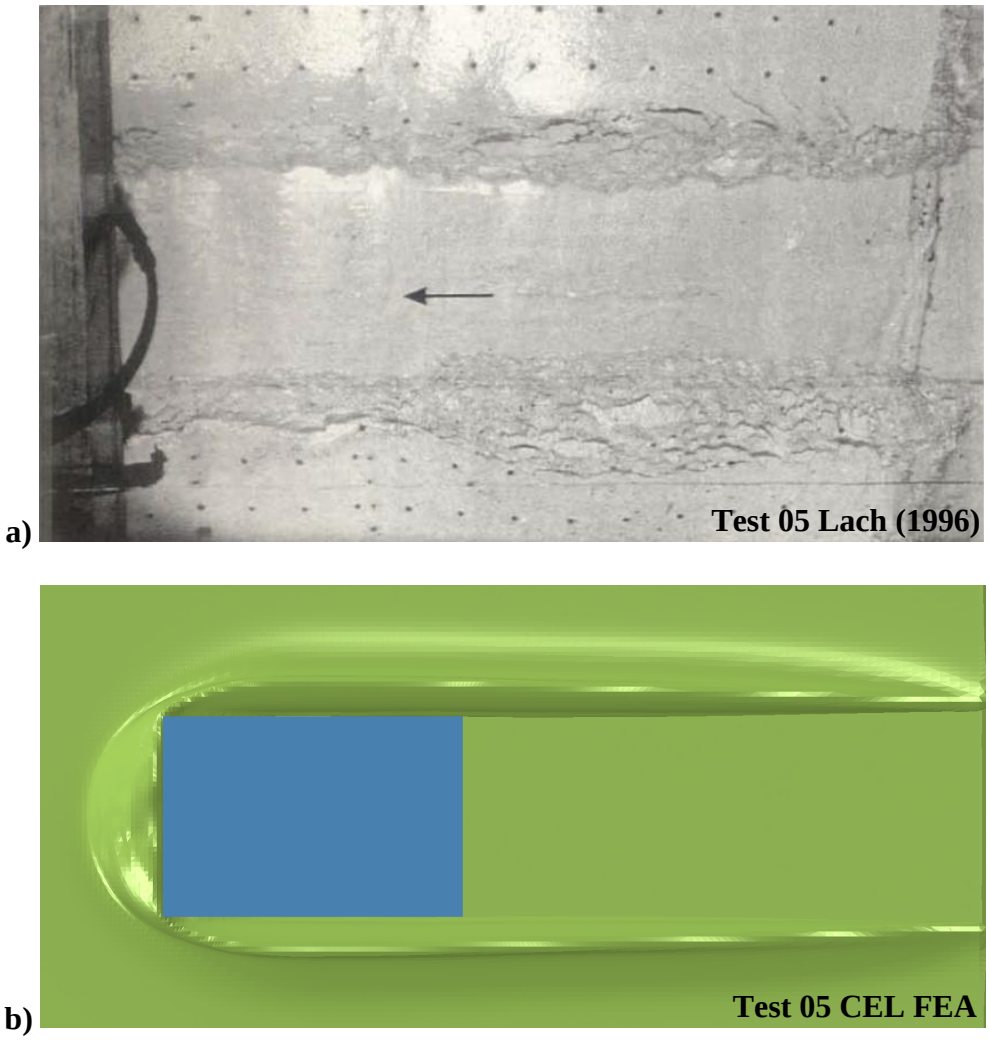

Figure 6.15. Experimental and numerical soil berm development

6.1.4 Effect of Ice Keel Shape on Subgouge Soil Deformation

This section describes a numerical study assessing the effect of keel shape on subgouge soil deformations. The importance of keel shape on soil resistance was recognized by Abdelnour et al. (1981) and later examined further by Prasad (1985) in a modelling study on the effect of varying keel shapes on soil resistance in sand. The former used inverted pyramid and rectangular prismatic shapes while the latter used shapes that examined keel angle and keel curvature in plan and profile views of the keel. The effect of keel angle has been studied in detail and in general it has been shown that with decreasing angle from horizontal, vertical forces increase and there is greater subduction of soil displacements.

The majority of physical centrifuge testing of the ice gouge process in clay has been carried out using prismatic indenters with 15°, 30° and 45° attack angles (e.g. Woodworth-Lynas et al, 1996; Lach, 1996; Schoonbeek & Allersma, 2006). Timco & Burden (1997) stated an average keel angle of 26.6° with a standard deviation of 13.4° based on seventy measurements of first-year ice ridges. Kovacs & Mellor (1974) state an average keel angle of 33° for first-year ridges. Hence, the aforementioned model studies are in the appropriate range with respect to average keel angle. It is prudent to question however, if the average keel angle is representative of the local keel area in contact with the seabed. Wright et al. (1981) investigated the geometry of eleven multi-year ridges or ridge fragments and provided cross sectional shape profiles. The irregular and stepped nature of keel shapes is apparent. Not to detract from the generation of average keel shapes for use in certain study areas (e.g. global stability analysis), however, for ice

gouging analysis, the chosen keel angle and shape should reflect the part of the gouging feature that is in contact with the seabed.

Based on results obtained using an analytical ice keel (inclined plate)-soil interaction model, Croasdale et al. (2005) arrived at several notable conclusions. With regards to shape effect, it is established that steeper keels (greater angle from horizontal) produce deeper gouges. In addition, it is discussed that conventional practice for designing pipelines against subgouge soil deformations is very conservative, as subgouge soil deformations are derived from tests on very shallow keels (Croasdale et al., 2005). Hence, the semi-empirical subgouge soil deformation calculated for the extreme gouge event, may not coincide with the subgouge deformations produced by the keel that is responsible for the event.

Recent laboratory experiments examining the effect of object geometry on penetration into the seabed support the fact that steeper keels penetrate deeper into the seabed (Ivanovic et al., 2010). The local curvature of the gouging keel perpendicular to the gouge direction was also shown to be of importance. In the case of a rectangular prism (i.e. 90 degree attack angle) with a sharp edge versus a chamfered edge, the sharp edge penetrated deeper into the soil, while the curved edge allowed the soil to flow under the object thus reducing the penetration. With shallow global keel attack angles, the soil is pushed forward and compressed vertically causing large vertical reaction forces that act against downward gouging (Ivanovic et al., 2010). A detailed discussion on subgouge failure mechanisms for 15° and 30° keel angles is provided by Kenny et al. (2007). The

effects of keel angle on subgouge soil deformations are discernible and the subsequent transfer effects to buried pipelines must be considered.

Building on previous numerical studies of the ice gouge process, Liferov et al. (2014) studied the factors influencing gouge depth, subgouge soil deformations and pipeline strain demand. Ice gouging simulations using a custom-developed code (Liferov et al., 2014) showed that ice ridges with steeper attack angles resulted in deeper gouges; with other parameters held constant, and the keel attack angle had the strongest correlation with the gouge depth. Furthermore, using ABAQUS/Explicit CEL to model the coupled ice keel/soil/pipeline interaction, Liferov et al. (2014) demonstrated that increasing the keel attack angle (i.e. steeper keel face) resulted in reduced pipe deformation and stress. Considering these effects together, possibly over-conservative parameter combinations should be avoided.

The key points from Liferov et al. (2014) echo the work by Croasdale et al. (2005) who emphasized the inherent conservatism in not accounting for the influence of keel attack angle on the gouge depth and subgouge soil deformation – given that current approaches are derived from 15° attack angle data. Croasdale et al. (2005) showed a linear increase in the gouge depth with attack angle; they did not directly address the effect on subgouge soil deformations. Physical tests conducted by Ivanovic et al. (2012) also demonstrate increased gouge ("penetration") depth with attack angle; studies by Kioka et al. (1998) exhibited the same trend. The work by Pike and Kenny (2012a) and Liferov et al. (2014) highlighted the effect of shallow vs. steep keel angles on subgouge soil deformation, showing that shallow keels produce greater subgouge soil deformations

to a greater vertical extent. This work has highlighted some important aspects of subgouge soil deformations that should be high priority for consideration in the ice gouge design process:

- The effects of keel attack angle on the formation of extreme gouges and subgouge soil deformations can have a significant impact on the predicted pipeline strain demand;
- Current empirical formulations are based on subgouge soil deformations resulting from shallow keel (mostly 15°) interactions with the seabed - however, it has been shown that steep keels are more likely to cause the extreme gouge events;
- Subgouge soil deformations have been shown to be more severe in terms of magnitude and vertical extent for shallow keels compared to steep keels at the same gouge depth;
- Assigning the same gouge depth for keels with varying attack angle is not justified as they likely have different occurrence probability.

In the present study, a sensitivity analysis was conducted to assess the effects of keel shape in the gouge and transverse gouge directions. The soil properties, and ice/soil interface behavior are consistent with Case 10 above in Section 6.1.3.1 for the comparison study against Lach (1996). The analyzed shapes in Figure 6.16 were inspired by Prasad (1985) and Ivanovic et al. (2010). Each model keel was gouged through the seabed at a constant depth and width of about 1.2 m and 10 m, respectively, for a width to depth ratio of approximately 8.3. This also means a constant initial projected area of

about 12 m^2. The leftmost keel can be classified as a shallow angled keel at one extreme, while its neighbor, the rectangular prism, may be considered the steep extreme. The remaining keels from left to right were included to assess curvature effects in the gouge and transverse gouge directions, respectively.

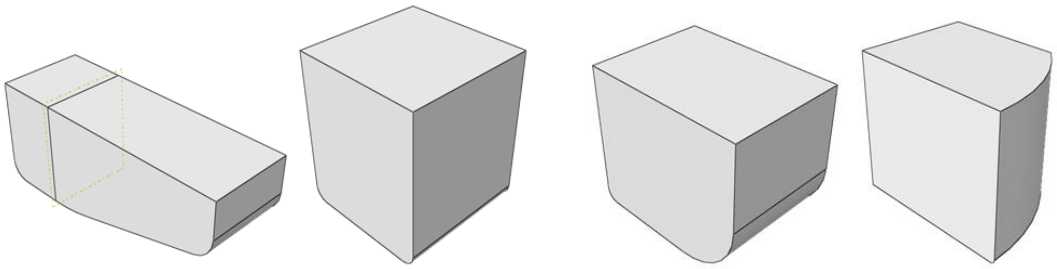

Figure 6.16. Analyzed keel shapes, from left to right: (a) shallow angle, (b) rectangular prism, (c) gouge curvature, and (d) transverse curvature

The relative effect that shallow and steep keels have on subgouge soil deformations is evident in Figure 6.17 (zero reflects the base gouge level). The shallow keel transmits soil displacements extending much deeper than the steep keel. In fact, the steep keel seems to cut through the soil, causing minimal disturbance to the subgouge sediments. The model keel with curvature in the transverse gouge direction exhibited similar centerline subgouge soil deformation; however, the relative ease of soil clearing mechanisms reduced horizontal forces and the lateral extent of subgouge deformations. As expected, the model keel with curvature in the gouge direction acted to partially compress the soil causing subgouge soil deformations to extend deeper than the rectangular prism keel.

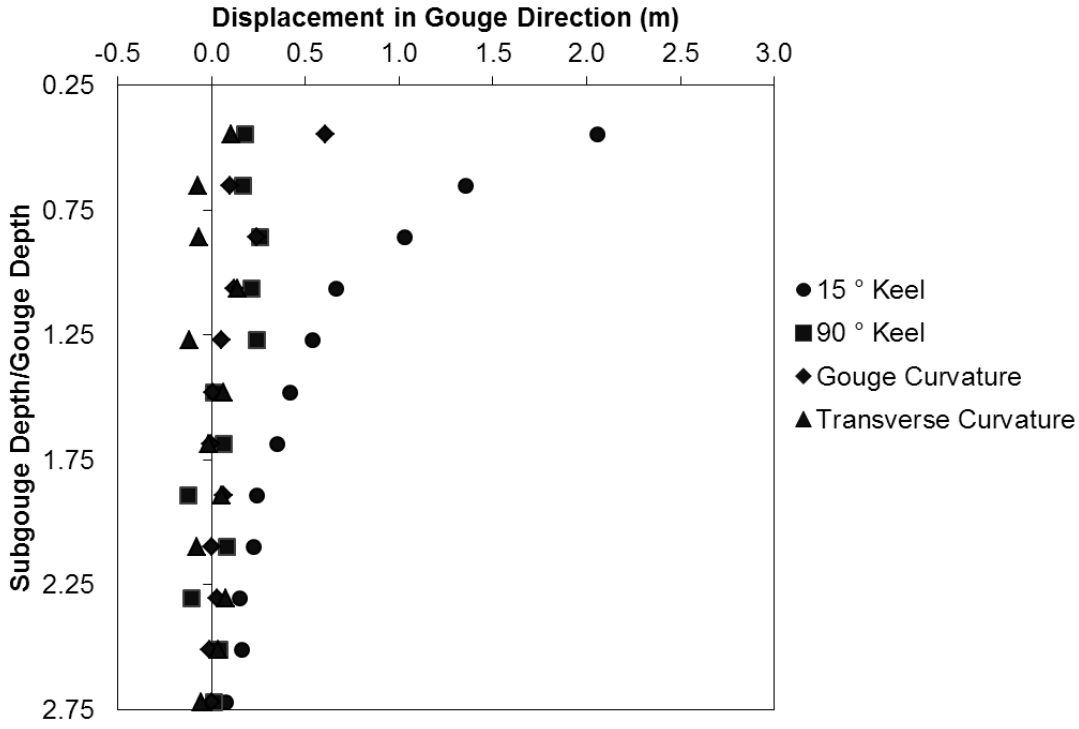

Figure 6.17. Shallow and steep keel induced subgouge soil displacements

6.1.5 Effect of Geotechnical Properties on Subgouge Soil Deformation

Extreme gouges are heavily concentrated on the Western Central region of the Canadian Beaufort shelf in comparison to the Eastern Central shelf where there is a change in surficial sediment from clay to sandier sediments, respectively. The majority of new extreme scours occur in surficial sediment type clay and it is indicated that ice keels can easily penetrate soft recent marine sediments, but do not gouge more competent underlying layers (Blasco et al., 2011). This relationship with softer sediments was also discussed by previous researchers (Kovacs & Mellor, 1974; Shearer & Blasco, 1986). For a similar water depth and ice regime, the former indicated that the maximum

concentration of seabed gouges are found where the sediments are soft and areas found not gouged were areas where the sub-bottom record indicated a hard, reflective bottom with no sub-bottom return suggesting the existence of coarse-grained material.

Crooks et al. (1986) provided an average undrained shear strength profile for recent Beaufort Sea clays that projected zero strength at the mudline with a linear increase in strength with depth of 6 kPa/m. Using data provided by Crooks et al. (2007) and Rogers et al. (1993), constitutive models were developed for the Amauligak F24 and Tarsiut P45 sites in order to assess the effects of varying soil profiles on the ice gouging process. The varying soil profiles (Figure 6.18) were input to the baseline numerical prototype of Test 05 described above and the results were compared.

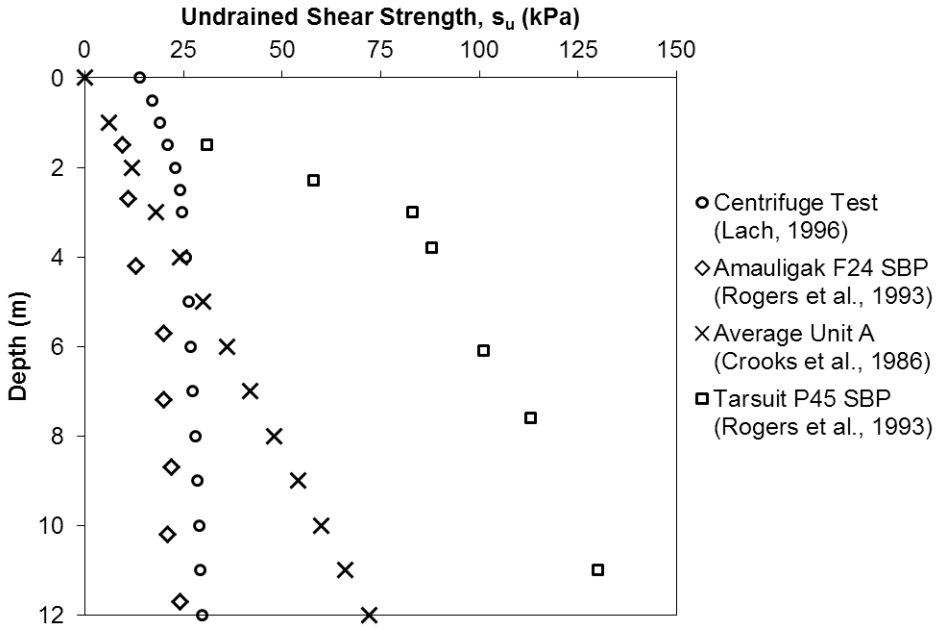

Figure 6.18. Undrained shear strength profiles of some Beaufort Sea clays

As illustrated in Figure 6.19, the very weak soils in the upper layer of the Amauligak profile are compressed and sheared relatively easily in comparison with the somewhat stiffer soils characteristic of the Test 05 profile. On the other hand, the Tarsiut soil profile which reaches high strengths quickly has the effect of extending the soil deformation field deeper and further horizontally.

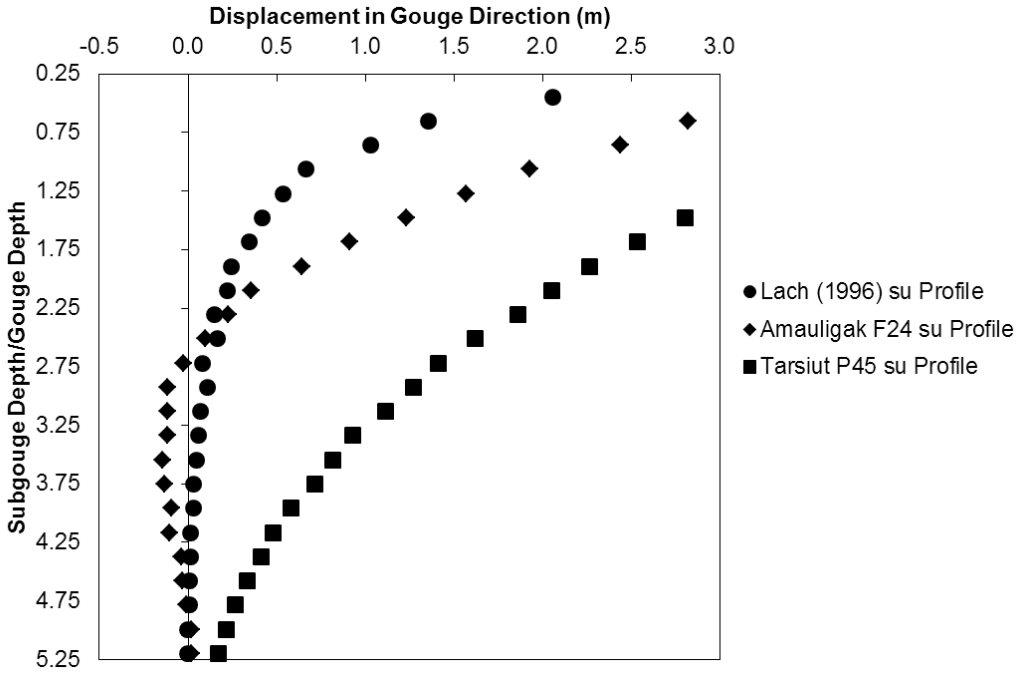

Figure 6.19. Effect of varying soil strength profiles on horizontal subgouge soil deformations

As discussed by Crooks et al. (2007), it is recognized that geotechnical properties vary across a site in any stratum. In the context of the design and installation of a buried pipeline, one might expect an even greater variation along its length. From the above discussions on the effects of keel shape and soil strength profile, it is evident that

subgouge soil deformations are very sensitive to these parameters. From an engineering design standpoint, these effects should be considered inside a framework that can account for the cross variance of parameters.

6.1.6 Summary

This Section has demonstrated the use of continuum finite element modelling to examine the effects of key parameters in the ice gouging process. Undrained shear strength and shear modulus profiles with depth were derived using known relationships with overconsolidation ration and plasticity index. The numerical model results of a baseline analysis were shown to compare against existing centrifuge data. The effect of ice keel shape on subgouge soil deformation was assessed. It was shown that steep (high attack angle) keels produce less severe subgouge soil deformations. The variability of soil strength profiles from marked sites in the Canadian Beaufort Sea was shown, and the effects of which were assessed numerically. As expected, soil strength profile has a significant effect on subgouge soil deformation fields.

A main outcome of this section is the enhancement of the constitutive model to capture the variation of undrained shear strength with depth to improve the simulated horizontal subgouge soil deformation response and keel reaction force prediction. A second, and very practical outcome that should be considered in pipeline design against ice gouging relates to the ice keel shape effect. The shape effect shows that gouge depth increases with keel attack angle (e.g. Ivanovic et al., 2010; Liferov et al., 2014), but vertical forces and the magnitude and extent of horizontal subgouge soil deformations decrease. This suggests that keels responsible for producing deeper gouges may not have

as large of an effect on the subgouge soil deformation field as anticipated from the PRISE engineering equations developed for shallow attack angles. The ice feature kinematic motion during gouging events was examined by Drover and Kenny (2012) for varying shapes of the ice feature.

6.2 Pipe/Soil Interaction in Cohesive Soil

6.2.1 Lateral Pipe/Soil Interaction

The lateral soil resistance against pipe movement is an important aspect of pipeline design against geohazards. For instance, in the decoupled structural analysis of pipeline response to subgouge soil deformations due to ice gouging, the ultimate lateral soil resistance limits the amount of force that can be transmitted to the pipeline (see Section 6.3.3). This section describes CEL FE modelling of lateral buried pipe/soil interaction in cohesive soil. The objectives are to address the required mesh density to obtain convergence in the force-displacement response, examine the influence of burial depth on the force-displacement response and soil failure mechanisms, and compare the numerical results against existing data and guideline recommendations.

6.2.1.1 Mesh Sensitivity

As discussed above, the Eulerian-Lagrangian contact interface is automatically tracked using an enhanced immersed boundary method (Abaqus, 2016). As suggested by Abaqus (2016), a rectangular grid of elements was used in the present study to determine the required mesh size to maintain adequate resolution of the pipe/soil contact interface and provide convergence for the soil reaction force-pipe displacement response. The

mesh sensitivity study summarized in Table 6.4 was conducted for pipe/soil interaction in clay. The analyses were conducted on a standard desktop machine using 4 cpus.

The pipeline diameter is D = 0.95 m and the burial depth ratio H/D = 2. The total unit weight was taken as 17.5 kN/m^3 and the undrained shear strength is assumed s_u = 45 kPa. The elastic regime was defined by E = 300 s_u and ν = 0.499. The Tresca yield criterion is used with a von Mises (circular) failure surface. The effect of the assumed undrained constitutive model (Section 3.1) is examined in the following subsection. The pipeline/soil interface contact was modelled using the general contact option available in ABAQUS/Explicit. Surface based contact was enforced using the Coulomb friction model, with a friction coefficient of 1.0 and maximum interface shear stress, τ_{max}, equal to half the undrained shear strength.

Table 6.4. Mesh sensitivity analyses for lateral pipe/soil interaction in clay

Case	Eulerian Mesh Size (m)	s_u (kPa)	Yield Stress (kPa)	Failure Surface	Run Time
1	0.095 (D/10)	45	2 s_u	von Mises	13 min.
2	0.1425 (D/6.67)	45	2 s_u	von Mises	7 min.
3	0.19 (D/5)	45	2 s_u	von Mises	5 min.

The characteristic mesh size ranges from 1/10 to 1/5 of the outer pipe diameter. The 3D Eulerian elements were cube shaped and extended one element into the page. Figure 6.20 shows a profile view of the buried pipe, the initial soil volume, the initial void

space, and the mesh discretization for Cases 1 and 3. The analysis run time for Case 1 (4 CPUs on a standard desktop computer) was about 13 minutes.

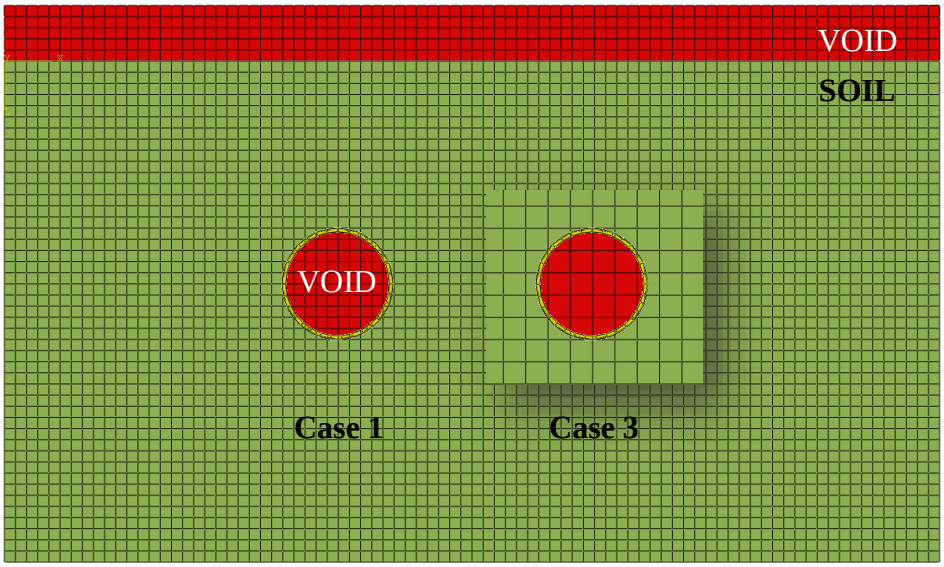

Figure 6.20. Case 1 mesh size schematic

Given the short analysis time, and Abaqus' recommendation for a simple rectangular grid of elements, optimization of the mesh design that may incorporate biased mesh size away from the soil/pipe boundary was not conducted for these cases. However, for pipe/soil contact within a larger multibody interaction model (e.g. ice/soil/pipieline interaction) requiring considerably larger soil volume, mesh optimization is important to minimize analysis run times that can quickly become days, instead of minutes. This is considered in the following Section 6.3.

Figure 6.22 shows the force-displacement response for each analysis case. There is a stark contrast in the response between Cases 1 and 3. Case 3 predicts very unstable

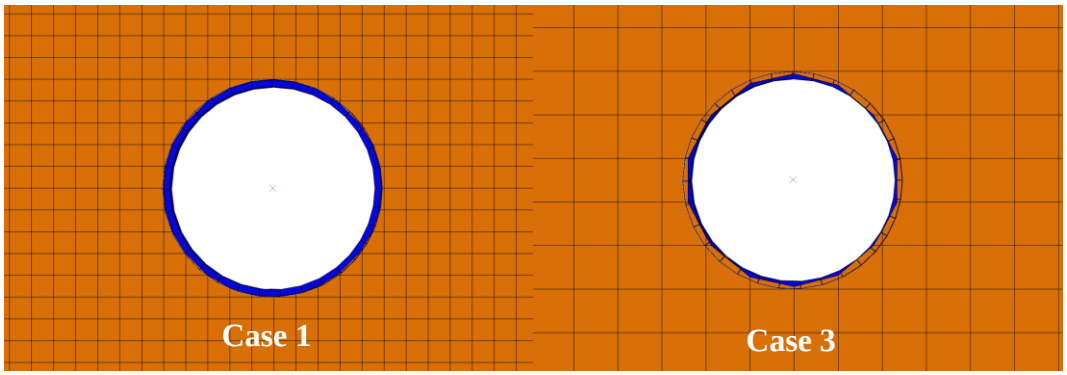

Figure 6.21. Initial resolution of pipe/soil contact interface

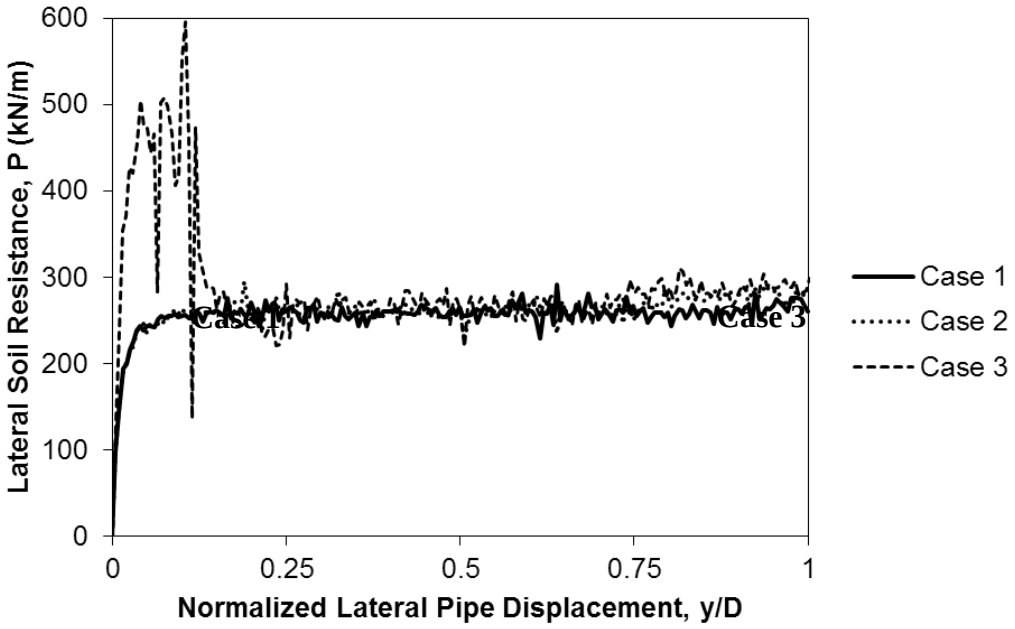

Figure 6.22. Mesh size effect on lateral pipe/soil interaction force-displacement response

behaviour before 0.25D pipe displacement. This is related to the initially tracked contact interface for Case 3 that does not adequately define the interface boundaries, as shown in Figure 6.21. In comparison, Case 1 shows clear definition of the contact boundary and

provides a relatively smooth response. The significant instability in Case 3 is related to the predictor-correction algorithm in the penalty stiffness method whereby the penalty spring stiffness is trying to self-correct to overcome the predicted overclosure.

6.2.1.2 Effect of Undrained Cohesive Constitutive Model

As discussed in Section 3.1, total stress analysis for undrained cohesive soil behaviour can be implemented using the Tresca or von Mises failure surface. For the von Mises failure surface, the yield stress is constant (independent of the polar angle in the deviatoric plane), and the choice of yield stress is up to the analyst depending on the governing stress path leading to shear failure (triaxial compression or plane strain). In any event, the yield stress will be a maximum of about 15% higher if the circumscribed (matching triaxial compression) von Mises failure surface is chosen.

Table 6.5. Analyses to test effect of constitutive model on lateral pipe/soil interaction

Case	Yield Stress	Yield Surface	Run Time
1a	$\sigma_y = 2s_u$	Circular von Mises	13 min.
1b	$\sigma_y = \sqrt{3}s_u$	Circular von Mises	13 min.
1c	$c' = s_u$	Hexagonal Tresca	16 min.

A sensitivity study was conducted to test the three potential methods discussed in Section 3.1, as summarized in Table 6.5. Case 1a matches the Case 1 analysis in the previous Section 6.2.1.1; Case 1b tests the plane strain yield stress assumption with the

von Mises failure surface, while Case 1c uses the hexagonal yield surface (Mohr-Coulomb with $\phi = 0$ conditions) with the effective cohesion intercept set equal to s_u.

The analysis shows that Case 1a predicts peak lateral soil resistance about 9% higher than Case 1b and 1c (Figure 6.23). Since plane strain boundary conditions are applied, the consistent response between Case 1b and 1c was expected, since the yield stress in Case 1b was based on matching the Tresca (hexagonal) yield surface in plane strain. It is interesting to note that while the maximum yield stress difference between Case 1a and 1b is 15%, the Case 1a lateral soil resistance is only 9% higher.

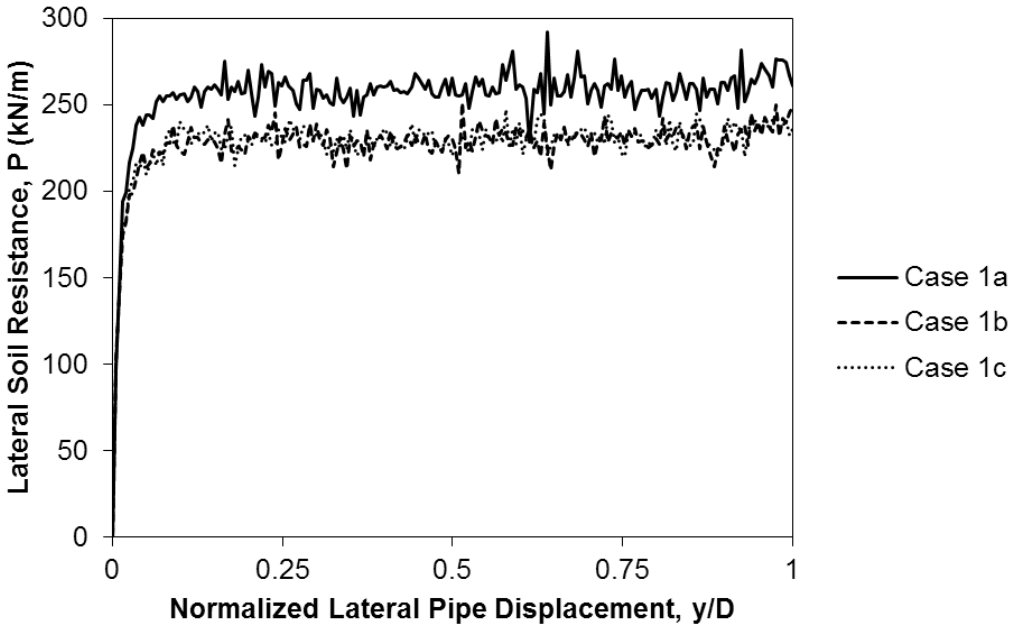

Figure 6.23. Undrained constitutive model effect on lateral pipe/soil interaction force-displacement response

6.2.1.3 Effect of Burial Depth Ratio

An FEA sensitivity study was conducted to evaluate the lateral interaction factor as a function of the pipe burial depth ratios (H/D = 1, 2, 3, 4, and 6), with other parameters (γ, D, s_u, E, ν) consistent with the previous analysis. The plane strain von Mises yield stress ($\sigma_y = \sqrt{3}\ s_u$) was used with the von Mises failure surface for each analysis with varying burial depth.

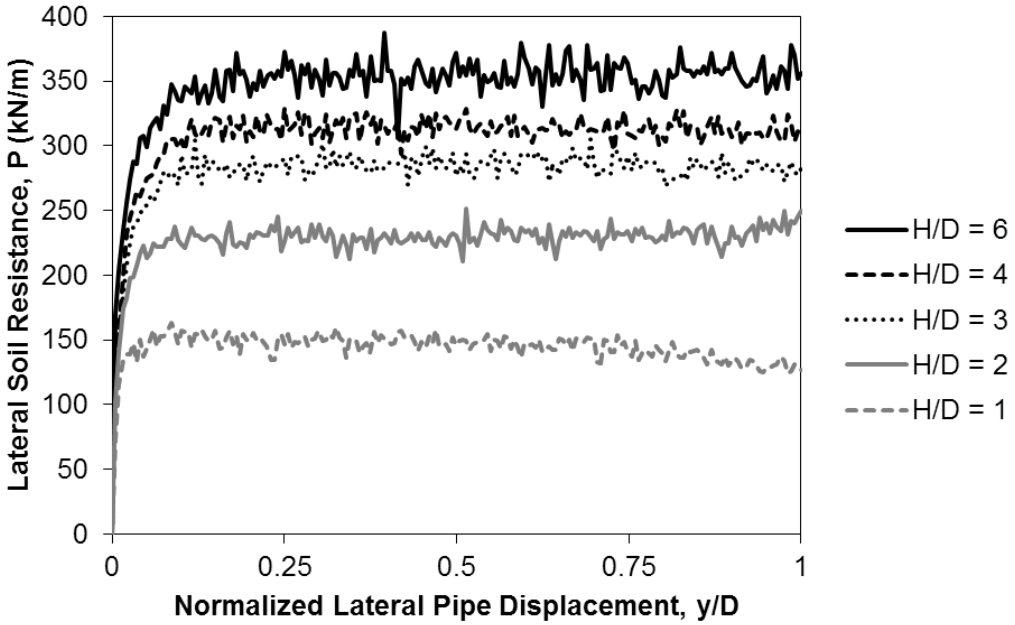

Figure 6.24. Lateral soil resistance vs. normalized pipe displacement

The resulting force-displacement curves provided in Figure 6.24 show increasing soil resistance proportional to H/D ratio. The relative increase in the maximum lateral resistance is high at shallow burial depths, compared to the deep cases where the force-displacement curves begin to converge at H/D = 4 to 6. Rowe and Davis (1982) found

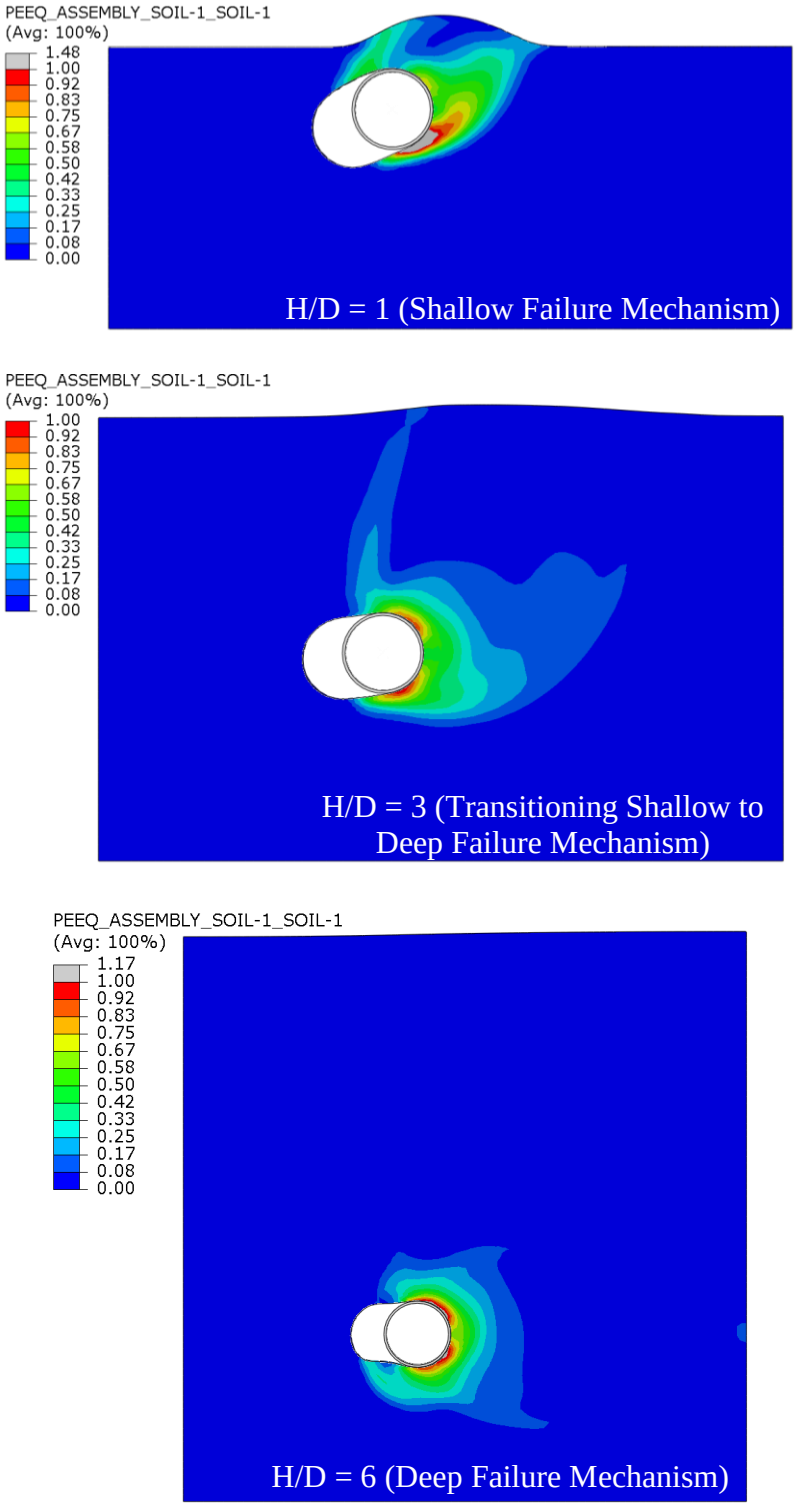

Figure 6.25. Failure mechanisms for lateral pipeline/soil interaction analysis with increasing H/D ratio

that the transition between shallow and deep failure mechanisms occurs at around H/D = 3 for vertical anchor plates buried and moved laterally in clay, in accordance with later studies by Phillips et al. (2004b) for pipe/soil interaction in clay.

Figure 6.25 shows the effect that increasing burial depth has on the soil failure mechanism. The equivalent plastic strain (PEEQ) contours are shown that represent the accumulated plastic soil strain. The resultant soil bulge protruding from the soil surface was significant for the shallow burial depth (H/D = 1) case, and became insignificant for H/D greater than 4. This was also apparent by examining the respective regions of high plastic strain; in the shallow case, the zone extends to the soil surface, whereas in the deeper case, the zone was focused concentrically around the pipeline. A decrease in upward movement of the pipeline was also observed with increasing burial depth due to the increase in soil weight above the pipeline.

In Figure 6.26, the basic results from this study were compared with the estimates of lateral interaction factor provided by Phillips et al. (2004a) using ABAQUS/Standard, and against Hansen's (1961) model as suggested by the ASCE (1984) and ALA (2001) guidelines. The curve generated using the recent PRCI (2009) guidelines that consider the passive wedge weight term was also plotted and agrees quite well with the numerical results of Phillips et al. (2004b) and the present study. The CEL analysis thus confirms the influence of the passive wedge weight term on the horizontal bearing capacity factor.

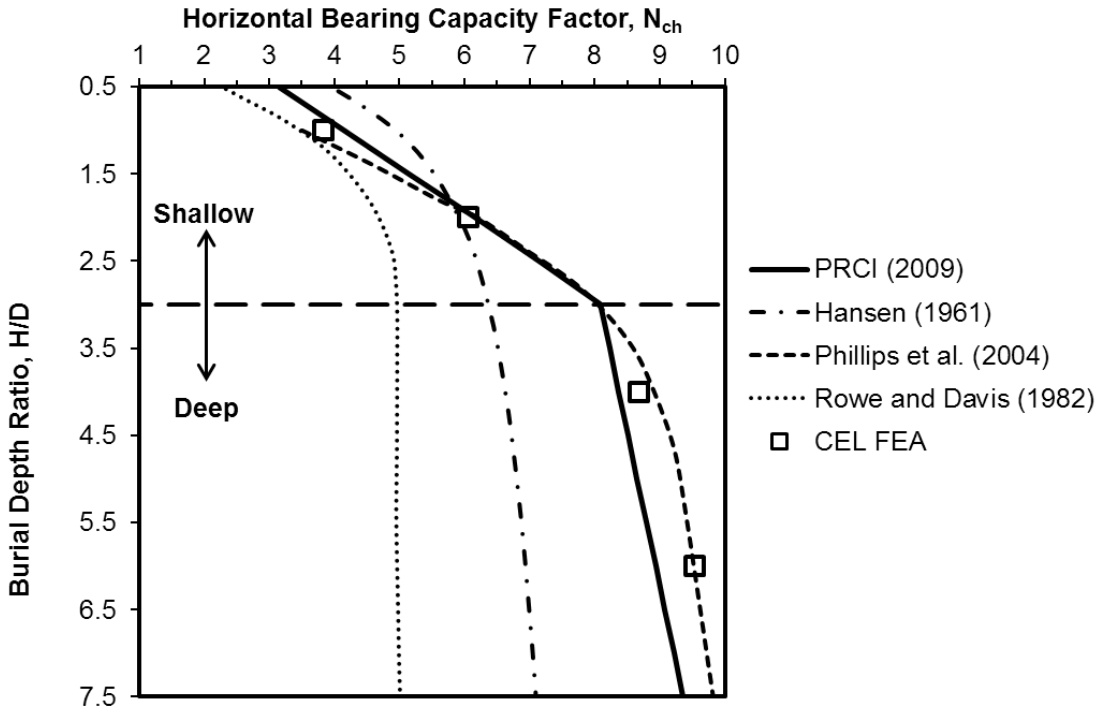

Figure 6.26. Estimate of horizontal bearing capacity factor as a function of H/D ratio

6.2.2 Oblique Lateral-Axial Pipe/Soil Interaction

An idealization in the orthogonal soil spring resistance curves applied in structural beam/spring models is decoupling such that three-dimensional effects such as shear load transfer between adjacent springs is ignored. However, structural models provide an efficient means to conduct engineering assessments and provide input to informed decision making (Seo et al., 2011). Current engineering practice for pipeline design against the ice gouge hazard applies only the horizontal subgouge soil displacement to the lateral soil springs (e.g. Figure 2.7). Based on this approach, the pipe mechanical response would be affected only by the lateral-axial coupling effect, as there would be no vertical

pipe movement. Hence, the present study focuses on addressing the coupled oblique lateral-axial soil resistance for undrained loading events in cohesive soil. The ABAQUS/Explicit ALE FE model for oblique lateral-axial pipe/soil interaction is introduced in Section 4.4.

6.2.2.1 Case Study

A study was conducted to assess the effect of oblique pipe movement in the lateral-axial plane on the axial and lateral bearing capacity factors. The burial depth ratio (ratio of depth to pipe springline to pipe diameter) was approximately 3.6 and the pipe diameter was 0.41 m (16 in.). The soil was assumed to be uniform undrained clay with medium strength and was modelled using an elastic-perfectly plastic von Mises failure surface with the yield stress defined by $\sigma_y = 2\ s_u$ (Section 3.1). An undrained shear strength, $s_u = 45$ kPa, was assumed. The elastic response was defined by a modulus ratio, $E/s_u = 100$, and Poisson's ratio, $\nu = 0.499$, to simulate incompressibility. The pipeline was moved in the lateral-axial plane at varying oblique angles from pure axial (0°), to pure lateral (90°). The finite element model is described in Section 4.4.

For undrained soil/structure interaction events, it is common to assume that an interface shear stress limit (τ_{max}) exists that is some fraction of s_u (e.g. Chatterjee, 2011). As local soil remoulding may occur at the pipe/soil interface, τ_{max} may be approximated by the remoulded undrained shear strength (s_{ur}) of the cohesive material. In this study, it is assumed that the interface shear stress limit equates to s_{ur}. Hence, in this context, soil sensitivity (S_t) is the ratio between the undrained shear strength and the interface shear stress limit, to simulate strength loss due to remolding at the interface. A friction

coefficient (μ) is also applied that defines the ratio of shear stress to normal stress before τ_{max} is reached. An interface friction coefficient, $\mu = 0.27$ was used, with $\tau_{max} = 0.5s_u$. The influence of the interface friction coefficient on the maximum axial load is examined through a sensitivity study described below.

6.2.2.2 Mesh Sensitivity Study

Since lateral pipeline deformations would impart the greatest demand on mesh distortion, a study was conducted to examine the effects of mesh density as well as mesh design, or initial mesh configuration on capturing the reaction forces due to large lateral pipeline movement. The fine mesh was characterized by 36 elements circumferentially in contact with the pipe, and was compared against the response with 24 elements. It was found that for the adaptive meshing algorithm it was not beneficial to increase the mesh density of the soil in a uniform fashion around the circumference initially in contact with the pipeline.

As shown in Figure 6.27, the elements belonging to the relatively fine uniform mesh are highly compressed. Correspondingly, in Figure 6.28 it is shown that the lateral reaction forces cannot be captured beyond about 0.6D. In comparison, the uniform medium mesh density incorporates an increased element length in the lateral direction. The improvement in predicting the lateral reaction force beyond 0.6D is seen in Figure 6.28. Alternatively, the mesh can be designed to accommodate lateral displacement, as depicted in Figure 6.27. Element compression is reduced and the lateral forces can be predicted through larger lateral displacement, per the accommodating mesh curve in Figure 6.28.

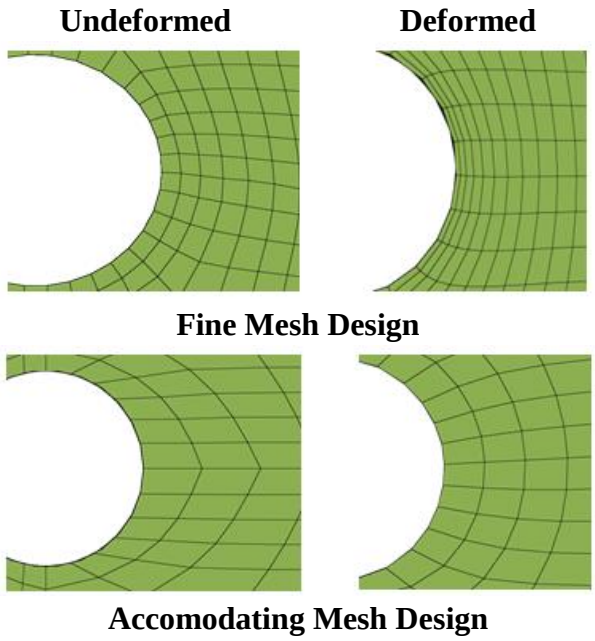

Figure 6.27. Effect of mesh design on adaptive mesh configuration after pipe displacement

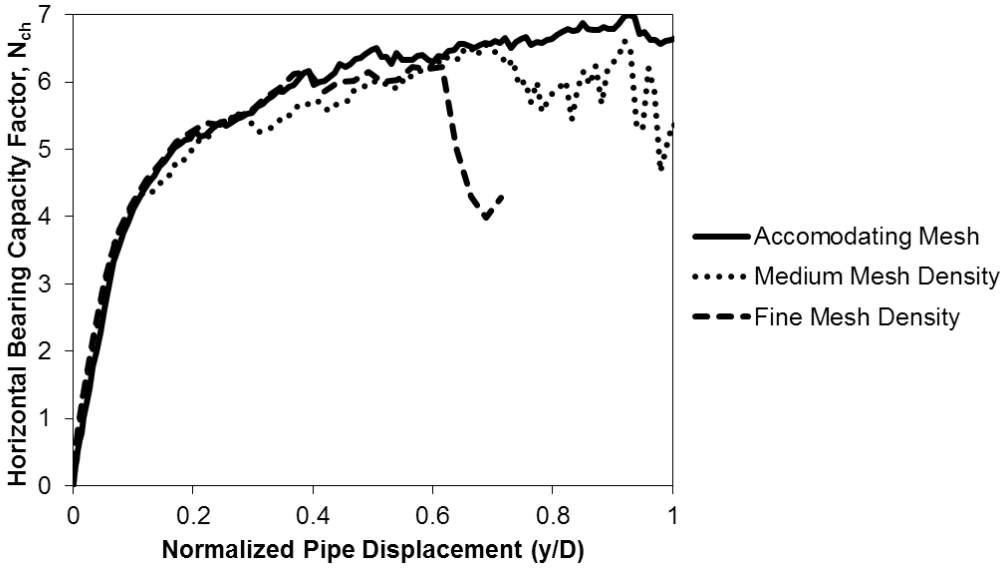

Figure 6.28. Effect of mesh density and design on the lateral force-displacement response

6.2.2.3 Derivation of Analytical Equation for Maximum Axial Soil Resistance

At the onset of pipe movement in the FE simulation, the pipeline is in full circumferential contact with the surrounding soil. As the pipeline is displaced progressively at an oblique angle, a gap is created between the trailing side of the pipe and the soil (Figure 6.29). At approximately 0.25D displacement, contact is engaged only on the leading side of the pipe. This means that there is no contribution to the axial soil resistance on the trailing side of the pipe, i.e. the interface shear stress is activated only over half of the circumference ($\pi D/2$). It is important to account for the reduction in the contact area in the interpretation of the mobilized axial soil resistance.

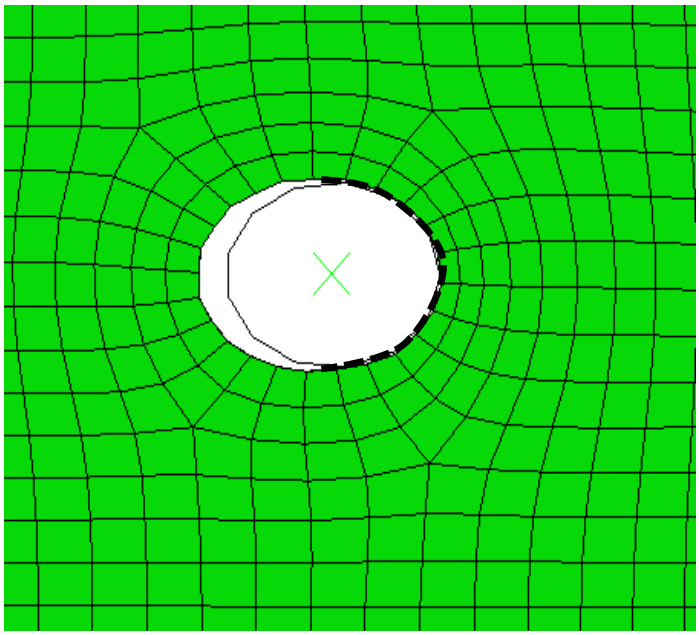

Figure 6.29. Pipe-soil interface contact during oblique lateral-axial pipe movement

The ultimate lateral (F_y) and axial (F_x) forces were normalized by the following relationships:

$$N_y = F_y/(s_u DL) \tag{6.1}$$

$$N_x = F_x/(s_u DL) = \alpha\pi \tag{6.2}$$

where D is the pipeline diameter, L is the pipeline length in contact with the soil, and s_u is the soil undrained shear strength. For oblique pipeline movements, an upper limit to the axial reaction force may be calculated by assuming that the maximum occurs when the interface shear stress limit is applied over half of the pipe circumference for the length in contact, as discussed above. This gives:

$$F_{x,max} = \tau_{max}\left(\frac{\pi D}{2}\right)L \tag{6.3}$$

The maximum normalized axial reaction force, N_y can be approximated by:

$$N_{x,max} = \frac{\tau_{max}\left(\frac{\pi D}{2}\right)L}{s_u DL} = \left(\frac{\pi}{2}\right)\left(\frac{\tau_{max}}{s_u}\right) \tag{6.4}$$

Relating the upper bound normalized axial reaction force to the clay sensitivity (S_t) yields:

$$N_{x,max} = \left(\frac{\pi}{2}\right)\left(\frac{1}{S_t}\right) \tag{6.5}$$

6.2.2.4 Numerical Results and Comparison with Analytical Equation

The relative effect of incorporating a shear stress limit on the axial and lateral reaction forces is evident in Figure 6.30 and Figure 6.31. As discussed above, the effect is more prominent in relation to the prediction of axial forces; the effects on lateral bearing are not severe. In the present study, a clay sensitivity of 2 was assumed, giving $N_{x,max}$ equal to approximately 0.79 based on Equation (6.5). As shown in Figure 6.30, the maximum axial interaction factor is limited by this relationship.

The normalized axial load increases with slight misalignment due to lateral pressure imposed on the pipe surface, which is consistent with other studies (e.g. Kennedy et al., 1977). At larger angles of attack, greater than 5 degrees, the soil failure mechanism evolves toward shear deformation through the soil mass. For attack angles greater than 70 degrees the soil failure mechanism is predominantly by lateral bearing mode. For attack angles less than 70 degrees, the numerical simulations indicate the normalized axial reaction force exhibits sensitivity with the defined soil shear stress limit at the pipe/soil interface.

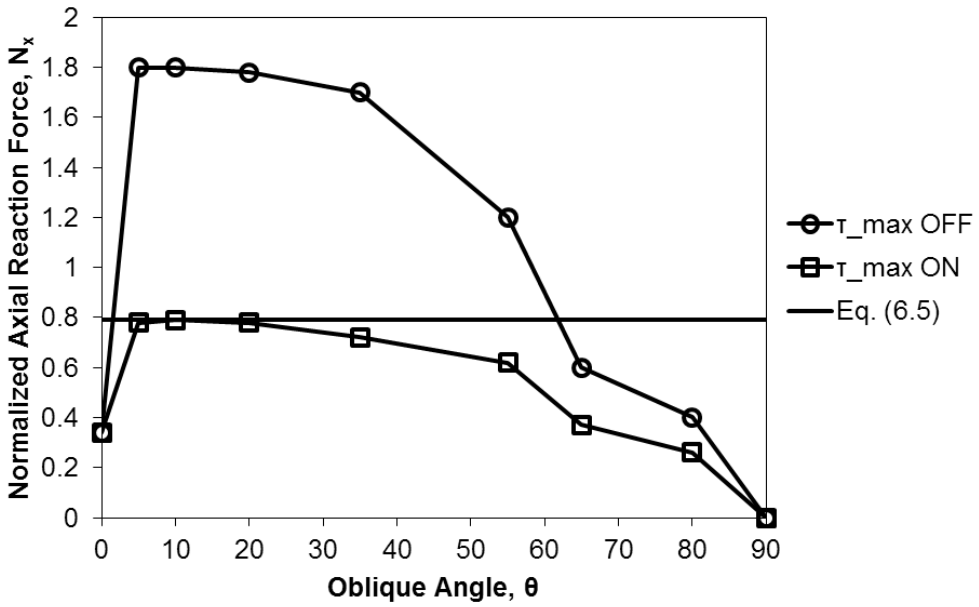

Figure 6.30. Normalized axial soil reaction force vs. oblique angle

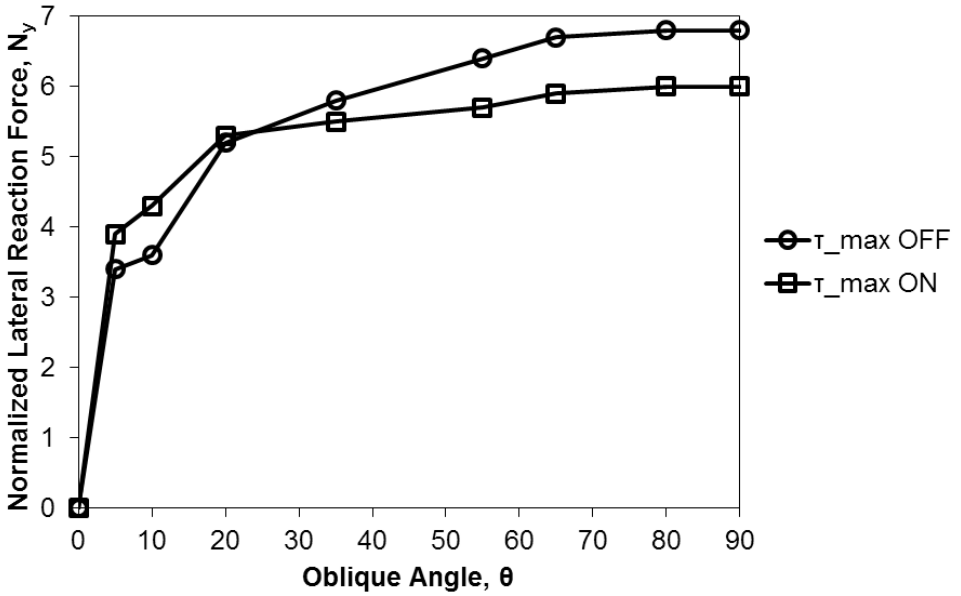

Figure 6.31. Normalized lateral soil reaction force vs. oblique angle

The normalized axial loads double when the interface shear stress varies from a maximum 0.5 s_u to a condition where the interface shear stress has no defined shear stress limit and is equal to the static interface friction coefficient multiplied by the applied normal stress. Thus, the interface shear stress is governed by the defined interface friction coefficient, normal stress state and failure mechanisms developed during the pipe/soil interaction event (i.e. $\tau_{max} = \mu\sigma_N$).

For contact conditions with no defined limit on the interface shear stress, the normalized lateral-axial yield envelope (Figure 6.32) is consistent with several studies using ABAQUS/Standard and LS-DYNA ALE numerical modelling procedures (Phillips et al., 2004a; Seo et al., 2011). These studies have also observed the transition from an axial (i.e. interface slip) to lateral bearing (i.e. shear through the soil mass) dominant

failure mechanism with increasing oblique angle. The significant difference between these investigations and the current study is the amplitude of normalized axial reaction force.

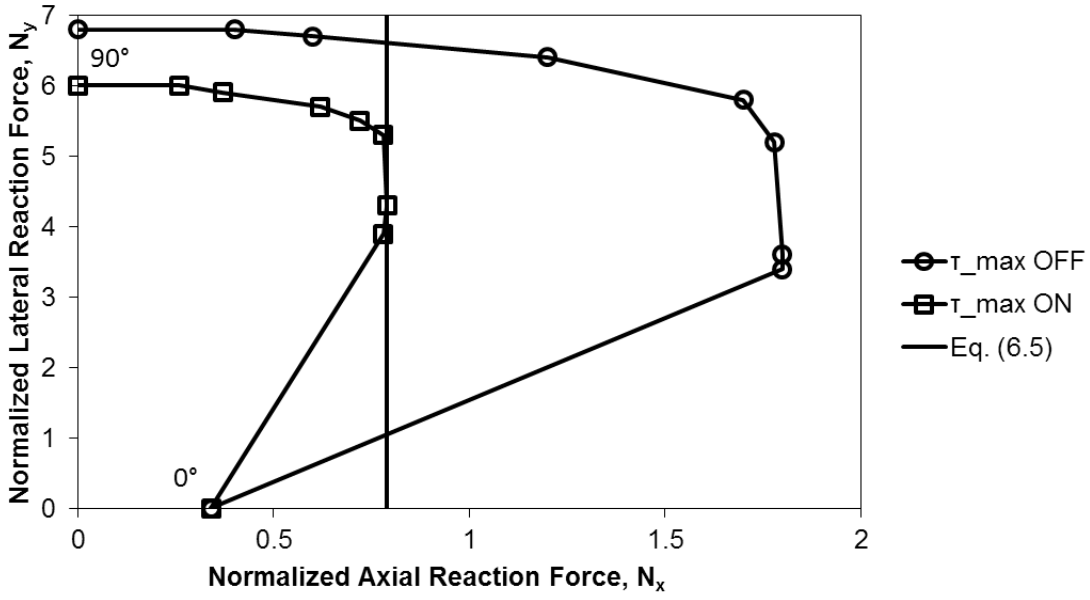

Figure 6.32. Axial-lateral interaction force diagram

A further sensitivity study, summarized in Table 6.6, was conducted to examine the effects of the assumed friction properties for oblique pipe/soil interaction in undrained cohesive material, and to test Equation (6.5) for varying clay sensitivity. For buried pipelines, if the normal contact pressure is sufficient, the interface shear stress limit will govern the soil resistance in the axial direction. In this study, friction coefficients of 0.268, 1.0 and 5.0 were applied to assess the effect on the interface behaviour prior to the mobilization of τ_{max}. The soil sensitivity, S_t (it is assumed that $S_t = s_u/s_{ur} = s_u/\tau_{max}$) was

also varied (1.0, 1.33, 2.0) to assess the effect of altering the maximum interface shear stress on the maximum normalized axial soil resistance. To illustrate the effect of excluding the shear stress limit option, two additional cases were analyzed with μ=0.268 and rough friction, both without τ_{max}. The lateral-axial pipe/soil interaction analysis was conducted using an oblique angle equal to 10° related to the expected peak axial resistance at this level (Phillips et al., 2004b).

Table 6.6. Summary of FE runs for examination of friction properties

Case	Friction Coefficient, μ	Sensitivity
1	0.268	2.0
2	1.0	2.0
3	5.0	2.0
4	1.0	1.33
5	1.0	1.0
6	0.268	τ_{max} = OFF
7	Rough	τ_{max} = OFF

The effect of changing the friction coefficient is illustrated below in Figure 6.33. For each case, it is seen that the axial resistance is limited by Equation (6.5). As mentioned above, initially the full circumference of the pipe is in contact with the soil and eventually contact is lost on the trailing side of the pipe. The artificially high friction coefficient produces an artificial peak resistance that results from relatively high shear stresses when the full pipe diameter is in contact with the soil. From the peak to about 0.25D, contact is released on the trailing side of the pipe, hence the reduction in axial

resistance. If the objective of the oblique lateral-axial FE simulation is to develop a failure envelope defined by the normalized maximum lateral and axial resistance, it may be erroneous to select the artificial peak as the ultimate axial resistance. In this instance, this would lead to an overestimation of the maximum oblique axial resistance by a factor of about 1.7. However, for large displacement continuum analysis, the behaviour before 0.25D may not drastically affect the solution, as the shear stress limit is governing at large relative displacements.

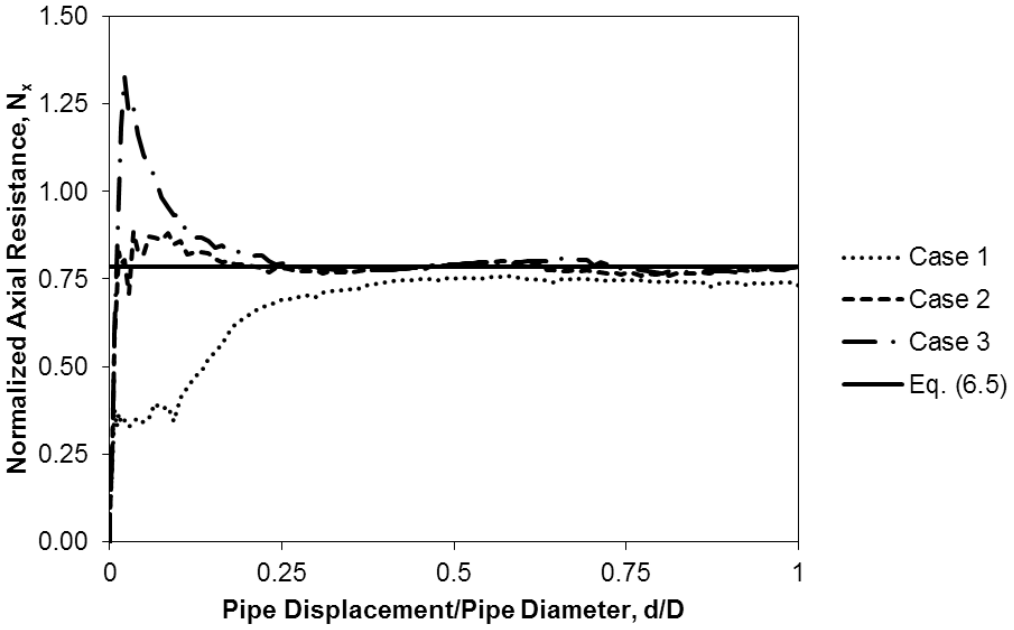

Figure 6.33. Effect of friction coefficient on normalized axial soil resistance

The clay sensitivity was varied at low levels from S_t = 1, 1.33, 2 giving respective values of the maximum normalized axial resistance, $N_{y,max}$ = 1.57, 1.18, 0.79 using Equation (6.5). Most clay actually exhibits sensitivity in the range of 2 to 4 (Holtz and

Kovacs, 1981). As expected, with increasing soil sensitivity, the axial soil resistance decreases accordingly.

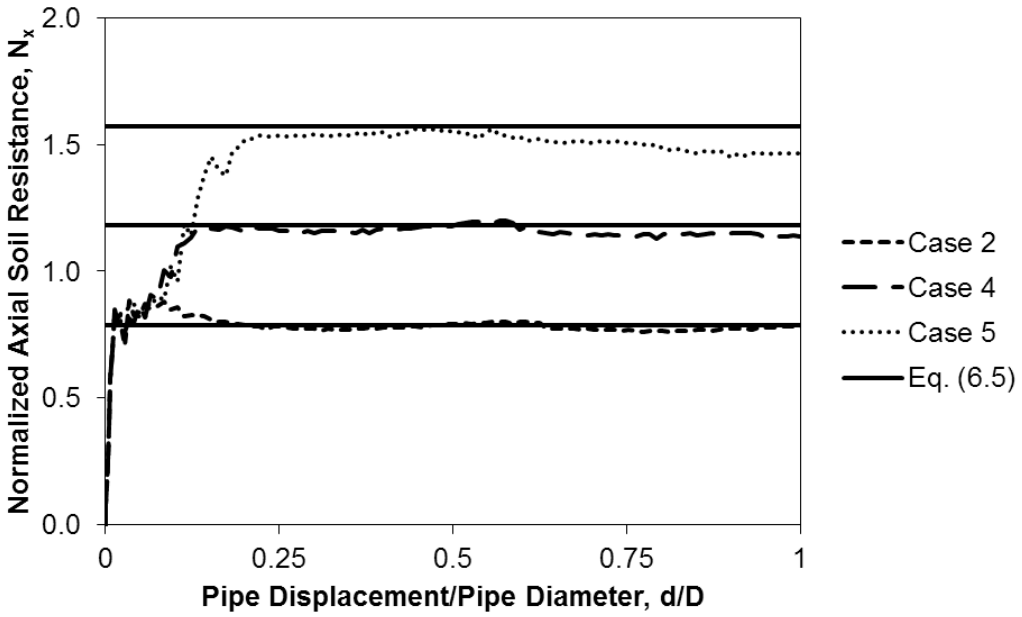

Figure 6.34. Effect of clay sensitivity on normalized axial soil resistance

If the interface shear stress is not limited, unrealistic contact shear stresses could develop that exceed the undrained shear strength of the underlying clay material, the maximum axial resistance can be overestimated, and for large displacement analysis, the interface condition will not realistically capture undrained behaviour. Cases 6 and 7 were analyzed to illustrate the effect of assuming a relatively smooth interface friction coefficient and a rough condition, without application of τ_{max}.

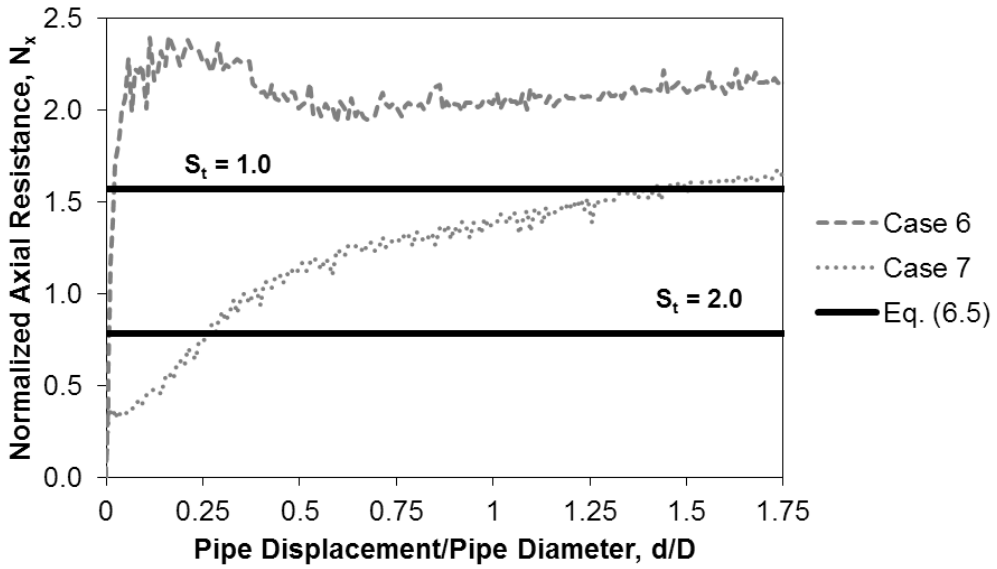

Figure 6.35. Effect of not enforcing the interface shear stress limit

In Figure 6.35 the normalized axial force-displacement curves for a rough and relatively smooth friction coefficient are plotted against the maximum normalized axial resistance assuming that the interface shear stress limit is equal to the undrained shear strength, $S_t = 1.0$, and half the undrained shear strength, $S_t = 2.0$. It is evident from this figure that the interface shear stress exceeds the undrained shear strength of the clay material in both cases at large displacements. When $S_t = 1.0$, the smooth curve shows minimal exceedance of s_u at the interface after large displacements; however, the rough condition results in an interface shear stress that is about $1.35s_u$. When $S_t = 2.0$ ($\tau_{max} = 0.5s_u$) the interface shear stress limit is exceeded by a factor of about 2.7 and 2.0 for the rough and relatively smooth condition.

These results provide insight for the oblique loading case; however, the concept may not be extensible for the pure axial condition, as the soil response and subsequent interface behaviour may change. By extension to the pure axial condition, it may be logical to assume that the shear stress limit is activated over the entire pipe circumference (πD); hence, the maximum normalized axial resistance would double in relation to the oblique case described above (3). However, the interface shear stress limit can only be mobilized in the FE simulation by assuming an artificially high friction coefficient such that even at very low normal stresses τ_{max} will be reached. This assumption would be inconsistent with relatively lower experimental adhesion factors presented by Paulin et al. (1998) and Rizkalla et al. (1996). The lower experimental values may be caused by insufficient normal stresses around the pipeline circumference to fully mobilize the interface shear strength.

For the pure axial condition, the limit soil resistance has been expressed by total and effective stress models (Schaminee et al., 1990; Cappelletto, 1998; Scarpelli et al., 2003). The total stress method (α method), as discussed above, assumes that the total interface shear force per unit length is some fraction (α) of the undrained shear strength (i.e. adhesion factor) mobilized over the pipe/soil contact circumference. The effective stress method (β method) assumes that the shear strength mobilized at the interface is related to the effective vertical stress at the level of the pipe axis, with a relationship given by:

$$F_y = 0.5(1 + K)\tan\delta'\gamma' HD = \beta\sigma'_v\pi D \quad (6.6)$$

where K is the at rest lateral earth pressure coefficient, δ' is the interface friction angle, γ' is the effective soil unit weight, H is the depth to the pipe springline, and σ'_v is the effective vertical stress (Cappelletto, 1998; Scarpelli et al., 2003). The β parameter can be regarded simply as an interface friction factor, depending on both the interface friction angle and the earth pressure coefficient. Schaminee et al. (1990) proposed a variation of the β method that accounts for the normal stresses acting on the pipeline as well as the pipe self-weight. The value of the interface friction angle depends on both the pipeline coating materials and the backfill used for covering the pipeline (Scarpelli et al., 2003). For FEA using ABAQUS/Explicit, the user is limited to using a lateral earth pressure coefficient of unity, hence β is linked directly to the friction coefficient, $\beta = \tan(\delta') = \mu$. Results presented by Cappelletto et al. (1998) suggested that the β method gives better predictions of the axial reaction forces in comparison to the α method, even for mainly cohesive soils.

In the present study, since total stress conditions were assumed, for the pure axial condition the average normal contact pressures on the pipeline can be approximated by the total vertical stress at springline. The β method formulation can be used to approximate the soil resistance to axial pipe movement, based on the assumed friction coefficient and the average normal pressures acting on the pipeline. Hence, the assumed soil shear resistance per unit length can be approximated by Equation (6.6), except replacing the effective vertical stress by the total vertical stress. In the present study (e.g. $\gamma \cong 16.2$ kN/m3, H = 1.46, D = 0.4064 m, L = 3 m, $\mu = 0.268$ this gives an estimate for N_y of about 0.44 that is in close agreement with result from FEA of about 0.36 (Pike et al,

2012c). Furthermore, the adhesion factor based on these results would be about 0.12, consistent with the results of Paulin et al. (1998). Cappelletto et al. (1998) also interpreted the adhesion factor according to the effective stress method, and found a good fit with available experimental results.

While an interface shear stress limit (e.g. $\tau_{max} = 0.5s_u = 22.5$ kPa) was applied in the total stress analysis, with μ=0.268 the average normal stresses at the interface would have to be greater than or equal to about 84 kPa in order to mobilize the shear stress limit; this is a factor of about 3.5 greater than the total vertical stress at the pipe springline (23.7 kPa). This implies that the burial depth ratio would have to increase by the same factor; hence the burial depth ratio would have to increase to about 13 in order to mobilize the shear stress limit at the interface during axial pipe movement. Changing the friction coefficient to 1.0 would mean that the required normal stress to activate the shear stress limit would be equal to τ_{max} and already achieved at H/D = 3.6, however, this may be an unrealistic approximation. As shown by Cappelletto et al. (1998), tests in clayey soils using a polyethylene coated 24 inch pipe, at H/D $\cong$ 3.4, resulted in residual β values of about 0.25.

As discussed by Phillips et al. (2004a), the soil failure mechanism under axial pipe loading is restrained within a very thin layer of soil surrounding the pipe. From extensive studies of the interface behaviour in the case of foundation piles, the soil response is essentially drained, as the region affected by the shearing is very small, so that excess pore pressures generated in the interaction process can rapidly vanish (Cappelletto et al., 1998). However, as the oblique angle increases from pure axial to lateral, the failure

mechanism can change to include bearing failure in the soil, as well as frictional shear at the interface. Subsequently, more of the soil is involved in oblique pipe/soil interaction and pore pressures may not be able to dissipate as readily. Hence, numerical analysis of oblique pipe/soil interaction may benefit from adopting a dual approach whereby a realistic drained friction angle is applied in combination with an interface shear stress limit. This would ensure that under pure axial loading, when normal stresses are low, an appropriate axial response is achieved, while as the mechanism changes to include more of the surrounding soil under oblique loading, the undrained shear strength (or some fraction thereof due to remoulding) would not be exceeded.

6.2.3 Summary

This subsection has shown that large deformation FE tools can accommodate orthogonal and oblique pipe movements assuming undrained conditions in clay materials. In the lateral direction, the CEL results were shown to agree with Phillips et al. (2004a) at varying H/D ratio, accounting for the soil weight term that has been adopted by the PRCI (2009) guidelines. For oblique lateral-axial pipe movements, the treatment of the interface tangential friction was shown to have an effect on the failure envelope that defines the transition of soil resistance from pure axial to pure lateral pipe movement. The influence of the interface shear stress limit was to reduce the maximum axial load, at small angles of lateral misalignment, in comparison with the assumption that only the interface friction coefficient applies. An analytical expression was derived to predict the maximum axial soil resistance and shown to accurately predict the FE results.

6.3 Coupled Ice/Soil/Pipeline Interaction in Cohesive Soil

This section presents work from a paper submitted and accepted to a special edition of the Canadian Geotechnical Journal on Pipeline Geotechnics. Some sections in the published paper are covered throughout this thesis, and where this occurs, relevant sections of the thesis are referenced to avoid repetition.

6.3.1 Motivation

To support and facilitate engineering design of arctic offshore pipelines (e.g. Been et al., 2013; Lanan et al., 2011,2001; Lever, 2000), current practice utilizes a decoupled engineering model to characterize the system demand (i.e. subgouge soil deformations), based on free field ice gouge events, that define imposed displacement boundary conditions on a structural finite element model used to simulate pipe/soil interaction and assess load effects (e.g. Barrette, 2011; Been et al., 2013; Clark et al., 1994; Kenny et al., 2007,2004,2000; Nixon et al., 1996; Phillips et al., 2005; Woodworth-Lynas et al., 1996).

However, these commercial projects have incorporated conservative methodologies that reflect the inherent data uncertainty and model error associated with this idealized pipeline engineering design framework. Limitations and deficiencies of the structural beam/spring (i.e. Winkler) model have been raised in previous studies (e.g. Eltaher, 2014; Konuk et al., 2007,2006; Lele et al., 2013,2011; Nobahar et al., 2007b; Peek and Nobahar, 2012; Phillips and Barrett, 2012). The primary issue relates to question in geomechanics with respect to the inadequacy of Winkler-type models to account for realistic continuum soil behaviour as related to:

1) Superposition Errors: The decoupled modelling framework assumes the free-field subgouge displacement field can be superimposed on the pipe/soil model as an initial displacement boundary condition. This approach ignores the relative motion (trajectory) between the pipe and soil during the gouge event, relative stiffness effects between the pipe and soil, and pipeline interference effects on the soil deformation field and failure mechanisms (Kenny et al., 2000; Peek and Nobahar, 2012), and
2) Directional Load Decoupling: The Winkler-type model idealizes the soil continuum through a series of discrete, uncoupled soil spring elements that represent soil forces on three mutually orthogonal axes. There is no interaction between soil springs at different locations along the pipeline length and the spring force relies only on the displacement at a point that is not directly influenced by adjacent springs. This issue has been highlighted through physical and numerical modelling studies on oblique pipe/soil interaction events (e.g. Cocchetti et al., 2009a,b; Daiyan, 2013; Kenny and Jukes, 2015; Nyman, 1984; Phillips et al., 2004a; Pike and Kenny, 2012; Rossiter and Kenny, 2012a).

The Winkler-type model also does not address the spatial distribution of soil strength parameters (e.g. modulus, friction angle, dilation angle) and nonlinear soil behaviour (e.g. strain softening, compaction, dilation) that occurs during large deformation, ice gouge and pipe/soil interaction events (e.g. Eltaher, 2014; Been et al.,

2011; Lele et al., 2013,2011; Pike et al., 2014a,b,2013; Rossiter and Kenny, 2012a,b). This aspect is not addressed in this study.

From the pipeline perspective, the structural beam elements do not account for second order effects due to section ovalization and warping associated with large deformation that may result in local mechanisms such as buckling and strain localization.

In this paper, through a comparative numerical simulation case study, which utilized structural and continuum finite element modelling procedures, the significance of superposition error and directional load decoupling is addressed. Although previous studies have provided valuable insight on these issues (e.g. Konuk et al., 2007; Peek and Nobahar, 2012; Phillips and Barrett, 2012), a unique contribution of this study is the methodology used to establish and incorporate the soil load-deformation relationships and subgouge soil deformation fields on a more consistent basis across the numerical modelling procedures, which is essential for the comparative assessment. The qualitative and quantitative characteristics of the predicted subgouge soil deformation field and pipeline mechanical response are the primary metrics for this evaluation.

A parameter case study is conducted using structural pipe/soil interaction models to assess different technical approaches for defining the magnitude and distribution of the subgouge soil deformation field, and the soil spring load-displacement relationships on the predicted pipe response. This provides a comparative basis to evaluate superposition error and model uncertainty using the same numerical simulation procedures. The influence of superposition error and directional load decoupling is also examined through comparison between structural and coupled continuum interaction models. Based on these

outcomes, the potential impact on current pipeline engineering design practice for ice gouge environments is also explored.

6.3.2 Numerical Modelling Framework

6.3.2.1 Overview

The case study examines the variance in predicted outcomes of pipeline mechanical response using structural (i.e. beam/spring) and continuum (i.e. shell/brick) finite element modelling procedures. The primary objective is to gain an improved understanding on the significance of superposition error and directional load decoupling through a systematic analysis on an equivalent basis. The mathematical and engineering models that form the basis of this numerical modelling framework used in the case study are highlighted in this section.

For the structural finite element simulations predicting load effects on buried pipelines in ice gouge environments, empirical relationships and continuum finite element modelling procedures are used to define both the system demand (i.e. subgouge soil deformations field) and soil load-displacement response (i.e. soil spring elements). The mathematical models defining the subgouge soil deformation field are based on (1) the empirical Pressure Ridge Ice Scour Experiment (PRISE) model (Woodworth-Lynas et al., 1996), as well as (2) free-field (i.e. ice keel/seabed) and (3) coupled (i.e. ice keel/seabed/pipe) numerical simulations, conducted in this study, using the Coupled Eulerian Lagrangian (CEL) formulation. The soil spring load-displacement relationship was defined using (1) industry practice guidelines (PRCI, 2009) and (2) numerical

simulations of rigid pipe/compliant soil interaction events, conducted in this study, using the CEL formulation for plane strain conditions.

Continuum finite element modelling procedures, within the CEL formation, are used to simulate the pipeline mechanical response for coupled ice keel/seabed/pipe interaction events. The results can be directly compared with prediction from the structural modelling study.

6.3.2.2 System Demand: Free-Field Subgouge Soil Deformations

6.3.2.2.1 Empirical Model

The published paper incorporates a section on the empirical PRISE subgouge soil displacement field (Woodworth-Lynas et al., 1996) that is covered in this thesis in Section 2.2.1.

6.3.2.2.2 Continuum Finite Element Model: Procedure Calibration

The published paper incorporates a section on the free-field ice gouge FE model verification study that is covered in this thesis in Section 6.1.3.

6.3.2.2.3 Continuum Finite Element Model: Case Study

For the case study, the selected parameters are consistent with the investigation by Peek and Nobahar (2012). The ice keel was modelled as a rigid indenter with a 2 m depth, 10 m full width and 15° attack angle. Dimensions of the soil domain were 20 m deep, 30 m wide and 80 m long (Figure 6.36). The cohesive soil was defined by total unit weight of 19 kN/m^3 with an undrained shear strength of 50 kPa, elastic modulus of 10 MPa. A

total stress analysis (TSA), assuming undrained conditions, was performed in the continuum models with the Poisson's ratio assumed $\nu = 0.499$ to simulate incompressibility. The normal velocities at the soil (Eulerian) boundaries are set to zero and the model takes advantage of half-symmetry at the gouge centerline.

The free-field analysis is conducted in three steps: 1) the geostatic soil stresses are applied by gravity loading on the soil to reach equilibrium with the applied initial stress conditions 2) the keel is lowered into the model seabed to the prescribed gouge depth, and 3) the keel is displaced in the gouge direction. The soil does not settle during the geostatic step. The keel is translated rigidly and the reaction forces are recorded at the rigid body reference point. The subgouge displacements are tracked using tracer particles as shown in Figure 6.36.

For the ice keel, since a steady-state gouging condition is assumed, then rigid translation is applied (i.e. ignoring hydrostatic terms associated with heave, pitch and rotation are ignored), which is considered appropriate as gouges have been shown to maintain a consistent profile for long distances (Blasco et al., 2011).

Since the parameters used by Peek and Nobahar (2012) do not simulate a particular physical test, the results are compared with the PRISE empirical equations for the subgouge soil displacement field (Figure 6.37). Although the pipe is not incorporated within the free-field analysis, the subgouge soil displacement at the representative pipe location, examined by Peek and Nobahar (2012), is illustrated using closed circles.

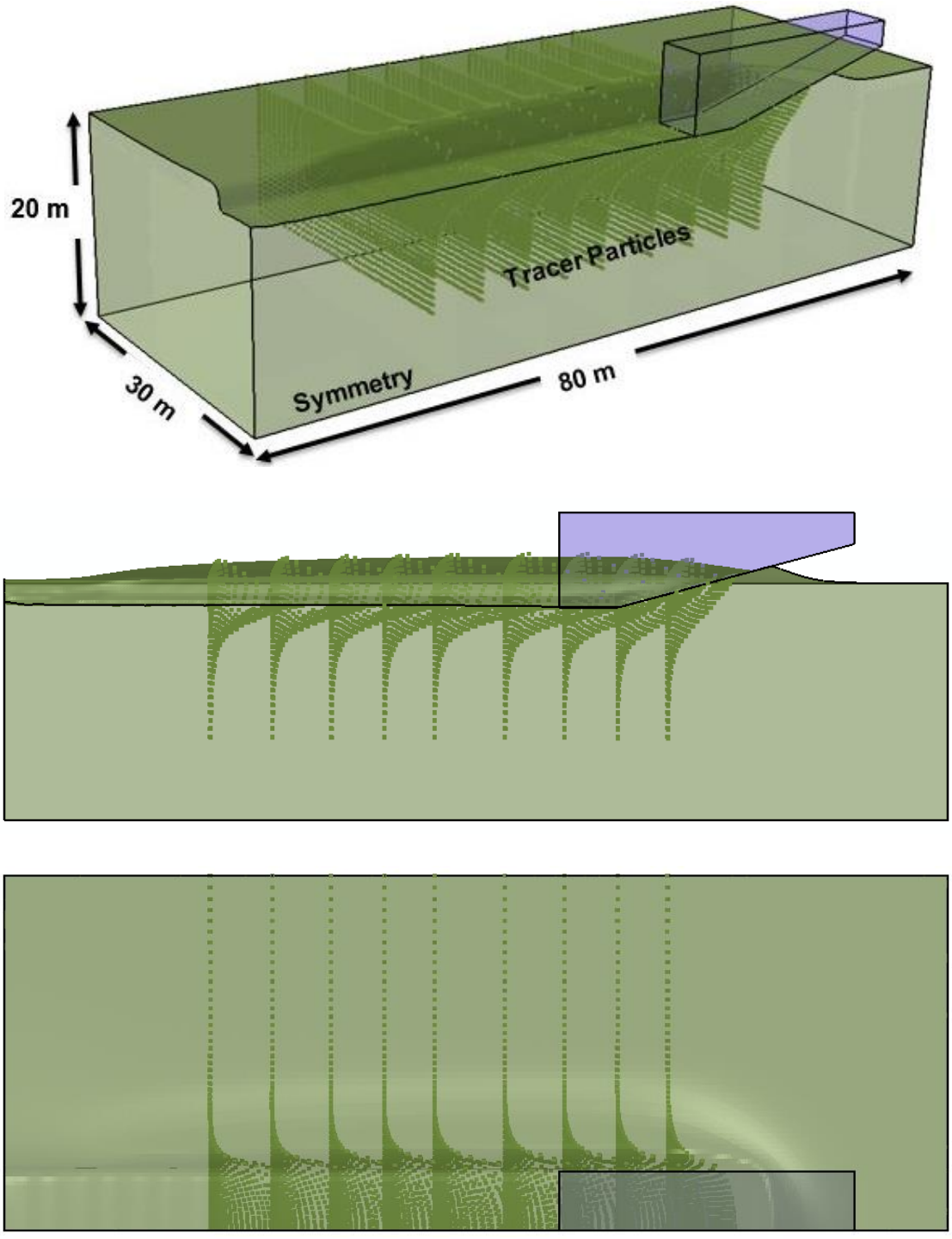

Figure 6.36. Free-field ice gouge model tracer particle deformations

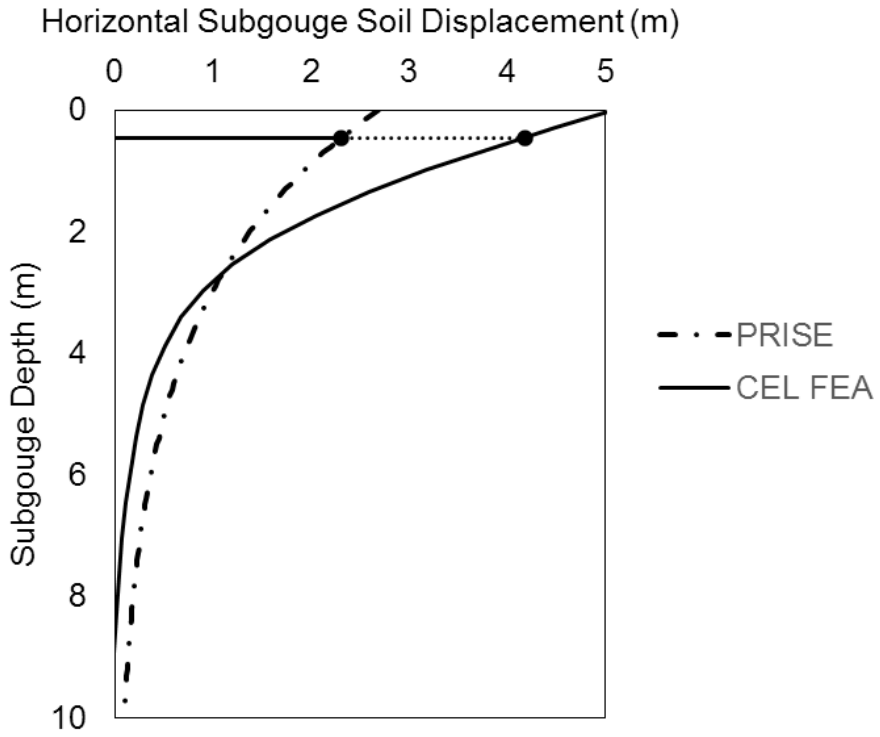

Figure 6.37. Centerline subgouge soil displacement in horizontal direction against subgouge depth

In comparison with the PRISE empirical relationship, as shown in Figure 6.37, the CEL simulation predicts larger magnitude of horizontal subgouge soil displacement, at the ice keel centerline, up to a profile depth of 3 m beneath the ice keel. These results are consistent with other continuum finite element simulations of free-field ice gouge events where the observed discrepancy extends to a profile depth approximately equal to the gouge depth (e.g. Kenny et al., 2007b; Panico et al., 2012; Phillips et al., 2010). Similar analysis conducted by Peek and Nobahar (2011) showed greater maximum horizontal subgouge soil displacement at the pipe springline compared to PRISE, though less than the present study due to slight differences in the model parameters, e.g. von Mises plane

strain yield stress ($\sqrt{3}\ s_u$) criterion compared to the Treca yield stress ($2\ s_u$). For the parameter case study, the system demand related to the subgouge soil deformations will assess the significance of model error on the predicted pipeline response within a consistent framework and on an equivalent basis.

In terms of the vertical subgouge soil deformation (Figure 6.38), the results illustrate a similar trend with the observations on the horizontal soil subgouge displacement field (Figure 6.37). This discrepancy between the finite element simulations and PRISE equation for vertical subgouge soil deformations is consistent with other studies (e.g. Phillips and Barrett, 2010; Pike et al., 2011a). This is an open area for further research to resolve and understand the issues driving this discrepancy.

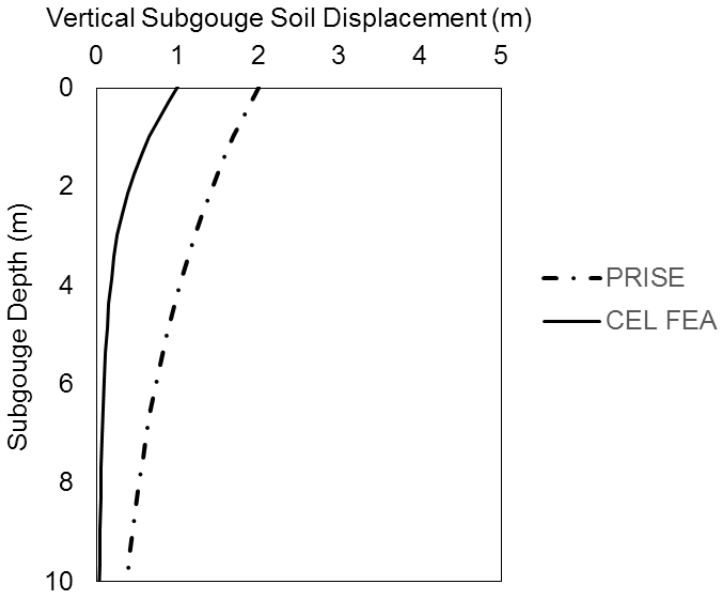

Figure 6.38. Centerline subgouge soil displacement in vertical direction against subgouge depth

The three-dimensional subgouge displacement field, for the gouge direction, transverse lateral and transverse vertical directions, as predicted by the CEL simulation is illustrated in Figure 6.39. The displacement field represents the free-field subgouge soil deformations at the representative pipe springline location that will be used in the structural pipe/soil interaction modelling and analysis. The corresponding PRISE horizontal subgouge soil displacement field, at the same depth, is also shown for comparison.

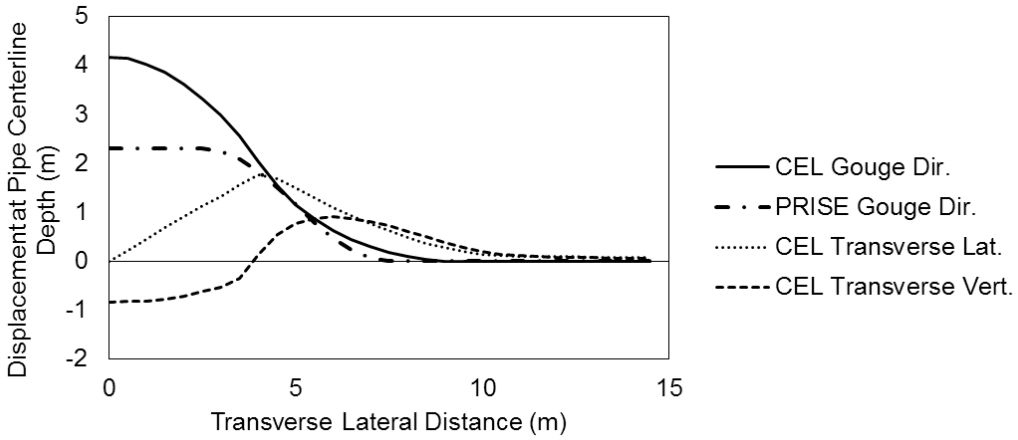

Figure 6.39. Free-field subgouge soil displacements from CEL model and PRISE equation

The transverse lateral displacement profile indicates the soil clears away from the gouge centerline toward the free edge and reaches maximum amplitude at 80% of the ice keel width (i.e. 5 m is the ice keel half-width due to the line of symmetry). The transverse vertical displacement profile illustrates the soil is pushed downwards (i.e. subduction) beneath the keel that transitions to upward clearing processes at 80% of the ice keel

width. These observations are consistent with the soil particle trajectories observed during ice gouge experiments in clay as reported by Been et al. (2008) for an ice keel with a 15° attack angle. The displacement field attenuates within a transverse lateral distance of one gouge width from the ice keel centerline.

6.3.2.3 System Response: Structural Pipe/Soil Interaction Model

6.3.2.3.1 Soil Spring Load-Displacement Relationships: Empirical Basis

The soil continuum response can be idealized through a series of discrete springs, which represent the generalized mechanical response of a segmented soil slice, connected to the pipe. The spring elements represent the soil load-displacement response per unit length of pipe that act on three, mutually orthogonal axes to the pipeline centerline defined along the longitudinal, transverse horizontal, and transverse vertical directions. For the empirical basis, the soil spring load-displacement relationships are defined by engineering guidelines with bilinear (i.e. elastic-perfectly plastic), piecewise multilinear or hyperbolic functions to represent the nonlinear response characteristics (e.g. ALA, 2005; PRCI, 2009). In this study the PRCI (2009) guidelines are used.

6.3.2.3.2 Soil Spring Load-Displacement Relationships: CEL Simulation

CEL modelling procedures were developed to establish the soil load-displacement relationships for the transverse lateral, upward and downward bearing directions relative to the pipe longitudinal axis (Section 4.3). This provides an equivalent basis when comparing predicted pipeline response, across the parameter case study, to assess the factors influencing model variance associated with soil spring formulations (i.e. PRCI

relationships as discussed in the previous section) and different modelling procedures (i.e. structural and continuum finite element models) for decoupled and coupled ice gouge events.

CEL analysis was not conducted for the case of axial pipe displacement, where the axial resistance would be governed by the assumed interface friction coefficient. For axial pipe movement, the CEL simulations are inherently constrained by limitations in the numerical procedures (e.g. mesh density, linear reduced integration element, single phase material in total stress analysis) and treatment of the interface soil mechanics (e.g. drained behaviour through a thin annular disk into a larger soil domain with undrained behaviour), which cannot be fully addressed in the current CEL modelling framework (e.g. Pike et al., 2011a; Wijewickreme and Weerasekara, 2015,2010). Based on the PRCI (2009) guidelines, a lower bound adhesion factor (α = 0.22), which corresponds to an undrained shear strength of 50 kPa, was used in the structural models. This approach is conservative where the reduced axial soil resistance allows for greater axial pipe feed-in when the subgouge soil displacement field is applied.

The model dimensions and boundary conditions simulating plane strain conditions are illustrated in Figure 6.40. The pipe is modelled as a rigid body using solid continuum elements (C3D8R) and the soil reaction forces are monitored at a reference point tied to the pipe segment. For the lateral pipe/soil interaction analysis, the pipe is free to move vertically during the lateral motion. For the vertical pipe/soil interaction cases, only the prescribed vertical displacement is allowed.

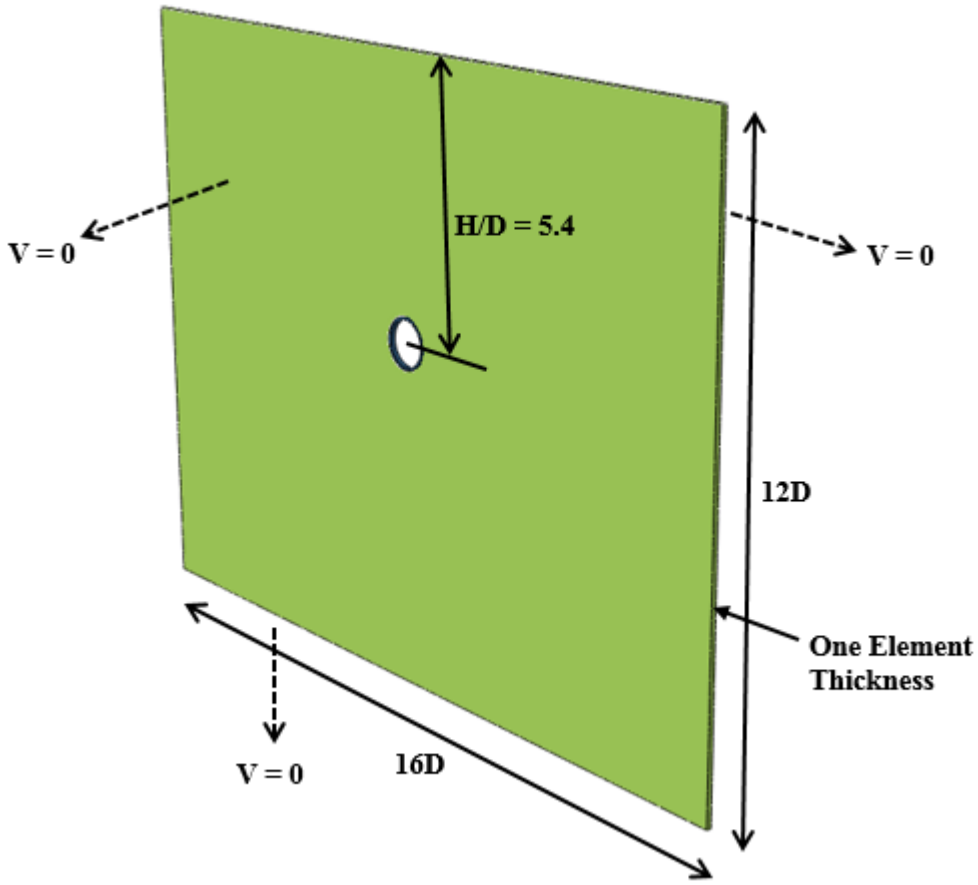

Figure 6.40. Plane strain model for CEL FEA soil resistance curves

The soil properties and conditions (e.g. geostatic stress) are consistent with the free-field CEL ice gouge simulations, as presented in the previous section. The pipe segment springline depth is 2.457 m based on the 2 m gouge depth and 0.5D initial clearance below the base of the ice keel, which is equal to a burial depth ratio of 5.4 (i.e. pipe springline depth/pipe diameter). The analysis is conducted in two steps: 1) the geostatic soil stresses are applied and 2) the pipe is displaced a distance of one pipe diameter (1D) in each direction.

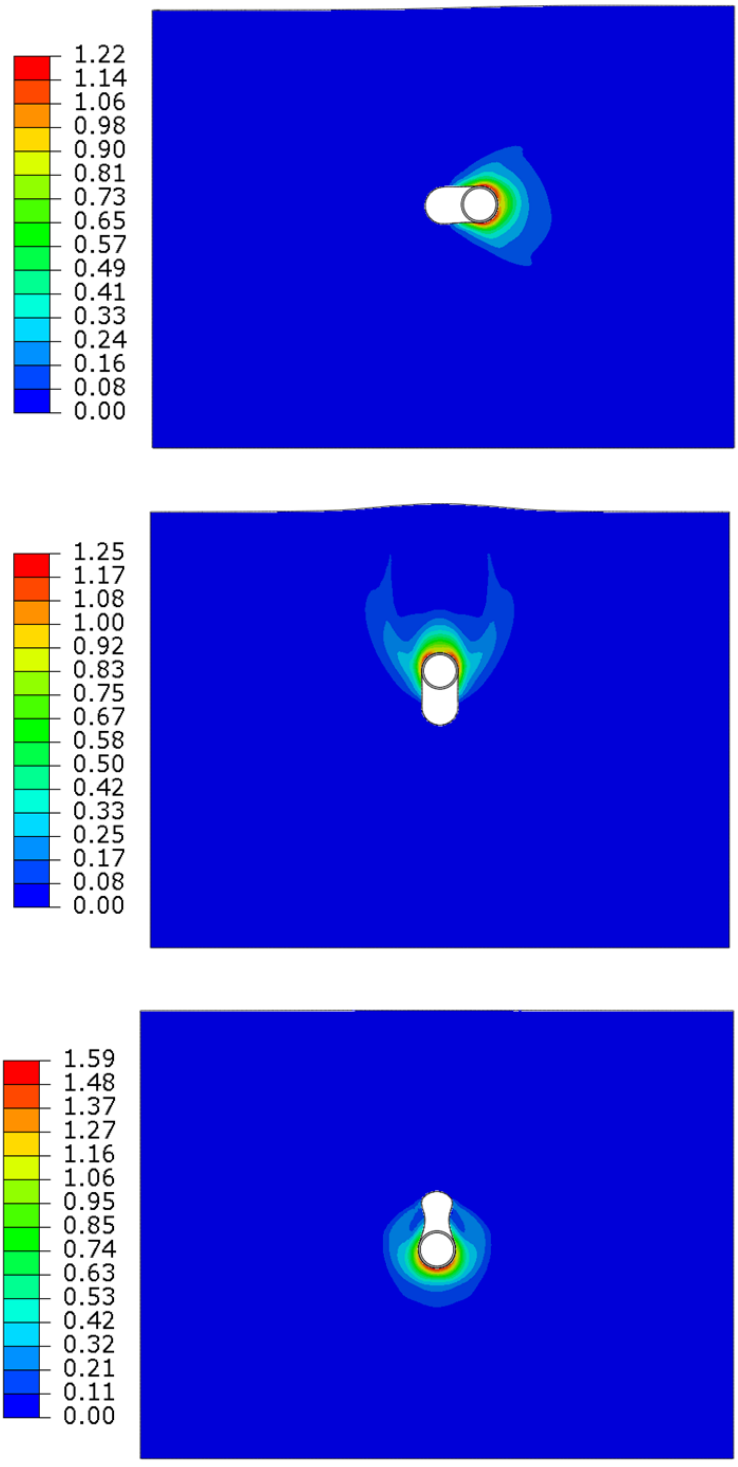

Figure 6.41. Plastic strain (max. in-plane principal) contours for CEL pipe/soil interaction analyses

As shown above in Figure 6.41, plastic strain develops within a localized region on the leading pipe face for each loading direction. The response is representative of deep burial conditions (e.g. Audibert and Nyman, 1975,1977; Phillips et al., 2004a; Pike and Kenny, 2011b). For vertical upward loading, the plastic strain contours propagate toward the free surface with heave motion expressed.

For each loading direction in the CEL simulations, the soil load-displacement response is compared with equivalent relationships based on the PRCI (2009) guidelines (Figure 6.42a,b,c). The axial load-displacement relationship based on the PRCI (2009) guidelines is shown for reference in (Figure 6.42d).

The elastic behaviour, for the continuum CEL analysis and hyperbolic soil springs relationships based on the PRCI (2009) guidelines are in agreement for the lateral and vertical bearing uplift loading directions (Figure 6.42a,b). There is greater discrepancy between these modelling approaches for the vertical downward bearing case (Figure 6.42c).

For the lateral and vertical bearing uplift loading directions (Figure 6.42a,b), there is general correspondence between the CEL analysis and PRCI (2009) guidelines with respect to the general characteristics of the nonlinear load-displacement relationship (e.g. rate of change of the tangent stiffness) and mobilization to peak load response. However,

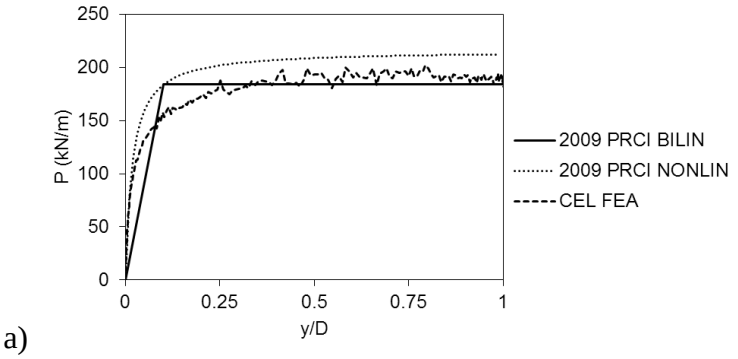

a)

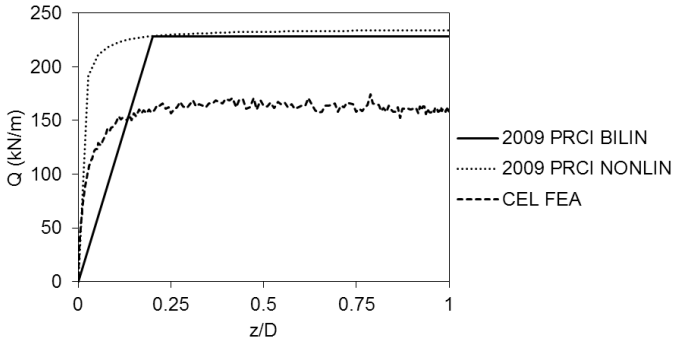

b)

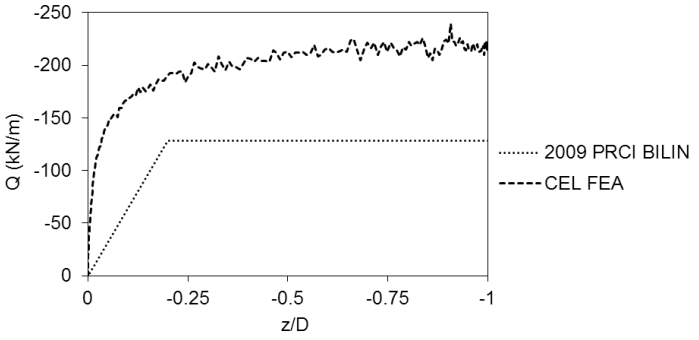

c)

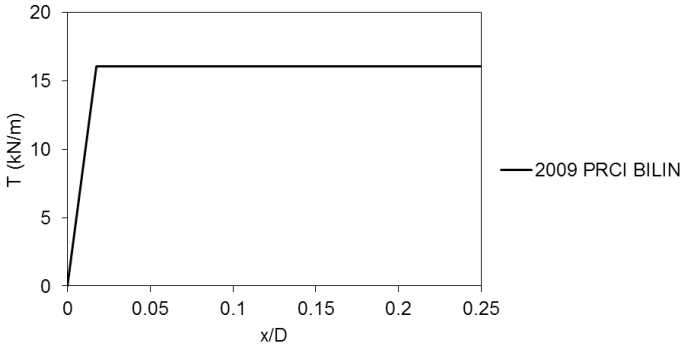

d)

Figure 6.42. Force-displacement curves

there are differences in the predicted force magnitudes for each loading direction (Figure 6.42a,b,c).

For lateral bearing (Figure 6.42a), the PRCI (2009) bilinear and hyperbolic, and CEL simulations exhibit general agreement and tend to converge at a lateral displacement of 0.4 pipe diameters, which is applicable for large deformation ice gouge events.

The maximum vertical uplift force (Figure 6.42b) predicted by CEL was less, by a factor of 0.7, than the maximum vertical uplift force as specified by PRCI (2009) guidelines. For vertical uplift, the PRCI (2009) guidelines are based on theoretical analysis and results from small-scale laboratory tests. However, results (maximum vertical uplift force) from recent physical tests show a similar level of discrepancy between the test data and industry guidelines (Liu et al., 2015). The maximum vertical bearing force (Figure 6.42c) predicted by CEL was 1.5 times greater than the maximum vertical uplift force as specified by PRCI (2009) guidelines, which is based on a continuous strip footing.

6.3.2.3.3 Structural Pipeline Model

The pipeline mechanical response is idealized using a 2-node, linear hybrid structural beam element (i.e. PIPE31H). Using isotropic material properties for Grade 415 material, the pipe constitutive model was defined using conventional J_2 plasticity theory with a von Mises yield surface and isotropic hardening rule. The stress-strain relationship was defined as piecewise elastic-plastic relationship consistent with the study by Peek and Nobahar (2012).

6.3.2.4 System Response: Fully Coupled CEL Models

6.3.2.4.1 Background

There are a number of studies that have used continuum finite element modelling procedures to investigate fully coupled ice keel/seabed/pipeline interaction events (e.g. Hossain et al., 2011; Barette, 2011; Konuk et al., 2006,2005; Lele et al., 2013,2011; Nobahar et al., 2007b; Panico et al., 2012; Phillips and Barrett, 2012; Pike et al., 2011a,b; Peek and Nobahar, 2012). These studies have identified key parameters influencing the coupled ice gouge event that include the ice keel feature geometry (i.e. width, depth, angle of attack), soil characteristics (i.e. type, physical properties, strength parameters) and pipeline geometry (i.e. diameter, burial depth).

In comparison with continuum finite element analysis of coupled ice gouge events, the general observation from these studies has been the decoupled structural modelling procedures provide generally conservative results with respect to pipeline mechanical response and cannot adequately capture the complex nonlinear mechanics, interaction and failure processes that occur during these events. A recent study (Phillips and Barrett, 2012), however shows reasonable correspondence between reduced-scale centrifuge tests on coupled ice keel/soil/pipe interaction event with decoupled structural pipe/soil interaction models that have integrated the effects of directional load coupling within the soil spring formulation (e.g. Daiyan, 2013; Phillips et al., 2004a; Rossiter and Kenny, 2012a).

The primary motivation for conducting coupled CEL simulations in this study is to provide an equivalent basis and integrated framework for the comparison between

modelling approaches when evaluating the significance of superposition error and directional load decoupling effects on the predicted soil and pipeline mechanical response. Other studies have conducted comparative assessment of the decoupled and coupled numerical simulation tools but have only addressed subsets of the analysis conducted in this study.

For example, in the study by Konuk et al. (2006), only free-field subgouge deformations were applied to the decoupled structural model, and the soil properties used in the ALE simulations did not correlate with those used to generate the soil spring load-deformation relationships implemented in the structural beam/spring model. The ALE simulations defined a comparatively weaker soil response that resulted in a biased comparison.

For buried pipelines in cohesive soil, assuming undrained loading conditions, subject to ice gouge events, Nobahar et al. (2007a,b) defined the soil properties on a consistent basis within each modelling environment. The pipeline mechanical response was found to be moderated when using the continuum finite element modelling procedures in comparison with the pipe deformation and strain predictions from the structural based model. The differences were attributed to the idealizations of the Winkler-type approach to errors associated with direction load decoupling (i.e. “slice-to-slice” coupling).

These concepts were further explored in a following study (Peek and Nobahar, 2012) where the soil spring force-displacement relationships were established through continuum finite element modelling. The study concluded directional load decoupling

could not account for observed discrepancy between modelling approaches and cited superposition error as the contributing factor. However, the subgouge deformation field imposed in the decoupled structural model was based on free-field ice gouge simulations and not a fully coupled ice gouge event as investigated in this study. The physical presence of the pipeline leads to impedance of the soil deformation and flow around the obstruction (i.e. pipeline) and thus only one perspective of the superposition error is addressed.

It is from this perspective the primary motivation of the present study was formulated where further understanding on the significance of the superposition error, as identified by Peek and Nobahar (2012), can be explored.

6.3.2.4.2 CEL Modelling Procedures

The coupled ice/seabed/pipeline interaction model is based on an extension of the free-field CEL procedures where the element size is refined to 0.1 m within the Eulerian domain surrounding the buried pipeline, which is modelled using S4R shell elements. There are 40 shell elements around the circumference to model the pipe, and the element length in the axial direction is 0.125 m, consistent with Peek and Nobahar (2012). The Eulerian mesh does not conform to the pipe circumference; rather the element volume fraction defines the soil surface in contact with the outer pipe surface, which is enforced through the surface polarity option.

To reduce the computational effort, the symmetry boundary condition at the pipe shell model on the gouge centerline is defined. To account for the effects of axial feed-in, axial stiffness and end boundary conditions, a structural beam/spring model extension

from the continuum domain for an additional 5 km length, in the horizontal plane and orthogonal to the direction of travel for the ice keel. The continuum shell/structural beam transition is defined by a distributing coupling constraint. The pipe is modelled using PIPE31H elements, 0.5 m in length, and connected to SPRINGA soil elements, which are defined using the continuum CEL simulations discussed in the previous section.

The modelling procedures for the soil properties and state are consistent with the CEL simulation on free-field ice gouge events. An isotropic Coulomb friction model is used to define the ice keel/soil and pipe/soil interfaces with friction coefficients of 0.3 and 1.0, respectively. There is no relative motion when the equivalent frictional stress on the interface is less than the pre-defined critical stress, which is proportional to the contact pressure. In these simulations, the shear stress limit is capped at half the undrained shear strength (i.e. 25 kPa).

The analysis is conducted in four steps: 1) the geostatic stress state is established in the soil, 2) the keel is lowered to the prescribed gouge depth while the internal pressure (12 MPa) is applied to the shell (S4R) elements and an equivalent temperature change is applied to the structural (PIPE31H) elements (this is due to internal software limitations when defining a coupled constraint where the effects of internal pressure are not transferred to the structural elements), 3) the change in temperature (ΔT = 50 °C) is applied to both structural and continuum pipeline models, and 4) the keel is displaced in the gouge direction.

The seabed reaction forces for the free-field and coupled ice gouge simulations are illustrated in Figure 6.43. The base of the keel crosses the initial pipe location at 27 m of

displacement, where the pipeline does not have any appreciable influence on the magnitude of seabed reaction forces. The increased response noise, for the coupled CEL simulation relative to the free-field case, is due to the effects of mass scaling, applied to the pipe shell elements in order to increase the stable time increment to a minimum of 5×10^{-5} s, wave dispersion effects and numerical smoothing associated with the advection phase that may also affect the computational results.

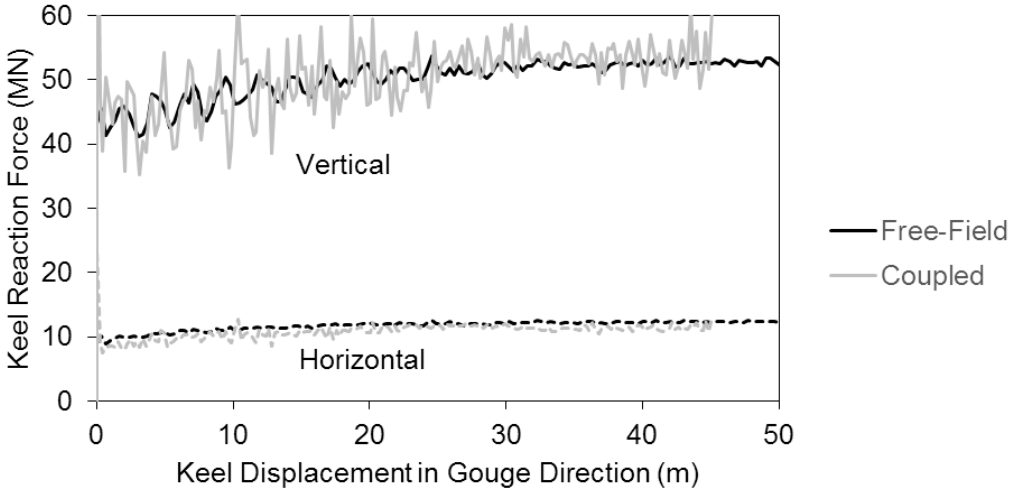

Figure 6.43. Seabed reaction forces in free-field and coupled simulations

The pipe trajectory (Figure 6.44) illustrates a complex path that can not be accounted for when using subgouge soil deformations based on free-field ice gouge events within the decoupled structural pipe/soil interaction modelling environment (e.g. Konuk et al., 2006; Pike and Kenny, 2011a; Pike et al., 2011b).

Although equilibrium conditions were not affected (Figure 6.43), the soil kinematics and flow mechanisms were influenced by the coupled interaction due to the presence of a buried pipe (Figure 6.45). The soil displacement on the pipe facing side, in reference to the ice keel, was monitored using tracer particles throughout the coupled CEL simulation. The tracer particle motion, positioned at the pipe springline depth, was compared with the tracer particle motion from the free-field CEL simulations and predicted subgouge soil deformation field based on the empirical PRISE model.

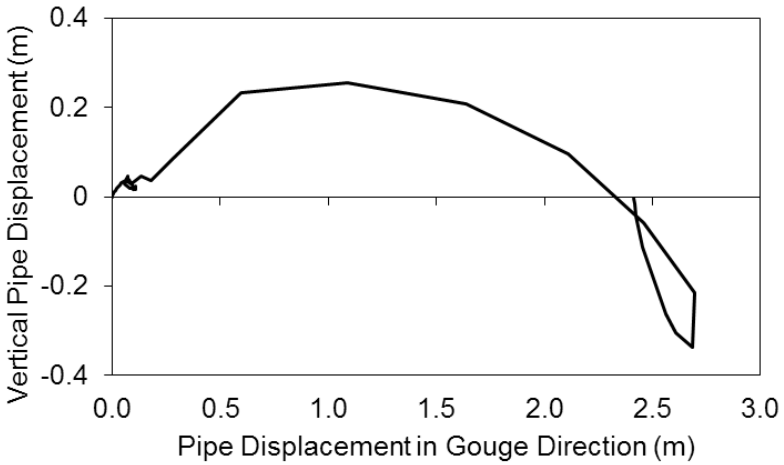

Figure 6.44. Pipe trajectory at gouge centerline

Based on the coupled CEL simulations, the distribution of horizontal subgouge soil deformations (i.e. direction of ice keel motion), at the pipe springline, was moderated by the presence of the pipeline, particularly within the gouge width zone (Figure 6.45a). The free-field CEL simulations predicted relatively higher (by a factor of 1.25) subgouge

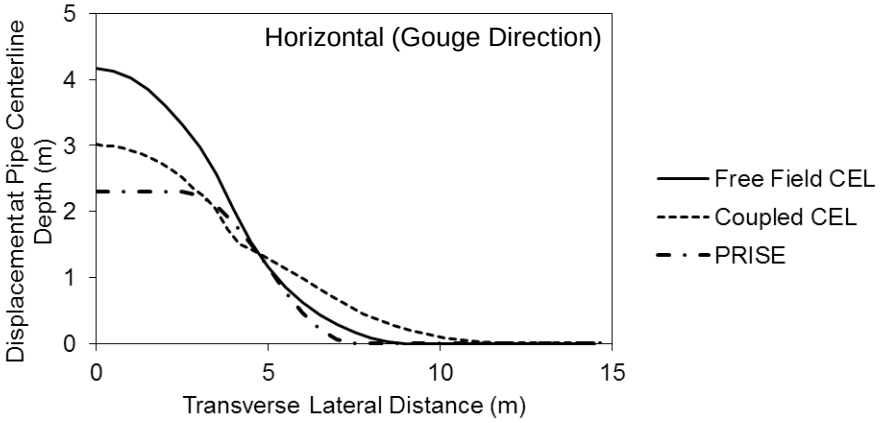

a)

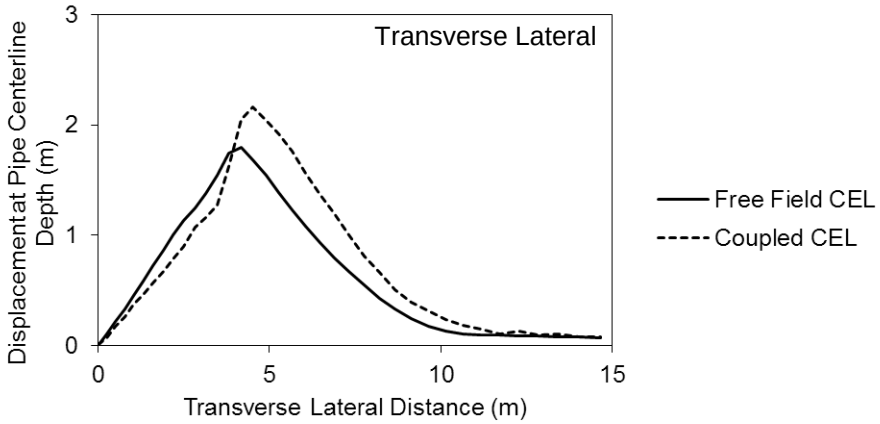

b)

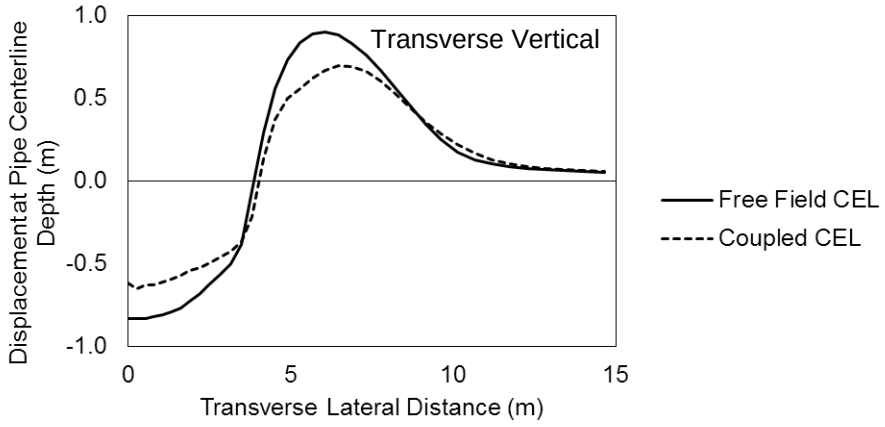

c)

Figure 6.45. Comparison of free-field and coupled CEL subgouge soil displacements at the pipe springline

soil deformations, whereas the PRISE model predicted comparatively lower (by a factor of 0.75) subgouge soil deformations. At the ice gouge width (5 m) boundary, the three modelling approaches predicted similar magnitude of horizontal subgouge soil deformations. For a distance of one gouge width from the ice keel centerline, the coupled CEL simulation predicted greater soil motion, which is consistent with the literature (e.g. Kenny et al., 2007b; Phillips et al., 2010) and may be attributed to interaction effects with the buried pipe. The peak magnitude and "sinusoidal" attenuation with increasing distance from the gouge centerline is generally consistent with the PRISE model. As shown in Figure 6.45b, based on the CEL simulations the distribution of transverse lateral (i.e. directed along the pipe length, normal to the direction of ice keel motion in the horizontal plane) subgouge soil deformations was not significantly influenced by the pipeline. The pipeline tends to divert soil flow along the pipe axis that builds up to the edge of the ice keel width in response to the changing boundary conditions and pipeline curvature.

The distribution of transverse vertical (i.e. normal to the direction of ice keel motion in the vertical plane) subgouge soil displacements was moderated by the pipeline and exhibited a reduction in the relative magnitude when compared with the free-field CEL simulations. It is expected this response would be influenced by other factors including the ice gouge geometry (e.g. depth, width), soil properties (e.g. plastic flow, compressibility, dilatation) and pipeline geometry (e.g. diameter, burial depth, cover depth).

The analysis demonstrates the importance of model bias when establishing the magnitude and distribution of the three-dimensional subgouge soil deformation field. The corresponding influence on the pipeline mechanical response is addressed in later sections.

6.3.3 Relative Performance of Structural and Continuum Modelling Techniques – Parameter Case Study

6.3.3.1 Overview

For the decoupled structural (pipe/soil) modelling procedures, the subgouge soil deformation field was established by using (1) the PRISE empirical model, and the predicted subgouge soil deformation field at the pipe springline based on (2) free-field (i.e. ice keel/soil) and (3) coupled (i.e. ice keel/soil/pipe) ice gouge events using continuum CEL simulations. The soil spring resistance curves were established using either (1) the PRCI (2009) recommendations, or (2) plane strain continuum CEL finite element simulations. The fully coupled (i.e. ice keel/seabed/pipe interaction) CEL simulations the modelling procedures explicitly incorporate the subgouge soil deformation fields and soil constitutive behaviour (i.e. load-displacement relationships). The technical basis for these models was presented in the previous section.

This parameter case study only provides a preliminary assessment on the effects of superposition error and directional load decoupling effects on the soil and pipe mechanical response. The problem involves complex, interdependent relationships with respect to the driving forces, kinematic constraints and boundary conditions (e.g. ice

gouge depth, width, attack angle, bearing pressure), soil mechanics (e.g. type, strength properties, dilation) and pipeline characteristics (e.g. diameter, burial depth). For example, deep and narrow keels will impose a “point load” with fewer constraints in comparison with a wider ice gouge event where plane strain conditions prevail near the keel centerline. A larger diameter pipeline located at shallow burial depths will have greater interference effects on the soil kinematics and deformation field than smaller diameter pipeline located at the same burial depth.

6.3.3.2 Decoupled Structural Model: Parameter Analysis

In this section, sensitivity of the decoupled structural model in terms of the predicted pipeline mechanical response is examined with respect to different technical approaches for defining the magnitude and distribution of the subgouge soil deformation field, and the soil spring load-displacement relationships. In the figures presented, the legend has used an annotation scheme characterizing the engineering models used in this study in order to facilitate interpretation. The legend format is (Soil Subgouge Displacement Field Model, Soil Spring Model) where the modelling approach used to define the soil subgouge displacement field can be expressed as (PRISE, Free Field CEL, or Coupled CEL), and the modelling approach used to define the soil spring load-displacement relationships can be expressed as (PRISE, CEL). For example, the decoupled structural model employing the PRISE empirical subgouge deformation field with the CEL simulation to define the soil behaviour would be annotated (PRISE, CEL). Table 6.7 summarizes the 6 permutations examined in this study.

For all simulations, the finite element model and described in Section 4.5 was utilized. The pipeline half-length (5,030 m) was discretized with a constant pipe element length of 0.5 m (approximately one pipe diameter).

Table 6.7. Structural model analysis definition

Subgouge Soil Deformation Field	Soil Spring Resistance	Figure Notation
PRISE (Woodworth-Lynas, 1996)	PRCI (2009)	(PRISE, PRCI)
PRISE (Woodworth-Lynas, 1996)	Plane strain CEL	(PRISE, CEL)
Free-Field CEL	PRCI (2009)	(Free-Field CEL, PRCI)
Free-Field CEL	Plane strain CEL	(Free-Field CEL, CEL)
Coupled CEL	PRCI (2009)	(Coupled CEL, PRCI)
Coupled CEL	Plane strain CEL	(Coupled CEL, CEL)

The original PRISE engineering model was developed with empirical expressions that characterized the subgouge soil displacement field in the horizontal plane along the direction of ice keel motion for steady-state events (Woodworth-Lynas et al., 1996). A tentative equation was proposed for the magnitude and distribution of vertical, downward subgouge soil deformations at the gouge centerline (e.g. Phillips et al., 2010; Woodworth-Lynas et al., 1996). To simplify the computational effort, a number of studies have not considered the effects of vertical soil movement when using decoupled structural engineering models to predict the effects of ice gouge events on buried pipelines (Been et al., 2013; Kenny et al., 2000; Lanan et al., 2001; Nixon et a., 1996). In this study, for the

decoupled structural models using the PRISE empirical model for subgouge deformations, the influence of vertical subgouge soil displacement was not considered.

For the decoupled structural modelling analysis, the pipe displacement response in the horizontal (i.e. in the direction of ice keel translation), transverse lateral (i.e. pipe longitudinal axis) and transverse vertical directions shown in Figure 6.46. Differences in the predicted pipe response can be explained in reference to the imposed subgouge soil deformation field (Figure 6.45) and soil spring load-displacement relationships (Figure 6.42). The pipeline response is governed by complex interaction and dependencies with pipe mechanical properties (i.e. axial and bending stiffness), and the magnitude and distribution of geotechnical loads (i.e. soil spring yield force, mobilization distance) and imposed kinematic boundary conditions (i.e. subgouge soil displacement field), which ultimately influence the pipe deformation and strain response (i.e. axial feed-in, curvature).

Although different modelling procedures were incorporated, the pipe deformation response exhibits common attributes. The lateral (Figure 6.46a), axial pipe (Figure 6.46b) and vertical (Figure 6.46c) pipe displacement response exhibited a nonlinear distribution with distance from the ice keel centerline and were influenced by the boundary conditions associated with the ice keel width (i.e. inflection points in the response at an axial distance of 5 m). The lateral and vertical pipe displacement response attenuated within 1.5 gouge widths from the ice keel centerline. Attenuation of the axial displacement field requires much longer distances to mobilize the virtual anchor through the distributed longitudinal soil forces.

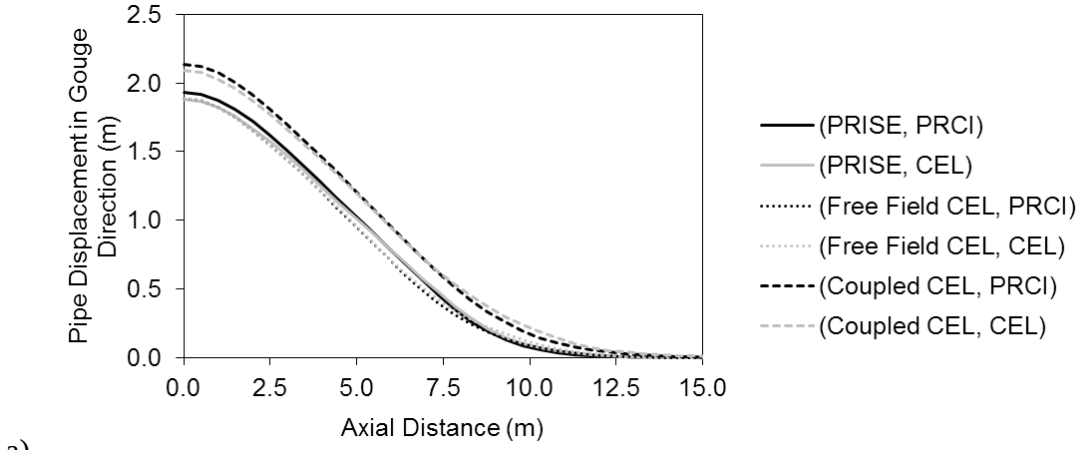

a)

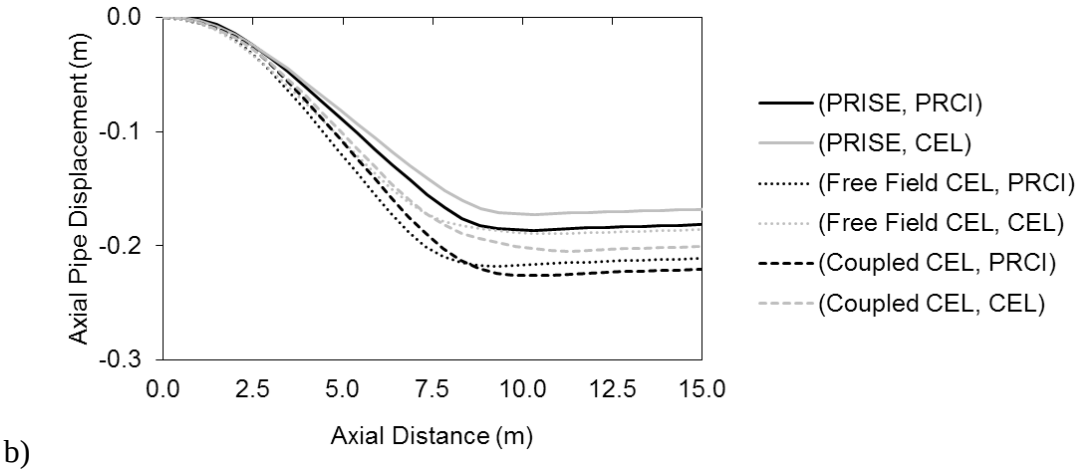

b)

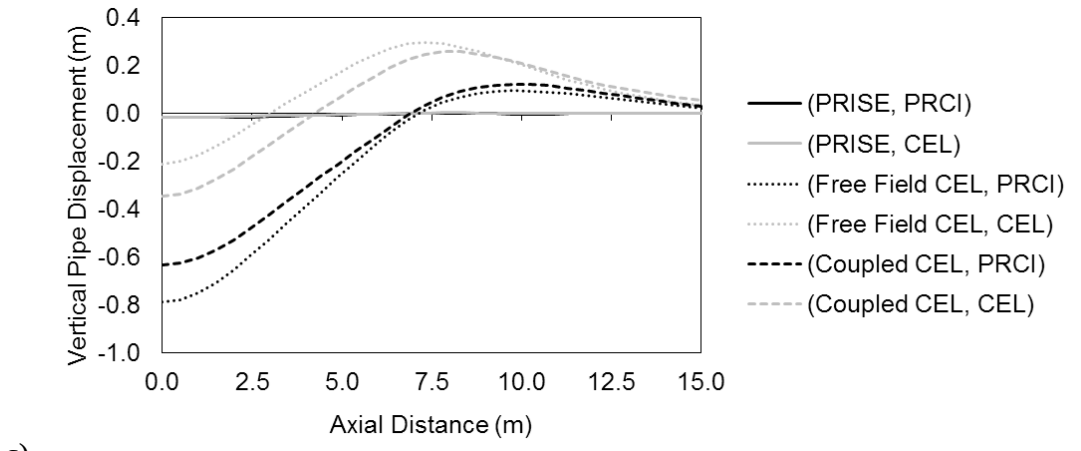

c)

Figure 6.46. Structural model pipe displacements

The lateral (Figure 6.46a) and axial pipe displacement response (Figure 6.46b) was primarily influenced by the magnitude and distribution (attenuation) of subgouge soil deformations (Figure 6.45). The soil load-displacement relationships (PRCI, CEL) in the lateral direction (Figure 6.42a) were effectively similar, and identical for the axial (Figure 6.42d) loading direction. As shown in (Figure 6.42), the mobilization distance to yield are fractions of the pipe diameter and thus the geotechnical loads are primarily distributed plastic forces in the zone of interest. Somewhat counterintuitive, the structural models using the coupled CEL subgouge soil deformation field exhibited the largest displacement relative to the other modelling approaches. The lateral (a) pipe displacement response suggests the simulations were also influenced by model bias due to the superposition error, where the structural models using the coupled CEL subgouge soil deformation field have a different response in comparison with the models using free-field subgouge soil deformations.

Variation in the vertical pipe displacement response (Figure 6.46c) is primarily related to the vertical uplift and bearing soil reaction forces (Figure 6.42b,c) that directly influences the pipe curvature response and shaped by the subgouge soil deformation field (Figure 6.45c). The CEL soil springs have greater bearing resistance and lower clamping forces (i.e. uplift) that results in reduced relative downward pipe movement with greater uplift response and difference in pipe curvature (Figure 6.46c). The PRISE empirical model does not explicitly account for vertical subgouge displacement and thus does not influence the pipe response.

The longitudinal distribution of pipeline logarithmic axial strain is shown in Figure 6.47 with an inset schematic illustration of the pipe tension (T) and compression (C) faces shown in Figure 6.47a. At the ice keel centerline, the peak strain response is observed with the trailing pipe face in tension (Figure 6.47a) and the leading pipe face in compression (Figure 6.47b). Due to the pipeline deformation and curvature response, the axial strains change sense at inflection points along the pipeline length with the inflection point associated with the boundary conditons with the edge of the ice keel at distance of 0.5 gouge width (5 m) from the ice keel centerline.

Although the structural models incorporating the coupled CEL subgouge soil deformation field and CEL soil spring load-displacement relationships had the largest magnitude of pipe lateral and axial displacement (Figure 6.46a,b), the maximum pipe strain response (both tension and compression) was associated with the free-field CEL subgouge soil displacements and PRCI (2009) soil spring resistance curves. The use of a coupled CEL subgouge soil deformation field provides some reduction on the strain response, which can be attributed to superposition effects, but the results have less significance than reported by Peek and Nobahar (2012). The minimum pipe strain response were predicted when using the two-dimensional PRISE subgouge soil deformation model, however, this approach does not include any vertical component of subgouge soil deformations and thus underestimates the pipe strain response.

Tensile strain values exceeding 2% and compression strain values exceeding 1% will require further detailed assessment through laboratory testing, and physical and numerical modelling. Project specific pipeline mechanical performance criteria will need

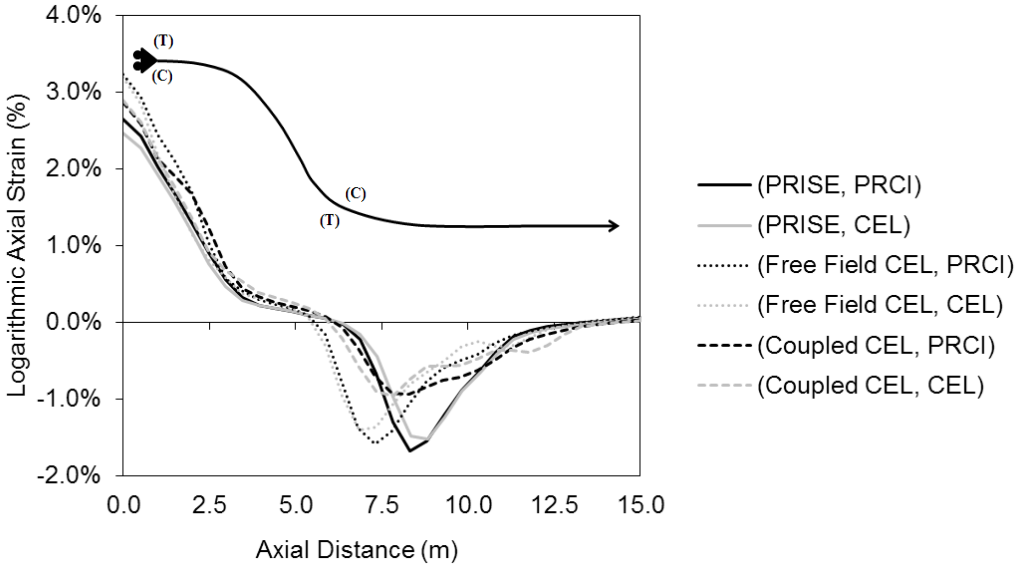

a)

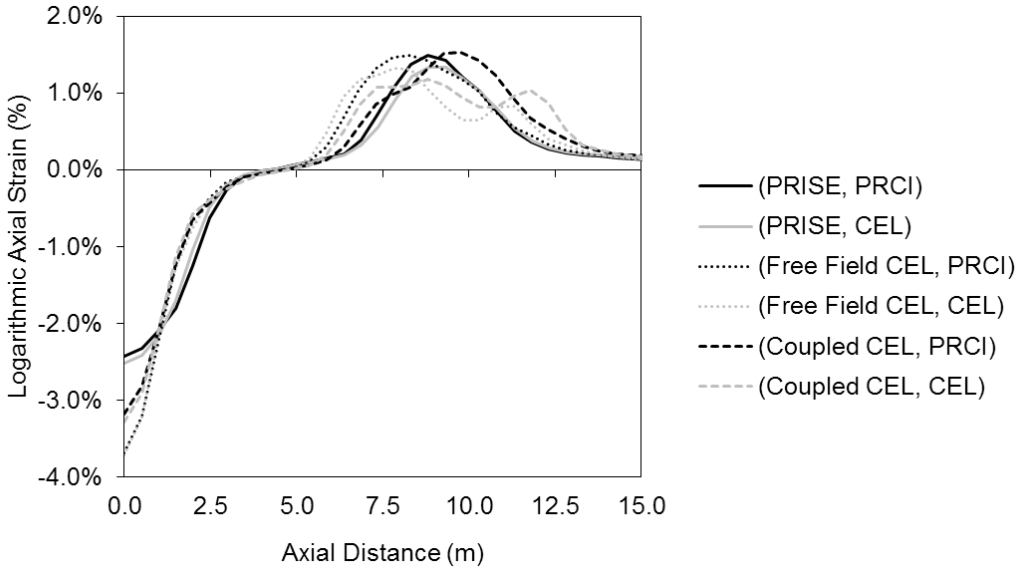

b)

Figure 6.47. Distribution of logarithmic axial strain for the decoupled structural models for the a) trailing and b) leading edges of the pipe

to be established with respect to the girth weld capacity (i.e. leakage and burst limit states) and local section stability (i.e ovalization and buckling for serviceability and ultimate limit states, respectively); see for example Fairchild et al., (2014), Fatemi and Kenny, (2011,2012), Kenny et al., (2016), Kibey et al. (2010) and Wang et al. (2007).

In the preceding case studies, the lower bound adhesion factor ($\alpha = 0.22$), as defined by the PRCI (2009) guidelines, was used to define the axial soil resistance, which primarily influence pipeline axial feed-in and curvature. Using the coupled CEL subgouge soil deformation field, the significance of an upper bound adhesion factor ($\alpha = 0.54$) on the pipe axial strain response was examined. The upper bound and lower bound adhesion factors correspond with an ultimate axial soil resistance of 38.7 kN/m and 16 kN/m, respectively.

As shown in Figure 6.48, the logarithmic compressive axial strain was reduced by a factor of 0.7 when using the upper bound adhesion factor. Hence, this is a case where the lower bound adhesion factor conservatively leads to higher pipe strains due to the increased axial feed-in effects. The adhesion factors derived from physical tests (e.g. Paulin et al., 1998; Cappelletto et al., 1998) at $s_u \approx 50$ kPa give a range from approximately 0.15 to 0.4. The lower bound approximation ($\alpha = 0.22$ at $s_u = 50$ kPa) is within range of the test data, and provides a conservative result; hence, there may be some incentive to increase the axial resistance towards the upper bound adhesion level to reduce the axial feed-in. This outcome has significant implications on pipeline engineering design (e.g. see Kenny et al, 2007b,2004,2000) with respect to target burial

depth requirements to satisfy pipe mechanical performance criteria (e.g. tensile strain at girth welds, local buckling).

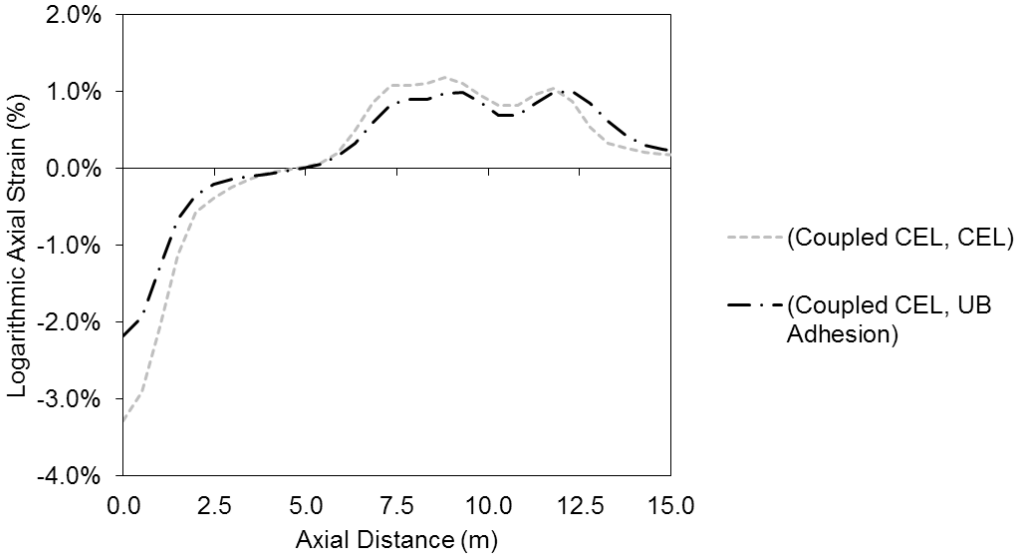

Figure 6.48. Effect of adhesion factor on structural pipe compressive strain (α_{LB} = 0.22, α_{UB} = 0.54)

6.3.3.3 Comparison Between Structural and Fully Coupled Continuum Models

To address the last objective for this study, as shown in Figure 6.49, the fully coupled, continuum CEL modelling procedures (Contin. Coupled CEL) exhibited comparatively larger lateral (Figure 6.49a) and axial (Figure 6.49b) pipe displacement response than the corresponding predictions when using structural modelling procedures. For the continuum coupled CEL model, the pipeline experiences a maximum displaced

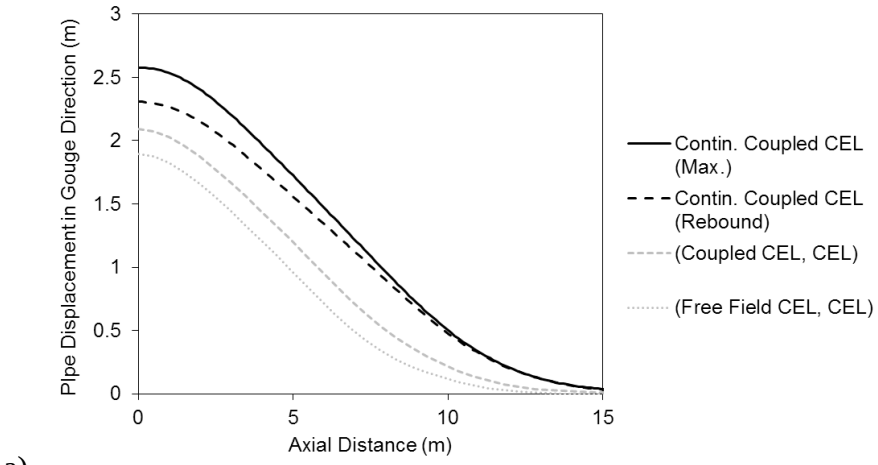

a)

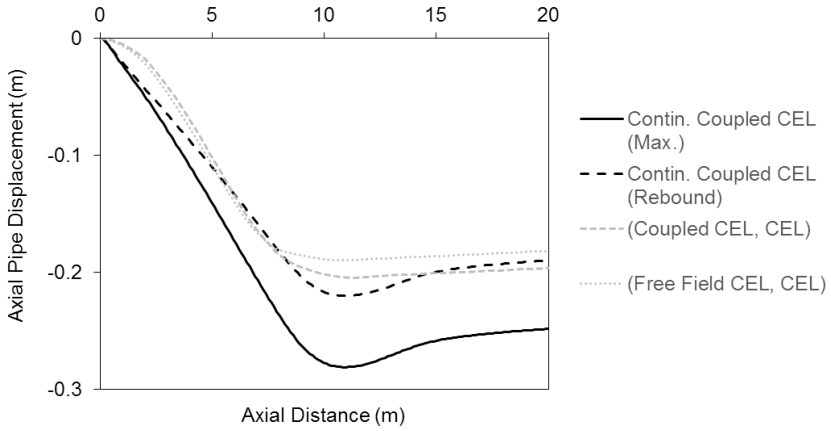

b)

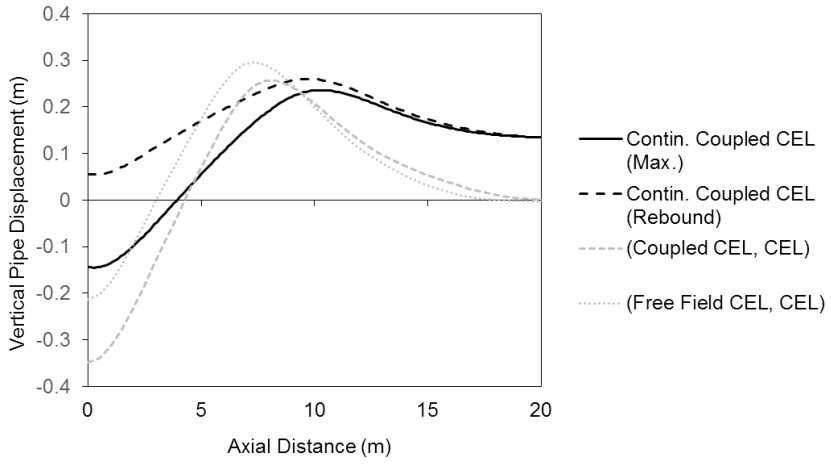

c)

Figure 6.49. Structural and continuum pipe displacements along the pipe axis

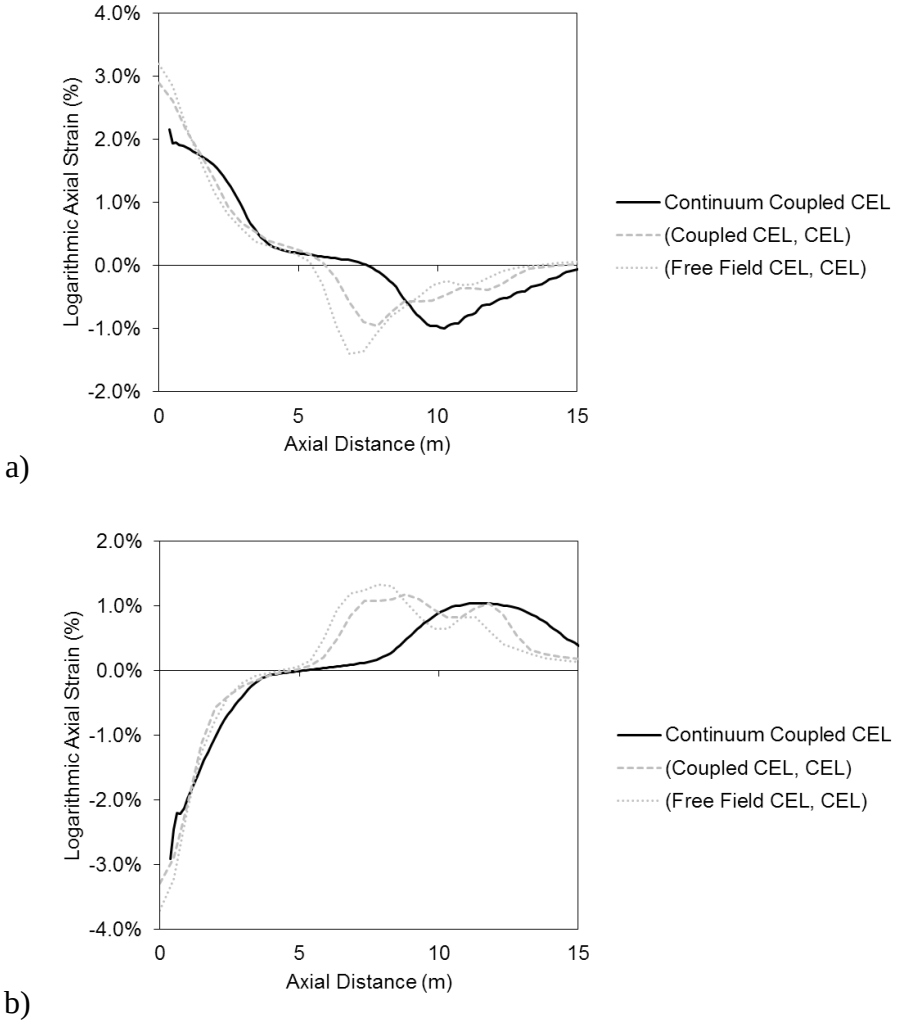

Figure 6.50. Comparative distribution of logarithmic axial strain for the decoupled structural models (Coupled CEL, CEL & Free Field CEL, CEL) and fully coupled continuum model along the a) trailing and b) leading edges of the pipeline

configuration (Max.) as the ice keel passes over the pipe, and then rebounds (Rebound) through elastic unloading after the ice keel has travelled past the pipe centerline. In the structural modelling procedures, the magnitude and distribution of the subgouge soil deformation field is based on the steady state (Max.) condition.

Similar to the primary outcome for the structural model parameter study, although the fully coupled, continuum CEL models predict higher lateral and axial deformations, the pipe curvature is moderated and thus exhibits a lower magnitude of logarithmic axial pipe strain (Figure 6.50). At the pipe centerline, where axial strains have the largest magnitude, the structural models predict higher compressive and tensile axial strain magnitudes by a factor of 1.3 and 1.6, respectively. The importance of superposition error in predicting pipe mechanical response for ice gouge events has been demonstrated, however, the impact may be less significant than previously considered and requires further investigation across a broader parameter range. The significance of directional lo ad decoupling on the simulation of ice gouge events also requires further study to determine how the strain fields illustrated in Figure 6.50 may "line up" and converge.

Although there are valid criticisms and caveats when using the Winkler-type model, based on the outcomes from this study there remains further research needed to establish the practical limits of application and bound envelope on conservatisms when addressing the ice gouge problem. As discussed by Sancio et al. (2011) and Been et al. (2013), the importance of coupled ice/soil/pipeline interaction models should, and will likely, play a role in pipeline engineering practice when evaluating ice gouge events.

6.3.4 Summary

A comparative performance assessment of structural and coupled continuum finite element modelling procedures to simulate ice gouge effects on buried pipelines was conducted. The parameter case study examined the model error associated with the engineering basis used to define the subgouge soil deformation field and soil load-

displacement relationships. Empirical models, industry practice guidelines and CEL simulations were used in this study. The primary goals for this investigation were to evaluate the significance of superposition error and infer the importance of directional load coupling effects across the numerical simulation framework on a consistent and equivalent basis.

Although the structural models predict conservative estimates of the pipe axial strain response, the relative discrepancy with continuum simulations was not as significant as suggested by previous studies (e.g. Kenny et al., 2007b, Konuk et al., 2006) for the parameters examined. Based on the decoupled structural model, the adhesion factor was shown to have a considerable impact on reducing the peak strain level at the pipe centerline due to increased soil resistance for pipe axial feed-in. The study highlighted areas where the decoupled structural modelling procedures can be deficient that include the importance to incorporate the effects of vertical subgouge soil deformations, elastic unloading (springback) and pipe trajectory during a gouge event.

Further research is needed to explore the significance of directional load coupling (e.g. Phillips and Barrett, 2012) and superposition error (e.g. Peek and Nobahar, 2012) for ice gouge events across a wider parameter range. This may include characterization of the ice keel (e.g. depth, width, attack angle, shape), soil (e.g. type, strength, stratification, native and backfill conditions), and pipeline (e.g. diameter, clearance or cover depth, axial pipe/soil adhesion or interface properties, contact mechanics). This will further delineate the relative performance between structural and coupled continuum modelling procedures. For example, it is expected the relative pipe/soil stiffness and interference

effects on subgouge soil deformations will be more significantly influenced by larger diameter pipelines with small clearance distances between the base of the ice keel and pipeline crown. There is also the need to conduct laboratory investigations to further refine soil constitutive models and physical modelling to verify the coupled continuum finite element modelling procedures.

6.4 Numerical Modelling of Lateral Pipe/Soil Interaction in Granular Material

The objectives of the collaborative research program between Memorial University, Queen's University and the Wood Group were defined above in Section 5.1. In parallel with the physical testing program, the author was responsible for the numerical modelling aspects where the goal was to develop a robust finite element tool that incorporated realistic granular material behaviour in order to accurately capture the force-displacement response during lateral pipe/soil interaction and the strain localization mechanisms that were captured in the physical testing program through PIV analysis. The CEL finite element model for lateral pipe/soil interaction was described in Section 4.3. The general and specific aspects of the soil constitutive model for synthetic olivine sand were presented throughout Section 3.2.

This Section describes the application of the CEL finite element modelling technique to simulate the current study large-scale test dataset using the outlined constitutive modelling procedures. The development and use of the CEL method for pipe/soil interaction accounting for nonlinear constitutive soil behaviour using the subroutine described above, is a novel contribution.

The present study tools for simulating pipe/soil interaction in cohesionless soils were developed in the context of application to more complex pipeline geohazard interaction scenarios such as ice/soil/pipeline interaction; hence, the use of the CEL method that can accommodate severe soil deformation was selected. In addition, the modified Mohr Coulomb soil constitutive model for granular materials was formulated for three-dimensional finite element models, rather than purely plane strain two-dimensional applications (e.g. Roy et al., 2015). For large relative pipe movements in soil, the CEL method provides a robust modelling framework whereby the potential applications are not limited as with the Lagrangian and ALE schemes that experience mesh distortion and convergence issues.

6.4.1 Finite Element Analysis of Queen's Lateral Pipe/Soil Interaction Tests

As discussed above, 3D numerical tools were developed for pipe/soil interaction that can accommodate large soil deformation. The CEL formulation is particularly well suited for modelling complex scenarios such as large deformation geohazards that involve soil/structure interaction with both rigid and deformable structures. The large scale tests conducted at the Queen's University GeoEngineering Center were simulated using the CEL model in order to validate the modelling framework for a subset of the more complex ice/soil/pipeline interaction scenario. As with any FE study, it is recommended that confidence is established in the modelling procedures incrementally; i.e. starting with a simple model or a subset of the larger more complex scenario. This is especially important where multiple bodies are involved in complex contact interactions.

The CEL model described in Section 4.2.5 was applied to simulate the dense tests conducted at H/D = 1.0 and H/D = 3.0 in dense sand. A deeper case at H/D = 7.0 was also simulated for dense conditions, though the physical test program did not include a test at this depth under dense conditions. A modified Mohr-Coulomb model was utilized to capture nonlinear strain hardening and softening and pressure effects on the peak friction and dilation angles. The parameters were discussed in Section 3.2.3, and the mobilization of effective friction angle and dilation angle was applied using the nonlinear hardening and softening model described in Section 2.4.4.2.

The CEL analysis results were compared to the physical test data to assess the capability of the numerical and constitutive modelling procedures to reasonably capture the force-displacement response, pipe trajectory and localization of shear strain in the form of shear bands.

6.4.2 Description of Constitutive Model Sensitivity Parameters

A sensitivity study was conducted to examine the influence of the enhanced constitutive model on the pipe/soil interaction force-displacement response and strain localization. The elastic modulus was defined using the Janbu (1963) parameters K = 340 and n = 0.41 as described in Section 3.2.2.2. The Poisson's ratio was assumed $\nu = 0.4$ to reflect minimal compression before dilation that is observed for dense sand at low stress levels. The elastic parameters were kept consistent in all analysis cases. The cohesion was kept to a minimal amount equal to 0.25 kPa in all analysis cases. The constitutive parameters used for the comparison are summarized in the following Table 6.8.

Table 6.8. Constitutive model sensitivity study (plasticity)

Case	$\phi'_p{}^{tx}$	$\phi'_p{}^{tx}$ (max)	ϕ'_{cv}	ψ	ψ (max)	$\phi'_p{}^{ps}$	$\phi'_p{}^{ps}$ (max)
1	--	--	--	0.0	--	45.0	--
2	--	--	--	20.0	--	61.0	--
3	--	--	45.0	--	20.0	--	61.0
4	Eq. (6.7)	54.6	45.0	$\frac{\phi'^{tx}_p - \phi'_{cv}}{0.48}$	20.0	$\phi'_{cv} + 0.8\psi$	61.0
5	Eq. (6.7)	57.0	45.0	$\frac{\phi'^{tx}_p - \phi'_{cv}}{0.6}$	20.0	$\phi'_{cv} + 0.8\psi$	61.0

The first two cases examine the influence of constant friction and dilation angles on the lateral pipe/soil interaction response. In Case 1, the assumed critical state friction angle ϕ'_{cv} = 45° is used, and the critical state nondilatant assumption ψ = 0° is also enforced. Case 2 considers a constant dilation angle ψ = 20°, with a constant peak friction angle estimated as $\phi'_p{}^{ps}$ = 61.0 according to Bolton's (1986) plane strain flow rule. Hence, the response in Case 1 should provide a minimum soil resistance to pipe movement, and the nondilatant volumetric response should result in minimum pipe uplift. On the other hand, in Case 2 the constant peak friction angle should provide an upper bound soil resistance and the constant peak dilation angle should provide maximum pipe uplift due to the continual volumetric expansion with shear strain.

Since the physical test observations in dense sand show a clear peak horizontal bearing capacity factor, with post-peak softening, enhancements to the soil constitutive

behavior are necessary to account for realistic soil behavior that also exhibits peak and post-peak softening behavior. Case 3 considers mobilized friction and dilation angles varying with increased deviatoric strain, while pressure dependency is not enforced. This establishes a baseline case to compare with Case 4 and Case 5 that consider the peak friction angle as a function of mean effective stress in addition to strain softening and hardening.

As described in Section 3.2.3, the peak triaxial friction angle can be estimated based on the mean effective stress, p' at failure. This equation is repeated here with a new equation number for ease of reference:

$$\phi'^{tx}_{p} = -12.73 \log p' + 78.8 \tag{6.7}$$

The dilation angle is assumed to be consistent between triaxial and plane strain conditions, as is the critical state friction angle, in line with Bolton's (1986) study. As discussed in Section 2.4.2, the critical state friction angle can be slightly higher in plane strain compared to triaxial compression conditions, and the residual friction angle (e.g. Rowe's friction angle ϕ_f) has also been shown to increase with decreasing confining stress. These effects can be examined through sensitivity study to test the influence of the large displacement friction angle on the residual soil resistance against lateral pipe movement.

The peak dilation angle varies with the peak triaxial compression friction angle based on the following equation that follows Bolton's (1986) form:

$$\psi_p = \frac{\phi'^{txc}_{p} - \phi'_{cv}}{r} \tag{6.8}$$

The coefficient r has been shown to vary from approximately 0.5 to 0.6, as shown in Section 2.4.1.2. A sensitivity analysis is conducted to examine the influence of Equation (6.8) on the pipe/soil interaction simulation with Case 4 and Case 5 using 0.48 and 0.6, for the coefficient r, respectively. The dilation angle is limited to 20° in accordance with Rowe's (1962) suggested maximum dilatancy factor. Similarly, since the triaxial compression friction angle relationship can predict high friction angles at low confining pressure, which cannot be verified from available test data, then $\phi'_p{}^{tx}$ is also limited based on Bolton's (1986) flow rule.

The equations defining the hardening and softening of the peak friction and dilation angles were presented in Section 2.4.4.2 and are repeated here for ease of reference (note that in the following equations, the deviatoric strain replaces the accumulated strain). The hardening region is defined by:

$$\phi'_m = \phi'_o + \sin\left(\frac{2\sqrt{\gamma^p \gamma_p^p}}{\gamma^p + \gamma_p^p}\right)\sin\left(\phi'_p - \phi'_o\right) \tag{6.9}$$

and the softening region is defined by:

$$\phi'_m = \phi'_{cv} + \left(\phi'_p - \phi'_{cv}\right) \times \exp\left[-\left(\frac{\gamma^p - \gamma_p^p}{\gamma_c^p}\right)^2\right] \tag{6.10}$$

The parameters $\gamma_p{}^p$ and $\gamma_p{}^p$ are calibrated based on the FE simulation of the triaxial test data as summarized in Section 3.2.3, with each parameter set equal to 0.08. The initial friction angle ϕ'_o is estimated taken as the approximated interparticle friction angle 40.2° based on Horne (1965).

Based on the parameters outlined above, the variation of peak friction and dilation angles with mean effective stress for triaxial compression and plane strain conditions are plotted for Case 4 and Case 5 in Figure 6.51 and Figure 6.52. Further laboratory testing (triaxial compression and plane strain) is required to provide the necessary data to better calibrate the strength-dilatancy relationship parameters.

Each case summarized above is applied to numerical simulations of the tests that were conducted under dense conditions at H/D = 1 and H/D = 3. The following subsections describe the results of the analysis in terms of the pipe/soil interaction force-displacement response, pipe vertical displacement, and numerical capture of the strain localization observed through PIV techniques from the physical tests.

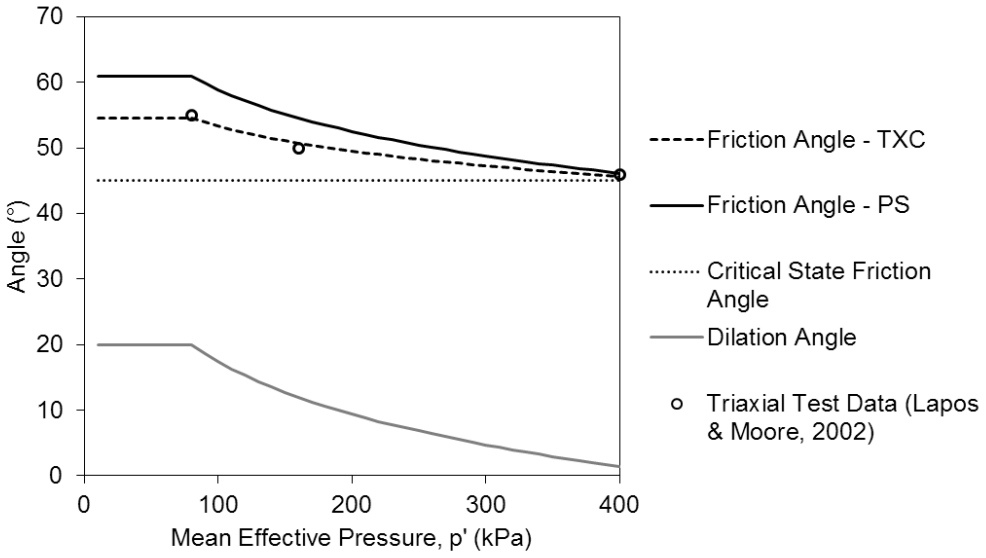

Figure 6.51. Case 4 variation of parameters

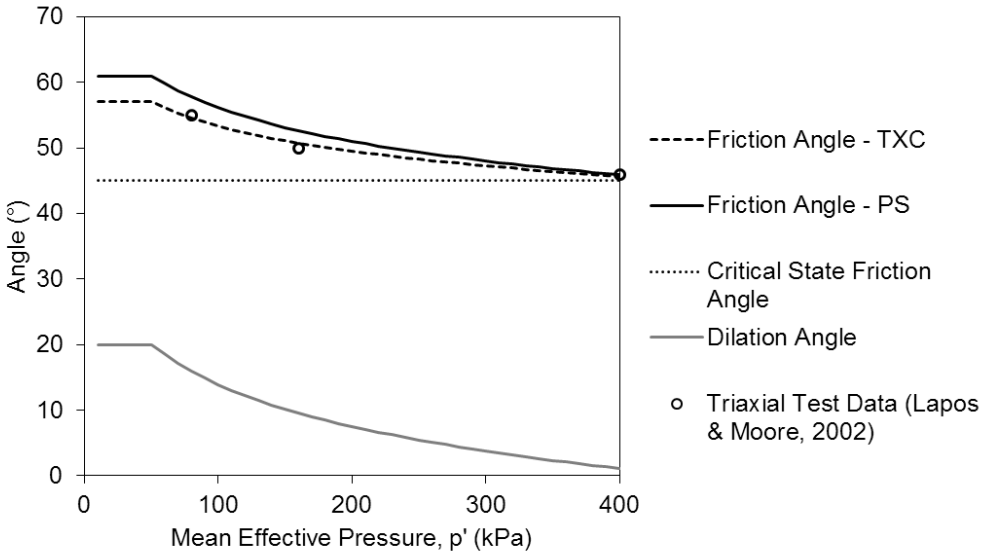

Figure 6.52. Case 5 variation of parameters

6.4.3 Mesh Sensitivity Study

The objective of this section is to establish the sensitivity of both the built-in Mohr-Coulomb (MC, Section 3.2.1) and the modified Mohr-Coulomb (MMC, Section 3.2.2) model to changes in the mesh size. The Case 1 and Case 3 (Table 6.8) constitutive parameters are selected for the comparison. The influence of varying the mesh size is assessed in terms of the force-displacement, pipe uplift and strain localization response.

The element sizes (i.e. characteristic edge length), d_{FE}, selected for the comparison are based on the estimated shear band thickness, $d_B = 16\ d_{50}$ (Muhlhaus and Vardoulakis, 1987). The mean grain size d_{50} = 0.74 mm was estimated based on the grain size distribution of synthetic olivine (Figure 3.14); hence, the estimated shear band thickness is d_B = 12 mm. The element sizes for the sensitivity are summarized in Table 6.9. As discussed in Section 4.1.3, a rectangular grid of uniformly sized Eulerian elements is

recommended best practice by Abaqus (2016) to attain accurate results; this approach has been adopted in the current study.

Table 6.9. Mesh sensitivity element sizes

Case	Element Size, d_{FE} (mm)
A	$d_{FE} = d_B = 12$ mm
B	$d_{FE} = 2\ d_B = 24$ mm
C	$d_{FE} = 3\ d_B = 36$ mm
D	$d_{FE} = 4\ d_B = 48$ mm

6.4.3.1 Mohr-Coulomb Model (H/D = 3)

The Case 1 (Table 6.8) parameters were used to assess the mesh sensitivity for element sizes summarized in Table 6.9; thus the sensitivity analysis cases are denoted Case 1A to 1D.

6.4.3.1.1 Force-Displacement and Pipe Uplift Response (MC)

The force-displacement mesh sensitivity results show that the peak bearing capacity factor compares well for the range of mesh density considered (Figure 6.53). The initial peak N_{qh} for Case 1D is around 7.2 compared to about 8 for Case 1A to 1C, however, the residual N_{qh} is in good agreement.

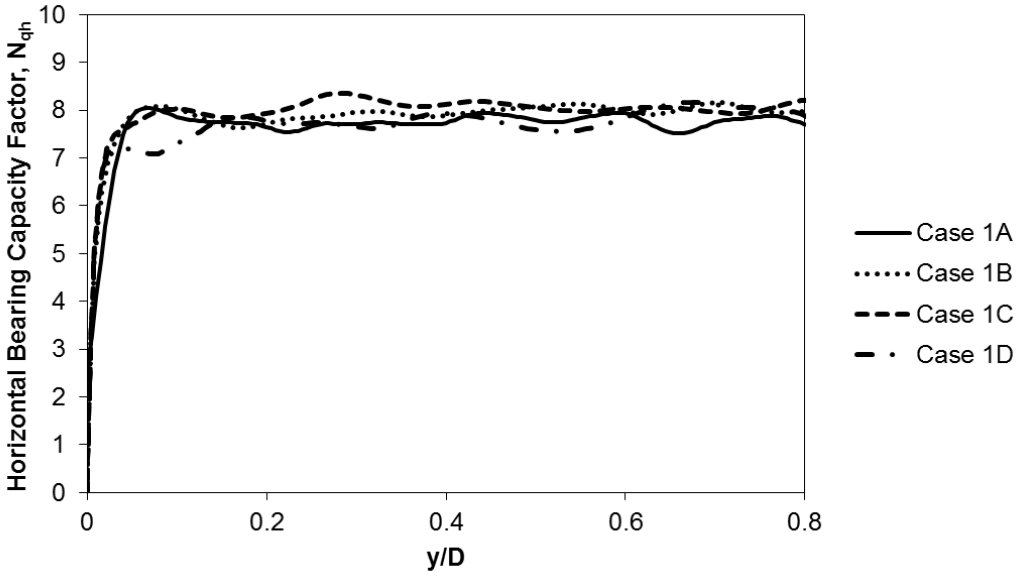

Figure 6.53. Force-displacement response mesh sensitivity (MC; H/D = 3)

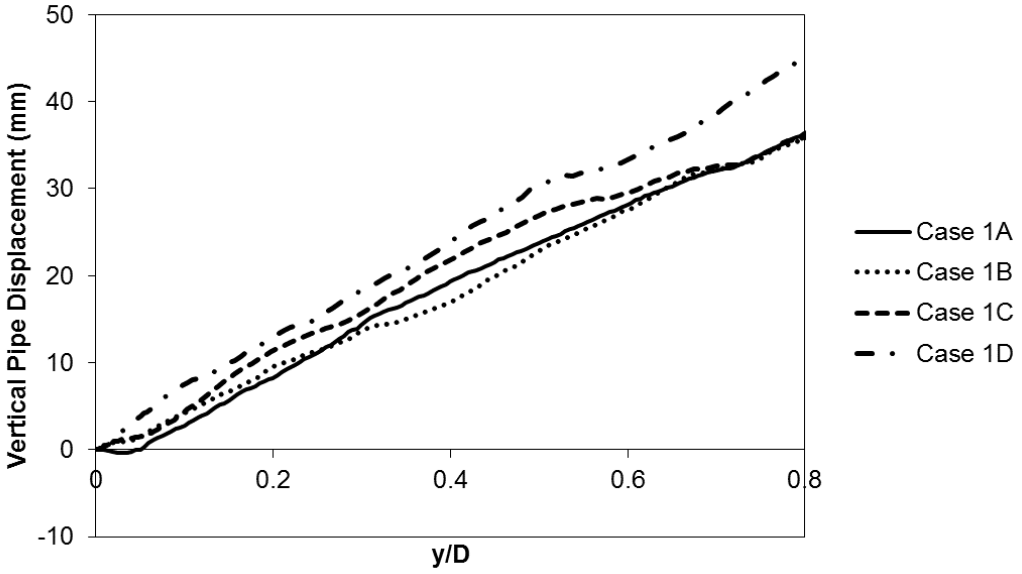

Figure 6.54. Pipe uplift response mesh sensitivity (H/D = 3)

The pipe uplift mesh sensitivity results (Figure 6.54) show that the Case 1C and 1D response tends to diverge from Case 1A. The Case 1B response is very similar to Case 1A. Based on convergence in both the force-displacement and pipe uplift response for Case 1A and 1B, it appears that Case 1B provides sufficient mesh density. The Case 1B element size d_{FE} = 24 mm is approximately 0.1 D. The mesh sensitivity is further explored by examining the localization of plastic deviatoric strain in the next subsection.

6.4.3.1.2 Soil Strain Localization (MC)

The following Figure 6.55 to Figure 6.58 show the plastic deviatoric strain (Equation 3.21) contours for Case 1A to 1D respectively, at a relative pipe displacement of 0.5 D. The strain contour level is capped at 1.0 (or 100%) in each figure to show the extent of strain localization on a consistent basis. In each case, there is a discernible pattern showing three shear bands that define the passive wedge (primary band on leading side of the pipe) and active wedge (secondary and tertiary bands on the trailing side of the pipe). However, the strains exceeding 100% are decreasingly localized from Case 1A to 1D. The infill behind the pipe increases with decreasing element size. The thickness over which the strain localization occurs (shear band thickness) increases with element size.

6.4.3.2 Modified Mohr-Coulomb Model (H/D = 3)

The Case 3 (Table 6.8) parameters were used to assess the mesh sensitivity for element sizes summarized in Table 6.9; thus the sensitivity analysis cases are denoted Case 3A to 3D.

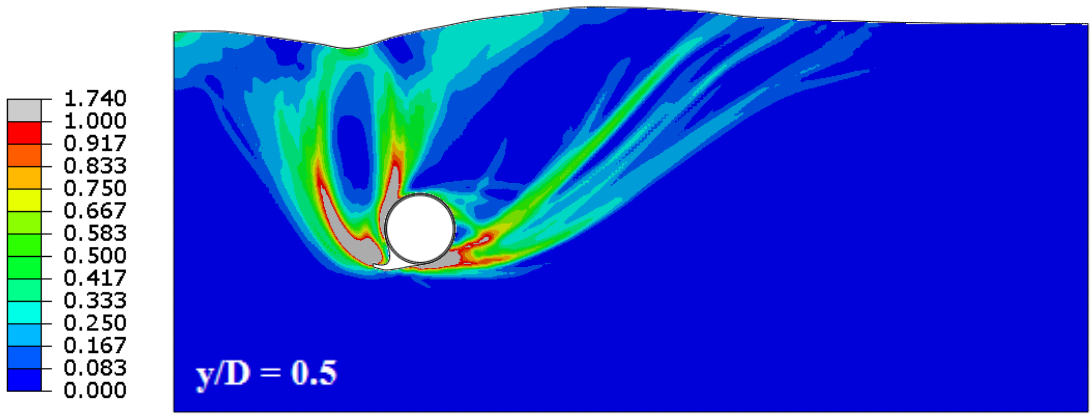

Figure 6.55. Case 1A plastic deviatoric strain contour

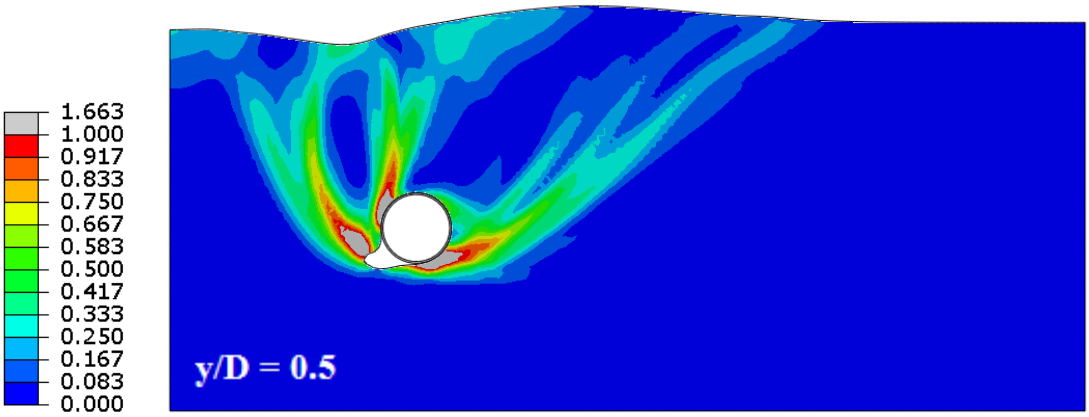

Figure 6.56. Case 1B plastic deviatoric strain contour

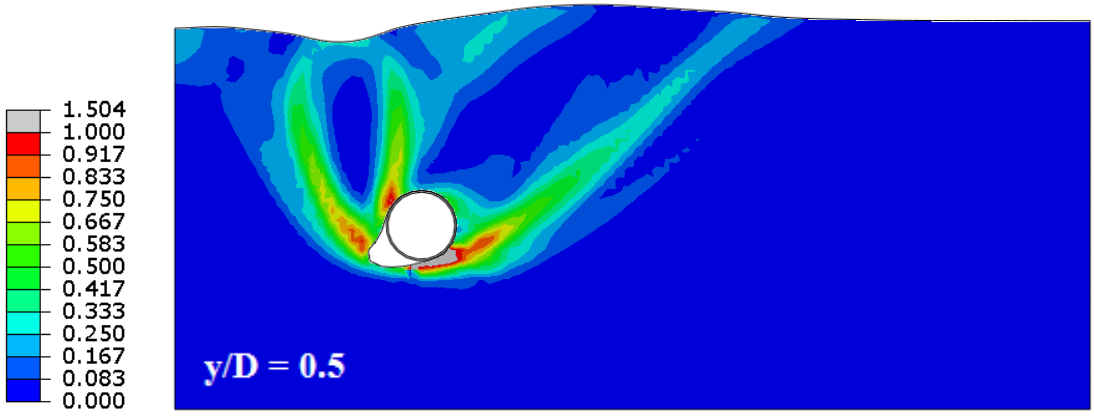

Figure 6.57. Case 1C plastic deviatoric strain contour

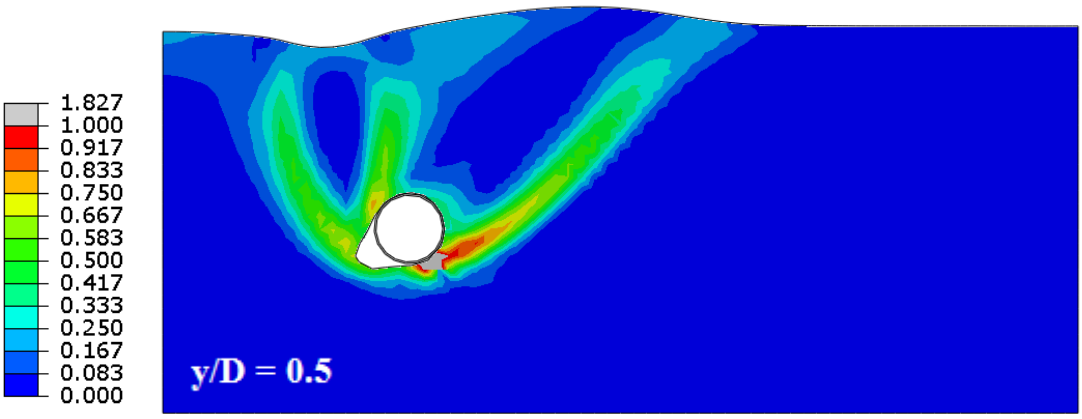

Figure 6.58. Case 1D plastic deviatoric strain contour

6.4.3.2.1 Force-Displacement and Pipe Uplift Response (MMC)

The force-displacement response for Case 3A to 3D is shown in Figure 6.59. Overall, by decreasing the element size, the Case 3C and 3B force-displacement curves converge towards the Case 3A result. Case 3D shows relatively greater instability in the softening and residual response. The Case 3A and 3B results are similar, though the softening response is delayed in Case 3B (y/D ≈ 0.25) compared to Case 3A (y/D ≈ 0.2).

The residual bearing capacity factor prediction is approximately in accordance with N_{qh} = 8 predicted by Case 1A to 1D above (Figure 6.53); this was expected as the friction angle in Case 3 softens to the critical state value ϕ'_{cv} = 45.0 considered in Case 1.

In Case 3A, the peak N_{qh} is reached after about y/D = 0.1, and corresponds to about 10 mm pipe uplift (Figure 6.60). The residual N_{qh} is reached at about y/D = 0.2 and corresponds to about 20 mm pipe uplift. Case 3C predicts less pipe uplift, with the vertical displacement not reaching 20 mm until about y/D = 0.43; correspondingly, the

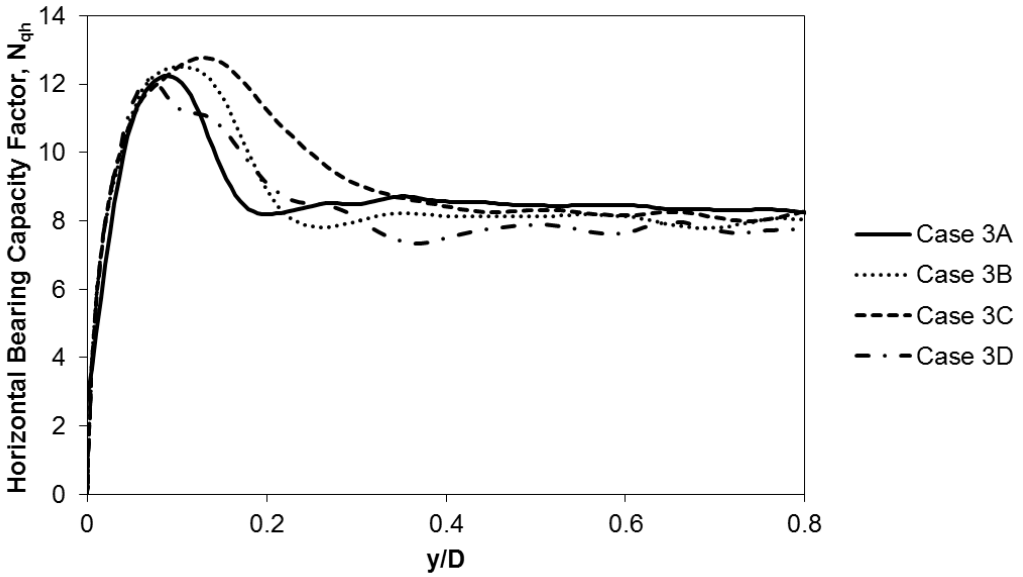

Figure 6.59. Force-displacement response mesh sensitivity (MMC; H/D = 3)

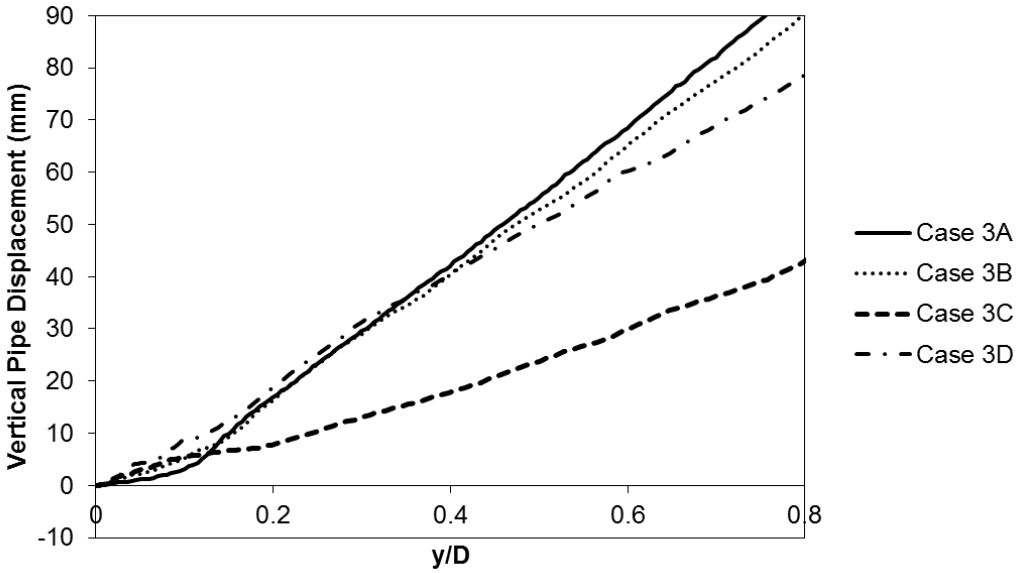

Figure 6.60. Pipe uplift response mesh sensitivity (MMC; H/D = 3)

force-displacement response does not soften to the residual state until the same level of pipe displacement. By comparing Case 3C and 3D, spurious mesh sensitivity is clear at this range of element size. This is visible through examining both the force-displacement and pipe uplift response (Figure 6.60). The Case 3C pipe uplift response predicts about half the magnitude of vertical pipe displacement compared to Case 3D. Convergence is seen in the pipe uplift response comparing Case 3A and 3B.

Based on the results presented herein, the recommended element size, when using the MMC model is $d_B \leq d_{FE} \leq 2\ d_B$. The instability in the response shown for Case 3C and 3D should be avoided.

6.4.3.2.2 Soil Strain Localization (MMC)

The plastic deviatoric strain contours for Case 3A to 3D are presented in Figure 6.61 to Figure 6.64. Similar to the results presented above for Case 1, the plastic deviatoric strain is capped at 100%, and the localization of strain > 100% is increased with reducing element size. Compared to the Case 1 series analyses, strain localization in the shear bands are relatively well defined for Case 3. The reduction of the shear band thickness with element size is clearly observed, especially in the primary shear band defining the passive wedge on the leading side of the pipe.

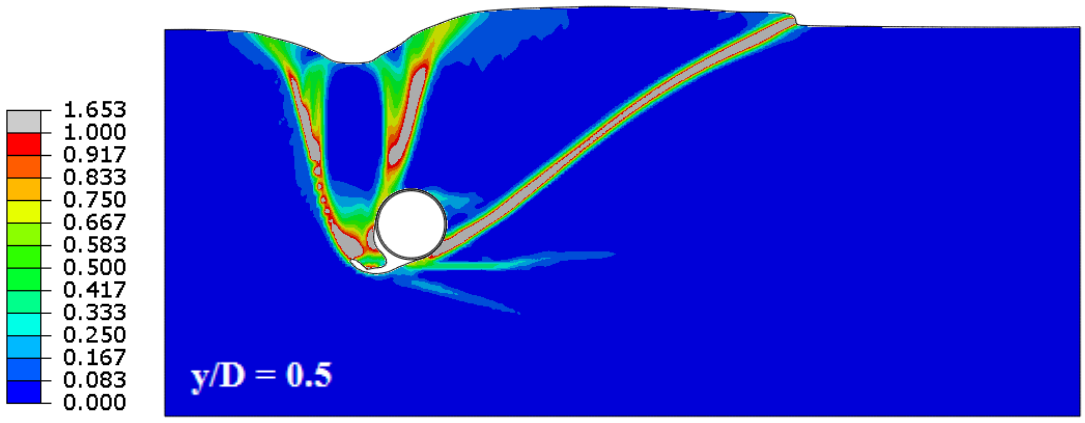

Figure 6.61. Case 3A plastic strain deviatoric contour

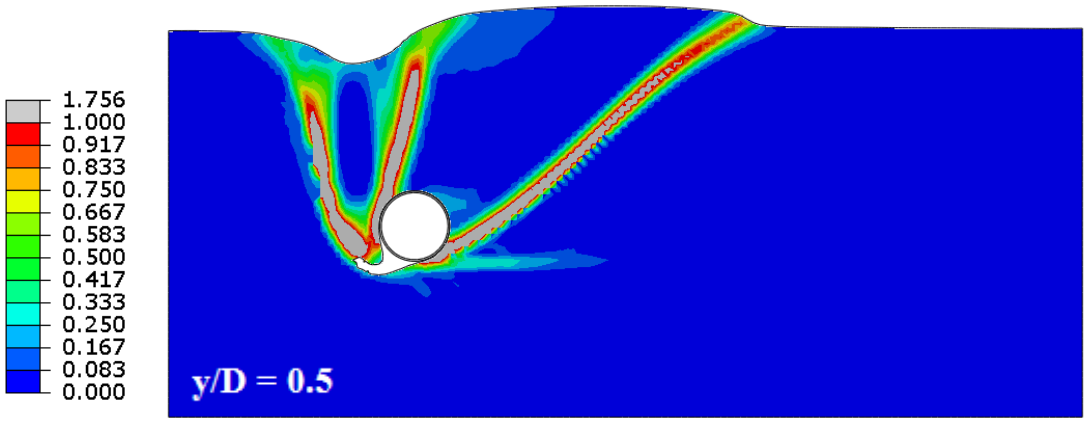

Figure 6.62. Case 3B plastic deviatoric strain contour

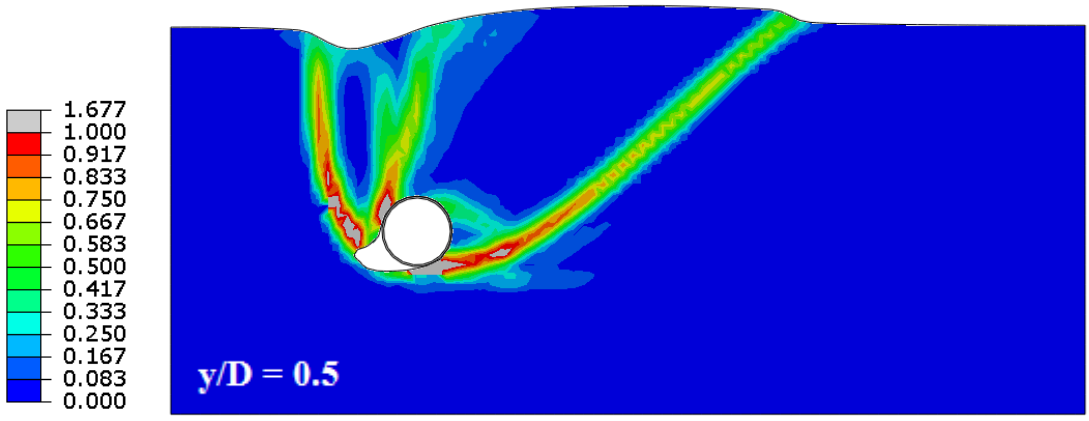

Figure 6.63. Case 3C plastic deviatoric strain contour

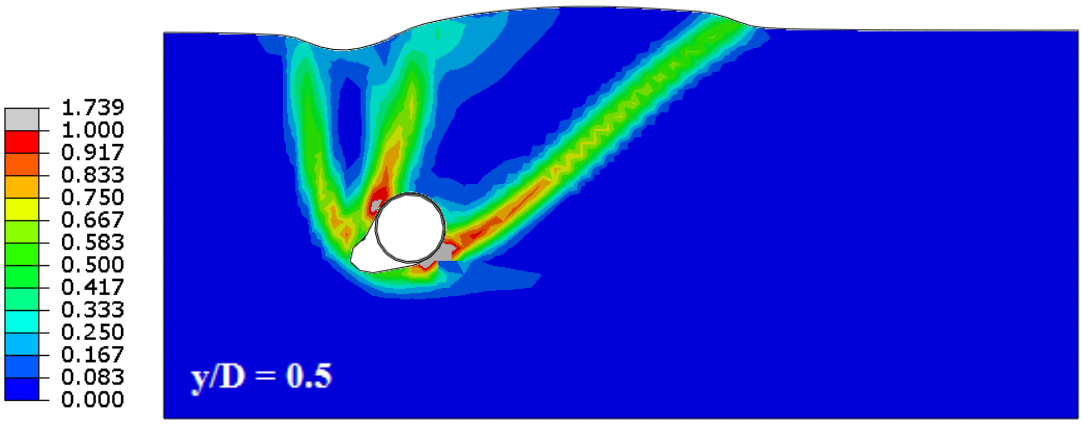

Figure 6.64. Case 3D plastic deviatoric strain contour

6.4.4 Comparison of Physical and Numerical Results

Following the mesh sensitivity results presented above, an element size equal to the shear band thickness, $d_{FE} = d_B = 16\ d_{50} \approx 12$ mm, was used for the suite of analyses presented in this section. The CEL model predictions of force-displacement, pipe uplift and shear strain localization are compared directly to the test data for H/D = 1 and 3, and the analysis extended to a deeper case H/D = 7. The five sets of constitutive parameters outlined in Section 6.4.2 (Table 6.8) were used to assess the influence of increasing complexity in the constitutive modelling procedures, i.e. Case 1 and 2 use the built-in MC model, Case 3 uses the MMC model with strain hardening/softening and Case 4 and 5 uses the MMC model with strain hardening/softening including the effect of mean effective stress on the peak friction and dilation angles.

6.4.4.1 Burial Depth Ratio, H/D = 1

6.4.4.1.1 Force-Displacement and Pipe Uplift Response (H/D = 1)

The following Figure 6.65 and Figure 6.66 shows a plot of the force-displacement and pipe uplift data for tests 5, 7 and 8 (dense conditions, H/D =1, D = 0.254) along with the numerically predicted response using the CEL FE model for Case 1 and 2 described above. The test data shows a variance on the predicted peak N_{qh} factor of about 15%. The Case 1 ($\phi' = 45°$, $\psi = 0°$) analysis predicts a bearing capacity factor about 30% less than the residual value from the tests. The bearing capacity factor reaches the constant value after lateral pipe movement about 2% of the pipe diameter. The pipe vertical displacement agrees with the test data suggesting that the response is due to mainly geometric effects, rather than volumetric expansion at this shallow burial depth; i.e. the pipe has a natural tendency for uplift due to its circular shape that is not resisted by the shallow soil cover.

The response for Case 2 shows a peak N_{qh} that slightly over-predicts test 7. However, due to the unrealistic volumetric expansion associated with the constant peak dilation angle and lack of vertical restraint due to shallow soil cover, the pipe uplift is largely over-predicted. Due to the large uplift response, the lateral soil resistance drops after about 0.3D pipe movement due to the reduced cover.

It is clear that neither Case 1, nor Case 2 provide a response that is consistent with the test results. The 30% under-prediction of the residual soil resistance in Case 1 suggests that the assumption for the residual friction angle may not be applicable to the stress levels experienced at this burial depth level. The peak friction angle provides a

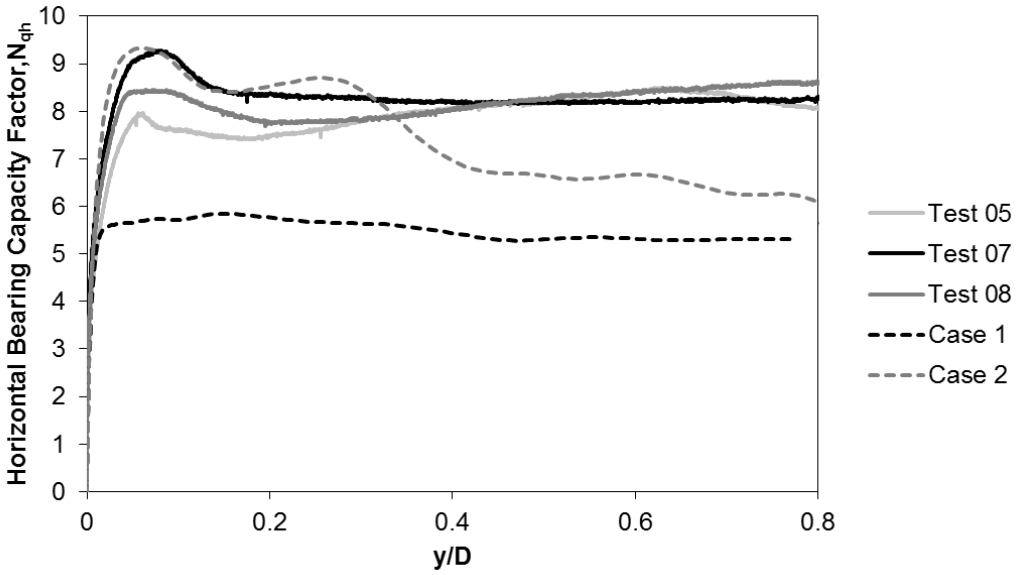

Figure 6.65. Case 1 and 2 force-displacement response

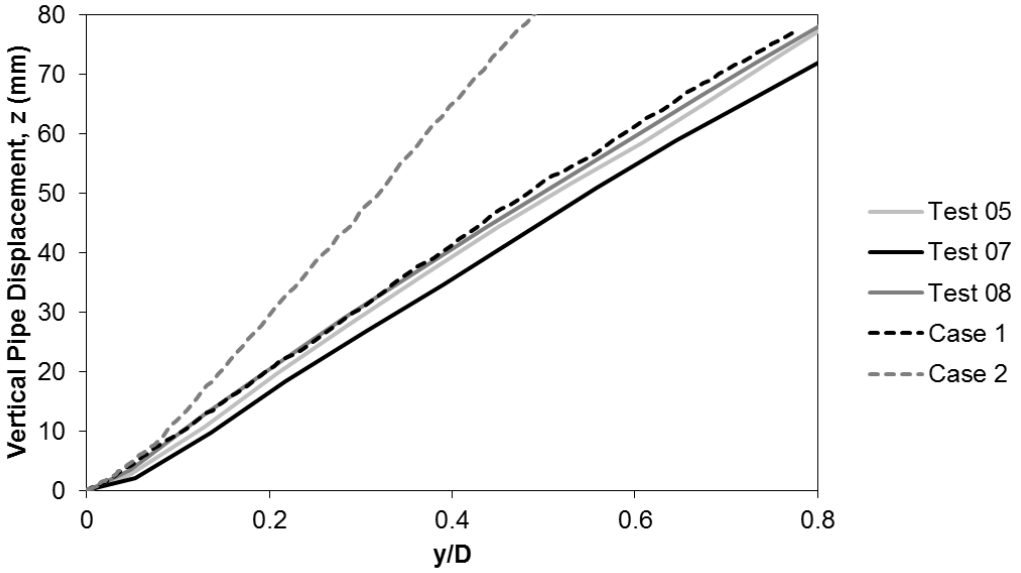

Figure 6.66. Case 1 and 2 vertical pipe displacement

peak N_{qh} that is reasonably consistent with the test results, but the over-prediction is due to the combined effect of the constant peak friction and dilation angle. This provides the motivation for developing the modified Mohr-Coulomb model that can capture realistic soil behavior helping to improve the numerical model towards predicting a more accurate response to avoid under or over-conservatism. As described in Section 3.2.2, the built-in Mohr Coulomb model was enhanced to account for variations in the friction and dilation angle with plastic deviatoric strain and mean effective stress.

As discussed above, Case 3 considers mobilized friction and dilation angles that are appropriately selected to account for low pressure effects, but do not vary depending on the mean effective stress throughout the simulation. This allows examination of the pressure dependency effects on the numerical response in Case 4 and 5. The numerical predictions of force-displacement and pipe uplift are presented in Figure 6.67 and Figure 6.68 for Cases 3, 4 and 5. It is apparent that the force-displacement response is very similar amongst each case. The influence of considering strain softening is seen in the response as the bearing factor is reduced with pipe displacement. The numerical peak bearing capacity is in line with the test data, and the residual bearing capacity factor is under-predicted by about 30% and following the Case 1 results.

The numerical pipe uplift response agrees well with the test data, especially for Case 5 that considers a slightly smaller dilation associated with r = 0.6, rather than r = 0.48 in Case 4. In Case 5 there is slightly less uplift before 0.1D pipe movement and there is a correspondingly higher mobilized bearing factor.

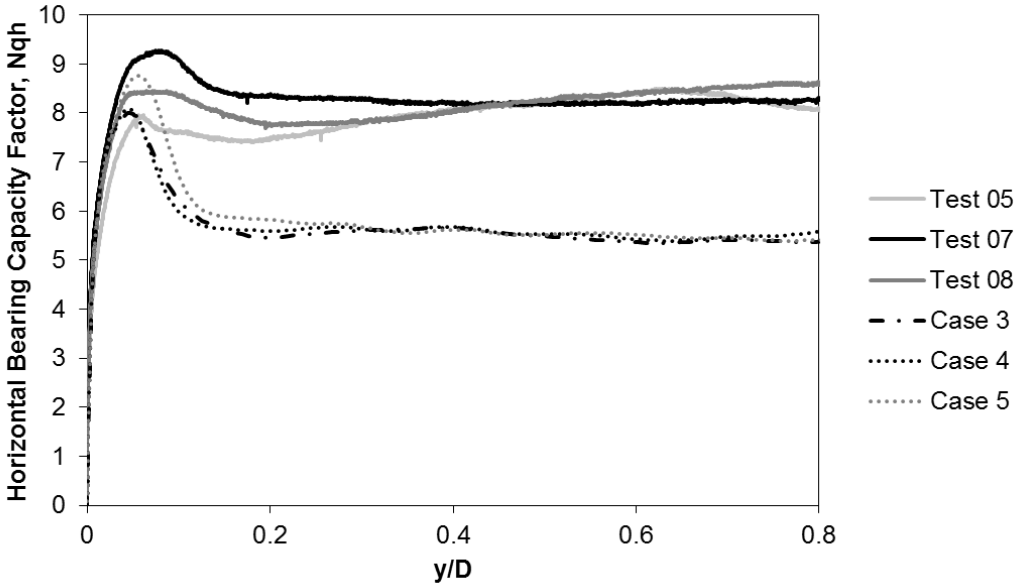

Figure 6.67. Case 3 to 5 force-displacement response

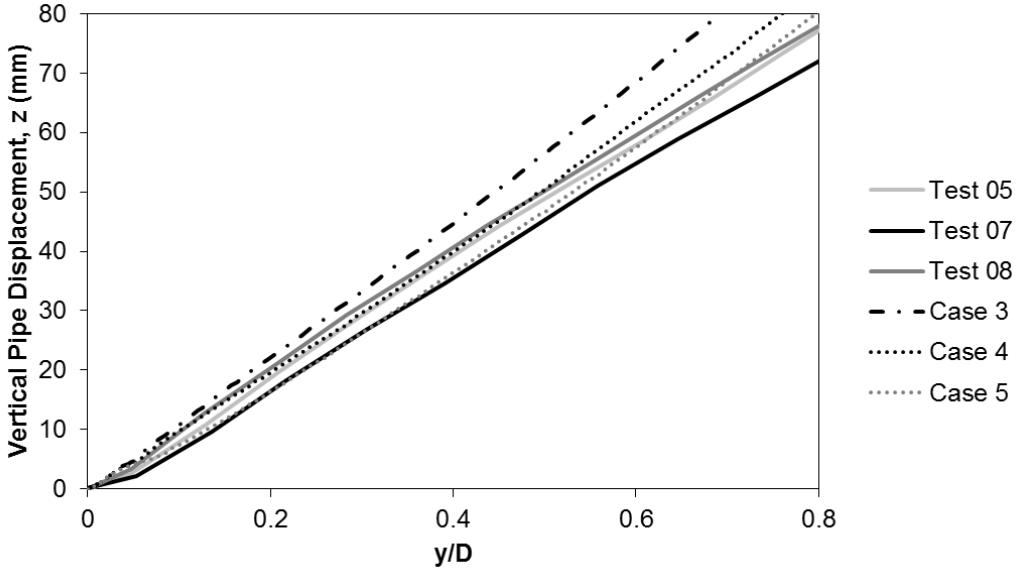

Figure 6.68. Case 3 to 5 vertical pipe displacement

The numerical pipe trajectory is in line with the test data, while the residual bearing capacity factor is under-predicted, suggesting that a higher frictional strength is being mobilized in the physical tests along the primary shear band defining the passive wedge. As discussed above in Section 2.4.2, a higher residual friction angle is common at low confining stress, especially for angular granular materials, which may help explain the discrepancy and can be tested through sensitivity analysis.

6.4.4.1.2 Soil Strain Localization (H/D = 1)

The incremental displacement and shear strain fields produced with PIV analysis are provided in Figure 6.69 and Figure 6.70. The passive wedge failure mechanism associated with shallow burial is clearly defined. The primary shear band is present that defines the separation between the high displacement zone within the passive wedge and the undisturbed soil below. There is a region of high displacement and shear strain over the trailing side of the pipe associated with soil flow into the depression left behind the pipe. The shear strain contour indicates a faint shear band from the crown of the pipe extending down towards the primary shear band.

Case 1 (Figure 6.71) and 2 (Figure 6.72) show a passive wedge failure mechanism, with strain localization occurring over a wide band. The band of plastic shear strain exceeding 1.0 (100%) does not extend to the soil surface. Case 2 shows relatively large volume of soil in the passive wedge due to the constant high dilation angle compared to the nondilatant Case 1. Due to the volumetric expansion with shearing, there is less infill on the trailing side of the pipe in Case 2. The relatively high pipe uplift is also apparent due to the relatively high volumetric expansion as the pipe moves laterally.

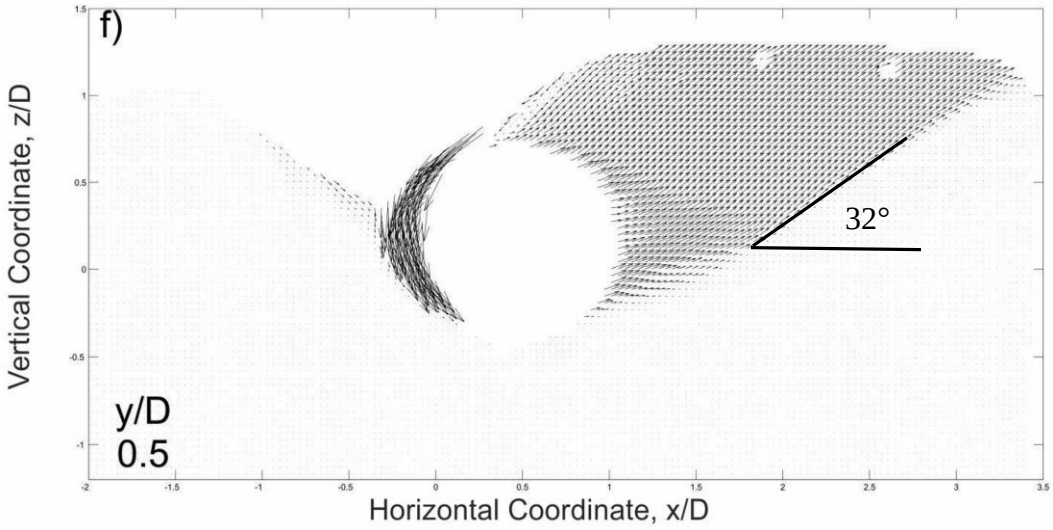

Figure 6.69. Incremental displacement field plot; Test 07 H/D = 1 (Burnett, 2015)

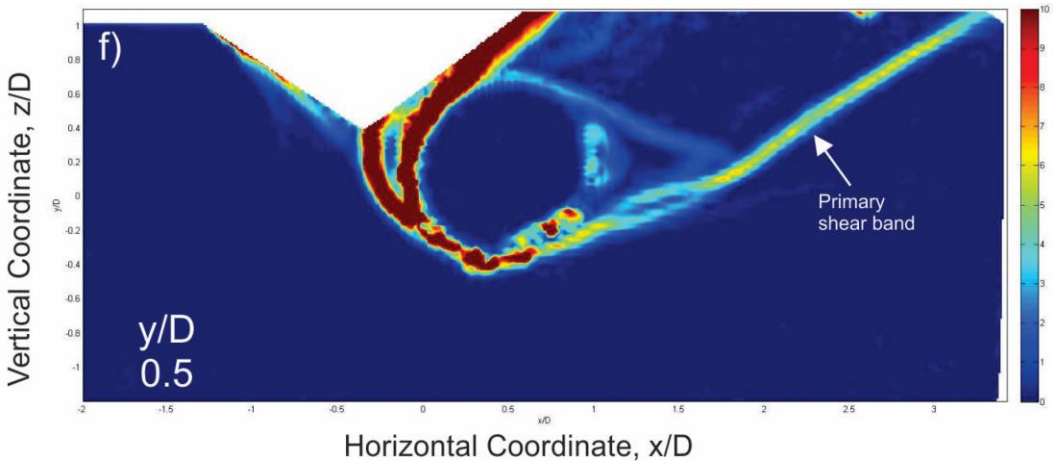

Figure 6.70. Incremental shear strain plot; Test 07 H/D = 1 (Burnett, 2015)

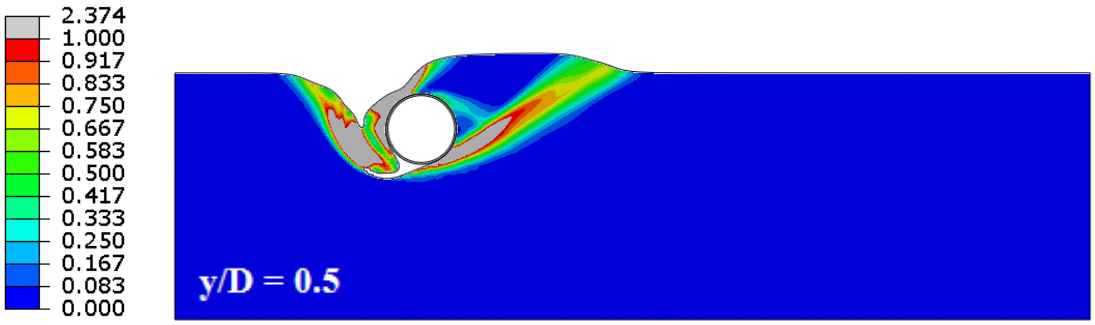

Figure 6.71. Case 1 plastic deviatoric strain contour plot (H/D = 1)

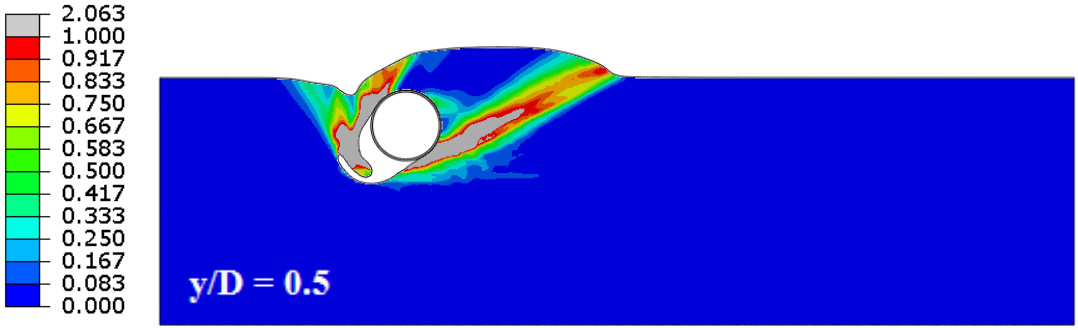

Figure 6.72. Case 2 plastic deviatoric strain contour plot (H/D = 1)

Cases 3 through 5 accounting for strain hardening/softening behavior show an improved response in terms of the strain localization defining the primary shear band; this is evident by comparing Figure 6.73 to Figure 6.75 with Figure 6.71 and Figure 6.72. The deviatoric strain greater than 100% is localized in a narrow band that extends to the soil surface. The numerically predicted primary shear band is consistent with the observed test results; however, as discussed above, the assumed critical state friction angle under-predicts the residual lateral resistance by about 30%. The high strain level indicating soil flow over the trailing side of the pipe is also evident.

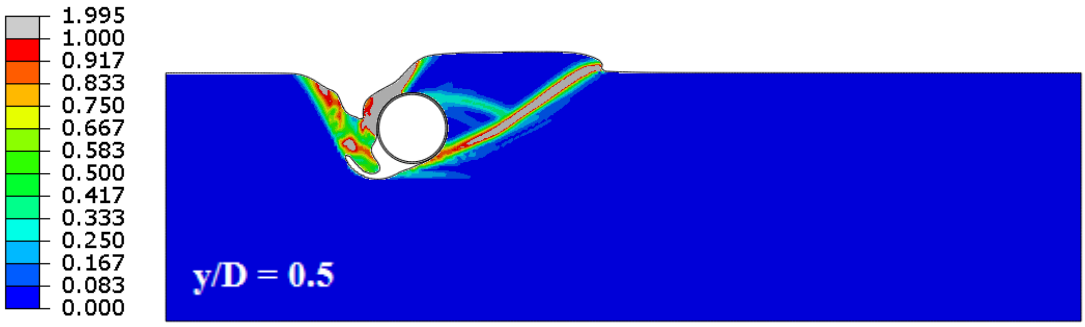

Figure 6.73. Case 3 plastic deviatoric strain contour plot (H/D = 1)

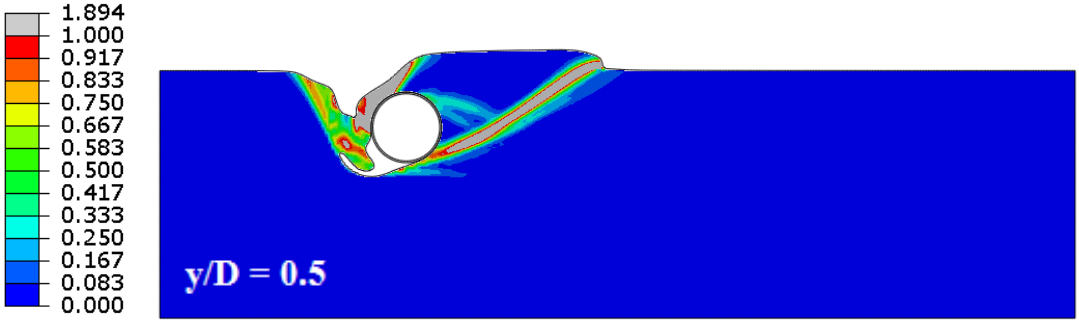

Figure 6.74. Case 4 plastic deviatoric strain contour plot (H/D = 1)

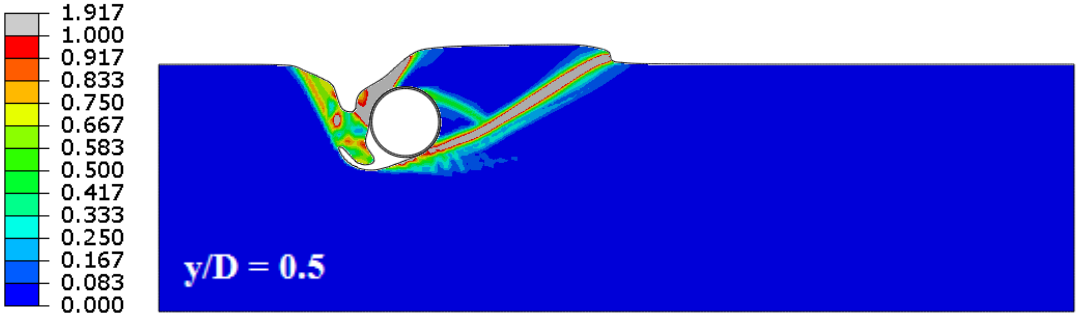

Figure 6.75. Case 5 plastic deviatoric strain contour plot (H/D = 1)

Case 3 (Figure 6.73) considered without pressure dependency gives results that are very similar to Cases 4 (Figure 6.74) and 5 (Figure 6.75). Case 4 and 5 assume that

the mobilized friction and dilation angle does not vary with mean effective stress below p' = 70 and 50 kPa. As discussed above, the peak friction angle is limited below these stress levels based on the assumption that the dilatancy contribution is limited to $\psi = 20°$. Direct shear tests conducted by the author confirms this upper dilation limit (Appendix B, Figure 9.2), and indeed the assumed peak friction angle is effective in predicting the peak bearing factor (Figure 6.67).

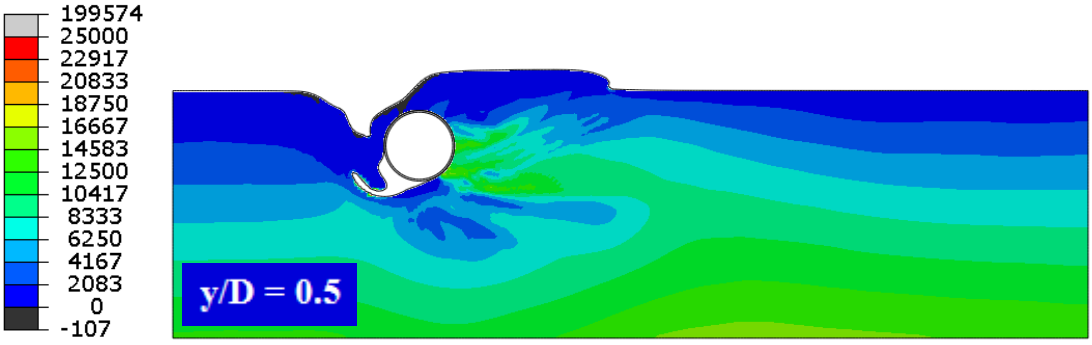

Figure 6.76. Case 3 mean effective stress contour plot (H/D = 1)

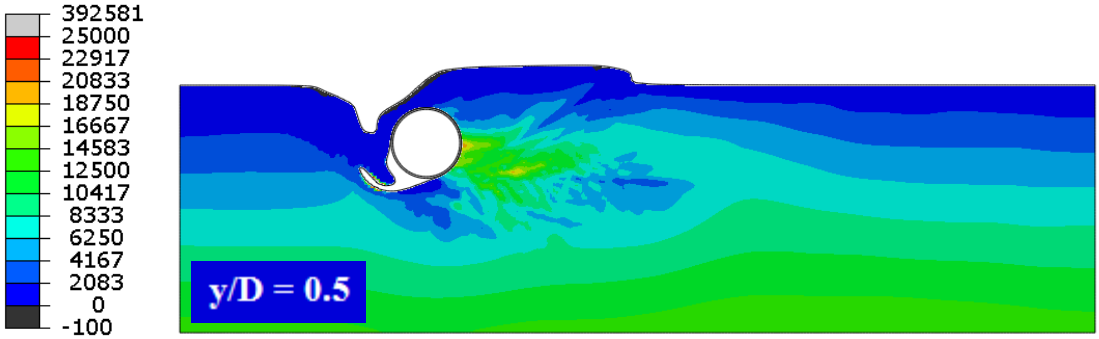

Figure 6.77. Case 5 mean effective stress contour plot (H/D = 1)

In Case 3 and Case 5, the mean effective stress during the simulation is presented in Figure 6.76 and Figure 6.77, respectively; the p' contour limit is set to 25 kPa. The stresses in front of the leading side of the pipe range from about 15 kPa to 20 kPa. The initial mean stress at the pipe centerline prior to pipe displacement is about 4 kPa, meaning that p' increases in front of the pipe by a factor of five (5). Since the soil behavior over this stress range is difficult to quantify, it is relatively more important to determine a best estimate of a representative low stress level peak friction and dilation angle, and the variance of these parameters with deviatoric strain. The plane strain values can be translated and calibrated from triaxial compression test data, or direct shear test data from tests conducted at low stress levels; though plane strain laboratory test results are of course desirable due to direct applicability.

6.4.4.2 Burial Depth Ratio, H/D = 3

6.4.4.2.1 Force-Displacement and Pipe Uplift Response (H/D = 3)

The physical test result for Test 11 (dense conditions, H/D = 3, D = 0.254 m) and the CEL finite element model simulation results for Cases 1 and 2 are shown in Figure 6.78. The previous comparison cases for H/D = 1 tests under dense conditions showed about a 15% variance in the predicted peak bearing capacity factor between the three tests conducted. Hence, while only one test was conducted at H/D = 3 in dense conditions, the same level of variance in the physical tests results might also be expected.

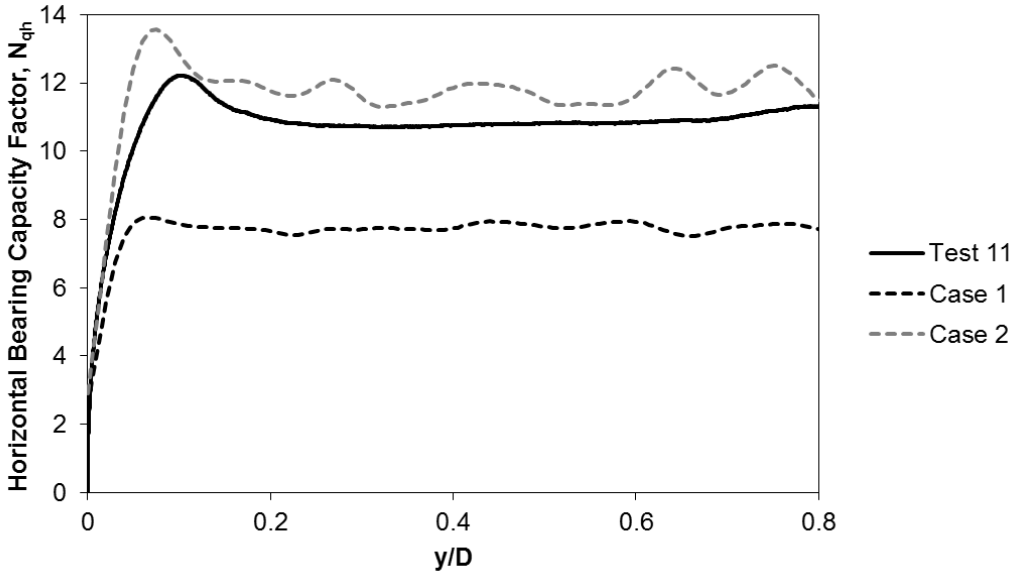

Figure 6.78. Force-displacement response Case 1 and 2 (H/D = 3)

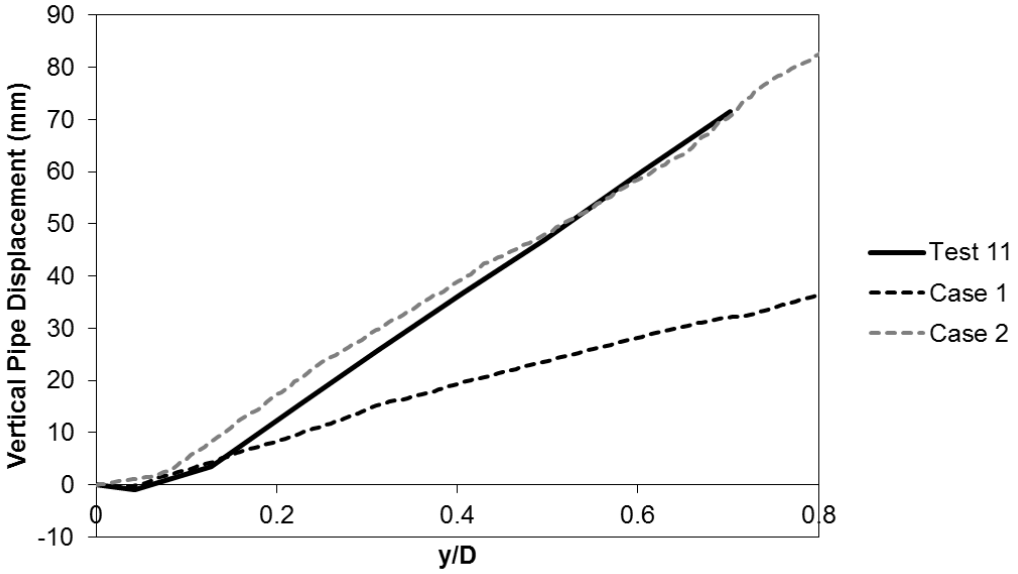

Figure 6.79. Pipe uplift response Case 1 and 2 (H/D = 3)

Case 1 shows a bearing capacity factor plateau at about N_{qh} = 8 that is about 20% less than the residual bearing factor in Test 11 (Figure 6.78). This is an improvement compared to the 30% under-prediction at H/D =1 (Figure 6.65), suggesting that ϕ'_{cv} = 45° is closer to the residual friction angle at the increased stress level at the higher burial depth. In Case 2 ϕ' = 61° and ψ = 20° over-predicts the peak bearing factor and slightly over-predicts the residual bearing factor.

The pipe uplift numerical response is plotted against the test data in Figure 6.79. The nondilatant assumption in Case 1 results in under-prediction of the pipe uplift; unlike the above Case 1 prediction for H/D = 1, there is adequate soil cover (overburden) at H/D = 3 to suppress the uplift. The pipe uplift for Case 2 is slightly overpredicted before about 0.5D pipe movement and converges with the test data past this point.

The CEL FE results for Cases 3 to 5 are plotted against the test data in Figure 6.80. The strain hardening and softening response is captured in the numerical force-displacement curves. The pressure independent Case 3 response is in accordance with the pressure dependent Cases 4 and 5. The peak bearing factor agrees very well with the test result. The residual bearing factor is achieved after about 0.2D pipe movement in the numerical and physical response. For Case 3 through 5, the residual bearing factor is slightly improved towards the test data compared to Case 1 that assumes critical state friction and nondilatant response; though N_{qh} is about 17% under-predicted.

As shown below in Figure 6.81, Case 5 provides a slight improvement in the pipe uplift response compared to Case 3 and 4 as it assumes a slightly smaller dilation angle with increased mean effective stress due to the higher value of r (0.6 vs. 0.48). However,

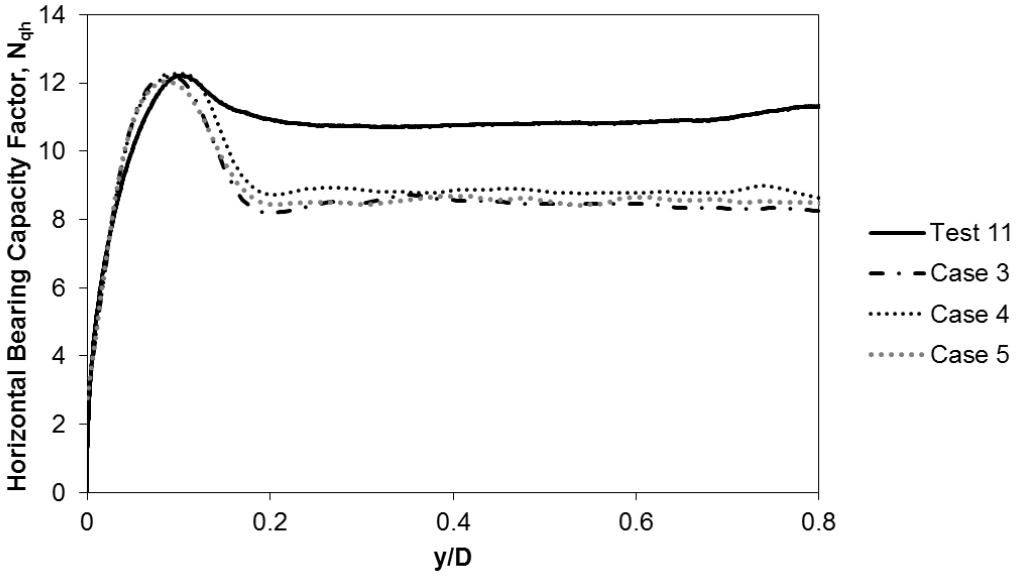

Figure 6.80. Force-displacement response Case 3 to 5 (H/D = 3)

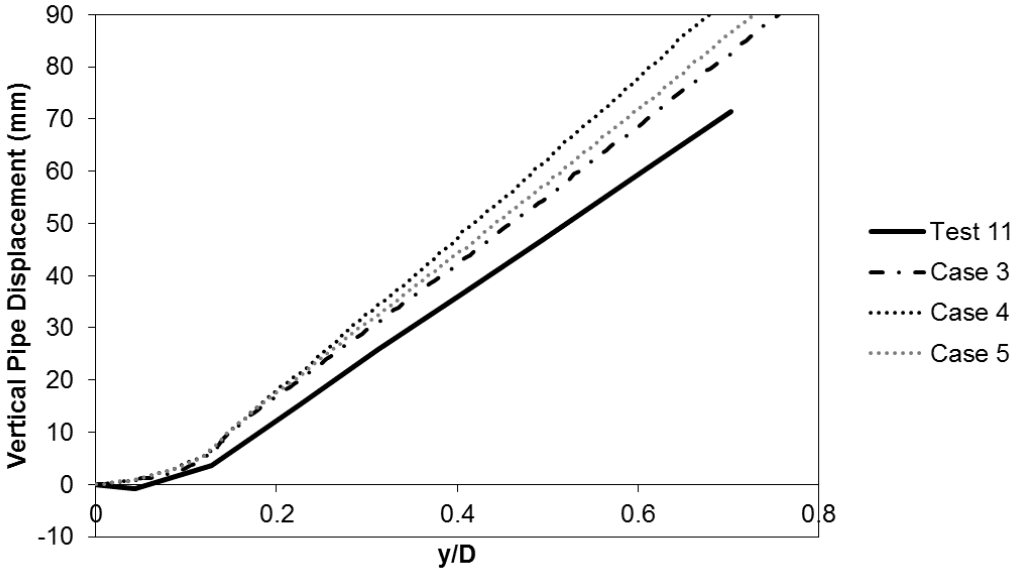

Figure 6.81. Pipe uplift response Case 3 to 5 (H/D = 3)

similar to above for H/D = 1, the response predicted in Case 3 is very similar to Cases 4 and 5, further suggesting a greater relative importance in determining best estimate low pressure strength and dilation parameters, rather than fully defining the pressure dependency at higher stress levels that are not attained at low burial depths H/D = 1 to 3.

6.4.4.2.2 Soil Strain Localization (H/D = 3)

The incremental displacement and shear strain fields produced with PIV analysis are provided in Figure 6.82 and Figure 6.83. The passive wedge failure mechanism associated with shallow burial is defined by the primary shear band, similar to the mechanism at H/D =1. The active soil wedge is delineated by two shear bands that are slightly tilted from pure vertical, and there is a flow zone in the void left behind the pipe due to soil infill.

The incremental deviatoric strain plots at 0.5D pipe displacement are provided for constitutive parameter sensitivity Cases 1 through 5 in Figure 6.84 to Figure 6.88. The Case 1 deviatoric strain contour plot indicates passive and active failure, though the localization of strains is not captured in comparison to the test PIV analysis. The primary shear band is not clearly defined, nor is the active wedge strongly formed by strain localization. The deviatoric strains exceeding 100% are isolated in the immediate area below and behind the pipe and do not extend to the soil surface.

The Case 2 result shows a wide primary shear band that extends further laterally on the leading side, and there is considerably increased volume contained in the passive wedge with relatively more surface expression compared to Case 1.

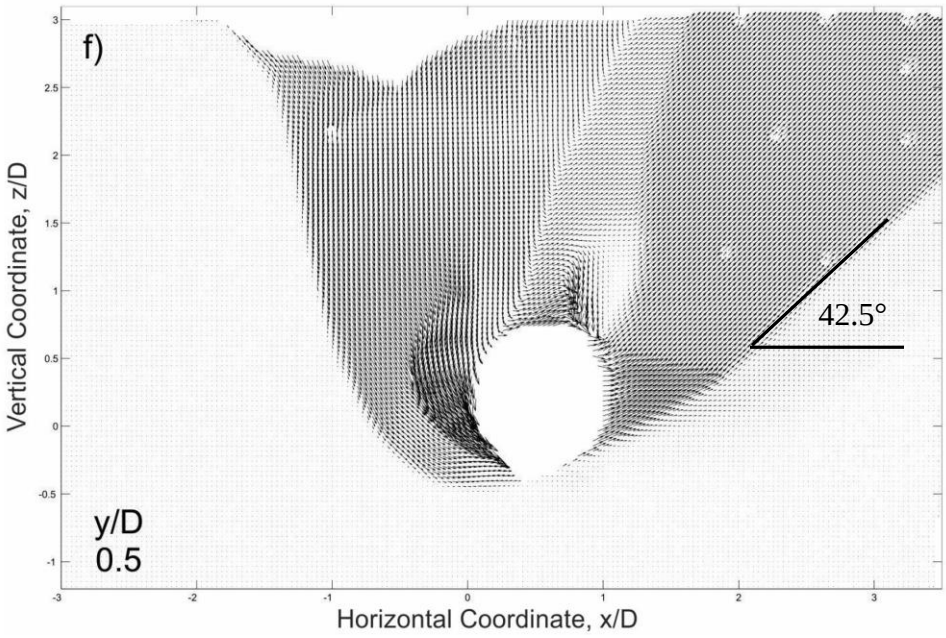

Figure 6.82. Incremental displacement field plot; Test 11 H/D = 3 (Burnett, 2015)

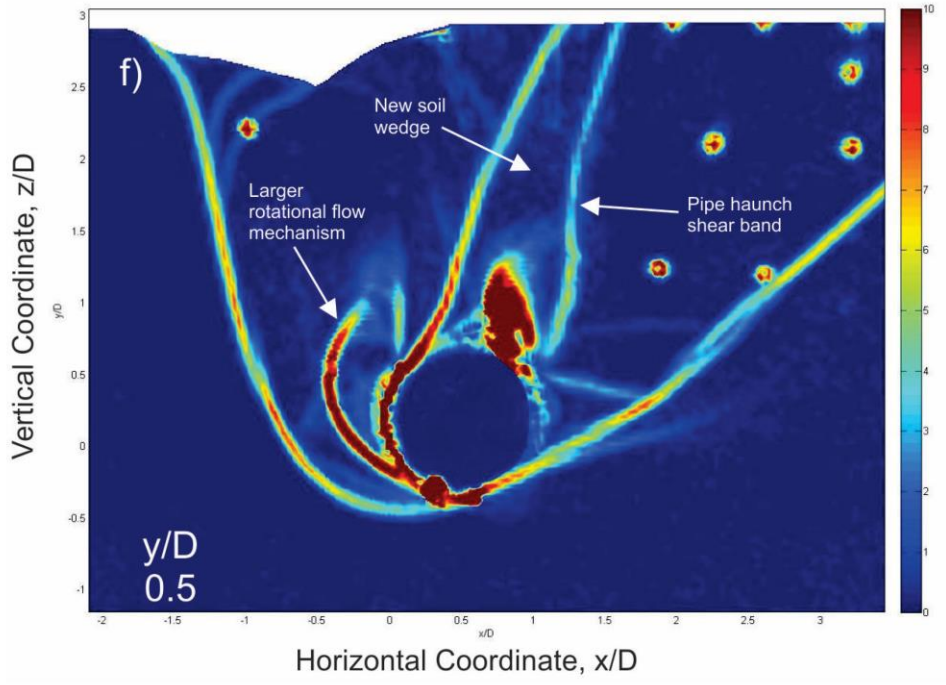

Figure 6.83. Incremental shear strain plot; Test 11 H/D = 3 (Burnett, 2015)

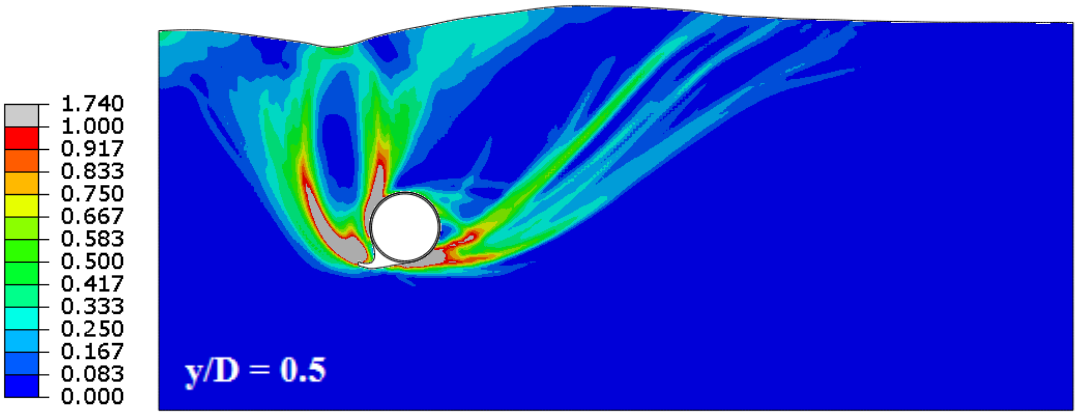

Figure 6.84. Case 1 plastic deviatoric strain contour (H/D = 3)

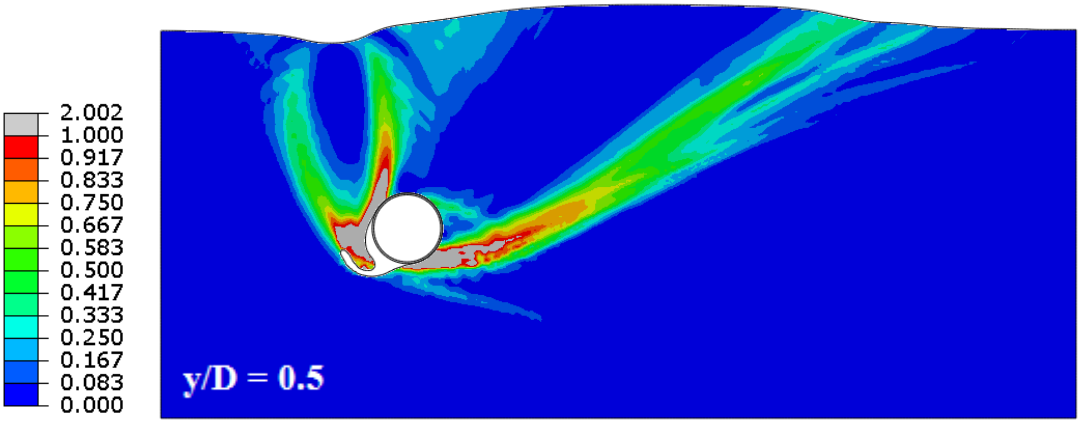

Figure 6.85. Case 2 plastic deviatoric strain contour (H/D = 3)

The Case 3 to 5 deviatoric strains are localized forming the primary passive shear band observed in the PIV analysis. The deviatoric strains ≥ 100% extend from the base of the pipe at an angle upwards to the soil surface. The active wedge on the trailing side of the pipe is also formed by two nearly vertical, slightly curved shear bands due to the soil falling into the void left as the pipe moves laterally.

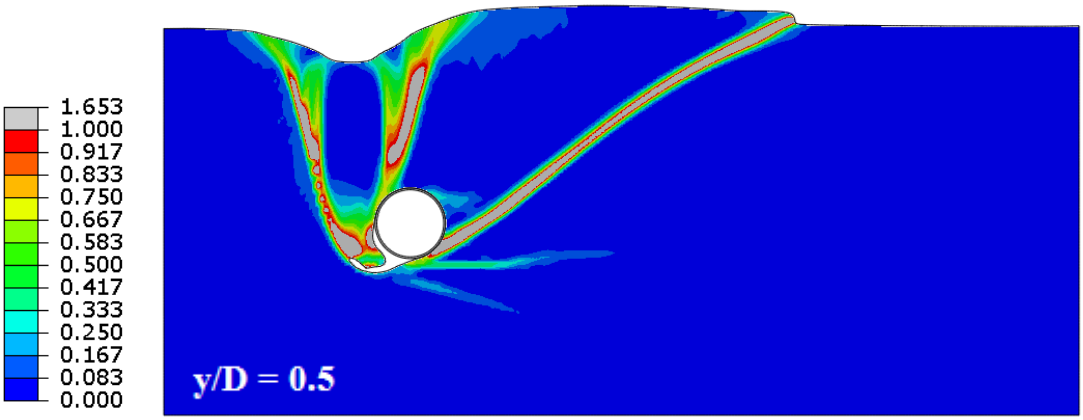

Figure 6.86. Case 3 plastic deviatoric strain contour (H/D = 3)

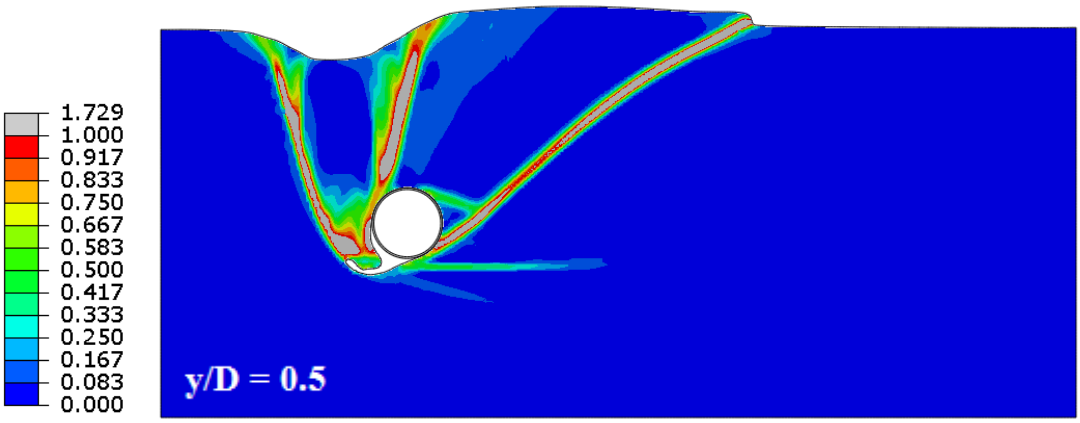

Figure 6.87. Case 4 plastic deviatoric strain contour (H/D = 3)

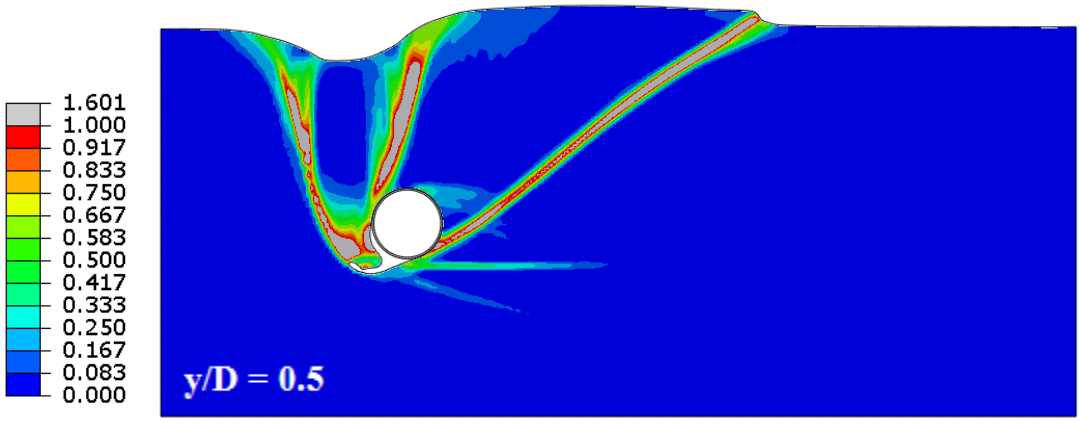

Figure 6.88. Case 5 plastic deviatoric strain contour (H/D = 3)

As discussed above, the force-displacement response amongst Cases 3 to 5 is very similar and does not show strong dependency on friction and dilation angle dependency at higher stresses not experienced throughout the numerical simulation. Likewise, the strain localization predictions are also very similar, with only slight variations in the primary shear band associated with the pipe uplift response. The pipe haunch shear band captured in the PIV analysis is not captured in the numerical results. It is difficult to conclude if this observed mechanism can be regularly expected due to the lack of repetitive testing at this burial depth. There is a slight localization of strain at the pipe haunch that is predicted numerically, however, the formation of a fourth shear band (i.e. pipe haunch shear band) extending vertically is not captured. It may be such that the clustered zone of high strain at the pipe haunch observed through PIV analysis is an anomaly for this test.

The mean effective stress contours for Case 3 and 5 are plotted below in Figure 6.89 and Figure 6.90. The upper limit p' is set at 50 kPa, and is exceeded in a zone extending about one pipe diameter on the leading side of the pipe. Immediately in front of the pipe, the maximum p' is on average about 75 kPa after 0.5D pipe movement, compared to about 12 kPa under initial geostatic conditons. The mean effective stress in the active wedge and the majority of the passive wedge remains at very low stress levels. Hence, as discussed above, predicting the low stress peak friction angle and dilation angle, and mobilization thereof is of primary importance in terms of predicting the peak bearing factor, and in terms of capturing the strain localization effects at shallow burial depths.

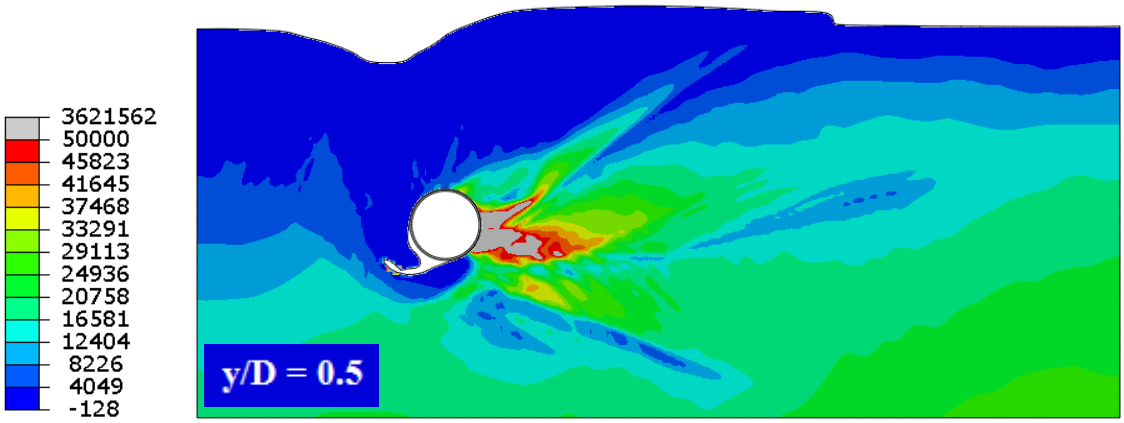

Figure 6.89. Case 3 mean effective stress contour plot (H/D = 3)

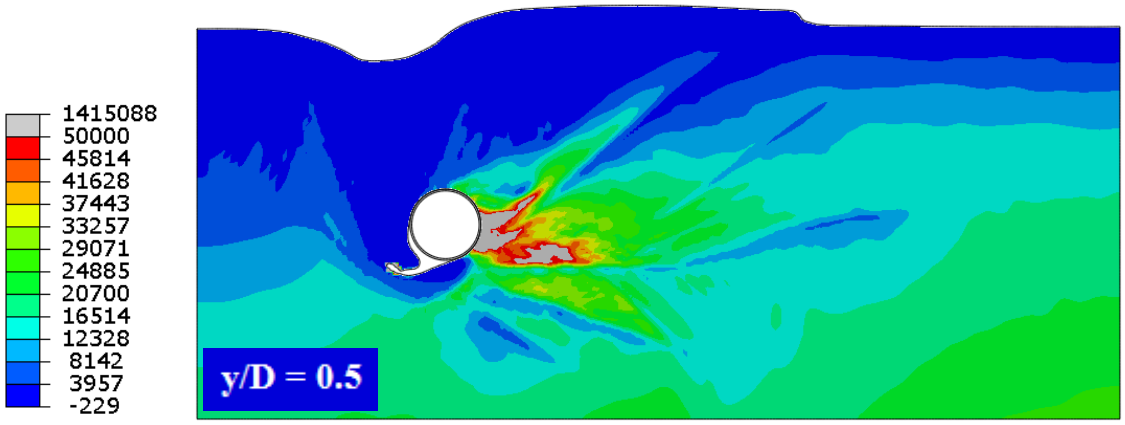

Figure 6.90. Case 5 mean effective stress contour (H/D = 3)

6.4.4.3 Burial Depth Ratio, H/D = 7

6.4.4.3.1 Force-Displacement and Pipe Uplift Response (H/D = 7)

The analysis for a relatively deep burial condition (H/D = 7) was conducted using the Case 5 constitutive parameters. The physical test program did not include a test under

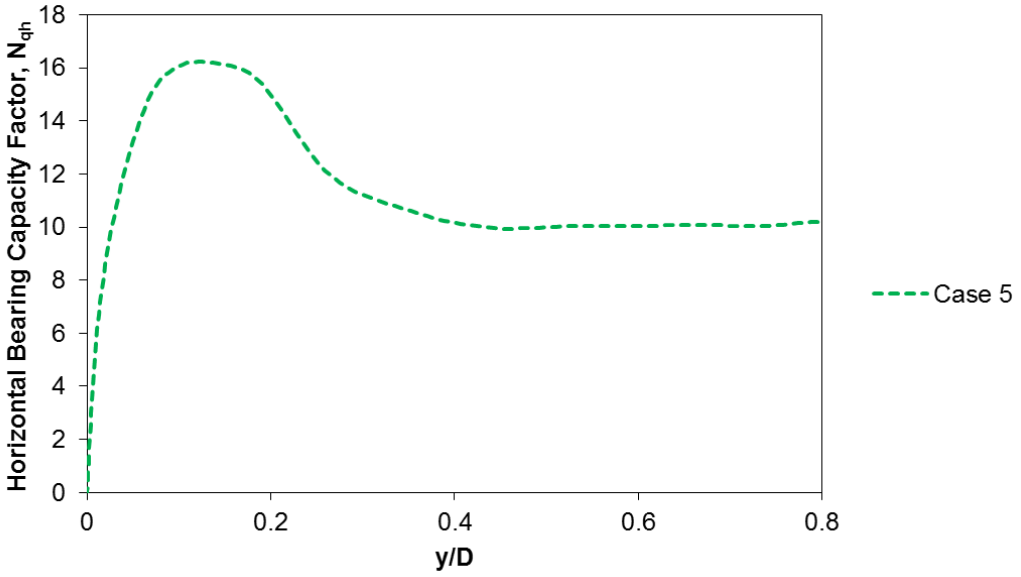

Figure 6.91. Force-displacement response for Case 5 (H/D = 7)

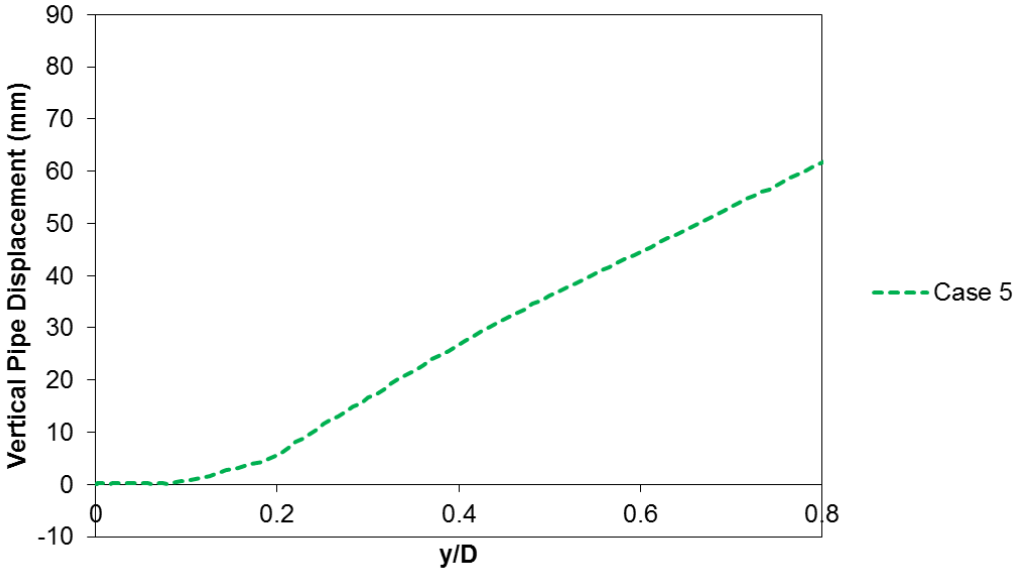

Figure 6.92. Pipe uplift response for Case 5 (H/D = 7)

dense conditions at H/D = 7, hence there is no direct physical test comparison. The force-displacement response shows a peak N_{qh} = 16.2 softening to N_{qh} = 10.

The pipe uplift response indicates less vertical displacement compared to H/D = 3 conditions due to the increased overburden at H/D = 7 that prevents upward movement. However, the pipe uplift does indicate that the shallow burial failure mechanism is realized in the numerical simulation; the deep burial mechanism is associated with concentric soil failure caused by pure lateral movement due to the suppression of uplift caused by the high overburden stress.

6.4.4.3.2 Soil Strain Localization (H/D = 7)

The plastic deviatoric strain field is shown in the following Figure 6.93. The strain field shows the shallow burial failure mechanism defined by the passive and active wedge failure mechanisms extending to the soil surface. However, deviatoric strains exceeding 100% do not extend to the soil surface as predicted for the relatively shallow H/D =1 and 3 cases. Further FEA is recommended to assess the influence of deeper burial conditions and define the transition from shallow to deep failure mechanisms. However, physical modelling becomes increasingly difficult under deeper conditions, especially with large pipe diameters, as the required soil depth begins to exceed the practical limits of the laboratory test set-up.

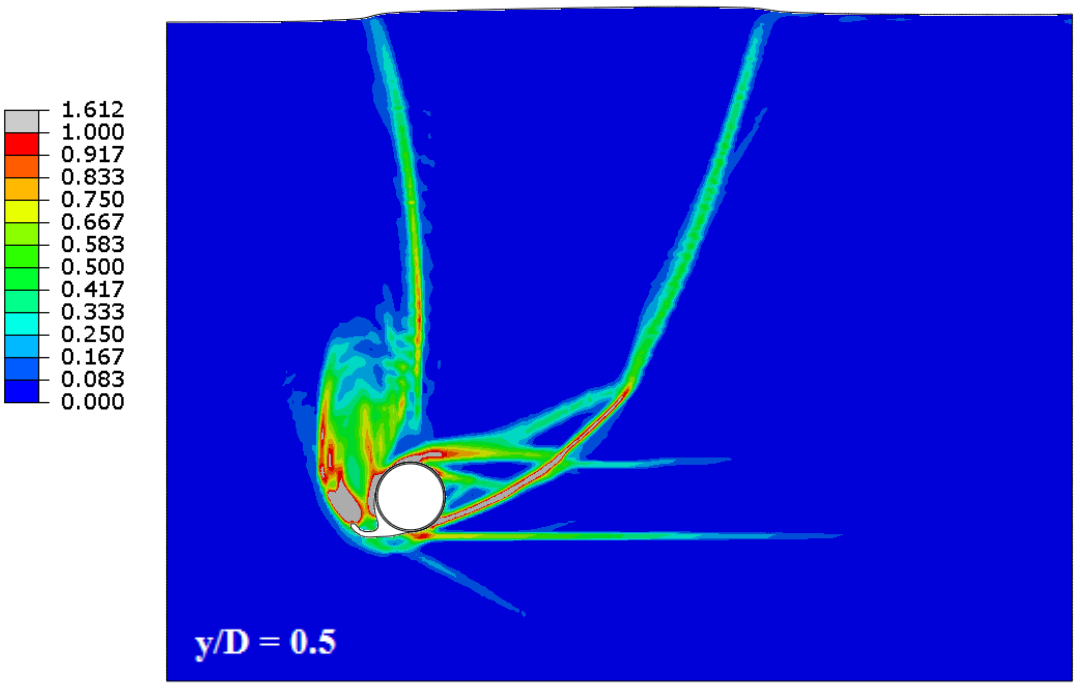

Figure 6.93. Plastic deviatoric strain contour plot (H/D = 7)

6.4.5 Residual Friction Angle and Effective Cohesion Effect on Pipe/Soil Interaction

The residual horizontal bearing capacity factor ($N_{qh,res}$) predicted numerically was about 20% to 30% less than the test data for H/D = 3 to H/D = 1. The $N_{qh,res}$ is related to the critical state friction angle that was assumed ϕ'_{cv} = 45 based on previous work (e.g. Almahakeri, 2013). The analyses using the MMC model, with strain softening to the assumed critical state value, predicted $N_{qh,res}$ in line with the MC model when critical state parameters were used. This indicates that the model results are consistent in terms of the expected $N_{qh,res}$, however, the discrepancy between the physical and numerical results requires further attention.

The effects of low pressure on the peak friction angle were taken into account, resulting in good correspondence between the peak bearing capacity factor ($N_{qh,peak}$) predicted numerically and in the physical tests. However, the effect of low pressure on the residual friction angle was not taken into account. As discussed in Section 2.4.2, Rowe's friction angle ϕ_f, which can be considered as the residual friction angle, has been shown to increase with decreasing confining pressure, especially for angular sands. Since the physical tests were conducted using angular synthetic olivine sand, this effect is likely the source of error between the numerical and physical results for $N_{qh,res}$.

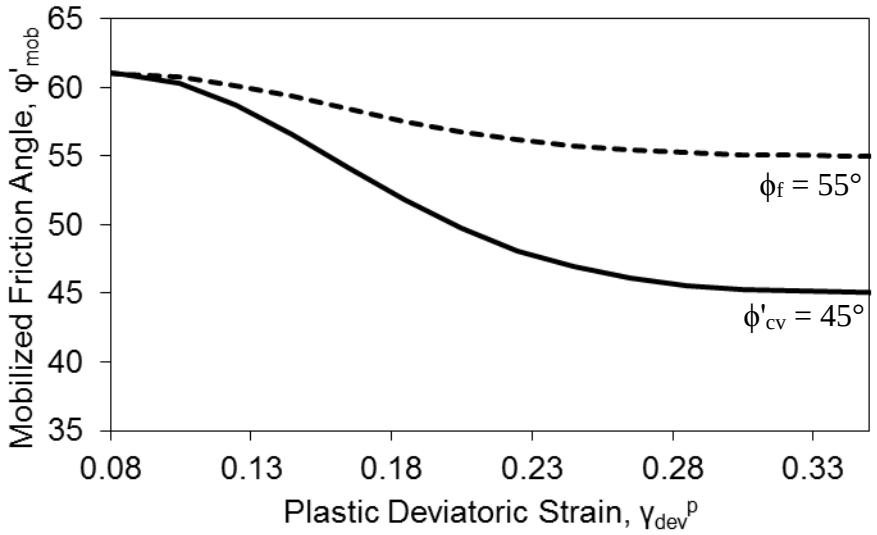

Figure 6.94. Strain softening to residual vs. critical state friction angle

The influence of $\phi_f > \phi'_{cv}$ at low confining pressure will be examined in this section. At H/D = 1, the initial confining stress at the pipe centerline is about 4 kPa, and as shown above in Figure 6.76, the mean stresses increase by about 4 to 5 times adjacent

the leading face of the pipe. Hence, even during the test, the mean effective stress level in the soil is well below values typically measured in triaxial compression tests, for example. A sensitivity study was conducted to examine the influence strain softening to $\phi_f = 55.0°$ (rather than $\phi'_{cv} = 45.0°$) on the residual horizontal bearing capacity factor; the strain softening curves are illustrated above in Figure 6.94.

Another parameter that may exhibit sensitivity at extremely low pressure is the assumed effective cohesion intercept, c'. For cohesionless materials, a small amount of cohesion is typically applied in FEA studies to promote numerical stability. The present study assumed c' = 0.25 kPa as some numerical difficulties were experienced when using c' = 0.1 kPa, related to the rapid soil infill on the trailing side of the pipe, in some cases. However, based on the literature for ice/soil and pipe/soil interaction studies, the assumed c' can range depending on the magnitude required to reach numerical stability; e.g. 0.1 to 0.3 kPa (Jung and Zhang, 2011), 1.2 kPa (Phillips and Barrett, 2011), 4 kPa (Daiyan et al., 2011). Hence, the present study considered c' = 1 kPa as a sensitivity parameter to assess the response at H/D = 1, where it would theoretically have the most impact due to the very low soil stress levels (i.e. initially 4 kPa at the pipe centerline) relative to c'.

The Case 3 analysis for H/D = 1 (Section 6.4.4.1) was repeated with a variation in the softening response towards an increased residual friction angle (Figure 6.94), i.e. Case 3B. Another analysis, Case 3C, was conducted with the same parameters as Case 3B, only with an increased c' = 1.0 kPa instead of c' = 0.25 kPa.

The force-displacement results from the parameter study are provided in Figure 6.95. The analysis shows that the increased residual friction angle in Case 3B provides a

higher $N_{qh,res}$ compared with Case 3, while the peak values are consistent. The error reduces to about 12% from 30%, hence, a significant improvement is seen in the response. The Case 3C analysis with c' = 1 kPa shows an increase in both the $N_{qh,peak}$ and $N_{qh,res}$. The Case 3C force-displacement response falls within range of the test data up to about y/D = 0.3, and under-predicts the test data by about 15% at large displacements.

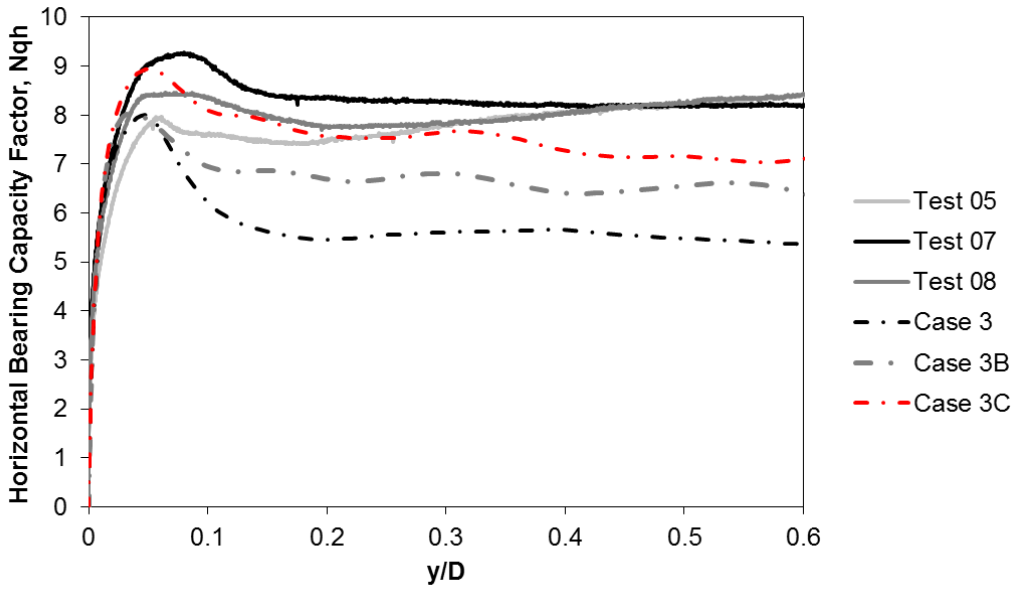

Figure 6.95. Effect of residual friction angle and cohesion on force-displacement response (H/D = 1)

Based on the above sensitivity study, the nuances of FEA for simulating the behavior of cohesionless soil are brought to light. There is of course an element of "curve-fitting" involved in first deriving the constitutive parameters, and subsequently calibrating the values to match physical test data results. The constitutive parameters used in the present study were based on the best available data, and were systematically

addressed through the above sensitivity studies. The peak bearing capacity factors were predicted well within range of the available test data. There is less certainty on the residual response that can be calibrated by small adjustments in the constitutive parameters as shown above.

There is limited information available to characterize the behavior at low stress levels, and there does not exist any plane strain laboratory test data for the synthetic olivine material used in the physical tests. The author recommends a suite of tests conducted under triaxial compression and plane strain conditions that will investigate:

- characterization of the low stress behavior;
- stress-dilatancy relationship (i.e. Bolton's plane strain flow rule);
- translation between peak triaxial compression friction angles;
- relationship and variance in the critical state friction angle between plane strain and triaxial compression conditions; and
- variance in the residual friction angle with reduced confining stress.

6.4.6 Summary

The CEL model developed in ABAQUS/Explicit was used to simulate the large-scale tests conducted at the Queen's University GeoEngineering Centre. The research program objectives to predict the force-displacement response and the soil strain localization behaviour using a robust numerical and constitutive modelling framework were demonstrated. The constitutive modelling procedures are based on the laboratory test data and do not require iterative calibration in order to provide a reasonable approximation of the soil behaviour. The numerical results showed reasonable agreement

with the lateral force-displacement, and pipe trajectory test data. Furthermore, the strain localization in the form of shear bands was reasonably matched with the test data produced using PIV provided by Burnett (2015).

The author's involvement in the physical testing program was discussed above in Section 5.1.1. The physical tests conducted through the collaborative research program add to the field of lateral pipe/soil interaction in granular material, and the contribution to the database for large-scale, practical pipeline diameters is significant.

This study presents the first numerical analysis of these tests that can be used as a baseline approach for further study, which the author encourages. The influence of low confining stress on the peak effective friction angle, that affects the predicted horizontal bearing capacity factor, was demonstrated. There is a lack of mechanical laboratory test data at low confining pressures to fully understand the soil behaviour, and this should be addressed in future research.

7 Conclusions and Recommendations

7.1 Overview

An integrated research framework involving (1) soil behaviour/laboratory testing (2) physical modelling and (3) numerical analysis was used to develop and validate numerical tools in the context of pipeline design against large deformation geohazards in cohesive and cohesionless soil. Several research papers have been published from this work and have been presented at targeted conferences related to engineering for arctic and harsh environments, and large deformation pipeline geohazards. Dissemination of outcomes from this thesis include eight (8) conference papers and two (2) journal manuscripts, which are summarized in Appendices F and G.

Given the lack of physical test data for fully coupled ice/soil/pipeline interaction as a basis to verify the developed finite element tools, prudent action was taken to build confidence in the numerical analysis for subsets (i.e. ice/soil interaction and pipe/soil interaction) of the fully coupled interaction event. Given the natural existence of both clay and sand seabeds, the numerical and constitutive models for examining pipe/soil interaction events were developed for both soil types.

The free-field ice gouge and pipe/soil interaction CEL FE model results were verified against available data in the literature for undrained cohesive soils. Fully coupled ice/soil/pipeline interaction was investigated for cohesive soil, and a study was conducted to compare coupled continuum CEL FEA with the conventional decoupled approach to pipeline design against ice gouging.

In cohesionless soil, the CEL FE numerical predictions were verified against the large-scale physical test data produced as part of the overall current study research program. Numerical simulation of free-field ice gouging and coupled ice/soil/pipeline interaction events in cohesionless soil was not addressed in this thesis; however, the developed numerical and constitutive modelling procedures can be extended for future study.

The following sections summarize the main objectives, outcomes and contributions of the work conducted and presented in this thesis. Section 7.2 is related to Phase I of the research program that was focused on free-field numerical ice gouge analysis, numerical buried pipe/soil interaction analysis and subsequently, fully coupled ice/soil/pipeline interaction events in cohesive soil. Section 7.3 is related to Phase II of the research that involved physical and numerical modelling of large-scale lateral buried pipe/soil interaction.

7.2 Cohesive Soil

7.2.1 Free-Field Ice Gouging

Continuum CEL FE modelling procedures, available in ABAQUS/Explicit, were improved to advance the study of ice gouging processes in cohesive (i.e. clay) soil. The motivation was to reduce uncertainty in the numerical simulation tools for predicting subgouge soil deformations that may impact the engineering design of pipelines located in ice environments. Optimization of the pipeline burial depth and reducing trenching

requirements promotes the technical and economic feasibility of offshore oil and gas projects.

To this end, state-of-the-art modelling procedures were developed to simulate centrifuge ice gouge tests (Lach, 1996). Enhanced constitutive modelling procedures to account for the undrained shear strength and stiffness profiles with depth were incorporated. Compared to assuming a constant profile, the varying profile improved the horizontal subgouge soil displacement and keel reaction forces predicted using FEA compared with centrifuge test results. The developed modelling procedures, which incorporate a varying undrained shear strength profile, provides a contribution by improving the engineering modelling procedures for the analysis of ice gouging events in clay.

The outcome of the work done to assess the keel shape effect highlights the importance of considering the keel angle in estimating subgouge soil displacements. It has been shown that steep keel angles cause deeper gouges; however, this study demonstrated that the effect on subgouge soil deformations is greatly reduced for steep keel angles in contrast to shallow angles. This suggests the current state of practice is conservative where the effects of shallow keel angles may benefit by accounting for the shape effect.

7.2.2 Pipe/Soil Interaction

Pipe/soil interaction studies, through numerical simulation, were undertaken to assess the soil response to pipe movement for pure lateral, and oblique lateral-axial loading events in clay. The influence of oblique loading is a 3D effect that may influence

pipe/soil interaction processes during ice gouge events. The objective was to build on the large deformation FEA capability by establishing consistency with previous numerical analysis and defined failure envelopes. The CEL FEA lateral bearing factors were shown to be consistent with previous numerical studies and current engineering guideline recommendations.

The influence of interface behaviour on the lateral-axial soil failure envelope for oblique lateral-axial pipe/soil interaction was assessed. It was shown that the axial resistance to pipe movement can increase significantly with relatively small pipe misalignment from pure axial motion, i.e. about 5° to 10° oblique attack angles. The interface shear stress limit was shown to limit the maximum axial soil resistance, which is important when considering undrained interface conditions. An analytical equation was derived to predict the maximum axial soil resistance based on the interface shear stress limit, and was shown to accurately predict the FE results.

7.2.3 Ice/Soil/Pipeline Interaction

The pipeline mechanical response was studied using continuum CEL and decoupled structural beam/spring modelling approaches. A case study was conducted to comparatively assess each approach by applying the subgouge deformation field in a consistent manner that had not been achieved in previous studies. In this study, the subgouge soil deformation field used as input to the structural model analysis was derived from continuum FEA of the fully coupled ice/soil/pipeline interaction event. Previous work utilized the free-field results that were not influenced by the presence of the

pipeline. The analysis approach in this study has thus advanced the state-of-the-art for addressing the decoupled structural model superposition error.

Previous work has shown that pipeline strain results from the structural model are generally conservative compared to coupled continuum analysis. The comparison study examined, in this thesis, the pipeline strains from the coupled continuum and decoupled structural models showing that the results may not be conservative as previously considered. The study showed a methodology for performing the relative assessment between the approaches, and should be further utilized to examine the influence of the pipeline obstruction on the subgouge soil deformation field for a wider range of parameters.

7.3 Cohesionless Soil

7.3.1 Physical Modelling

Phase II of the research program involved physical and numerical modelling of large-scale lateral pipe/soil interaction in cohesionless soil. The research program was a collaborative effort between Memorial University of Newfoundland, Queen's University and the Wood Group. A detailed review of existing physical test data for lateral pipe/soil interaction was conducted to help define aspects of the physical test set-up and matrix of cases. The dataset also served as a basis for the initial verification of the numerical and constitutive modelling procedures.

The study revealed an extensive dataset for lateral pipe/soil interaction tests. This compiled dataset provides a large collection of information that can be used to inform

decisions on the selection of force-displacement criteria for pipe/soil interaction analysis. For shallow burial conditions, equations were developed for the lateral bearing factor and mobilization of the ultimate lateral soil resistance. In particular, the equations for the mobilization distance provide an updated approach to account for loose and dense conditions.

The physical large-scale lateral pipe/soil interaction test program, performed at the Queen's University GeoEngineering Center, was summarized in this study. Further details are provided in a recent companion study (Burnett, 2015). The tests examined both the load-displacement as well as the localized soil failure response using PIV techniques from images captured using high resolution photographs of the tests in progress through transparent sidewalls. The test results were added to the existing dataset and were shown to agree favorably with existing guidelines for the design of buried pipes.

In addition to making a contribution to the existing publicly available dataset for physical large-scale lateral pipe/soil interaction test data, the detailed inspection of the soil displacement and shear strain localization over a practical range of pipe diameters and burial depths under dense and loose granular soil conditions is a major new contribution to the field.

7.3.2 Constitutive Modelling

The present study addressed the conversion of laboratory test results (e.g. triaxial compression) to plane strain parameters for use within the constitutive models for numerical simulations. A review of the existing relationships and a new approach to

estimate the peak plane strain friction angle based on triaxial compression data is provided.

A detailed review of plane strain and triaxial test data was conducted in order to assess the application of flow rules and empirical equations to estimate the peak friction angle and dilation angle. Bolton's relative dilatancy index was shown to provide a good estimate of the peak dilation angle for dense conditions.

The importance of using a consistent formula for calculating the dilation angle was shown, as some conclusions in the literature based on different equations lead to relatively high estimates of the dilation angle, leading to inconsistent conclusions with respect to established flow rules linking the dilative and shear behaviour of granular materials.

A study on the material angularity highlighted its influence on the interparticle friction angle that affects the peak friction angle. It was shown that higher angularity leads to higher peak friction angles, especially at low confining pressures.

The use of laboratory test data to derive constitutive parameters was demonstrated. The procedures were shown to provide agreement between the numerical and physical test results. A modified Mohr-Coulomb constitutive model that accounted for mobilization of strength and dilation properties as a function of plastic deviatoric strain and mean effective stress was implemented using a user subroutine (VUSDFLD) written in FORTRAN. Available formulations for the mobilization were outlined and applied. The inclusion of strain-softening enabled the initiation and propagation of shear band failure mechanisms. The deviatoric strain component is integrated such that the

formulation can be applied to both 2D and 3D applications, which is important from the perspective of applying the approach to a broader class of 3D geomechanics problems.

7.3.3 Numerical Modelling Procedures

CEL modelling procedures for large deformation problems involving pipe/soil interaction have been developed and verified using an integrated study framework. The CEL model developed herein was shown to reasonably predict the load-displacement response and soil strain localization compared against the physical test results. The author has been responsible for major developments of this technique for applications including free-field ice gouging, ice keel/soil/pipeline interaction and plane strain orthogonal and oblique pipe/soil interaction. Contributions to the field of pipeline design against geohazards including ice gouging have been significant, especially in the novel use of CEL procedures to accurately predict physical test data through comprehensive development of the finite element model including derivation of constitutive relationships for cohesive and cohesionless soils.

7.4 Recommendations

7.4.1 Pipeline Design Against Ice Gouging

The present study was undertaken to advance constitutive and numerical modelling procedures related to large deformation geohazards, in the context of ice gouging in arctic environments. Conventional pipeline design against the ice gouge hazard involves structural beam-spring analysis with decoupled soil displacement inputs. The use of continuum 3D FE models is not yet practical in a probabilistic assessment

(structural reliability analysis) due to the analysis run times; however, designs should be supplemented with advanced 3D numerical models for critical scenarios. Given these constraints, there are two major research areas that require further study:

1) The superposition error related to applying the decoupled soil displacement field should be further assessed over a broad range of keel angle, gouge width and depth, soil type and strength, and pipeline diameter. The soil displacement field should account for the presence of the pipeline as it obstructs the soil flow, limiting the displacement in comparison to the free-field scenario. This would allow better assessment of the level of conservatism in the pipe response that is generally seen in the structural FE approach in comparison to the continuum analysis.
2) The numerical models for fully coupled ice/soil/pipeline interaction would benefit from large-scale test data to provide the necessary basis for complete validation. More testing would allow further verification of the promising results regarding the pipe response in the tests conducted by Sancio et al. (2011).

There remain uncertainties in the constitutive modelling procedures for undrained clay related to the unrealistic soil berms developed during the numerical simulations due to assumption of saturated continuum, undrained soil behaviour. It may be possible to limit this numerical effect by introducing a tension-cut off mechanism in the constitutive modelling framework.

The present study has not addressed free-field ice gouging or coupled ice/soil/pipeline interaction events in cohesionless materials. Previous work (Eskandari et al., 2012) used the NorSand material model to simulate free-field ice gouging in sand that required a significant effort to develop the user material subroutine. Recent centrifuge gouge tests in sand conducted by Yang (2009) should be used as a basis to compare the present study free-field ice gouge numerical model and constitutive modelling framework (i.e. modified Mohr-Coulomb).

The current approach in pipeline design against ice keel interaction includes the assumption that direct ice/pipeline contact constitutes a failure case. It is recommended that physical tests and numerical analysis be conducted to test this assumption accounting for ice failure mechanics in direct contact interactions.

7.4.2 Pipe/Soil Interaction

The lateral pipe/soil interaction physical testing study provided a detailed review of existing data that may be integrated into guideline recommendations. The study found a wealth of existing information, and identified gaps in the dataset that bring to light potential areas for future work. The following activities are recommended:

1) Conduct physical tests using practical energy pipe diameters approaching and including deep burial conditions to better delineate the transition from shallow to deep burial failure mechanisms;
2) Update guidelines to highlight the influence of the laboratory testing method in determining the friction angle used to determine the bearing factors.

3) Conduct regression analysis on the physical test dataset to test empirical equations for the lateral bearing factor as a function of the available parameters.

Physical tests for orthogonal pipe/soil interaction are generally conducted under plane strain conditions. Hence, as discussed in this thesis, the constitutive parameters used for plane strain FEA should be appropriately translated from the source data (e.g. direct shear or triaxial compression test results) where plane strain data is not available. This was done for the numerical analysis conducted in the present study to simulate the large-scale lateral pipe/soil interaction tests conducted at Queen's University.

The mechanical properties of synthetic olivine should be tested using the newly available testing equipment at Memorial University; this would allow verification of the plane strain parameters used in the numerical analysis.

The numerical analysis of oblique pipe/soil interaction in cohesive soil assuming undrained conditions generated a predictive equation for the maximum axial soil resistance; it would be interesting to verify the numerical results with physical test data. While not addressed explicitly in this work, in cohesionless soils, there remains uncertainty on the lateral-axial soil failure envelope, particularly at low oblique attack angles, that would benefit from further numerical analysis to assess the differences seen in physical test results.

8 References

Abdalla, B., Pike, K., Eltaher, A., Jukes, P. & Duron, B. 2009, "Development and Validation of a Coupled Eulerian Lagrangian Finite Element Ice Scour Model", *Proceedings of the 28th International Conference on Ocean, Offshore and Arctic Engineering (ISOPE)*, May 31 – June 5, 2009, 6p.

Abdelnour, R., Lapp, D., Haider, S., Shinde, S.B. & Wright, B. 1981, "Model Tests of Sea Bottom Scouring", *Proceedings of the 6th International Conference on Port and Ocean Engineering under Arctic Conditions (POAC)*, July 27 - 31, 1981, pp. 688-705.

Ahmed, S.M.U. 1972, *A study of the influence of confining pressure on the behavior of sands*, M.Eng., McGill University.

ALA 2001, *Guideline for the design of buried steel pipe*, American Lifelines Alliance.

Al-Hussaini, M.M. 1973, "Influence of Relative Density on the Strength and Deformation of Sand Under Plane Strain Conditions", *ASTM Special Technical Publications*, no. 523, pp. 332-347.

Almahakeri, M. 2013, *Stability of buried steel and glass fibre reinforced polymer pipes under lateral ground movement*, Ph.D., Queen's University.

Alshibli, K., Batiste, S. & Sture, S. 2003, "Strain Localization in Sand: Plane Strain versus Triaxial Compression", *Journal of Geotechnical and Geoenvironmental Engineering*, vol. 129, no. 6, pp. 483-494.

Alshibli, K. & Sture, S. 2000, "Shear Band Formation in Plane Strain Experiments of Sand", *Journal of Geotechnical and Geoenvironmental Engineering*, vol. 126, no. 6, pp. 495-503.

Anastasopoulos, I., Gazetas, G., Bransby, M., Davies, M. & El Nahas, A. 2007, "Fault Rupture Propagation through Sand: Finite-Element Analysis and Validation through Centrifuge Experiments", *Journal of Geotechnical and Geoenvironmental Engineering*, vol. 133, no. 8, pp. 943-958.

Andersen, K. & Schjetne, K. 2013, "Database of Friction Angles of Sand and Consolidation Characteristics of Sand, Silt, and Clay", *Journal of Geotechnical and Geoenvironmental Engineering*, vol. 139, no. 7, pp. 1140-1155.

ASCE 1984, *Guidelines for the Seismic Design of Oil and Gas Pipeline Systems*, ASCE Committee on Gas and Liquid Fuel Lifelines.

Audibert, J.M.E. & Nyman, K.J. 1977, "Soil restraint against horizontal motion of pipes", *Journal of the Geotechnical Engineering Division ASCE*, vol. 103, no. NGT10, pp. 1119-1142.

Audibert, J.M.E. & Nyman, K.J. 1975, "Coefficients of Subgrade Reaction for the Design of Buried Piping", *ASCE Specialty Conference on Structural Design of Nuclear Plant Facilities*, December 8 - December 10, 1975, pp. 109-141.

Babaei, M.H. & Sudom, D. 2014, "Ice-Seabed Gouging Database: Review and Analysis of Available Numerical Models", *Proceedings of the Arctic Technology Conference*, February 10 - 12, 2014, 9p.

Badv, K. & Daryani, K.E. 2010, "An investigation into the upward and lateral soil-pipeline interaction in sand using finite difference method", *Iranian Journal of Science and Technology*, vol. 34, no. B4, pp. 433-445.

Balachowski, L. 2006, "Scale Effect in Shaft Friction from the Direct Shear Interface Tests", *Archives of Civil and Mechanical Engineering*, vol. 6, no. 3, pp. 13-28.

Barrette, P. 2011, "Offshore pipeline protection against seabed gouging by ice: An overview", *Cold Regions Science and Technology*, vol. 69, no. 1, pp. 3-20.

Barrette, P.D. & Sudom, D. 2014, "Ice-soil-pipeline interaction during seabed gouging in physical tests: Database analysis and outstanding issues", *Proceedings of the Arctic Technology Conference*, February 10 - 12, 2014, 8p.

Barrette, P. & Sudom, D. 2012, "Physical simulations of seabed scouring by ice: Review and database", *Proceedings of the 22nd International Offshore and Polar Engineering Conference, ISOPE*, Rhodes, Greece, June 17 - 22, 2012, pp. 381-388.

Bathurst, R.J., Keshavarz, A., Zarnani, S. & Take, W.A. 2007, "A simple displacement model for response analysis of EPS geofoam seismic buffers", *Soil Dynamics and Earthquake Engineering*, vol. 27, no. 4, pp. 344-353.

Bathurst, R.J., Zarnani, S. & Gaskin, A. 2007, "Shaking table testing of geofoam seismic buffers", *Soil Dynamics and Earthquake Engineering*, vol. 27, no. 4, pp. 324-332.

Been, K., Fredj, A. & Comfort, G. 2011, "Pipeline strains in soft clay backfill subject to ice gouging", *Journal of Pipeline Engineering*, vol. 10, no. 2, pp. 87-98.

Been, K., Peek, R., Croasdale, K. & Verlaan, P. 2013, "Subscour Displacements for Pipeline Design: State of Practice for Kashagan Project", *Proceedings of the 22nd International Conference on Port and Ocean Engineering under Arctic Conditions*, June 9 - 13, 2013, 10p.

Been, K. & Jefferies, M.G. 1985, "State Parameter for Sands", *Geotechnique*, vol. 35, no. 2, pp. 99-112.

Been, K., Jefferies, M.G. & Hachey, J. 1991, "Critical state of sands", *Geotechnique*, vol. 41, no. 3, pp. 365-381.

Been, K., Sancio, R.B., Ahrabian, D., Van Kesteren, W., Croasdale, K. & Palmer, A. 2008, "Subscour displacement in clays from physical model tests", *Proceedings of the International Pipeline Conference*, September 29 - October 3, 2008, 7p.

Benson, D.J. 1997, "Mixture theory for contact in multi-material Eulerian formulations", *Computer Methods in Applied Mechanics and Engineering,* vol. 140, no. 1-2, pp. 59-86.

Benson, D.J. & Okazawa, S. 2004, "Contact in a multi-material Eulerian finite element formulation", *Computer Methods in Applied Mechanics and Engineering,* vol. 193, no. 39-41, pp. 4277-4298.

Benson, D.J. & Okazawa, S. 2004, "Eulerian - Lagrangian coupling in finite element calculations with applications to machining", *Proceedings of the ASME/JSME Pressure Vessels and Piping Conference*, July 25 - 29, 2004, pp. 115-120.

Blasco, S., Carr, E., Campbell, P. & Shearer, J. 2011, "Impact of environmental factors on the distribution of extreme scouring (gouging) events, Canadian Beaufort shelf", *Proceedings of the 21st International Conference on Port and Ocean Engineering under Arctic Conditions 2011 (POAC)*, July 10 - 14, 2011, 10p.

Bolton, M.D. 1986, "The strength and dilatancy of sands", *Geotechnique,* vol. 36, no. 1, pp. 65-78.

Bolton, M.,D. 1987, "Discussion: The strength and dilatancy of sands", *Geotechnique,* vol. 37, no. 2, pp. 219-226.

Borges, R.G. & Oliveira, J.R.M.S. 2011, "Multidirectional Analysis of Pipeline-soil Interaction in Clay", *2nd International Symposium on Frontiers in Offshore Geotechnics, ISFOG 2010*, November 8 - 10, 2010, pp. 773-778.

Burland, J.B. 1987, "Nash Lecture - The Teaching of Soil Mechanics - A Personal View", *9TH European Conf on Soil Mechanics and Foundation Engineering: Groundwater Effects in Geotechnical Engineering,* August 31 - September 3, 1987, pp. 1427-1447.

Burnett, A. 2015, *Investigation of Full Scale Horizontal Pipe-Soil Interaction and Large Strain Behaviour of Sand*, M.A.Sc., Queen's University.

Calvetti, F., di Prisco, C. & Nova, R. 2004, "Experimental and numerical analysis of soil-pipe interaction", *Journal of Geotechnical and Geoenvironmental Engineering,* vol. 130, no. 12, pp. 1292-1299.

Cappelletto, A., Tagliaferri, R., Giurlani, G., Andrei, G., Furlani, G. & Scarpelli, G. 1998, "Field full scale tests on longitudinal pipeline-soil interaction", *Proceedings of the International Pipeline Conference (IPC)*ASME, , June 7 - 11, 1998, pp. 771-778.

Castro, G. 1969, *Liquefaction of sands*, Ph.D., Harvard University.

Cathie, D.N., Jaeck, C., Ballard, J.C. & Wintgens, J.F. 2005, "Pipeline geotechnics - state-of-the-art", *Frontiers in Offshore Geotechnics: ISFOG 2005,* Taylor & Francis Group, London, September 19 - 21, 2005, pp. 95-114.

C-CORE 2008, Pipeline Integrity for Ground Movement Hazards. Report prepared for United States Department of Transportation, C-CORE Report R-07-082-459v2, December 2008.

CEPA 2015, *The different types of pipelines in Canada*. Available: http://www.cepa.com/wp-content/uploads/2015/09/CEPA-PipeLinesInfographic-2015_final.pdf

CEPA 2014, *Pipeline Watercourse Management: Recommended Practices, 1st Edition*, Canadian Energy Pipeline Association, Calgary, AB, Canada.

Cerato, A.B. & Lutenegger, A.J. 2006, "Specimen size and scale effects of direct shear box tests of sands", *Geotechnical Testing Journal*, vol. 29, no. 6, pp. 507-516.

Chakraborty, T. & Salgado, R. 2010, "Dilatancy and Shear Strength of Sand at Low Confining Pressures", *Journal of Geotechnical and Geoenvironmental Engineering*, vol. 136, no. 3, pp. 527-532.

Chatterjee, S., Randolph, M.F., White, D.J. & Wang, D. 2011, "Large deformation finite element analysis of vertical penetration of pipelines in seabed", *2nd International Symposium on Frontiers in Offshore Geotechnics: ISFOG 2010*, Taylor & Francis - Balkema, Perth, WA, Australia, November 8 - 10, 2010, pp. 785-790.

Cho, G., Dodds, J. & Santamarina, J. 2006, "Particle Shape Effects on Packing Density, Stiffness, and Strength: Natural and Crushed Sands", *Journal of Geotechnical and Geoenvironmental Engineering*, vol. 132, no. 5, pp. 591-602.

Christian, H.A. & Morgenstern, N.R. 1986, "Compressibility and stress history of holocene sediments in the Canadian Beaufort Sea", *3rd Canadian Conference on Marine Geotechnical Engineering*, St. John's, NL, pp. 275-300.

Chu, J. 1995, "An experimental examination of the critical state and other similar concepts for granular soils", *Canadian Geotechnical Journal*, vol. 32, no. 6, pp. 1065-1075.

Cocchetti, G., di Prisco, C. & Galli, A. 2009, "Soil-pipeline interaction along unstable slopes: A coupled three-dimensional approach. Part 2: Numerical analyses", *Canadian Geotechnical Journal*, vol. 46, no. 11, pp. 1305-1321.

Cocchetti, G., di Prisco, C., Galli, A. & Nova, R. 2009, "Soil-pipeline interaction along unstable slopes: A coupled three-dimensional approach. Part 1: Theoretical formulation", *Canadian Geotechnical Journal*, vol. 46, no. 11, pp. 1289-1304.

Cornforth, D.H. 1973, "Prediction of drained strength of sands from relative density measurements", *ASTM Special Technical Publications*, , no. 523, pp. 281-303.

Cox, M.R.B. 2008, *The influence of grain shape on dilatancy*, Ph.D., The University of Arizona.

Croasdale, K., Comfort, G. & Been, K. 2005, "Investigation of ice limits to ice gouging", *Proceedings of the 18th Int. Conf. on Port and Ocean Engineering Under Arctic Conditions*, June 26 - 30, 2005, pp. 23-32.

Crooks, J., Been, K., Becker, D. & Jefferies, M. 2006, "Geology, characterization and properties of Beaufort Sea Clays", *Proceedings of the Second International Workshop*

on Characterisation and Engineering Properties of Natural Soils, eds. K.K. Phoon, D.W. Hight, S. Leroueil & T.S. Tan, Taylor & Francis, , November 29 - December 1, 2006, pp. 1855.

Daiyan, N. 2013, *Investigating Soil/Pipeline Interaction During Oblique Relative Movements*, PhD, Memorial University of Newfoundland.

Daiyan, N., Kenny, S., Phillips, R. & Popescu, R. 2011, "Investigating pipeline-soil interaction under axial-lateral relative movements in sand", *Canadian Geotechnical Journal*, vol. 48, no. 11, pp. 1683-1695.

Das, B.M. 2002, "Shear Strength of Soil" in *Principles of Geotechnical Engineering*, Fifth edn, Brooks/Cole, Pacific Grove, CA, USA, pp. 337-340.

Davies, G., Marley, M. & Mork, K. 2011, "Limit State Design Methodology for Offshore Pipelines against Ice Gouging - Industry Guidelines from the ICEPIPE JIP", *Proceedings of the Arctic Technology Conference*, February 7 - 9, 2011, 22p.

Davis, E.H. 1968, "Theories of plasticity and the failure of soil masses" in *Soil Mechanics: Selected Topics*, ed. I.K. Lee, Butterworth, London, pp. 341-380.

Desrues, J. & Hammad, W. 1989, "Shear Banding Dependency on Mean Stress Level in Sand", *2nd International Workshop on Numerical Methods for Localization and Bifurcation of Granular Bodies*, September 25 – 30, 1989, pp. 57-67.

di Prisco, C. & Galli, A. 2006, "Soil-pipe interaction under monotonic and cyclic loads: experimental and numerical modelling", *Proceedings of the First Euro Mediterranean Symposium in Advances on Geomaterials and Structures (AGS '06)*, pp. 755-760.

Dickin, E.A. 1988, "Stress-displacement of buried plates and pipes", *Proceedings of the International Conference on Geotechnical Centrifuge Modelling - Centrifuge '88*, A.A. Balkema, Paris, France, Apr 25 - 27, 1988, pp. 205-214.

Dietz, M.S. & Lings, M.L. 2006, "Postpeak strength of interfaces in a stress-dilatancy framework", *Journal of Geotechnical and Geoenvironmental Engineering*, vol. 132, no. 11, pp. 1474-1484.

Donea, J., Huerta, A., Ponthot, J.-. & Rodriguez-Ferran, A. 2004, "Chapter 14: Arbitrary Lagrangian-Eulerian Methods" in *Encyclopedia of Computational Mechanics*, John Wiley & Sons Ltd., pp. 1-25.

Drover, E.A. & Kenny, S.P. 2012, "Bounds on Iceberg Motions During Contact with Subsea Equipment and the Seabed", *Proceedings of the Twenty-second (2012) International Offshore and Polar Engineering Conference*, June 17 - 22, 2012, pp. 1280 - 1286.

Duncan, J.M. & Chang, C. 1970, "Nonlinear analysis of stress and strain in soils", *Journal of the Soil Mechanics and Foundations Division*, vol. 96, no. 5, pp. 1629-1653.

Dutton, M. 2012, *Digital image correlation for evaluating structural engineering materials*, M.A.Sc., Queen's University.

El-Amam, M.M. & Bathurst, R.J. 2004, "Experimental design, instrumentation and interpretation of reinforced soil wall response using a shaking table", *International Journal of Physical Modelling in Geotechnics*, vol. 4, pp. 13-32.

El-Amam, M.M., Bathurst, R.J. & Hatami, K. 2004, "Numerical modeling of reinforced soil retaining walls subjected to base acceleration", *13th World Conference on Earthquake Engineering*, August 1 – 6, 2004, 15p.

El-Gebaly, S., Paulin, M., Lanan, G. & Cooper, P. 2012, "Ice gouge interaction with buried pipelines assessment using advanced coupled eulerian lagrangian", *Proceedings of the Arctic Technology Conference*, December 3 - 5, 2012, 12p.

Eltaher, A. 2014, "Gaps in Knowledge and Analysis Technology of Ice Gouge - Pipeline Interaction", *Proceedings of the Arctic Technology Conference*, February 10 - 12, 2014, 10p.

Eskandari, F., Phillips, R. & Hawlader, B. 2012, "Finite Element Analyses of Seabed Response to Ice Keel Gouging", *Proceedings of the 65th Canadian Geotechnical Conference (GeoManitoba)*, September 30 - October 3, 2012, 8p.

Eskandari, F., Phillips, R. & Hawlader, B. 2011, "Ice Gouging Analysis Using NorSand Critical State Soil Model", *Proceedings of the Pan-Am CGS Geotechnical Conference*, October 2 - 6, 2011, 8p.

Fairchild, D.P., Tang, H., Shafrova, S.Y., Cheng, W. & Crapps, J.M. 2014, "Updates to Exxonmobil's modelling approach for tensile strain capacity prediction", *Proceedings of the Twenty-fourth (2014) International Ocean and Polar Engineering Conference*, Busan, Korea, June 15 - 20, 2014, pp. 487-496.

Fallah, S., Gavin, K. & Moradabadi, E. 2015, "Estimation of spudcan penetration using a probabilistic Eulerian finite element analysis", *Proceedings of the 3rd International Symposium on Frontiers in Offshore Geotechnics (ISFOG 2015)*, June 10 - 12, 2015, pp. 1281-1286.

Fatemi, A. & Kenny, S. 2012, "Characterization of initial geometric imperfections for pipelines and influence on compressive strain capacity", *22nd International Offshore and Polar Engineering Conference*, Rhodes, Greece, June 17 -22, 2012, pp. 550-556.

Foray, P., Balachowski, L. & Rault, G. 1998, "Scale Effect in Shaft Friction Due to the Localisation of Deformations", *Proc. Int. Conf. Centrifuge 98*, pp. 211-216.

Foseco 2000, "Sands and Green Sand" in *Ferrous Foundryman's Handbook*, ed. J.R. Brown, Butterworth-Heinemann, Oxford, pp. 147.

Garnier, J., Gaudin, C., Springman, S.M., Culligan, P.J., Goodings, D., Konig, D., Kuttervii, B., Phillips, R., Randolph, M.F. & Thorel, L. 2007, "Catalogue of scaling laws and similitude questions in geotechnical centrifuge modelling", *International Journal of Physical Modelling in Geotechnics*, vol. 3, pp. 1-23.

Gautier, D.L. 2011, "U.S. Geological Survey circum-arctic resource appraisal", *Proceedings of the Arctic Technology Conference,* February 7 - 9, 2011, 4p.

Giuliani, G. 2013, *Experimental study of ice gouging in a sand seabed*, Ph.D., University of Aberdeen.

Guo, P.J. & Stolle, D.F.E. 2005, "Lateral pipe-soil interaction in sand with reference to scale effect", *Journal of Geotechnical and Geoenvironmental Engineering,* vol. 131, no. 3, pp. 338-349.

Guo, P. 2005, "Numerical modeling of pipe-soil interaction under oblique loading", *Journal of Geotechnical and Geoenvironmental Engineering,* vol. 131, no. 2, pp. 260-268.

Guo, P. & Su, X. 2007, "Shear strength, interparticle locking, and dilatancy of granular materials", *Canadian Geotechnical Journal,* vol. 44, no. 5, pp. 579-591.

Han, Y., Lim, H. & Jeong, S. 2013, "The Strength and Deformation Characteristics of Jumunjin Sand under Low Confining Stresses", *Journal of the Korean Geotechnical Society,* vol. 30, no. 2, pp. 33-42.

Hanna, A. 2001, "Determination of plane-strain shear strength of sand from the results of triaxial tests", *Canadian Geotechnical Journal,* vol. 38, no. 6, pp. 1231-1240.

Hansen, J.B. & Christensen, N.H. 1961, *The ultimate resistance of rigid piles against transversal forces,* Geoteknisk Institut, Copenhagen.

Hikooei, B.H. 2013, *Numerical Modeling of Pipe-Soil Interaction Under Transverse Direction*, M.Eng., University of Calgary.

Hivon, E. 1983, *Stress History in the Beaufort Sea: An Initial Study*, Geological Survey of Canada, Ottawa, ON, Canada.

Horne, M.R. 1965, "The Behaviour of an Assembly of Rotund, Rigid, Cohesionless Particles. I", *Proceedings of the Royal Society of London.Series A, Mathematical and Physical Sciences,* vol. 286, no. 1404, pp. 62-78.

Horne, M.R. 1965, "The Behaviour of an Assembly of Rotund, Rigid, Cohesionless Particles. II", *Proceedings of the Royal Society of London.Series A, Mathematical and Physical Sciences,* vol. 286, no. 1404, pp. 79-97.

Hossain, K., Banneyake, R., Abdalla, B., Bell, G., Eltaher, A. & Jukes, P. 2011, "Ice keel-seabed-pipeline interaction simulation: Ice Pipe JIP extracts", *Journal of Pipeline Engineering,* vol. 10, no. 2, pp. 105-114.

Hsu, T., Chen, Y. & Hung, W. 2004, "Soil Friction Restraint of Oblique Pipelines in Dense Sand", *13th World Conference on Earthquake Engineering,* August 1-6, 2004, 14p.

Hsu, S.T. & Liao, H.J. 1998, "Uplift behaviour of cylindrical anchors in sand", *Canadian Geotechnical Journal,* vol. 35, no. 1, pp. 70-80.

Hsu, S. 2005, "A constitutive model for the uplift behavior of anchors in cohesionless soils", *Journal of the Chinese Institute of Engineers,* vol. 28, no. 2, pp. 305-317.

Hsu, T. 1996, "Soil restraint against oblique motion of pipelines in sand", *Canadian Geotechnical Journal,* vol. 33, no. 1, pp. 180-188.

Hsu, T. 1993, "Rate effect on lateral soil restraint of pipelines", *Soils and Foundations,* vol. 33, no. 4, pp. 159-169.

Hsu, T., Chen, Y. & Hung, W. 2006, "Soil restraint to oblique movement of buried pipes in dense sand", *Journal of Transportation Engineering,* vol. 132, no. 2, pp. 175-181.

Hsu, T., Chen, Y. & Wu, C. 2001, "Soil friction restraint of oblique pipelines in loose sand", *Journal of Transportation Engineering,* vol. 127, no. 1, pp. 82-87.

Hynes, F.G. 1996, *Centrifuge modelling of ice scour in sand*, M.Eng., Memorial University of Newfoundland.

Ivanovic, A., Neilson, R., Giuliani, G. & Bransby, M. 2010, "Influence of object geometry on penetration into the seabed", *Proceedings of the Second International Symposium on Frontiers in Offshore Geotechnics (ISFOG),* November 8 - 10, 2010, pp. 859 - 864.

Ivanovic, A., Neilson, R.D. & Giuliani, G. 2012, "Influence of Iceberg Geometry On Soil Resistance In Sand", *Offshore Site Investigation and Geotechnics: Integrated Technologies - Present and Future,* September 12 - 14, 2012, pp. 573 - 578.

Janbu, N. 1963, "Soil Compressibility As Determined By Oedometer And Triaxial Tests", *Proceedings of the 3rd European Conference on Soil Mechanics and Foundation Engineering*, pp. 19-25.

Jefferies, M. & Been, K. 2006, *Soil liquefaction: a critical state approach*, Taylor & Francis, London; New York.

Jefferies, M.G. 1993, "Nor-Sand: a simple critical state model for sand", *Geotechnique,* vol. 43, no. 1, pp. 91-103.

Jewell, R.A. 1989, "Direct shear tests on sand", *Geotechnique,* vol. 39, no. 2, pp. 309-322.

Jiang, M. & Zhang, W. 2015, "DEM analyses of shear band in granular materials", *Engineering Computations,* vol. 32, no. 4, pp. 985-1005.

Jung, J.K. 2011, *Soil-Pipe Interaction Under Plane Strain Conditions*, Ph.D., Cornell University.

Jung, J.K. & Zhang, K. 2011, "Finite element analyses of soil-pipe behavior in dry sand under lateral loading", *Pipelines 2011: A Sound Conduit for Sharing Solutions,* July 23 - 27, 2011, pp. 312-324.

Karimian, H., Wijewickreme, D. & Honegger, D. 2006, "Buried pipelines subjected to transverse ground movement: Comparison between full-scale testing and numerical

modeling", *25th International Conference on Offshore Mechanics and Arctic Engineering*, June 4 - 9, 2006 - June 9, 7p.

Keaveny, J.M. & Mitchell, J.K. 1988, "Strength of fine- grained soils using the piezocone", *Use of In Situ Tests in Geotechnical Engineering (ASCE Geotechnical Special Publication No. 6*), June 23 – 25, 1986, pp. 668-685.

Kennedy, R.P., Chow, A.M. & Williamson, R.A. 1977, "Fault movement effects on buried oil pipeline", *Transportation Engineering Journal*, vol. 103, no. 5, pp. 617-633.

Kenny, S., Barrett, J., Phillips, R. & Popescu, R. 2007, "Integrating geohazard demand and structural capacity modelling within a probabilistic design framework for offshore arctic pipelines", *17th International Offshore and Polar Engineering Conference*, July 1 - 6, 2007, pp. 3057-3064.

Kenny, S., Gordon, R. & Swank, G. 2016, "Alternative Compressive Strain Capacity Performance Limits for Strain Based Design Applications", *Proceedings of the International Pipeline Conference*, September 26 - 30, 2016, 10p.

Kenny, S., Phillips, R., McKenna, R. & Clark, J.I. 2000, "Response of Buried Marine Arctic Pipelines to Ice Gouge Events", *Proceedings of the ETCE/OMAE 2000 Joint Conference: Energy For The New Millennium*, February 14 - 17, 2000, 8p.

Kenny, S., Phillips, R. & Nobahar, A. 2005, "PRISE Numerical Studies on subgouge deformations and pipeline/soil interaction analysis", *Proceedings of the International Conference on Port and Ocean Engineering Under Arctic Conditions (POAC)*, June 26 - 30, 2005, 10p.

Kenny, S. & Jukes, P. 2015, "Pipeline/Soil Interaction Modeling in Support of Pipeline Engineering Design and Integrity" in *Oil and Gas Pipelines*, John Wiley & Sons Inc., pp. 99-142.

Kenny, S., McKenna, R., Bruce, J., Nobahar, A., King, T. & Phillips, R. 2004, "Probabilistic design methodology to mitigate ice gouge hazards for offshore pipelines", *Proceedings of the 5th International Pipeline Conference (IPC)*American Society of Mechanical Engineers, New York, NY 10016-5990, United States, Oct 4 - 8, 2004, pp. 1925.

King, T., Phillips, R., Barrett, J. & Sonnichsen, G. 2009, "Probabilistic pipeline burial analysis for protection against ice scour", *Cold Regions Science and Technology*, vol. 59, no. 1, pp. 58-64.

Kondner, R.L. 1963, "Hyperbolic stress-strain response; cohesive soils", *ASCE -- Proceedings -- Journal of the Soil Mechanics and Foundations Division*, vol. 89, pp. 115-143.

Konrad, J.M. & Law, K.T. 1987, "Undrained shear strength from piezocone tests", *Canadian geotechnical journal*, vol. 24, no. 3, pp. 392-405.

Konuk, I., Liferov, P. & Loset, S. 2007, "Challenges in modelling ice gouge and pipeline response", *Proceedings of the 19th International POAC Conference*, June 27 - 30, 2007, pp. 760-773.

Konuk, I., Yu, S. & Gracie, S. 2005, "An ALE FEM Model of Ice Scour", *11th International Conference of the International Association of Computer Methods and Advances in Geomechanics*., June 19 – 21, 2005, 8p.

Konuk, I. & Gracie, R. 2004, "A 3-Dimensional Eulerian Finite Element Model for Ice Scour", *Proceedings of the 5th International Pipeline Conference*, October 4 - 8, 2004, pp. 1911-1918.

Konuk, I., Gurtner, A. & Yu, S. 2009, "A cohesive element framework for dynamic ice-structure interaction problems - Part I: Review and formulation", *28th International Conference on Ocean, Offshore and Arctic Engineering, May 31 – June 5, 2009*, pp. 33-41.

Konuk, I. & Yu, S. 2007, "A pipeline case study for ice scour design", *26th International Conference on Offshore Mechanics and Arctic Engineering (OMAE)*, June 10 - 15, 2007, pp. 163-169.

Konuk, I., Yu, S. & Fredj, A. 2006, "Do winkler models work: A case study for ICE scour problem", *Proceedings of OMAE06 25th International Conference on Offshore Mechanics and Arctic Engineering*, June 4 - 9, 2006, 7p.

Kovacs, A. & Mellor, M. 1974, "Sea ice morphology and ice as a geologic agent in the southern Beaufort Sea", The Coast and Shelf of the Beaufort Sea, Symp., Proc., eds. J.L. Reed & J.E. Sater, Arctic Institute of North America, San Francisco, CA, USA, January 7 - 9, 1974, pp. 113-164.

Lach, P.R. 1996, *Centrifuge modelling of large soil deformation due to ice scour*, Ph.D., Memorial University of Newfoundland (Canada).

Lade, P.V. & Duncan, J.M. 1976, "Stress Path Dependent Behaviour of Cohesionless Soils", *Journal of Geotechnical Engrn. Div., ASCE*, vol. 102, no. 1, pp. 51-65.

Lanan, G.A., Niedoroda, A.W. & Weeks, W.F. 1986, "Ice Gouge Hazard Analysis", *Proceedings of the Offshore Technology Conference (OTC)*, 10p.

Lanan, G.A., Cowin, T.G. & Johnston, D.K. 2011, "Alaskan Beaufort Sea Pipeline Design, Installation and Operation", *Proceedings of the Arctic Technology Conference*, February 7 - 9, 2011, 9p.

Lanan, G.A., Ennis, J.O., Egger, P.S. & Yockey, K.E. 2001, "Northstar Offshore Arctic Pipeline Design and Construction", *Proceedings of the Offshore Technology Conference*, April 30 - May 1, 2001, 8p.

Lancelot, L., Shahrour, I. & Al Mahmoud, M. 2006, "Failure and dilatancy properties of sand at relatively low stresses", *Journal of Engineering Mechanics*, vol. 132, no. 12, pp. 1396-1399.

Lapos, B. & Moore, I.D. 2002, "Evaluation of the strength and deformation parameters of olimag synthetic olivine", *Proceedings of the 55th Canadian Geotechnical and 3rd Joint IAH-CNC and CGS Groundwater Specialty Conferences*, pp. 729-734.

Lau, C.K. & Bolton, M.D. 2011, "The bearing capacity of footings on granular soils. II: Experimental evidence", *Geotechnique*, vol. 61, no. 8, pp. 639-650.

Lee, K.L. 1970, "Comparison of Plane Strain and Triaxial Tests on Sand", *Journal of the Soil Mechanics and Foundations Division*, vol. 96, no. SM3, pp. 901-923.

Leidersdorf, C., Gadd, P.E., Hearon, G.E., Hall, J.D. & Perry, C.J. 2008, "Coastal Engineering Design of the Oooguruk Project", *Proceedings of the Offshore Technology Conference*, May 5 - 8, 2008, 17p.

Lele, S.P., Hamilton, J.M., Panico, M. & Arslan, H. 2013, "Advanced Continuum Modeling to Determine Pipeline Strain Demand Due to Ice-Gouging", *International Journal of Offshore and Polar Engineering*, vol. 23, no. 1, pp. 22-28.

Lele, S.P., Hamilton, J.M., Panico, M. & Arslan, H. 2011, "Advanced Continuum Modeling to Determine Pipeline Strain Demand Due to Ice-Gouging", *Proceedings of the Twenty-first (2011) International Offshore and Polar Engineering Conference*, June 19-24, 2011, pp. 615-621.

Leussink, H. & Wittke, W. 1964, *Difference in Triaxial and Plain Strain Shear Strength*, American Society for Testing and Materials (ASTM), Philadelphia, PA, United States.

Lever, J.H. 2000, *Assessment of Millennium Pipeline Project Lake Erie Crossing: Ice Scour, Sediment Sampling, and Turbidity Modeling*, USACE.

Liferov, P. & Høyland, K.V. 2004, "In-situ ice ridge scour tests: experimental set up and basic results", *Cold Regions Science and Technology*, vol. 40, no. 1-2, pp. 97-110.

Liferov, P., Nes, H., Asklund, J., Shkhinek, K. & Jilenkov, A. 2014, "Ice Gouging and its Effect on Pipelines", *Proceedings of the Arctic Technology Conference*, February 10 - 12, 2014, 15p.

Lings, M.L. & Dietz, M.S. 2004, "An improved direct shear apparatus for sand", *Geotechnique*, vol. 54, no. 4, pp. 245-256.

Liu, R., Basu, P. & Xiong, H. 2015, "Laboratory tests and thermal buckling analysis for pipes buried in Bohai soft clay", *Marine Structures*, vol. 43, pp. 44-60.

Loktev, A., Bondarev, V., Kulikov, S. & Rokos, S. 2012, "Russian Arctic Offshore Permafrost", *Proceedings of the Offshore Site Investigation and Geotechnics Conference*, September 12 - 14, 2012, 8p.

Mahdavi, H., Kenny, S., Phillips, R. & Popescu, R. 2013, "Significance of geotechnical loads on local buckling response of buried pipelines with respect to conventional practice", *Canadian Geotechnical Journal*, vol. 50, no. 1, pp. 68-80.

Marachi, N.D., Duncan, J.M., Chan, C.K. & Seed, H.B. 1981, "Plane-Strain Testing of Sand", *Laboratory Shear Strength of Soil*, June 25, 1980, pp. 294-302.

Mayne, P.W. 2007, *Cone Penetration Testing State-of-Practice: Final Report*. Available: http://geosystems.ce.gatech.edu/Faculty/Mayne/papers/NCHRP%20CPT%20Synthesis%20(2007)%20color.pdf

Monroy, M. 2013, *Soil Restraints on Steel Buried Pipelines Crossing Active Seismic Faults*, Ph.D., University of British Columbia.

Moradi, G. & Abbasnejad, A. 2014, "PLASTIC STRAIN HARDENING AND SOFTENING IN SAND USING INTERNAL FRICTION ANGLE OF DIRECT SHEAR TEST", *Indian J. Sci. Res.*, vol. 7, no. 1, pp. 1294-1300.

Moradi, G. & Abbasnejad, A. 2014, "Frictional strain hardening and softening in sand using simple direct shear test parameters", *Electronic Journal of Geotechnical Engineering*, vol. 19 N, pp. 3351-3365.

Mühlhaus, H.B. & Vardoulakis, I. 1987, "The thickness of shear bands in granular materials", *Géotechnique*, vol. 37, no. 3, pp. 271-283.

Nanda, S. & Patra, N.R. 2015, "Determination of soil properties for plane strain condition from the triaxial tests results", *International Journal for Numerical and Analytical Methods in Geomechanics*, vol. 39, no. 9, pp. 1014-1026.

Nixon, J.F., Palmer, A. & Phillips, R. 1996, "Simulations for buried pipeline deformations beneath ice scour", *Proceedings of the International Conference on Offshore Mechanics and Arctic Engineering (OMAE*), Florence, Italy, June 16 - 20, 1996, pp. 383-392.

Nobahar, A., Popescu, R. & Konuk, I. 2001, "Parameter calibration of strain hardening/softening of sand from direct shear tests", *Computer methods and advances in geomechanics*, pp. 971-976.

Nobahar, A., Popescu, R. & Konuk, I. 2000, "Estimating Progressive Mobilization of Soil Strength", *Canadian Geotechnical Conference*, pp. 1311-1318.

Nobahar, A., Kenny, S., King, T., McKenna, R. & Phillips, R. 2007a, "Analysis and design of buried pipelines for ice gouging hazard: A probabilistic approach", *Journal of Offshore Mechanics and Arctic Engineering*, vol. 129, no. 3, pp. 219-228.

Nobahar, A., Kenny, S. & Phillips, R. 2007b, "Buried pipelines subject to subgouge deformations", *International Journal of Geomechanics*, vol. 7, no. 3, pp. 206-216.

Nyman, K.J. 1984, "Soil response against oblique motion of pipes", *Journal of Transportation Engineering*, vol. 110, no. 2, pp. 190-202.

Olimag Inc. 2016, *JETMAG Synthetic Olivine Pyroxene Sands for Blast Cleaning*, Olimag Inc., Thetford Mines, QC, Canada.

Oliphant, J. & Maconochie, A. 2007, "The axial resistance of buried and unburied pipelines", *Proceedings of the 6th International Offshore Site Investigation and Geotechnics Conference*, pp. 125-132.

Oliveira, J.R.M.S., Almeida, M.S.S., Almeida, M.C.F. & Borges, R.G. 2010, "Physical modeling of lateral clay-pipe interaction", *Journal of Geotechnical and Geoenvironmental Engineering*, vol. 136, no. 7, pp. 950-956.

Olson, N.A. 2009, *Soil Performance for Large-Scale Soil-Pipeline Tests*, Ph.D., Cornell University.

O'Rourke, M.J. & Liu, J.X. 2012, *Seismic Design of Buried and Offshore Pipelines*, MCEER-12-MN04, MCEER, Buffalo, NY.

O'Rourke, T.D. 2010, "Geohazards and large, geographically distributed systems", *Geotechnique*, vol. 60, no. 7, pp. 505-543.

Ovesen, N.K. 1964, "Anchor slabs, calculation methods and model tests", *Geoteknisk Institut (Danish Geotechnical Inst) -- Bulletin*, no. 16, pp. 39.

Palmer, A.C. & Been, K. 2011, "Pipeline Geohazards for Arctic Conditions" in *Deepwater Foundations and Pipeline Geomechanics* J. Ross Publishing Inc., Ft. Lauderdale, FL, USA, pp. 171-188.

Palmer, A.C., Konuk, I., Comfort, G. & Been, K. 1990, "Ice gouging and the safety of marine pipelines", *Proceedings of the 22nd Annual Offshore Technology Conference*, May 7 - 10, 1990, pp. 235-244.

Palmer, A.C., Ellinas, C.P., Richards, D.M. & Guijt, J. 1990, "Design of Submarine Pipelines Against Upheaval Buckling", *Proceedings of the 22nd Annual Offshore Technology Conference*, May 7 - 10, 1990, pp. 551-560.

Palmer, A.C., Konuk, I., Niedoroda, A.W., Been, K. & Croasdale, K.R. 2005, "Arctic seabed ice gouging and large sub-gouge deformations", *Proceedings of the 1st International Symposium on Frontiers in Offshore Geotechnics (ISFOG)*, Taylor and Francis/Balkema, Perth, WA, Australia, September 19 - 21, 2005, pp. 645-650.

Palmer, A. 2000, "Are we ready to construct submarine pipelines in the Arctic?", *Proceedings of the 32nd Annual Offshore Technology Conference*Offshore Technol Conf, Houston, TX, USA, May 1 - 4, 2000, pp. 737-744.

Panico, M., Lele, S.P., Hamilton, J.M., Arslan, H. & Cheng, W. 2012, "Advanced ice gouging continuum models: Comparison with centrifuge test results", *Proceedings of the 22nd International Offshore and Polar Engineering Conference*International Society of Offshore and Polar Engineers, Rhodes, Greece, June 17 - 22, 2012, pp. 504-510.

Paulin, M. 1998, *An Investigation into Pipelines Subjected to Lateral Soil Loading*, Ph.D., Memorial University of Newfoundland.

Paulin, M., Kenny, S., Palmer, A.C. & Caines, J.V.M. 2008, "Offshore Pipelines in Cold Regions - Environmental Loadings and Geotechnical Considerations", *Proceedings of the International Conference and Exhibition on Performance of Ships and Structures in Ice 2008 (ICETECH 2008)*, July 20 - 23, 2008, pp. 406-413.

Paulin, M.J., Phillips, R. & Boivin, R. 1995, "Centrifuge modelling of lateral pipeline/soil interaction - Phase II", *Proceedings of the 14th International Conference on Offshore Mechanics and Arctic Engineering (OMAE)*, June 18 - 22, 1995, pp. 107-123.

Paulin, M.J., Phillips, R., Clark, J.I., Trigg, A. & Konuk, I. 1998, "Full-scale investigation into pipeline/soil interaction", *Proceedings of the International Pipeline Conference (IPC)*, 1998, pp. 779-787.

Paulin, M. 2014, "Arctic Offshore Pipeline Design and Installation Challenges", *Proceedings of the Arctic Technology Conference*, February 10 - 12, 2014, 13p.

Peek, R., Been, K., Bouwman, V., Nobahar, A., Sancio, R. & Van Schalkwijk, R. 2013, "Buried pipeline response to ice gouging on a clay seabed large scale tests and finite element analysis", *22nd International Conference on Port and Ocean Engineering under Arctic Conditions (POAC)*, June 9 - 13, 2013, 10p.

Peek, R. & Nobahar, A. 2012, "Ice gouging over a buried pipeline: Superposition error of simple beam-and-spring models", *International Journal of Geomechanics*, vol. 12, no. 4, pp. 508-516.

Peric, D., Runesson, K. & Sture, S. 1992, "Evaluation of plastic bifurcation for plane strain versus axisymmetry", *Journal of Engineering Mechanics*, vol. 118, no. 3, pp. 512-524.

Peters, J.F., Lade, P.V. & Bro, A. 1988, "Shear Band Formation in Triaxial and Plane Strain Tests", *Advanced Triaxial Testing of Soil and Rock, ASTM STP 977*, pp. 604-627.

Phillips, R. & Barrett, J. 2011, "Ice Keel-Seabed Interaction: Numerical Modelling for Sands", *Port and Ocean Engineering under Arctic Conditions (POAC)*, July 10 - 14, 2011, 10p.

Phillips, R., Clark, J.I. & Kenny, S. 2005, "PRISE studies on gouge forces and subgouge deformations", *Proceedings of the International Conference on Port and Ocean Engineering Under Arctic Conditions (POAC)*, June 26 - 30, 2005, 10p.

Phillips, R., Nobahar, A. & Zhou, J. 2004b, "Trench effects on pipe-soil interaction", *Proceedings of the 5th Biennial International Pipeline Conference (IPC)*, October 4 - 8, 2004, pp. 321-327.

Phillips, R. & Barrett, J. 2012, "PIRAM: Pipeline Response to Ice Gouging", *Proceedings of the Arctic Technology Conference*, December 3 - 5, 2012, 6p.

Phillips, R., Barrett, J.A. & Al-Showaiter, A. 2010, "Ice keel-seabed interaction: Numerical modelling validation", *Proceedings of the Offshore Technology Conference*, May 3 - 6, 2010, 13p.

Phillips, R., Nobahar, A. & Zhou, J. 2004a, "Combined axial and lateral pipe-soil interaction relationships", *Proceedings of the 5th Biennial International Pipeline Conference (IPC)*, October 4 - 8, 2004, pp. 299-303.

Pike, K., Kenny, S. & Hawlader, B. 2013, "Advanced analysis of pipe/soil interaction accounting for strain localization", *Proceedings of the CGS GeoMontreal 2013 Conference*, 6p.

Pike, K., Kenny, S. & Hawlader, B. 2011a, "Advanced Numerical Simulations of Ice Gouge Events and Implications for Engineering Design", *International Conference on Port and Ocean Engineering Under Arctic Conditions (POAC)*, July 10 - 14, 2011, 10p.

Pike, K., Kenny, S., Hawlader, B. & Moore, I. 2014a, "Effects of Geohazards on Energy Pipelines: Technology Framework Supporting Engineering Design and Emerging Tools", *Proceedings of the GeoHazards 6 Conference*, June 15-18, 2014, 10p.

Pike, K.P. & Kenny, S.P. 2012c, "Lateral-Axial Pipe/Soil Interaction Events: Numerical Modelling Trends and Technical Issues", *Proceedings of the 2012 9th International Pipeline Conference (IPC2012)*, 6p.

Pike, K. 2009, "Advanced numerical modelling tools aid Arctic pipeline design", *Journal of Pipeline Engineering*, vol. 8, no. 3, pp. 191-194.

Pike, K. & Kenny, S. 2012b, "Numerical Pipe/Soil Interaction Modelling: Sensitivity Study and Extension to Ice Gouging", *Proceedings of the Arctic Technology Conference*, December 3 – 5, 2012, 8p.

Pike, K.P. & Kenny, S.P. 2012a, "Advanced continuum modeling of the ice gouge process: Assessment of keel shape effect and geotechnical data", *22nd International Offshore and Polar Engineering Conference*, Rhodes, Greece, June 17 – 22, 2012, pp. 1287-1292.

Pike, K. & Kenny, S. 2011c, "Advancement of CEL Procedures to Analyze Large Deformation", *Proceedings of the Offshore Technology Conference*, May 2 – 5, 2011, 10p.

Pike, K., Kenny, S. & Hawlader, B. 2014b, "Numerical and constitutive model development to aid design against pipeline geo hazards", *Journal of Pipeline Engineering*, vol. 13, no. 3, pp. 201-209.

Pike, K., Seo, D. & Kenny, S. 2011b, "Continuum modelling of ice gouge events: Observations and assessment", *Proceedings of the Arctic Technology Conference*, February 7 - 9, 2011, 11p.

Poorooshasb, F., Paulin, M.J., Rizkalla, M. & Clark, J.I. 1994, "Centrifuge modeling of laterally loaded pipelines", *Transportation Research Record*, , no. 1431, pp. 33-40.

Popescu, R., Konuk, I., Guo, P. & Nobahar, A. 2002, "Some aspects in numerical analysis of pipe-soil interaction", *2nd Canadian Specialty Conference on Computer Applications in Geotechnique*, pp. 290-297.

Potts, D.M. & Zdravkovic, L. 1999, "7. Simple elasto-plastic constitutive models" in *Finite Element Analysis in Geotechnical Engineering: Theory*, Thomas Telford Publishing, pp. 147-199.

Prasad, K.S.R., 1986, *Analytical and experimental modelling of iceberg scours*, M.Eng., Memorial University of Newfoundland.

PRCI 2009, *Guidelines for constructing natural gas and liquid hydrocarbon pipelines through areas prone to landslide and subsidence hazards*, Pipeline Research Council International.

Qiu, G., Henke, S. & Grabe, J. 2011, "Application of a Coupled Eulerian-Lagrangian approach on geomechanical problems involving large deformations", *Computers and Geotechnics*, vol. 38, no. 1, pp. 30-39.

Rajah, S. 2014, "Soil parameters for assessing axial and transverse behavior of restrained pipelines - Part 2: Transverse behavior", *Pipelines 2014: From Underground to the Forefront of Innovation and Sustainability*, American Society of Civil Engineers (ASCE), Portland, OR, August 3 - 6, 2014, pp. 1849-1863.

Ramamurthy, T. & Tokhi, V.K. 1981, "Relation of Triaxial and Plane Strain Strengths", *10th International Conference on Soil Mechanics and Foundation Engineering*, pp. 755-758.

Randolph, M.F. & House, A.R. 2001, "The complementary roles of physical and computational modelling", *International Journal of Physical Modelling in Geotechnics*, vol. 1, no. 1, pp. 1-8.

Rizkalla, M., Poorooshasb, F. & Clark, J. 1992, "Centrifuge Modeling of Lateral Pipeline/Soil Interaction", *Proceedings of the 11th Offshore Mechanics and Arctic Engineering Conference (OMAE)*, June 7 - 11, 1992, 13p.

Rizkalla, M., Trigg, A. & Simmonds, G. 1996, "Recent advances in the modeling of longitudinal pipeline/soil interaction for cohesive soils", *Proceedings of the 15th International Conference on Offshore Mechanics and Arctic Engineering (OMAE)*ASME, Florence, Italy, June 16 - 20, 1996, pp. 325-332.

Robert, D.J. 2010, *Soil-pipeline Interaction in Unsaturated Soils*, Ph.D., University of Cambridge.

Robertson, P.K. & Campanella, R.G. 1983, "Interpretation of cone penetration tests. Part II: Clay", *Canadian Geotechnical Journal*, vol. 20, no. 4, pp. 734-745.

Rossiter, C. & Kenny, S. 2012a, "Assessment of Ice/Soil Interactions: Continuum Modeling in Clays", *Proceedings of the Twenty-second (2012) International Offshore and Polar Engineering Conference*, June 17 - 22, 2012, pp. 1304-1311.

Rossiter, C. & Kenny, S. 2012b, "Evaluation of Lateral Vertical Pipeline/Soil Interactions", *Proceedings of the Arctic Technology Conference*, Dec 3 - 5, 2012, 13p.

Rowe, P.W. 1969, "The relation between the shear strength of sands in triaxial compression, plane strain, and direct shear", *Geotechnique*, vol. 19, no. 1, pp. 75-86.

Rowe, P.W. 1962, "The stress-dilatancy relation for static equilibrium of an assembly of particles in contact", *Proceedings of the Royal Society of London. Series A, Mathematical, Physical and Engineering Sciences*, pp. 500-527.

Rowe, R.K. & Davis, E.H. 1982b, "Behaviour of anchor plates in sand", *Geotechnique,* vol. 32, no. 1, pp. 25-41.

Rowe, R.K. & Davis, E.H. 1982a, "Behaviour of anchor plates in clay", *Geotechnique,* vol. 32, no. 1, pp. 9-23.

Roy, K., Hawlader, B., Kenny, S. & Moore, I. 2016, "Finite element modeling of lateral pipeline-soil interactions in dense sand", *Canadian Geotechnical Journal,* vol. 53, no. 3, pp. 490-504.

Sadrekarimi, A. & Olson, S.M. 2011, "Critical state friction angle of sands", *Geotechnique,* vol. 61, no. 9, pp. 771-783.

Sakanoue, T. 2008, "Study on soil-pipeline interaction due to large ground deformation", *The 14th World Conference on Earthquake Engineering (WCEE),* October 12-17, 2008, 7p.

Sancio, R., Been, K. & Lopez, J. 2011, "Large scale indenter test program to measure sub gouge displacements", *21st International Conference on Port and Ocean Engineering under Arctic Conditions (POAC),* Montreal, QC, Canada, July 10 – 14, 2011, 10p.

Scarpelli, G., Sakellariadi, E. & Furlani, G. 2003, "Evaluation of soil-pipeline longitudinal interaction forces", *Rivista Italiana Di Geotechnica,* vol. 4, pp. 24-41.

Schaminee, P.E.L., Zorn, N.F. & Schotman, G.J.M. 1990, "Soil Response for Pipeline Upheaval Buckling Analyses: Full-Scale Laboratory Tests and Modelling", *Proceedings of the Offshore Technology Conference*, pp. 563-572.

Schanz, T. & Vermeer, P.A. 1996, "Angles of friction and dilatancy of sand", *Geotechnique,* vol. 46, no. 1, pp. 145-151.

Schnaid, F., Sills, G.C., Soares, J.M. & Nyirenda, Z. 1997, "Predictions of the coefficient of consolidation from piezocone tests", *Canadian Geotechnical Journal,* vol. 34, no. 2, pp. 315-327.

Schoonbeek, I.S.S. & Allersma, H.G.B. 2006, "Centrifuge modelling of scouring ice keels in clay", *6th International Conference on Physical Modelling in Geotechnics,* Taylor and Francis/Balkema, Hong Kong, China, August 4 - 6, 2006, pp. 1291-1296.

Seo, D., Kenny, S. & Hawlader, B. 2011, "Yield Envelopes for Oblique Pipeline/Soil Interaction in Cohesive Soil using ALE Procedure", *Proceedings of the Pan-Am CGS Geotechnical Conference,* October 2 - 6,2011, 7p.

Shibuya, S., Mitachi, T. & Tamate, S. 1997, "Interpretation of direct shear box testing of sands as quasi-simple shear", *Geotechnique,* vol. 47, no. 4, pp. 769-790.

Shimobe, S. & Moroto, N. 1997, "Classical Study on Strength Parameters of Granular Soils", *Deformation and Progressive Failure in Geomechanics*, pp. 271-276.

Shimobe, S. & Miyamori, T. 1994, "Influence of stress path on plane strain deformation characteristics of sand", *Pre-failure Deformation of Geomaterials*, Sep 12 - 14, 1994, pp. 347-352.

Shumaker, S. 2011, "Contribution of lateral earth pressure resistance to restrain horizontal thrust in buried pipelines subcommittee", *Pipelines 2011: A Sound Conduit for Sharing Solutions*, ASCE, Seattle, WA, USA, July 23 - 27, 2011, pp. 358-371.

Tho, K.K., Leung, C.F., Chow, Y.K. & Swaddiwudhipong, S. 2013, "Eulerian finite element simulation of spudcan-pile interaction", *Canadian Geotechnical Journal*, vol. 50, no. 6, pp. 595-608.

Thornton, C. 1974, *Deformation of sand in plane strain and axisymmetric compression*, Ph.D., University of Aston.

Timco, G.W. & Burden, R.P. 1997, "An analysis of the shapes of sea ice ridges", *Cold Regions Science and Technology*, vol. 25, no. 1, pp. 65-77.

Tong, P.Y.L. 1970, *Plane strain deformation of sands*, Ph.D., The University of Manchester.

Toyosawa, Y., Itoh, K., Kikkawa, N., Yang, J.-. & Liu, F. 2013, "Influence of model footing diameter and embedded depth on particle size effect in centrifugal bearing capacity tests", *Soils and Foundations*, vol. 53, no. 2, pp. 349-356.

Trautmann, C.H. 1983, *Behaviour of pipe in dry sand under lateral and uplift loading*, Ph.D., Cornell University.

Trautmann, C.H. & O'Rourke, T.D. 1985, "Lateral force-displacement response of buried pipe", *Journal of Geotechnical Engineering*, vol. 111, no. 9, pp. 1077-1092.

Turner, J.E. 2004, *Lateral Force-Displacement Behavior of Pipes in Partially Saturated Sand*, M.Sc., Cornell University.

Vaid, Y.P. & Sasitharan, S. 1992, "The strength and dilatancy of sand", *Canadian Geotechnical Journal*, vol. 29, no. 3, pp. 522-526.

Vermeer, P.A. & de Borst, R. 1984, "Non-associated plasticity for soils, concrete and rock", *Heron*, vol. 29, no. 3, pp. 1-64.

Walters, J.V. & Thomas, J.N. 1982, "Shear zone development in granular materials", *Proceedings of the 4th International Conference on Numerical Methods in Geomechanics*, A. A. Balkema, Edmonton, AB, pp. 263-274.

Wanatowski, D. & Chu, J. 2007, "A New Plane-Strain Apparatus and Plane-Strain Tests on Sand", *Proceedings of the 16th Southeast Asian Geotechnical Conference*, 6p.

Wang, X., Kibey, S., Tang, H., Cheng, W., Minnaar, K., Macia, M.L., Kan, W.C., Ford, S.J. & Newbury, B. 2010, "Strain-based design - Advances in prediction methods of tensile strain capacity", *Proceedings of the 20th International Offshore and Polar Engineering Conference*, Beijing, China, June 20 - 25, 2010, pp. 376-382.

Wantland, G.M., O'Neill, M.W., Reese, L.C. & Kalajian, E.H. 1979, "Lateral stability of pipelines in clay", *Proceedings of the Offshore Technology Conference*Houston, Texas, May 5 - 8, 1979, pp. 1025-1034.

White, D.J., Take, W.A. & Bolton, M.D. 2003, "Soil deformation measurement using particle image velocimetry (PIV) and photogrammetry", *Geotechnique,* vol. 53, no. 7, pp. 619-631.

Wijewickreme, D. & Weerasekara, L. 2010, "Full-scale testing of buried extensible pipes subject to axial soil loading", *7th International Conference on Physical Modelling in Geotechnics, ICPMG 2010,* June 28 – July 1, 2010, pp. 657-662.

Wijewickreme, D. & Weerasekara, L. 2015, "Analytical modeling of field axial pullout tests performed on buried extensible pipes", *International Journal of Geomechanics,* vol. 15, no. 2, pp. 1-12.

Woodworth-Lynas, C., Nixon, D., Phillips, R. & Palmer, A. 1996, "Subgouge deformations and the security of Arctic marine pipelines", *Proceedings of the Offshore Technology Conference*, May 6 - 9, 1996, pp. 657-664.

Wright, B., Hnatiuk, J. & Kovacs, A. 1981, "Multi-year pressure ridges in the Canadian Beaufort Sea", *Coastal Engineering,* vol. 5, pp. 125-145.

Wu, W. 1990, "The behaviour of very loose sand in the triaxial compression test: Discussion", *Canadian Geotechnical Journal,* vol. 27, no. 1, pp. 159-162.

Yang, W. 2009, *Physical Modeling of Subgouge Deformations in Sand*, M.Eng., Memorial University of Newfoundland.

Yang, J. & Li, X. 2004, "State-Dependent Strength of Sands from the Perspective of Unified Modeling", *Journal of Geotechnical and Geoenvironmental Engineering,* vol. 130, no. 2, pp. 186-198.

Yang, Q.S. & Poorooshasb, H.B. 1997, "Numerical modeling of seabed ice scour", *Computers and Geotechnics,* vol. 21, no. 1, pp. 1-20.

Yimsiri, S., Soga, K., Yoshizaki, K., Dasari, G.R. & O'Rourke, T.D. 2004, "Lateral and upward soil-pipeline interactions in sand for deep embedment conditions", *Journal of Geotechnical and Geoenvironmental Engineering,* vol. 130, no. 8, pp. 830-842.

Yoshizaki, K. & Sakanoue, T. 2004, "Analytical study on soil-pipeline interaction due to large ground deformation", *13th World Conference on Earthquake Engineering*, 13p.

Zarnani, S. & Bathurst, R.J. 2009, "Influence of constitutive model on numerical simulation of EPS seismic buffer shaking table tests", *Geotextiles and Geomembranes,* vol. 27, no. 4, pp. 308-312.

Zarnani, S. & Bathurst, R.J. 2008, "Numerical modeling of EPS seismic buffer shaking table tests", *Geotextiles and Geomembranes,* vol. 26, no. 5, pp. 371-383.

Zhu, F. 1998, *Centrifuge modelling and numerical analysis of bearing capacity of ring foundations on sand*, Ph.D., Memorial University of Newfoundland.

9 Appendices

Appendix A – Physical Pipe/Soil Interaction Test Dataset

Table 9.1. Experimental lateral pipe/soil interaction data

Ref./Sand	Test	H/D	D	D/t	N_{qh}	γ_d	D_r	ϕ'	Test
Trautmann (1983) CU Filter Sand	6	1.5	0.102	15.9	6.5	14.8	0.0	31.0	DS
	8	1.5	0.102	15.9	6.0	14.8	0.0	31.0	DS
	15	1.5	0.102	15.9	6.5	14.8	0.0	31.0	DS
	7	3.5	0.102	15.9	7.5	14.8	0.0	31.0	DS
	16	3.5	0.102	15.9	6.9	14.8	0.0	31.0	DS
	18	3.5	0.102	15.9	7.3	14.8	0.0	31.0	DS
	20	5.5	0.102	15.9	7.9	14.8	0.0	31.0	DS
	21	8.0	0.102	15.9	11.2	14.8	0.0	31.0	DS
	31	11.0	0.102	15.9	10.7	14.8	0.0	31.0	DS
	10	1.5	0.324	34.1	7.2	14.8	0.0	31.0	DS
	11	1.5	0.324	34.1	7.3	14.8	0.0	31.0	DS
	17	1.5	0.324	34.1	7.1	14.8	0.0	31.0	DS
	12	3.5	0.324	34.1	10.6	14.8	0.0	31.0	DS
	13	3.5	0.324	34.1	10.7	14.8	0.0	31.0	DS
	52	3.5	0.324	34.1	10.9	14.8	0.0	31.0	DS
	45	1.5	0.102	15.9	7.9	16.4	0.51	36.0	DS
	26	3.5	0.102	15.9	7.9	16.4	0.51	36.0	DS
	27	3.5	0.102	15.9	7.9	16.4	0.51	36.0	DS
	29	3.5	0.102	15.9	7.2	16.4	0.51	36.0	DS
	30	3.5	0.102	15.9	7.2	16.4	0.51	36.0	DS
	46	5.5	0.102	15.9	10.7	16.4	0.51	36.0	DS
	51	8.0	0.102	15.9	12.8	16.4	0.51	36.0	DS
	48	11.0	0.102	15.9	12.5	16.4	0.51	36.0	DS
	49	11.0	0.102	15.9	12.5	16.4	0.51	36.0	DS
	22	1.5	0.102	15.9	8.4	17.7	0.86	44.0	DS
	23	3.5	0.102	15.9	10.9	17.7	0.86	44.0	DS
	24	5.5	0.102	15.9	14.8	17.7	0.86	44.0	DS
	25	8.0	0.102	15.9	17.1	17.7	0.86	44.0	DS
	32	11.0	0.102	15.9	22.6	17.7	0.86	44.0	DS
	14	3.5	0.324	34.1	11.0	17.7	0.86	44.0	DS

Ref./Sand	Test	H/D	D	D/t	N_{qh}	γ_d	D_r	ϕ'	Test
Dickin (1988) Erith Sand	-	0.5	1.0	-	3.41	14.25	-	39.2	TXC
	-	1.5	1.0	-	4.12	14.25	-	39.2	TXC
	-	2.5	1.0	-	4.22	14.25	-	39.2	TXC
	-	4.5	1.0	-	5.87	14.25	-	39.2	TXC
	-	6.5	1.0	-	5.22	14.25	-	39.2	TXC
	-	8.5	1.0	-	5.96	14.25	-	39.2	TXC
	-	0.5	1.0	-	8.95	15.99	-	46.6	TXC
	-	1.5	1.0	-	8.69	15.99	-	46.6	TXC
	-	2.5	1.0	-	8.89	15.99	-	46.6	TXC
	-	4.5	1.0	-	9.92	15.99	-	46.6	TXC
	-	6.5	1.0	-	10.35	15.99	-	46.6	TXC
	-	8.5	1.0	-	9.36	15.99	-	46.6	TXC
Hsu (1993, 2001) Taiwan Da Du River Sand	-	12.0	0.0381	6.0	7.98	15.21	0.21	33.0	DS
	-	14.0	0.0381	6.0	8.49	15.21	0.21	33.0	DS
	-	16.0	0.0381	6.0	8.50	15.21	0.21	33.0	DS
	-	0.50	0.0762	12.0	3.64	15.21	0.21	33.0	DS
	-	1.0	0.0762	12.0	4.51	15.21	0.21	33.0	DS
	-	2.0	0.0762	12.0	4.18	15.21	0.21	33.0	DS
	-	4.0	0.0762	12.0	5.43	15.21	0.21	33.0	DS
	-	6.0	0.0762	12.0	6.52	15.21	0.21	33.0	DS
	-	8.0	0.0762	12.0	7.66	15.21	0.21	33.0	DS
	-	10.0	0.0762	12.0	9.02	15.21	0.21	33.0	DS
	-	4.0	0.0381	6.0	11.28	17.17	0.94	42.0	DS
	-	10.0	0.0381	6.0	17.86	17.17	0.94	42.0	DS
	-	12.0	0.0381	6.0	20.25	17.17	0.94	42.0	DS
	-	14.0	0.0381	6.0	20.41	17.17	0.94	42.0	DS
	-	16.0	0.0381	6.0	20.58	17.17	0.94	42.0	DS
	-	0.5	0.0762	12.0	8.12	17.17	0.94	42.0	DS
	-	1.0	0.0762	12.0	6.83	17.17	0.94	42.0	DS
	-	2.0	0.0762	12.0	9.34	17.17	0.94	42.0	DS
	-	4.0	0.0762	12.0	11.71	17.17	0.94	42.0	DS
	-	6.0	0.0762	12.0	14.51	17.17	0.94	42.0	DS
	-	8.0	0.0762	12.0	17.12	17.17	0.94	42.0	DS
	-	10.0	0.0762	12.0	19.83	17.17	0.94	42.0	DS
	-	1.0	0.1524	24.0	2.89	15.20	0.21	33.0	DS
	-	2.0	0.1524	24.0	4.53	15.20	0.21	33.0	DS
	-	1.0	0.2286	36.0	3.13	15.20	0.21	33.0	DS
	-	2.0	0.2286	36.0	4.53	15.20	0.21	33.0	DS

Ref./Sand	Test	H/D	D	D/t	N_{qh}	γ_d	D_r	ϕ'	Test
Hsu (1993, 2001) Taiwan Da Du River Sand	-	1.0	0.3048	48.0	3.13	15.20	0.21	33.0	DS
	-	3.0	0.3048	48.0	6.56	15.20	0.21	33.0	DS
Calvetti et al. (2004)	-	1.35	0.05	-	8.77	-	0.20	32.0	TXC
	-	2.5	0.05	-	10.82	-	0.20	32.0	TXC
	-	3.5	0.05	-	11.82	-	0.20	32.0	TXC
	-	3.5	0.05	-	13.73	-	0.20	32.0	TXC
	-	3.5	0.05	-	14.71	-	0.20	32.0	TXC
	-	5.24	0.05	-	15.30	-	0.20	32.0	TXC
	-	7	0.05	-	16.12	-	0.20	32.0	TXC
	-	7	0.05	-	17.21	-	0.20	32.0	TXC
diPrisco & Galli (2006)	-	1.5	0.05	-	11.25	14.58	0.37	32.35	-
	-	2.5	0.05	-	12.28	14.58	0.37	32.35	-
	-	3.5	0.05	-	10.82	14.58	0.37	32.35	-
	-	1.5	0.05	-	19.37	16.48	1.00	42.12	-
	-	2.5	0.05	-	16.80	16.48	1.00	42.12	-
	-	3.5	0.05	-	19.98	16.48	1.00	42.12	-
Karimian et al. (2006) Fraser River	-	1.92	0.457	35.2	8.09	15.62	0.70	45.5	TXC
	-	1.92	0.457	35.2	7.93	15.64	0.70	45.5	TXC
	-	2.75	0.324	32.4	8.44	15.65	0.70	45.5	TXC
Sakanoue (2008) Chiba Sand	-	6.5	0.1	-	7.46	14.90	-	35.2	TXC
	-	6.5	0.1	-	11.3	16.20	-	42.0	TXC
Robert (2010) RMS Graded Sand	9	5.47	0.1204	-	14.7	16.59	0.36	-	-
	10	5.28	0.124	-	14.5	16.86	0.44	-	-
	11	5.28	0.124	-	15.2	16.98	0.47	-	-
Robert (2010) PERL Tokyo Gas Sand	10	5.7	0.1146	23.4	9.2	13.74	0.13	-	-
	9	5.7	0.1146	23.4	14.5	15.31	0.56	-	-
Burnett (2015) Synthetic Olivine Sand	12	1.0	0.6096	64.2	8.73	15.22	-	51.0	DS
	8	1.0	0.254	40.3	8.44	15.39	-	51.0	DS
	11	3.0	0.254	40.3	12.2	15.43	-	51.0	DS
	5	1.0	0.254	40.3	7.96	15.46	-	51.0	DS
	14	1.0	0.6096	64.2	8.95	15.57	-	51.0	DS
	7	1.0	0.2540	40.3	9.27	15.66	-	51.0	DS
	4	3.0	0.254	40.3	9.64	14.73	-	46.0	DS
	6	1.0	0.254	40.3	7.89	14.72	-	46.0	DS
	9	1.0	0.254	40.3	8.43	14.72	-	46.0	DS
	10	3.0	0.254	40.3	10.87	14.56	-	46.0	DS
	21	7.0	0.254	40.3	16.17	14.83	-	46.0	DS

Ref./Sand	Test	H/D	D	D/t	N_{qh}	γ_d	D_r	ϕ'	Test
Burnett (2015) Synthetic Olivine Sand	13	1.0	0.6096	64.2	8.07	14.56	-	46.0	DS
	15	1.0	0.6096	64.2	7.11	14.55	-	46.0	DS
Turner (2004) RMS Sand	2	6	0.1190	-	13.3	-	-	43.8	DS
	3	6	0.1190	-	14.8	17.46	-	44	DS
	6	6	0.1190	-	14.6	17.15	-	42	DS
	7	6	0.1190	-	13.6	17.42	-	43.7	DS
	8	6	0.1190	-	11.5	17.45	-	43.9	DS
	9	6	0.1190	-	12.5	17.29	-	42.9	DS
	10	6	0.1190	-	-	18.07	-	-	DS
	11	6	0.1190	-	-	15.87	-	-	DS
Turner (2004) Mix Sand	12	6	0.1190	-	11	17.36	-	41.5	DS
	13	15.4	0.1190	-	25.1	18.02	-	45.95	DS
	14	8.5	0.1190	-	22.2	18.11	-	46.75	DS
	16	19.7	0.1190	-	23.4	17.83	-	44.5	DS
	17	19.7	0.1190	-	25.9	17.88	-	44.85	DS
	24	6	0.1190	-	-	16.91	-	-	DS
	25	6	0.1190	-	-	16.69	-	-	DS

Appendix B – Synthetic Olivine Direct Shear Test Results

The author transported about 5 liters of the synthetic olivine sand from the Queen's Univ. GeoEngineering Center, to the geotechnical engineering laboratory at Memorial Univ. of Newfoundland (MUN). The sample was taken directly from the test pit where the large scale pipe/soil interaction tests were conducted. A series of direct shear tests were conducted on the soil at varying density and normal stress. Each test specimen had plan dimensions 60 mm x 60 mm, and the typical sample height was 25 mm. The following table summarizes the mass density, normal stress, peak direct shear friction angle, and residual (large displacement) friction angle. The shear stress for each test with horizontal shear box displacement is provided in Figure 9.1. The vertical displacement with horizontal shear box displacement is provided in Figure 9.2.

Table 9.2. Summary of direct shear tests conducted on synthetic olivine sand

Test	Mass Density, ρ (kg/m^3)	Normal Stress, σ_N (kPa)	$\phi'_{ds}{}^{p}$	$\phi'_{ds\text{-}ld}$
1	1727	300	47.4	42
2	1726	200	49.9	42
3	1729	96	50.7	42.6
4	1729	32	62.6	57
5	1725	16	67.6	59.6
6	1720	8	70.4	64.6
7	1546	300	40.5	40.5
8	1540	100	42.1	42.1
9	1515	16	47	47
10	1584	16	60.8	58.5

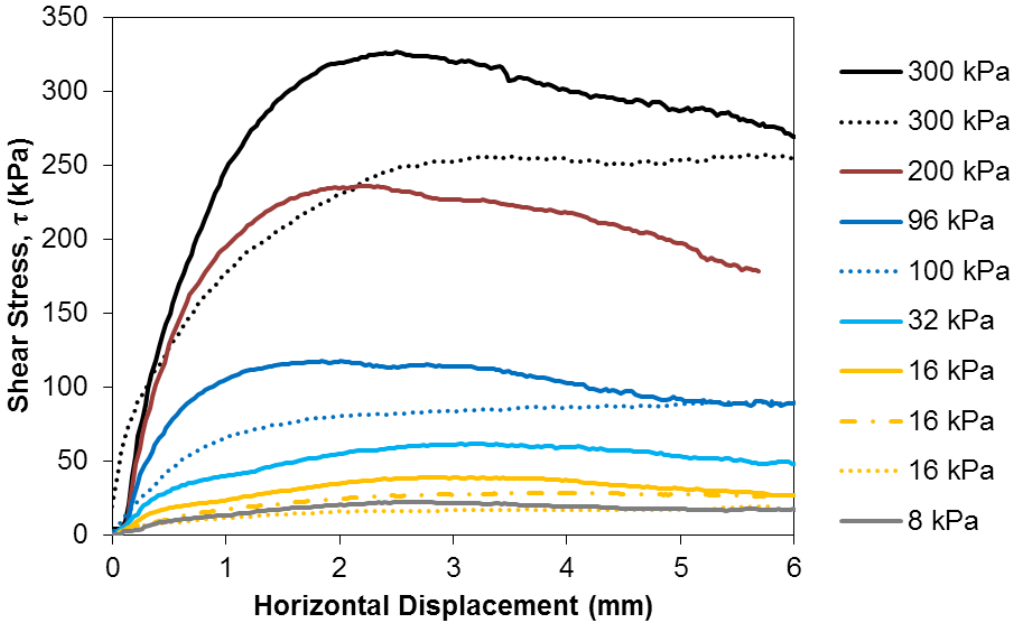

Figure 9.1. Shear stress vs. horizontal shear box displacement

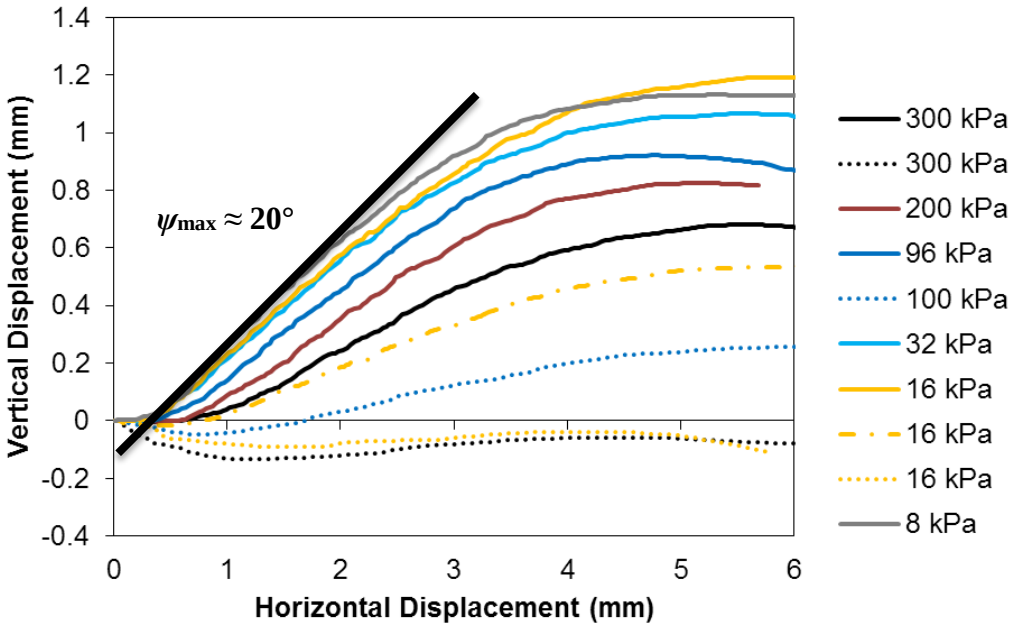

Figure 9.2. Vertical displacement vs. horizontal shear box displacement

Appendix C – Sand Characterization for Physical Test Dataset

Table 9.3. Sand characterization for physical lateral pipe/soil test dataset

Ref.	Trautmann (1983)/Olson (2009)	Robert (2010)/Olson (2009)	Robert (2010)	Karimian et al. (2006)	Calvetti et al. (2004)	Hsu (1993, 2001)	Sakanoue (2008)	Dickin (1988)	Audibert (1975)	Burnett (2015)
Sand Type	Cornell University (CU) Filter	RMS Graded (Cornell Sand)	PERL (Tokyo Gas)	Fraser River	--	Taiwan Da-Du River	Chiba	Erith	Carver	Synthetic Olivine
Roundness	SA to A	--	--	--	--	--	--	SR	SA to SR	A
G_s	2.74	2.694	2.646	2.70	--	2.68	2.7	2.65	--	3.2
e_{max}	0.817	0.705	0.946	0.94	--	0.787	--	--	--	--
e_{min}	0.469	0.393	0.5	0.62	--	0.514	0.559	--	--	--
d_{10} (mm)	0.23	0.24	0.13	0.15	--	0.21	--	0.125-0.25 (80%)	0.31	0.43
d_{30} (mm)	0.42	0.4	0.2	0.19	--	0.40	0.13		0.47	0.62
d_{50} (mm)	0.53	0.59	0.26	0.23	0.35	0.59	0.26	--	0.66	0.74
d_{60} (mm)	0.61	0.8	0.29	0.25	--	0.72	0.35		0.78	0.83
C_u	2.65	3.3	2.1	1.6	2.5	3.4	--	1.25	2.7	1.93
C_c	1.26	0.9	1.06	0.92	--	1.06	--	--		1.08

Appendix D – Sand Characterization for Plane Strain Test Data

Table 9.4. Sand characterization for plane strain test data

Reference	Shape	Type (ID)	G_s	C_u	d_{10}, d_{30}, d_{50}, d_{60} (mm)	e_{max}, e_{min}
Alshibli & Sture (2000)	A	Silica	2.65	1.5	1.13, 1.35, 1.6, 1.7	0.843, 0.677
Hanna (2001)	A	Silica (B)	2.63	2.3	- , - , 0.65, -	0.9, 0.5
Hanna (2001)	A	Silica (C)	2.64	2.0	- , - , 0.65, -	0.95, 0.4
Tong (1970)	A	Feldspar	2.57	1.8	0.11, 0.16, 0.19, 0.2	1.02, 0.63
Alshibli & Sture (2000)	SA	Quartz (No. 30)	2.65	1.33	0.43, 0.5, 0.54, 0.57	1.045, 0.752
Al-Hussaini (1973)	SA	Chattahoochee	2.66	2.2	0.24, 0.39, 0.48, 0.53	1.09, 0.59
Desrues & Hammad (1989)	SA	Hostun	2.65	1.7	- , - , 0.32, -	1.03, 0.68
Schanz & Vermeer (1996)	SA	Hostun	2.65	1.4	0.46, 0.54, 0.61, 0.64	1.04, 0.65
Tong (1970)	SA	Quartz (R. Mersey)	2.655	1.62	0.15, 0.21, 0.23, 0.24	0.86, 0.54
Tong (1970)	SR	Quartz (R. Welland)	2.66	-	-	0.94, 0.62
Dickin (1988)	SR	Quartz (Erith)	2.65	1.5	-	
Marachi et al. (1981)	R to SR	Quartz (Monterey)	-	1.25	- , - , 0.55, -	0.83, 0.53
Alshibli & Sture (2000)	R	Silica	2.65	1.95	0.12, 0.17, 0.22, 0.24	0.805, 0.486
Hanna (2001)	R	Silica (A)	2.65	2.4	- , - , 0.22, -	0.8, 0.4
Tong (1970)	R	Glass Ballatoni	3.03	-	-	0.79, 0.54

Appendix E – Sand Characterization for Triaxial Test Data

Table 9.5. Sand characterization for triaxial test data

	D_{50} (mm)	Fines (%)	e_{max}	e_{min}	G_s	e_Γ (1 kPa)	λ_{10}	M_{tc}	ϕ'_{cv}	Ref. *
(a) Laboratory Standard Sands										
Castro Sand C	0.28	0.0	0.990	0.660	-	0.988	0.038	1.37	34.0	1.
Hokksund	0.39	0.0	0.910	0.550	-	0.934	0.054	1.29	32.0	2.
Leighton Buzzard	0.12	5.0	1.023	0.665	-	0.972	0.054	1.24	31.0	2.
Monterey	0.37	0.0	0.820	0.540	-	0.878	0.029	1.29	32.0	2.
Ottawa	0.53	0.0	0.790	0.490	-	0.754	0.028	1.13	28.5	2.
Reid Bedford	0.24	0.0	0.870	0.550	-	1.014	0.065	1.29	32.0	2.
Ticino-4	0.53	0.0	0.890	0.600	2.67	0.986	0.056	1.24	31.0	2.
Ticino-8	0.53	0.0	-	-	-	0.943	0.031	-	31.0	2.
Ticino-9	0.53	0.0	-	-	-	0.970	0.050	-	31.0	2.
Toyoura	0.53	0.0	0.873	0.656	-	1.000	0.039	1.24	31.0	2.
Toyoura	0.16	0.0	0.981	0.608	2.65	1.043	0.085	-	31.0	2.
(b) Natural Sands										
Amauligak F-24	0.14	10.0	-	-	2.67	0.946	0.083	1.37	31.5	2.
Amauligak F-24	0.144	21.0	-	-	2.69	0.966	0.124	1.33	32.7	2.
Amauligak I-65	0.08	48.0	-	-	2.65	1.634	0.358	1.29	31.5	2.
Amauligak I-65	0.31	9.0	-	-	2.67	1.018	0.153	1.42	32.3	2.
Amauligak I-65	0.29	3.0	-	-	2.65	1.023	0.095	1.31	31.7	2.
Erksak	0.32	1.0	0.808	0.614	-	0.875	0.043	1.27	31.5	2.
Erksak	0.355	3.0	0.963	0.525	2.67	0.848	0.054	1.18	29.5	2.
Erksak	0.33	0.7	0.747	0.521	2.66	0.816	0.031	1.27	31.5	2.
Erksak	0.34	-	0.775	0.525	-	-	-	-	32.0	3.
Isserk	0.21	2.0	0.760	0.520	2.67	0.833	0.043	1.22	30.5	2.
Isserk	0.21	5.0	0.830	0.550	-	0.879	0.089	1.24	31.0	2.
Isserk	0.21	10.0	0.860	0.440	-	0.933	0.123	1.24	31.0	2.
Kogyuk	0.35	2.0	0.830	0.470	-	0.844	0.064	1.31	32.5	2.
Kogyuk	0.35	5.0	0.870	0.490	-	0.924	0.104	1.31	32.5	2.
Kogyuk	0.35	10.0	0.930	0.460	-	1.095	0.205	1.24	31.0	2.
Kogyuk	0.28	5.0	0.870	0.560	-	0.902	0.062	1.20	30.0	2.
Alaskan Beaufort	0.14	5.0	0.856	0.565	2.70	0.910	0.037	1.22	30.5	2.
Alaskan Beaufort	0.14	10.0	0.837	0.530	2.70	0.920	0.053	1.20	30.0	2.
Chek Lap Kok (Upper)	-	-	-	-	-	0.782	0.059	1.30	32.3	2.
Chek Lap Kok (Lower)	-	-	-	-	-	0.785	0.061	1.30	32.3	2.
Brasted River	0.26	-	0.788	0.471	2.68	-	-	-	32.6	4.
(c) Tailings sands										
Hilton Mines	0.2	2.5	1.050	0.620	-	1.315	0.170	1.42	35.0	2.
Oilsands Tailings	0.207	3.5	-	-	-	0.860	0.065	1.33	33.0	2.

* 1. Castro (1969) 2. Jefferies and Been (2006) 3. Vaid and Sasitharan (1991) 4. Cornforth (1973)

Appendix F – Relevant Publications: Ice/Soil/Pipeline Interaction in Cohesive Soil

OTC 22097

Continuum Modelling of Ice Gouge Events: Observations and Assessment

Kenton Pike, Donghee Seo, Memorial University of Newfoundland and Shawn Kenny, Memorial University of Newfoundland and Wood Group Chair in Arctic and Harsh Environments Engineering

Abstract

With the majority of estimated Arctic oil and gas reserves being held offshore, ice gouging will likely be a major consideration in the design of transport pipelines in these regions. The implications of the effects of ice gouging on buried pipelines are well understood. The ability to model this phenomenon using advanced numerical simulation tools has been proven in recent years, and is demonstrated in this paper. The uncertainty that revolves around these tools, due to limitations in the available physical dataset that can be utilized to validate the results, is discussed.

In this paper, a limited parametric study on the influence of ice keel attack angle and interface strength on the free-field subgouge displacement field, and subsequent effects on a buried pipeline is presented. The Coupled Eulerian Lagrangian finite element formulation available in ABAQUS/Explicit and the Arbitrary Lagrangian Eulerian formulation in LS-DYNA are used to conduct the numerical experiment. The results are shown and the observations are discussed in detail. Finally, an assessment in terms of the challenges of implementing the numerical tools in an engineering application is provided.

Introduction

Energy demand has promoted renewed interest in the exploration and field development of offshore hydrocarbon basins in the arctic and ice covered waters of the northern hemisphere. In these harsh environments, pipelines offer a safe and cost effective mode to transport hydrocarbon resources to the marketplace. The presence of ice features and potential interaction with the seabed impose significant engineering challenges for design, construction and operation of subsea pipelines. Key technical issues relate to establishing pipeline mechanical performance criteria and trenching requirements for pipeline protection that meet target safety levels and satisfy logistical and economic constraints.

Ice gouge events involve ice keel/seabed interaction, soil failure mechanisms, soil clearing processes and subgouge soil deformations [1,2]. As the magnitude of ice keel/seabed reaction forces can be an order greater than other conventional load events; such as anchor dragging and pullover, then direct ice/pipeline contact is not a viable design option for most ice gouge scenarios [3]. In the 1970's, the use of extremal statistics was considered sufficient to estimate the design gouge depth and corresponding trench depth requirements. Later, in the 1990's, it was realized this approach to avoid direct ice/pipeline contact was incomplete. This conclusion was primarily based on physical modelling studies highlighting the importance of subgouge soil deformations and potential effects on the pipeline mechanical response [4,5]. Early continuum finite element (FE) modelling investigations on ice gouge events did not achieve the research objectives due to technology constraints [1,6]. Two-dimensional simulation models were not representative of the ice gouge clearing processes, and three-dimensional analysis encountered numerical instability due to excessive element distortion.

Advancements in computer hardware and software technology, however, have provided a more robust numerical modelling framework to simulate ice gouge events. The Arbitrary Lagrangian Eulerian (ALE) method allows for the analysis of large deformation, large strain problems while maintaining high quality mesh regions within Lagrangian or Eulerian frameworks where mesh points move independently of material points. Numerical modelling strategies; such as ALE, have been used in the fields of fluid-structure interaction, large deformation solid mechanics and geomechanics with respect to nonlinear, large deformation problems involving strain localization [7].

Recent investigations have simulated free-field ice gouge events using ALE methods [1,2,8-12]. Data from free-field ice gouge events, simulated using centrifuge modelling, has been used to calibrate the numerical procedures [5,13]. Although other physical datasets exist [e.g. 14-18], there is limited information available in the public domain. The calibration and assessment of these numerical procedures has generally only examined seabed reaction forces, soil stress and strain field

POAC'11
Montréal, Canada

Proceedings of the 21st International Conference on
Port and Ocean Engineering under Arctic Conditions
July 10-14, 2011
Montréal, Canada

POAC11-100

Advanced Numerical Simulations of Ice Gouge Events and Implications for Engineering Design

Pike, K. [1], Kenny, S. [1,2] and Hawlader, B. [1]

[1]Memorial University of Newfoundland, St. John's, Canada
[2]Wood Group Chair in Arctic and Harsh Environments Engineering,
Memorial University of Newfoundland, St. John's, Canada

ABSTRACT

Over the past decade, numerical simulation tools have been developed to examine complex, nonlinear problems such as free-field ice gouge and coupled ice keel/seabed/pipeline interaction events. These advanced numerical models have provided valuable insight to failure mechanisms, clearing processes and subgouge soil deformations during ice gouge events. The basis for a validated simulation tool, however, has not been presented in the public domain. Published studies to date have provided results from sensitivity analysis based on partial calibration of the numerical modelling procedures. An assessment of the numerical simulation tools capabilities and technical constraints is needed. This study will address some of the major issues and discuss the path forward. Validation of the numerical modelling procedures to simulate ice gouge events will mitigate uncertainty, improve safety and reduce cost. This may unlock constraints that currently hinder the development of hydrocarbon resources, using subsea infrastructure, in ice gouge environments.

INTRODUCTION

Energy demand has promoted renewed interest in the exploration and field development of offshore hydrocarbon basins in the arctic and ice covered waters of the northern hemisphere. In these harsh environments, pipelines offer a safe and cost effective mode to transport hydrocarbon resources to the marketplace. The presence of ice features and potential interaction with the seabed impose significant engineering challenges for design, construction and operation of subsea pipelines. Key technical issues relate to establishing pipeline mechanical performance criteria and trenching requirements for pipeline protection that meet target safety levels and satisfy logistical and economic constraints.

Ice gouge events involve ice keel/seabed interaction, soil failure mechanisms, soil clearing processes and subgouge soil deformations (Kenny et al., 2007a,b). In the 1970's, the use of extremal statistics was considered sufficient to estimate the design gouge depth and corresponding trench depth requirements. Later, in the 1990's, it was realized this approach to avoid direct ice/pipeline contact was incomplete. This conclusion was primarily based on physical modelling studies highlighting the importance of subgouge soil deformations and

Proceedings of the Twenty-second (2012) International Offshore and Polar Engineering Conference
Rhodes, Greece, June 17–22, 2012

ISBN 978-1-880653-94-4 (Set); ISSN 1098-6189 (Set)

www.isope.org

Advanced Continuum Modeling of the Ice Gouge Process: Assessment of Keel Shape Effect and Geotechnical Data

Kenton Patrick Pike and Shawn Patrick Kenny
Memorial University of Newfoundland
St. John's, Newfoundland and Labrador, Canada

ABSTRACT

Ice gouging demands trenches of appropriate depths to protect pipelines and other seabed facilities from loads associated with ice keel impacts and subgouge soil deformations. Design trenches are a sensitive decision in terms of development economics, hence, the rationale for selecting trench depths must be well understood. Subgouge deformations are a critical and complex issue that requires careful consideration of expected gouge characteristics, ice keel shape, seabed sediment type and soil stratification, and ice keel properties. This paper describes a numerical study assessing the effect of keel shape on subgouge deformations. A brief review of publicly available geotechnical data is given and the effects of varying soil strength profiles are assessed. A method for determining constitutive model parameters suitable for solving the ice gouge problem based on undrained shear strength, overconsolidation ratio and index properties is described.

KEY WORDS: Ice gouge; coupled eulerian lagrangian; seabed penetration; rigidity index; shape effect

INTRODUCTION

Ice gouging is a critical factor in the design of oil and gas transport pipelines in reserve-rich offshore Arctic regions. Researchers widely acknowledge the negative effects that subgouge soil deformations can have on buried pipelines and have studied this issue in depth. The ice-soil-pipeline interaction process has recently been successfully modelled using advanced continuum finite element (FE) methods by several groups. As these models are extremely complex and often simplified assumptions are made for important details, there is uncertainty surrounding the use of these tools. These key assumptions, in the context of validating the numerical response are discussed.

A major concern for buried pipelines is the negative impact that subgouge deformations may impose on them. The geometric characteristics of the gouging ice feature influence soil failure mechanisms affecting subgouge deformations. The effects of ice keel attack angle, gouge width and gouge depth are generally understood. The frontal shape of the advancing keel has seen limited assessment. This paper provides results from a preliminary study examining this shape effect.

To design and install a buried pipeline in offshore arctic regions, it is foremost that the sea bottom surficial sediment type and soil profile is well defined. With regards to continuum numerical modelling to aid the design process, the most important aspect is the selection of an appropriate constitutive soil model that is capable of predicting observed soil behaviour. Complex constitutive models may require parameters that are uncommon to everyday engineering practice. The implementation of advanced numerical tools in an engineering application is a challenge in terms of data availability. This challenge is discussed and a review of accessible information concerning geotechnical zonation and properties in areas prone to ice gouging is provided.

BASELINE ANALYSIS

A series of nine centrifuge ice gouge tests in clay were conducted by Lach (1996) on the beam centrifuge at the University of Cambridge. In these tests, the "model iceberg" was represented by a rigid body that was free to heave and pitch. Test 5 (of 9) was stated as a baseline case to which the effect of soil state, keel angle, width, and buoyant weight of the model iceberg were compared. The 10 m wide model iceberg in test 5 achieved a steady-state gouge depth of 1.21 m. The soil undrained shear strength varied with depth and was highly overconsolidated in the upper third of the prepared soil bed. It was deemed that the modeled gouge event was sufficiently rapid for essentially undrained conditions to prevail (Lach et al, 1993).

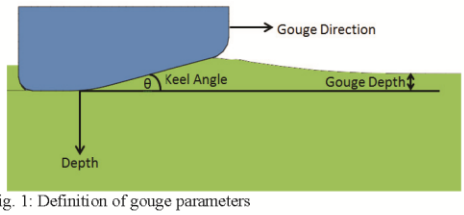

Fig. 1: Definition of gouge parameters

The Coupled Eulerian Lagrangian (CEL) finite element formulation available in ABAQUS/Explicit was used in developing a prototype numerical model of Test 5 mentioned above. The dimensions of the centrifuge test were scaled accordingly to develop a numerical test bed

OTC-22004-PP

Advancement of CEL Procedures to Analyze Large Deformation Pipeline/Soil Interaction Events

K. Pike, Doctoral Candidate and S. Kenny, Wood Group Chair Arctic and Harsh Environments Engineering, Memorial University of Newfoundland

Abstract

Pipeline/soil interaction involves complex interplay of soil type and strength, burial depth, pipeline displacement path, contact mechanics, soil strain localization, and pipe feed-in among other parameters. Further complexity is introduced in fully coupled models to simulate ice keel/seabed/pipeline interaction events for example, where ice keel/seabed interface contact, keel bearing pressures and subgouge soil deformations are important. In order to establish confidence in more complex models, sub-interaction scenarios can be extracted and simplified. This study focuses on pipeline/soil interaction in plane strain form to examine the effects that burial depth and pipe direction of travel have on soil failure mechanisms. The coupled eulerian lagrangian (CEL) method, used in this study, is shown to provide consistent results with past work. The implications of this work in the context of modelling ice keel/seabed/pipeline interaction and model verification are discussed.

Introduction

Offshore and onshore arctic pipelines are often buried to provide protection from environmental loads, natural hazards and mitigate risk. These pipeline systems may be subject to large deformation geohazards such as ice gouging, frost heave, thaw settlement, seismic fault movement and lateral spreading due to liquefaction. The imposed ground displacement field typically involves large soil deformations and strain based failure mechanisms. Load transfer effects will develop pipe bending and axial feed-in response that may result in significant global and local pipeline deformations.

In the past decade, there has been significant development in computational hardware and software technology. This has provided a robust simulation framework to address complex, nonlinear large deformation problems involving contact, material plasticity, strain localization and failure mechanisms. An example of this technology advancement is the Arbitrary Lagrangian Eulerian (ALE) formulation that has been used in the fields of fluid-structure interaction, large deformation solid mechanics and geomechanics [1].

For offshore arctic pipelines, there have been numerous studies illustrating the application of ALE techniques to analyse ice gouge events and assess load effects on buried infrastructure [2-8]. This has provided a more rational basis to address uncertainty and develop practical engineering solutions. The calibration and assessment of these numerical procedures has been primarily based on data from physical models of free-field ice gouge events at 1-g in flume tanks and at higher gravitational fields in reduced-scale centrifuge studies [9-11]. These studies, however, have only examined seabed reaction forces, soil stress and strain field distribution and horizontal subgouge soil deformations. Other factors such as geometric properties of the side and frontal berm, clearing process mechanisms, and vertical and lateral subgouge soil deformation has seen limited assessment [2,8]. Furthermore, the presence of buried infrastructure, such as a pipeline, has a significant influence on the subgouge deformation field and soil strain gradient with depth beneath the ice keel [2].

Consequently, detailed investigations are required to establish confidence in the numerical procedures with respect to data and model uncertainty, and the corresponding relative error. Demonstration of the numerical procedures to adequately simulate nonlinear contact mechanics, interface behaviour, local soil strain gradients, and failure mechanisms with minimal discretization error while maintaining computational efficiency is a demanding technical challenge. In addition, soil constitutive models may need to be improved or developed so that large soil deformation or multi-phase behavior can be simulated.

A significant volume of data exists on soil loads and failure mechanisms for interaction events with buried rigid pipelines. This database has been established through reduced-scale centrifuge simulations, larger-scale physical test programs, and

OTC 23731

Numerical Pipe/Soil Interaction Modelling: Sensitivity Study and Extension to Ice Gouging

Pike, K., Kenny, S.

Abstract

In predicting the geotechnical constraint against pipeline movement using finite element methods, the treatment of the pipe/soil interface contact behavior is of utmost importance, especially in the tangential direction. This study focuses on the interpretation of soil resistance to axial pipe movement in cohesive soil material for oblique loading, specifically the effect of changing the interface shear stress limit and friction coefficient. The main finding of the present study is that the incorporation of a shear stress limit in the definition of tangential shear behavior has a considerable effect on the axial pipeline reaction forces. Without the shear stress limit, the maximum axial forces due to oblique pipe movement are effectively doubled in comparison to a limit equal to half of the undrained shear strength. A simple analytical method is provided to estimate the maximum oblique axial soil resistance in undrained conditions. The effect of changing the assumed frictional behavior is also discussed with respect to predicting the soil reaction forces acting on an ice keel during an undrained gouging event in cohesive soil.

Introduction

Pipeline systems, that are surficial or buried, may be subject to oblique geotechnical loads as a result of large deformation geohazards, pipeline out-of-straightness and uneven seabed terrain. The geotechnical restraint against oblique pipe movement is a function of soil type and strength, burial depth, oblique displacement angle, contact mechanics, and soil strain localization among other parameters. Properly accounting for the mechanical behavior at the pipe/soil contact interface is a critical aspect in estimating the forces exerted on the pipe during oblique displacement. In the context of ice keel/soil/pipeline interaction, it is equally important to capture the correct behavior at the ice keel/soil interface, as this will affect the characterization of the geotechnical loads imposed on the pipeline system. Further complexity is introduced as the pipeline mechanical response is dependent on the ice keel bearing pressure, subgouge soil deformation and axial pipeline feed-in. This study focuses on pipeline/soil interaction in three-dimensional continuum form to examine the effect that the definition of interface contact properties has on axial interaction forces; the effect on lateral interaction forces has been previously studied (Pike and Kenny, 2011b, 2012a). In this study, the Arbitrary Lagrangian Eulerian (ALE) method (Abaqus/Explicit) is used to study oblique lateral-axial pipe/soil interaction. The coupled Eulerian Lagrangian (CEL) method is used to simulate ice keel/soil interaction. The geotechnical constraint in each case is discussed with respect to the applied contact interface properties.

This paper presents some preliminary analysis suggesting that there is uncertainty in predicting the axial geotechnical restraint against oblique lateral-axial pipe movement. The results show that the inclusion of a shear stress limit at the pipe/soil interface can reduce the interaction forces significantly. Further work is necessary to calibrate and validate the numerical modeling procedures. A physical testing program will be carried out to assess relatively simple pipe/soil interaction scenarios to examine contact mechanics and interface behavior in greater detail. The outcomes from this laboratory testing and physical modelling program will be used to assess and advance the capabilities of advanced numerical methods such as ALE to account for contact mechanics, strain localization and soil failure mechanisms.

Pipe/Soil Interface Friction Sensitivity

A sensitivity study was conducted to examine the effects of the assumed friction properties for oblique pipe-soil interaction in undrained cohesive material. For undrained loading events, it is common to assume that an interface shear stress limit (τ_{max}) exists that is some fraction (f) of the undrained shear strength (S_u) of the cohesive material (e.g. C-CORE,

Proceedings of the 2012 9th International Pipeline Conference
IPC2012
September 24-28, 2012, Calgary, Alberta, Canada

IPC2012-90055

LATERAL-AXIAL PIPE/SOIL INTERACTION EVENTS: NUMERICAL MODELLING TRENDS AND TECHNICAL ISSUES

Kenton Pike
Memorial University of Newfoundland
St. John's, NL, Canada

Shawn Kenny
Memorial University of Newfoundland
St. John's, NL, Canada

ABSTRACT

In predicting the geotechnical constraint against pipeline movement, it is imperative to properly account for frictional behavior at the pipe-soil interface, especially in the axial direction. The translation angle of the pipeline varies in reality; hence the effects of this variance must be captured in relation to the interaction forces in the lateral, axial and vertical directions. This study focuses on lateral-axial pipeline movement in cohesive soil material. The main finding of the present study is that the incorporation of a shear stress limit in the definition of tangential shear behavior has a considerable effect on the axial pipeline reaction forces. Without the shear stress limit, the axial forces are effectively doubled in comparison to a limit equal to half of the undrained shear strength. There is less of an effect on lateral interaction.

INTRODUCTION

Pipeline-soil interaction is a multi-parametric problem involving soil type and strength, burial depth, pipeline displacement path, contact mechanics, soil strain localization, and pipe feed-in among other parameters. In reality, pipeline out-of-straightness and uneven seabed terrain can give rise to both oblique geotechnical loading and oblique pipeline displacement. Extending pipeline-soil interaction to the context of more complex scenarios, such as ice keel-soil-pipeline interaction, adds further complexity. In order to properly account for the effects of ice keel bearing pressure, subgouge soil deformation and axial pipeline feed on pipe response, it is critical that the pipe-soil interface behavior is accurately taken into account. Therefore, confidence must be established primarily for the pipe-soil sub-interaction scenario. This study focuses on pipeline/soil interaction in three-dimensional continuum form to examine the effect that pipe trajectory has on axial and lateral interaction forces. The arbitrary lagrangian eulerian (ALE) method (Abaqus/Explicit) is used for the majority of the study, while some demonstrative examples are performed using the coupled eulerian lagrangian (CEL) method. The implications of this work in the context of modelling ice keel/seabed/pipeline interaction and model verification are discussed.

This paper presents some preliminary analysis suggesting that there is uncertainty in predicting axial interaction forces. The results show that the inclusion of a shear stress limit on the pipe-soil interface reduces the interaction forces significantly. Further work is necessary to calibrate and validate the numerical modeling procedures. A physical testing program will be carried out to assess relatively simple pipe-soil interaction scenarios.

NUMERICAL MODEL

To model axial-lateral pipe soil interaction a three-dimensional continuum finite element model was developed using Abaqus/Explicit. The ALE method with an adaptive soil mesh domain was employed to accommodate mesh distortion due to large soil displacement imparted by movement of the pipeline. The model dimensions and typical mesh resolution used for the results presented are shown in Figure 2. The burial depth ratio (ratio of depth to pipe springline to pipe diameter) is approximately 3.6 and the pipe diameter is 0.41 m (16 in.). The soil is assumed to be uniform undrained clay with medium

Offshore pipelines and ice gouge geohazards: Comparative performance assessment of decoupled structural and coupled continuum models

Pike, Kenton[1] and Kenny, Shawn[2,3]

[1] PhD Candidate, Department of Civil Engineering, Faculty of Engineering and Applied Science, Memorial University of Newfoundland, St. John's, NL, A1B 3X5, kenton.pike@mun.ca

[2] Associate Professor, Department of Civil and Environmental Engineering, Faculty of Engineering and Design, Carleton University, 1125 Colonel By Drive, Ottawa, ON, K1S 5B6, shawn.kenny@carleton.ca

[3] Adjunct Professor, Department of Civil Engineering, Faculty of Engineering and Applied Science, Memorial University of Newfoundland, St. John's, NL, A1B 3X5, spkenny@mun.ca

1 Abstract

Offshore pipelines in ice environments may be subject to unique geohazards such as seabed ice gouging. These events involve nonlinear processes including large deformations and strains, contact mechanics, and failure mechanisms.

Current pipeline engineering design practice employs decoupled, structural finite element modelling procedures to assess system demand and capacity. The inherent error and uncertainty within this approach drives conservative engineered solutions. Physical modelling and continuum numerical simulation tools complement this engineering framework to improve confidence in predicted outcomes.

The relative performance of engineering models, used in current practice, and numerical simulation tools, including structural and continuum finite element modelling procedures, to predict the deformation and strain response of a buried pipeline subject to an ice gouge event is examined. Refinements to the numerical modeling procedures and establishing a consistent and compatible reference framework for the performance evaluation differentiate this study from others, which are subsets of the current investigation. For the parameter analysis conducted, within an equivalent reference framework, the outcomes demonstrate key factors, including superposition error and directional load decoupling, that influence model error may not be as significant as previously considered. The scope and extent of this outcome is not fully understood and requires further investigations to delineate the significance across a wider parameter range.

Appendix G – Relevant Publications: Pipe/Soil Interaction in Cohesionless Soil

Advanced analysis of pipe/soil interaction accounting for strain localization

Kenton Pike, Shawn Kenny, Bipul Hawlader
Memorial University of Newfoundland, St. John's, NL, Canada

ABSTRACT
Advanced simulation tools with suitable capabilities for large deformation geomechanics must account for realistic soil behaviour. The coupled Eulerian-Lagrangian (CEL) method available in Abaqus/Explicit allows severe soil deformations, can be utilized with user defined constitutive behavior and scales well with respect to parallel processing simulation times. The CEL method (and other methods) is applied in this study to simulate pipe/soil interaction in dense sand. Strain-softening behavior is accounted for using a modified Mohr-Coulomb constitutive model that accounts for decreasing friction and dilation angles with increasing plastic shear strain.

RÉSUMÉ
Les instruments de simulation avancés avec les capacités convenables de la grande déformation geomechanics doivent représenter le comportement de sol réaliste. La méthode disponible dans Abaqus/Explicit, coupled Eulerian-Lagrangian (CEL), permet des déformations de sol sévères, peut être utilisé avec la conduite constitutive définie d'utilisateur et la balance bien en ce qui concerne les temps de simulation de traitement parallèles. La méthode CEL (et d'autres méthodes) est appliquée dans cette étude pour simuler l'action réciproque de pipe/sol dans le sable dense. La conduite adoucissant effort est estimée pour utiliser un Mohr-coulomb modifié constitutive le modèle qui représente la friction diminuante et les angles de dilatation avec l'augmentation de l'effort de tondage de plastique.

1 INTRODUCTION

The use of advanced numerical models to simulate large deformation problems that are primarily geotechnical, e.g., ice keel/pipe/soil interaction, is a powerful tool to study complex phenomena that are very expensive and difficult to model physically. It is of course essential that the numerical tool is properly calibrated and validated before it is extended with a broader range of parameters; and even then, care must be taken to ensure that the numerical results can be interpolated or extrapolated to the real situation. To tend towards reality, numerical tools should appropriately capture load transfer mechanisms, contact mechanics, reaction forces, and failure mechanisms.

This study presents the use of three advanced numerical tools to study pipe/soil interaction using Abaqus/Explicit. The analysis framework used for the analyses presented in the paper will be validated against large scale tests in progress. The explicit package contains methods for modeling large deformations that are inherent to geohazards that can cause interaction between buried pipelines and the surrounding soil. The main feature that is required is the capability to accommodate severe deformations. The Arbitrary Lagrangian Eulerian (ALE) method utilizes remeshing techniques to enable larger deformations than pure Lagrangian analyses. The coupled Eulerian-Lagrangian (CEL) method uses a fixed mesh whereby the material can flow through without experiencing mesh distortion. A third method available in Abaqus/Explicit, smooth particle hydrodynamics (SPH) is a meshless method that can also accommodate severe deformations without convergence problems. Each of these modeling techniques is discussed in detail.

In order to capture realistic failure mechanisms in large deformation geomechanics in dense sands, it is imperative to account for strain softening to initiate and propagate strain localizations, i.e., shear bands. Strain softening models must account for reduced friction and dilation angles with continuous shear strains to account for softening of the yield surface and control dilatancy. This paper applies a modified Mohr-Coulomb model that was developed by Anastasopoulos et al. (2007). A small number of test cases were performed to demonstrate the capability of each of the aforementioned numerical tools and identify limitations and notable aspects when analyzing the obtained results.

2 PIPE/SOIL INTERACTION IN DRY SAND

Audibert & Nyman (1975) described the general soil failure mechanisms in shallow burial model pipe/soil interaction tests in sand as being comprised of three (3) distinct zones: (1) an almost vertical active zone towards the back of the pipe, (2) a soil wall above the pipe that extended to the surface and (3) a passive wedge bound by a logarithmic spiral in front of the pipe; Trautmann & O'Rourke (1985) described similar mechanisms. Turner (2004) identified three shear bands associated with the failure mechanisms described above, as illustrated in Figure 1.

As discussed by Nobahar et al. (2001), soil materials exhibit non-linear behavior, and correct numerical simulation requires advanced constitutive models including a relatively large number of parameters and complicated calibration procedures. The occurrence of strain localization (shear bands) at large shear deformation further complicates numerical modeling. Strain localization is not a continuum phenomenon; rather, it is characterized by a length scale.

Effects of Geohazards on Energy Pipelines: Technology Framework Supporting Engineering Design and Emerging Tools

Kenton Pike
Memorial University of Newfoundland, St. John's, NL, Canada
Shawn Kenny
Carleton University, Ottawa, ON, Canada
Bipul Hawlader
Memorial University of Newfoundland, St. John's, NL, Canada
Ian D. Moore
Queen's University, Kingston, ON, Canada

ABSTRACT

Energy pipeline transportation systems are typically buried and may be subject to large deformation ground movements associated with operational parameters and natural events. Although modern computational tools provide robust, effective and efficient platforms for simulation of pipeline/soil interaction events, a comprehensive technology framework is needed to advance technical solutions in support of engineering design with confidence. This technology framework requires laboratory tests to refine constitutive models used within numerical algorithms and physical models to calibrate and evaluate the computational simulations. In this paper, elements of this technology framework are examined and results discussed from a research program developing advanced computational simulation tools, to assess the effects of large deformation ground movement events on buried pipelines. The importance of mesh topology, large deformations and strains, nonlinear material behaviour, contact mechanics and bifurcations on the strategies employed to develop the computational tools are explored. A discussion on current and future trends is also presented.

RÉSUMÉ

Systèmes de transport par pipeline de l'énergie sont généralement enterrés et peuvent être soumis à d'importants mouvements de sol de déformation associés à des paramètres de fonctionnement et les événements naturels. Bien que les outils informatiques modernes offrent des plates-formes robustes et efficaces pour la simulation d'événements d'interaction pipeline/sol, un cadre technologique globale est nécessaire pour promouvoir des solutions techniques à l'appui de la conception technique avec confiance. Ce cadre de la technologie exige des tests de laboratoire pour améliorer les modèles de comportement utilisés dans les algorithmes numériques et des modèles physiques pour calibrer et évaluer les simulations informatiques. Dans le présent document, les éléments de ce cadre de la technologie sont examinés et discutés les résultats d'un programme de recherche de développer des outils de simulation informatiques avancées, afin d'évaluer les effets des grands événements déformation de mouvements de terrain sur les canalisations enterrées. L'importance de la topologie de maillage, de grandes déformations et les souches, comportement des matériaux non linéaire, mécanique du contact et bifurcations sur les stratégies utilisées pour développer les outils de calcul sont explorées. Une discussion sur les tendances actuelles et futures est également présenté.

1 INTRODUCTION

Energy pipeline transportation systems provide an efficient, safe and economic mode of transport for the delivery of hydrocarbon products from resource areas to industrial and civilian end users. In 2012, the Canadian Energy Pipeline Association estimated the pipeline industry contributed more than $8.8 billion to the Canadian Gross Domestic Product (GDP) and more than $84 billion of hydrocarbon products for export. There is an estimated 830,000 km network of gathering, transmission and distribution pipelines servicing the oil and gas energy industry (CEPA, 2014). The estimated failure frequency for energy pipelines, measured as an annual frequency per 100 km pipeline system, was 10^{-3} to 10^{-2} for North America and Europe for data records back to 1980 (ASME, 2008).

The vast majority of onshore and offshore energy pipelines are in direct contact with the soil surface or are fully buried. The pipeline may be embedded within the soil to address requirements for flow assurance (e.g. thermal resistance), operational loads (e.g. upheaval buckling), external forces due to wave and current loads (e.g. on-bottom stability), and to afford protection from natural geohazards (e.g. slope failure, fault movement, ice gouging) and anthropogenic activities (e.g. fishing gear impact, excavator damage, mine subsidence). In this study, the effects of large deformation geohazards on buried energy pipelines are examined.

Buried pipelines are subject to operational loads (i.e. differential temperature and pressure relative to the ambient environment) and may be subject to soil loads or deformations due to geohazards (e.g. subsidence, seismic faulting, long-term slope movement). Current industry practice for simulating the pipeline-soil

Numerical and constitutive model development to aid design against pipeline geohazards

by Kenton Pike*[1], Prof. Shawn Kenny[2], and Prof. Bipul Hawlader[1]

1 Faculty of Engineering and Applied Science, Memorial University of Newfoundland, St John's, NL, Canada

2 Department of Civil and Environmental Engineering, Faculty of Engineering and Design, Carleton University, Ottawa, ON, Canada

PIPELINE GEOHAZARDS ARE seabed or ground movements that may cause damage to a pipeline. Displacement or movement of soils will affect onshore and offshore pipelines, whether they are laid on the seabed (i.e. surficial) or are buried. Although modern computational tools provide robust, effective, and efficient platforms for simulation of pipeline/soil interaction events, a comprehensive technology framework is needed to advance technical solutions in support of engineering design with confidence. This technology framework requires laboratory tests to refine constitutive models used within numerical algorithms and physical models to calibrate and evaluate the computational simulations. In this paper, elements of this technology framework are examined and results discussed from a research programme developing advanced computational simulation tools, to assess the effects of large-deformation ground-movement events on buried pipelines.

PIPELINES ARE OFTEN embedded within the soil to meet requirements for flow assurance, mitigate the effects of external loads (such as waves and currents), and for protection against geohazards and anthropogenic activities (for example, excavation, trawl gear). Some common pipeline geohazards are slope failures, fault movements, earthquakes, and erosion by waves or currents. In an arctic context, ice gouging, pit formation, and strudel scour pose significant threats to pipeline integrity [1]. Arctic pipeline geohazards exist in geotechnical zones containing cohesive and granular soil deposits: for example, extreme ice gouging due to ice ridges on the Canadian Beaufort shelf occurs predominantly in softer clay-type sediments, while areas with sandier sediments are gouged less severely [2]. On the Grand Banks offshore Newfoundland however, iceberg gouging occurs in areas of medium dense to dense sands [3].

Conventional practice for buried pipeline design is to idealize (Fig. 1) pipe-soil interaction using a series of beam and spring elements to represent the pipe and soil mechanical response, respectively [4]. The ALA (2001) guidelines [4] provide recommendations for both clay, assuming total stress conditions, and sand, assuming effective stress conditions, soil types. Structural-type finite-element (FE) modelling procedures are commonly used to simulate the pipe/soil interaction using beam and discrete orthogonal (axial, lateral, and vertical uplift and bearing) spring elements (for example Kenny *et al.* [5]). Recent studies have demonstrated this approach is better suited to problems with simple loading conditions (such as operational loads or small local displacements of soil or supports), but has been shown to be overly conservative for complex three-dimensional ground-deformation events, such as ice keel/soil/pipe interaction [6-8]. Peek and Nobahar [8] discuss in detail the underlying assumptions in applying the structural model to the ice/soil/pipeline interaction scenario, and suggest the structural model superposition error is of critical importance. Recent physical and computational modelling studies have highlighted the significance of independent spring response and lack of coupled interaction behaviour, which are considered to be important parameters for large deformation and oblique loading ground movement events, remains to be fully quantified [9, 10].

Advances in software and hardware technology have led to recent developments of three-dimensional continuum FE tools to help assess and address the above-mentioned technical

*Corresponding author's contact details:
tel: +1 709 689 3170
email: kenton.pike@mun.ca